



HAL
open science

Chemical modification and multi-function applications of nanocellulose

Ge Zhu

► **To cite this version:**

Ge Zhu. Chemical modification and multi-function applications of nanocellulose. Organic chemistry. Université Grenoble Alpes [2020-..], 2021. English. NNT : 2021GRALI084 . tel-03528736

HAL Id: tel-03528736

<https://theses.hal.science/tel-03528736v1>

Submitted on 17 Jan 2022

HAL is a multi-disciplinary open access archive for the deposit and dissemination of scientific research documents, whether they are published or not. The documents may come from teaching and research institutions in France or abroad, or from public or private research centers.

L'archive ouverte pluridisciplinaire **HAL**, est destinée au dépôt et à la diffusion de documents scientifiques de niveau recherche, publiés ou non, émanant des établissements d'enseignement et de recherche français ou étrangers, des laboratoires publics ou privés.

THÈSE

Pour obtenir le grade de

DOCTEUR DE L'UNIVERSITE GRENOBLE ALPES

Spécialité : **Matériaux, Mécanique, Génie Civil, Electrochimie**

Arrêté ministériel : 25 mai 2016

Présentée par

Ge ZHU

Thèse dirigée par **Alain DUFRESNE, Professeur, Grenoble INP**

préparée au sein du **Laboratoire Génie des Procédés Papetiers**
dans l'**École Doctorale IMEP-2 – Ingénierie, Matériaux,
Mécanique, Environnement, Énergétique, Procédés,
Production**

Chemical modification and multi-function applications of nanocellulose

Thèse soutenue publiquement le **27 octobre 2021**,
devant le jury composé de :

Dr, Nadia EI KISSI

Directeur de recherche au Laboratoire Rhéologie et Procédés, Président

Dr, Ana VILLARES

Chargée de recherche à l'INRAE de Nantes, Rapporteur

Pr. Etienne FLEURY

Professeur à l'INSA de Lyon, Rapporteur

Pr. Alain DUFRESNE

Professeur à Grenoble INP, Directeur de thèse



Acknowledgements

First of all, I would like to thank the members of my jury. Pr. Ana Villares and Pr. Etienne Fleury, thank you for accepting the invitation to review my PhD work. Pr. Nadia El Kissi, thank you for accepting to be president of the jury. Thanks a lot, to all the jury members for the constructive and relevant discussion both about the manuscript and the PhD defense.

I would like to thank my thesis supervisor Pr. Alain Dufresne, for his patience, support and guidance throughout my doctoral studies. His observations, advice and immense enthusiasm give me a good impression. Without his contribution, this thesis would not have been accomplished. I also would like to thank Pr. Gérard Mortha and Nathalie Marlin, who gave me lots of advice in my every year's CSI report.

Special thanks go to Cécile, Bertine and Jean-Luc (CERMAV), who provided access and instructions on the laboratory equipment and chemicals reservation. Thanks to Laura, who helped me with the operation of this thesis for 6 months during her internship. And thanks to the China Scholarship Council for the financial support.

I am grateful to all the PhD students and postdocs in the team of LGP2 for their kind help and suggestions. Thanks a lot to my colleagues and friends: Bai, Huan, Marlène, Ahlem, Bastien, Lorelei, Gabriel, Florian, João, Enrique, Clémentine, Maxime, Eva, Malek, Axelle, Claire, Etienne, Amina, Hugo and everyone else. My sincere thanks also go to LGP2 staff who always helped me: Sylvie, Franck, Lydia, Chu, Stephane, Mohamed, Philippe and others. I am also fortunate to have some great friends outside of work: Kaifeng, Hong, Shun, Lili, Wei, Xinming, Lingling, Chunjing, Wanqiu for their friendship and unfailing support.

My deepest thanks go to my parents and sister for their support and trust for all my life. My utmost thanks go to my wife, Chan, who without his sincere love, support, and patience in every single moment, I never ever could start and accomplish this thesis. Last but not the least, my biggest gift in the past three years is my little daughter. She was born on July 3, 2020 and brought us countless joys.

Acknowledgements

Table of Contents

Scientific Publications	9
Appendix and Abbreviations	11
General Introduction	15
Chapter 1. Literature Review	25
1.1 Brief Introduction to Nanocellulose	25
1.1.1 Cellulose Nanocrystals (CNC).....	25
1.1.2 Cellulose Nanofibrils (CNF)	27
1.1.3 Bacterial Cellulose (BC).....	28
1.2 Structure and Properties of Nanocellulose.....	29
1.2.1 Surface Chemistry and Colloidal Stability	29
1.2.2 Specific Surface Area	29
1.2.3 Aspect Ratio.....	30
1.2.4 Mechanical Properties	30
1.2.5 Rheological Properties.....	31
1.2.6 Thermal Properties	31
1.2.7 Optical Properties.....	32
1.2.8 Barrier Properties	33
1.3 Surface Modification of Nanocellulose.....	33
1.3.1 Physical Adsorption of Surfactants	33
1.3.2 TEMPO-mediated oxidation.....	36
1.3.3 Esterification.....	38
1.3.4 Silylation	40
1.3.5 Grafting onto	42
1.3.6 Grafting from.....	47
1.4 End Modification of Nanocellulose.....	53
1.5 Functional Applications of Nanocellulose.....	58
1.5.1 Biological Scaffolds	58
1.5.2 Thermal Insulation.....	59

1.5.3 Optical Functions	60
1.5.4 Adsorption and Environmental Treatment	61
1.5.5 Electrically Conducting Materials.....	68
1.5.6 EMI Shielding	69
1.6 References.....	70
Chapter 2. Synergistic reinforcing and cross-linking effect of thiol-ene-modified cellulose nanofibrils on natural rubber	93
Abstract	93
Keywords.....	93
2.1 Introduction.....	94
2.2 Experimental sections.....	96
2.2.1 Materials.....	96
2.2.2 CNF end modification via aldimine condensation.....	96
2.2.3 CNF end modification via carboxyamine condensation	97
2.2.4 Preparation of NR/CNF-x and NR/CNF-SH-x nanocomposites ..	97
2.2.5 Characterization.....	98
2.3 Results and discussion	100
2.3.1 Analysis of reducing end modification of CNF.....	100
2.3.2 Click reaction between CNF-SH-a and NR	104
2.3.3 Morphology of the nanocomposites.....	107
2.3.4 Mechanical properties of the nanocomposites	108
2.3.5 Successive tensile tests	110
2.3.6 Dynamic mechanical analysis.....	113
2.4 Conclusions.....	116
2.5 References.....	117
Chapter 3. Cellulose nanocrystal-mediated assembly of graphene oxide in natural rubber nanocomposites with high electrical conductivity.....	127
Abstract	127
Keywords.....	127
3.1 Introduction.....	128

3.2 Experimental	129
3.2.1 Materials.....	129
3.2.2 Preparation of CNC/GO nanohybrids.....	129
3.2.3 Preparation of NR/CNC/GO and NR/GO Composites.....	130
3.2.4 Characterization.....	130
3.3 Results and Discussion.....	131
3.3.1 Morphology and Thermal Stability.....	132
3.3.2 Zeta potential	134
3.3.3 FTIR spectra	135
3.3.4 SEM.....	136
3.3.5 Electrical Conductivity	137
3.3.6 Mechanical property.....	138
3.4 Conclusions.....	139
3.5 References.....	140
Chapter 4. Multifunctional Nanocellulose/Carbon Nanotubes Composite Aerogels for High-efficiency Electromagnetic Interference Shielding	149
Abstract	149
Keywords.....	149
4.1 Introduction.....	150
4.2 Experimental Section.....	152
4.2.1 Materials.....	152
4.2.2 Chemical functionalization of CNC with GTMAC.....	152
4.2.3 Preparation of nanocellulose-CNTs composite aerogels.....	153
4.2.4 Nanocellulose chemical and morphological analysis	153
4.2.5 Nanocellulose-based aerogels characterization.....	154
4.3 Results and Discussion.....	156
4.3.1 Synthesis of cationic cellulose nanocrystals.....	156

4.3.2 Nanocellulose chemical and morphological analysis	157
4.3.3 Characterization of nanocellulose-CNT aerogels	162
4.3.4 Electrical conductivity	166
4.3.5 Mechanical properties	168
4.3.6. EMI shielding Performance	170
4.4 Conclusions.....	173
4.5 References.....	174
General conclusion	185
Extended French Abstract	191

Scientific Publications (2018–2021)

Articles in Scientific Journals

1. Zhu G, Dufresne A. Conductive natural rubber/carbon black nanocomposites via thiol-modified cellulose nanofiber templated assembly. in preparation.
2. Zhu G, Giraldo Isaza L, Huang B, Dufresne A. Nanocellulose/carbon nanotubes composite aerogels for highly efficient electromagnetic interference shielding. *ACS Sustainable Chemistry & Engineering*, 2021, under review.
3. Zhu G, Dufresne A. Synergistic reinforcing and cross-linking effect of thiol-ene-modified cellulose nanofibrils on natural rubber. *Carbohydrate Polymers*, 2022, 278: 118954.
4. Zhu G, Giraldo Isaza L, Dufresne A. Cellulose nanocrystal-mediated assembly of graphene oxide in natural rubber nanocomposites with high electrical conductivity. *Journal of Applied Polymer Science*, 2021, 138(48): 51460.

Invited Book Chapters

1. Zhu G, Lin N. Surface chemistry of nanocellulose[J]. *Nanocellulose: from fundamentals to advanced materials*. John Wiley & Sons, 2019: 115-153.
2. Zhu G, Lin N, Dufresne A. Nanopolysaccharides in Environmental Treatments[J]. *Advanced Functional Materials from Nanopolysaccharides*. Springer, Singapore, 2019: 255-282.

Refereed Conference Proceedings

1. Ge Zhu, Alain Dufresne (2021/02), Poster, “Cellulose Composite Aerogel for Highly Efficient Electromagnetic Interference Shielding”, The 4th EPNOE Junior Scientist Meeting, online.
2. Ge Zhu, Alain Dufresne (2019/10), Poster, “Conductive natural rubber/carbon black nanocomposites via thiol-modified cellulose nanofiber templated

assembly”, 6th EPNOE International Polysaccharides Conference, Aveiro, Portugal.

3. Ge Zhu, Alain Dufresne (2019/05), Poster, “End-modified CNF enhancement to nanocomposites (natural rubber)”, The 5th PolyNat International Industries Forum, Grenoble, France.
4. Ge Zhu, Alain Dufresne (2019/03), Poster, “Dual-enhancement effect of electrostatic adsorption and chemical crosslinking for nanocellulose-based aerogels”, International Workshop: "On the future of glycoscience? ", Grenoble.

Appendix and Abbreviations

ABS	Acrylonitrile butadiene styrene
Ac	Sodium triacetoxyborohydride
AFM	Atomic force microscopy
AGU	Anhydroglucose unit
AHH	6-Amino-1-hexanethiol hydrochloride
AMC	7-amino-4-methylcoumarin
AMEO	Aminopropyltriethoxysilane
ATRP	Atom transfer radical polymerization
BC	Bacterial cellulose
BiBB	2-bromoisobutyrylbromide
BNA	Beycostat NA
BriB	2-bromoisobutyryl bromide
Br-MPBr	2-bromo-2-methylpropionyl bromide
CDMIPS	Chlorodimethyl isopropylsilane
ChNC	Chitin nanocrystals
CI	Crystallinity index
ClSO ₃ H	Chlorosulfonic acid
CNC	Cellulose nanocrystals
CNF	Cellulose nanofibrils
CNTs	Carbon nanotubes
CVD	Chemical vapor deposition
DMA	Dynamic mechanical analysis
DMAP	4-dimethylaminopyridine
DMF	N,n'-dimethylformamide
DMSiCl	Dimethylchlorosilanes
DMSO	Dimethyl sulfoxide

DO	Degree of oxidation
DODA-Br	Dimethyldioctadecylammonium bromide
DS	Surface substitution
EA	Elemental analysis
EDC	1-[3-(dimethylamino)propyl]-3-ethylcarbodiimide methiodide
EMI	Electromagnetic interference
FESEM	Field-emission gun scanning electron microscope
FTIR	Fourier-transform infrared spectroscopy
GO	Graphene oxide
GPC	Gel permeation chromatography
GTMAC	Glycidyltrimethylammonium chloride
HMC	7-hydrazino-4-methylcoumarin
LRP	Living radical polymerization
MCC	Microcrystalline cellulose
NaSA	Sodium salicylate
NHS	N-hydroxysuccinimide
NR	Natural rubber
OTR	Oxygen transmission rates
PCL	Polycaprolactone
PDMAEMA	Poly [2-(N,N-dimethyl amino) ethyl methacrylate]
PDMS	Polydimethylsilane
PEDOT	Poly(3,4-ethylene dioxythiophene)
PEG	Poly(ethylene glycol)
PEI	Polyethylenimine
PEO	Polyoxyethylene
PLA	Poly(lactic acid)
PLLA	Poly(L-Lactide)
PMDETA	Pentamethyl-diethylenetriamine

PMMA	Polymethyl Methacrylate
PMMAZO	Poly{6-[4-(4-methoxyphenylazo) phenoxy] hexyl methacrylate}
Poly(TBA)	Poly(tert-butyl acrylate)
PP	Polypropylene
PPgMA	Polypropylene
PS	Poly(styrene)
PSS	Poly(styrene sulfonate)
PtBA	Poly(t-butyl acrylate)
PU	Polyurethane
PVDF	Poly vinylidene fluoride
ROP	Opening polymerization
SA	Sodium alginate
SEC	Size exclusion chromatography
SEM	Scanning electron microscopy
SET-LR	Single electron transfer-living radical polymerization
TCNF	Tempo-oxidized cellulose nanofibrils
TEA	Triethylamine
TEC	Thermal expansion coefficient
TEM	Transmission electron microscope
TEMPO	2,2,6,6-Tetramethylpiperidine-1-oxyl
T _g	Glass-rubber transition temperature
TGA	Thermogravimetric analysis
THF	Tetrahydrofuran
WPU	Water-Borne Polyurethane
XPS	X-ray photoelectron spectroscopy
XRD	X-ray diffraction
ZP	Zeta potential

General Introduction

Cellulose is the most widespread renewable polymer resource with an amphiphilic structure in the biosphere, with an annual production of about 7.5×10^{10} tons.¹ Its main sources include the following: (i) agricultural residues (corn stalks, bagasse, coconut husks, rice straw, corn cobs, wheat husks, rice husks and palm oil residues); (ii) wood; (iii) food waste; (iv) crops; and (v) wastepaper and cardboard boxes.²⁻⁴ This virtually unlimited supply of sustainable cellulose provides a material with excellent physical and chemical properties that can be used in a wide range of applications.⁵ In industry, cellulose is widely used in paper, textiles, explosives and dietary fibers.⁶ Cellulose contains both crystalline and amorphous regions, and nanocellulose, the nanoscale form of cellulose, can be prepared by a mechanical or chemical process, that can be combined with enzymatic treatment. The repeating unit of the cellulose chain is a dimer of D-glucose. The end of each cellulose chain contains a hemiacetal group, which provides asymmetry in the direction of the cellulose chain.

Nanocellulose has many of the excellent properties of cellulose, including biocompatibility, low density, non-toxicity, and biodegradability. It also has some distinctive properties such as high reinforcing ability, mechanical strength and adjustable self-assembly properties in aqueous media, mainly attributed to the unique size, shape, surface chemistry, high aspect ratio and high crystallinity of these nanoparticles.⁷ The term "nanocellulose" includes different cellulose-based nanomaterials whose chemical and physical properties often vary depending on their source, but especially on their extraction method: cellulose nanocrystal (CNC), cellulose nanofiber (CNF), and bacterial nanocellulose (BNC). CNC and CNF are obtained using top-down methods, involving chemical or mechanical treatment, respectively. Mechanical shearing or acid hydrolysis will first weaken and destroy the amorphous domains and smallest crystalline regions to produce the desired nanocellulose. CNC is a highly crystalline rod-like fragment obtained by acid

hydrolysis down to the nanoscale. CNF can be obtained by mechanical shearing of cellulosic fibers, usually preceded by controlled acid hydrolysis, or chemical or enzymatic pretreatment, allowing the energy consumption associated with this treatment to be reduced. It has different structures and surface chemistry, depending on the production method, and is typically longer than CNC, at the micron scale.⁷ BNC is obtained by a bottom-up method, using bacterial cultures to synthesize nanocellulose. Other names for nanocellulose materials can be found in the literature, including nanofibrillated cellulose, microfibrillated cellulose, cellulose nanofibrils, cellulose nanowhiskers, cellulose whiskers, and nanocrystalline cellulose.

In the 21st century, the demand for food, water and energy is exploding due to the growing world population and rapid economic development. Society should rely more on renewable biomass resources to meet the growing demand. Sustainable development of society should focus more on products that are recyclable, easily degradable, friendly to the environment, and low health and safety risks. Based on its Young's modulus of 100-130 GPa, large specific surface area and high crystallinity, nanocellulose is expected to be used for manufacturing and developing various new valuable applications with low environmental and social impact.⁸ Nanocellulose is derived from renewable and abundant biomass resources and is considered as a good alternative to petroleum as a source of biofuels and various chemicals. Nanocellulose can now be produced industrially, and its production can reach several tons per day.⁹

Surface chemical modification is very important for the functionality and processability of the nanocomposites, so we focus on the large number of current surface modifications in Chapter 1. The surface properties of nanocellulose can be easily adjusted by physical and chemical modification methods.¹⁰⁻¹² Surface modified nanocellulose is an excellent platform that can be designed according to different objectives. The wide applications of nanocellulose are limited by its poor dispersibility in nonpolar solvents, incompatibility and poor interfacial adhesion to hydrophobic substrates. To solve this problem, researchers have attempted to modify the surface and

the structure of nanocellulose, mainly targeting the physical and chemical modification of the pendant surface hydroxyl groups(-OH). Different strategies of physical and chemical modification of nanocellulose aim at improving the efficiency of the separation process and changing the surface hydrophilicity/hydrophobicity, thus improving the compatibility and dispersion of nanocellulose in specific media.

Nanocellulose has very diverse applications in many interdisciplinary fields. When nanocellulose is intertwined, nanocomposites with high mechanical properties and porosity can be formed, such as nanopaper, nanocellulose films, aerogels and hydrogels. Its application can be extended to papermaking, environmental remediation, biology, medical, optoelectronics and engineering applications.¹³⁻¹⁶ Nanocellulose can be used to reinforce nanocomposites due to the formation of a strong continuous network in the matrix with high tensile stiffness and strength.^{17,18} The development and application of rigid nanocellulose reinforced polymer composites from renewable resources have attracted widespread attention in science and industry. With the growing public awareness for environmental friendliness and sustainability, nanocellulose is destined to play an important role in commercial applications.

This PhD project entitled “Chemical modification and multi-function applications of nanocellulose” started from October 2018. This thesis manuscript is a summary of my research on nanocellulose over the last three years with four chapters.

In **Chapter 1**, a literature review on the general background of the research is presented, focusing on the modification of nanocellulose and its functional applications.

In **Chapter 2**, two different end-modification methods of CNF are proposed. The thiol group (-SH) has been successfully grafted at the reducing end of CNF, which acts as a cross-linking site to react with unsaturated carbon chains of a rubber matrix. We explored the synergistic enhancement of biobased nanoscale reinforcing CNF-SH nanoparticles, which also possessed cross-linking sites for covalent coupling.

In **Chapter 3**, a green and powerful strategy for preparing cellulose nanocrystal (CNC)/graphene oxide (GO)/natural rubber (NR) nanocomposites hosting a 3D hierarchical conductive network was investigated.

In **Chapter 4**, a reliable aerogel system was prepared by integrating Tempo- oxidized

cellulose nanofibrils (TCNF), cationic cellulose nanocrystals (CNC), and sodium alginate (SA), with carbon nanotubes (CNTs) at various concentrations. This aerogel was used as an electromagnetic interference (EMI) shielding biomaterial.

References

- (1) Thomas, B.; Raj, M. C.; Athira, K. B.; Rubivah, M. H.; Joy, J.; Moores, A.; Drisko, G. L.; Sanchez, C. Nanocellulose, a Versatile Green Platform: From Biosources to Materials and Their Applications. *Chem. Rev.* **2018**, *118* (24), 11575–11625.
- (2) Metzger, J. O.; Hüttermann, A. Sustainable Global Energy Supply Based on Lignocellulosic Biomass from Afforestation of Degraded Areas. *Naturwissenschaften* **2009**, *96* (2), 279–288.
- (3) Mood, S. H.; Golfeshan, A. H.; Tabatabaei, M.; Jouzani, G. S.; Najafi, G. H.; Gholami, M.; Ardjmand, M. Lignocellulosic Biomass to Bioethanol, a Comprehensive Review with a Focus on Pretreatment. *Renewable and Sustainable Energy Reviews* **2013**, *27*, 77–93.
- (4) Limayem, A.; Ricke, S. C. Lignocellulosic Biomass for Bioethanol Production: Current Perspectives, Potential Issues and Future Prospects. *Progress in energy and combustion science* **2012**, *38* (4), 449–467.
- (5) Abitbol, T.; Rivkin, A.; Cao, Y.; Nevo, Y.; Abraham, E.; Ben-Shalom, T.; Lapidot, S.; Shoseyov, O. Nanocellulose, a Tiny Fiber with Huge Applications. *Current opinion in biotechnology* **2016**, *39*, 76–88.
- (6) Habibi, Y. Key Advances in the Chemical Modification of Nanocelluloses. *Chemical Society Reviews* **2014**, *43* (5), 1519–1542.
- (7) Klemm, D.; Kramer, F.; Moritz, S.; Lindström, T.; Ankerfors, M.; Gray, D.; Dorris, A. Nanocelluloses: A New Family of Nature-based Materials. *Angewandte Chemie International Edition* **2011**, *50* (24), 5438–5466.
- (8) Usov, I.; Nyström, G.; Adamcik, J.; Handschin, S.; Schütz, C.; Fall, A.; Bergström, L.; Mezzenga, R. Understanding Nanocellulose Chirality and

- Structure–Properties Relationship at the Single Fibril Level. *Nature communications* **2015**, *6* (1), 1–11.
- (9) Reid, M. S.; Villalobos, M.; Cranston, E. D. Benchmarking Cellulose Nanocrystals: From the Laboratory to Industrial Production. *Langmuir* **2017**, *33* (7), 1583–1598.
- (10) Biyani, M. V.; Foster, E. J.; Weder, C. Light-Healable Supramolecular Nanocomposites Based on Modified Cellulose Nanocrystals. *ACS Macro Letters* **2013**, *2* (3), 236–240.
- (11) Carlmark, A.; Malmström, E. Atom Transfer Radical Polymerization from Cellulose Fibers at Ambient Temperature. *Journal of the American Chemical Society* **2002**, *124* (6), 900–901.
- (12) Roy, D.; Semsarilar, M.; Guthrie, J. T.; Perrier, S. Cellulose Modification by Polymer Grafting: A Review. *Chemical Society Reviews* **2009**, *38* (7), 2046–2064.
- (13) Zander, N. E.; Dong, H.; Steele, J.; Grant, J. T. Metal Cation Cross-Linked Nanocellulose Hydrogels as Tissue Engineering Substrates. *ACS applied materials & interfaces* **2014**, *6* (21), 18502–18510.
- (14) Wang, Z.; Carlsson, D. O.; Tammela, P.; Hua, K.; Zhang, P.; Nyholm, L.; Strømme, M. Surface Modified Nanocellulose Fibers Yield Conducting Polymer-Based Flexible Supercapacitors with Enhanced Capacitances. *ACS nano* **2015**, *9* (7), 7563–7571.
- (15) Luo, W.; Schardt, J.; Bommier, C.; Wang, B.; Razink, J.; Simonsen, J.; Ji, X. Carbon Nanofibers Derived from Cellulose Nanofibers as a Long-Life Anode Material for Rechargeable Sodium-Ion Batteries. *Journal of Materials Chemistry A* **2013**, *1* (36), 10662–10666.
- (16) Weishaupt, R.; Siqueira, G.; Schubert, M.; Kämpf, M. M.; Zimmermann, T.; Maniura-Weber, K.; Faccio, G. A Protein-Nanocellulose Paper for Sensing Copper Ions at the Nano-to Micromolar Level. *Advanced Functional Materials* **2017**, *27* (4), 1604291.

- (17) Khalil, H. A.; Bhat, A. H.; Yusra, A. I. Green Composites from Sustainable Cellulose Nanofibrils: A Review. *Carbohydrate polymers* **2012**, *87* (2), 963–979.
- (18) Siró, I.; Plackett, D. Microfibrillated Cellulose and New Nanocomposite Materials: A Review. *Cellulose* **2010**, *17* (3), 459–494.

CHAPTER 1.

Literature Review on Nanocellulose

Table of contents – Chapter 1

Chapter 1. Literature Review	25
1.1 Brief Introduction to Nanocellulose.....	25
1.1.1 Cellulose Nanocrystals (CNC).....	25
1.1.2 Cellulose Nanofibrils (CNF).....	27
1.1.3 Bacterial Cellulose (BC).....	28
1.2 Structure and Properties of Nanocellulose.....	29
1.2.1 Surface Chemistry and Colloidal Stability	29
1.2.2 Specific Surface Area.....	29
1.2.3 Aspect Ratio	30
1.2.4 Mechanical Properties.....	30
1.2.5 Rheological Properties	31
1.2.6 Thermal Properties.....	31
1.2.7 Optical Properties.....	32
1.2.8 Barrier Properties	33
1.3 Surface Modification of Nanocellulose	33
1.3.1 Physical Adsorption of Surfactants.....	33
1.3.2 TEMPO-mediated oxidation.....	36
1.3.3 Esterification.....	38
1.3.4 Silylation.....	40
1.3.5 Grafting onto.....	42
1.3.6 Grafting from	47
1.4 End Modification of Nanocellulose	53

1.5 Functional Applications of Nanocellulose	58
1.5.1 Biological Scaffolds	58
1.5.2 Thermal Insulation	59
1.5.3 Optical Functions	60
1.5.4 Adsorption and Environmental Treatment	61
1.5.5 Electrically Conducting Materials	68
1.5.6 EMI Shielding	69
1.6 References	70

Chapter 1. Literature Review

Nanocelluloses, including cellulose nanocrystals, cellulose nanofibrils and bacterial cellulose, have become fascinating building blocks for the design of new biomaterials. Hundreds of scientific articles or patents have been published on nanocellulose research over the past twenty years, even if most studies focus on their basic physical and chemical properties as reinforcing phase and liquid crystalline self-ordering property. Yet, owing to their hydrophilic nature, their applications are generally limited to hydrophilic or polar media or matrices, which restricts their development. With the presence of a large number of chemical functionalities, mainly hydroxyl groups, within the structure of nanocellulose, these novel nanoparticles provide a unique platform for significant surface modification with the purpose of changing surface properties. These chemical modifications are prerequisites, sometimes unavoidable, to adapt the interfacial properties of nanocellulose substrates or to adjust their hydrophilic–hydrophobic balance. In addition, surface modification can introduce functional groups to the surface of nanocellulose contributing to specific properties, further extending their use to highly sophisticated applications.

1.1 Brief Introduction to Nanocellulose

1.1.1 Cellulose Nanocrystals (CNC)

Cellulose microfibrils formed during cellulose biosynthesis are 2-20 nm in diameter, depending on the source, and can be several micrometers in length. Each microfibril consists of crystalline domains interspersed with disordered amorphous regions. The preparation of cellulose nanocrystals involves a chemical hydrolysis process to dissolve the amorphous chains and release crystalline domains from cellulose fibers. Although few examples of producing CNC through processes involving enzymatic hydrolysis were reported,^{1,2} the main process for the isolation of CNC from cellulose fibers is based on strong acid hydrolysis, such as sulfuric acid(H₂SO₄), hydrochloric acid(HCl), phosphoric acid(H₃PO₄) etc. The first attempt to hydrolyze cellulose fibers with strong

acids (HCl/H₂SO₄) appeared in 1947 as reported by Nikerson and Habrle.³

Depending on the hydrolyzing agent, cellulose nanocrystals possessing different surface groups and surface chemistry can be prepared. Hydrolysis with hydrochloric acid preserves the hydroxyl groups of native cellulose but leads to less stable aqueous suspensions.⁴ With the combination of TEMPO and hypochlorous sodium, surface hydroxyl groups of cellulose nanocrystals can be selectively transformed into carboxyl groups, which may be useful for subsequent modification.⁵ The resulting CNC exhibits a crystalline structure similar to the original cellulose fibers. Typical procedures currently employed for the extraction of CNC consist of subjecting pure cellulosic materials to strong acid hydrolysis under strictly controlled conditions of temperature, agitation, and time. The nature of the acid and source of cellulose are extremely important for the properties of the prepared CNC (as shown in Figure 1.1).

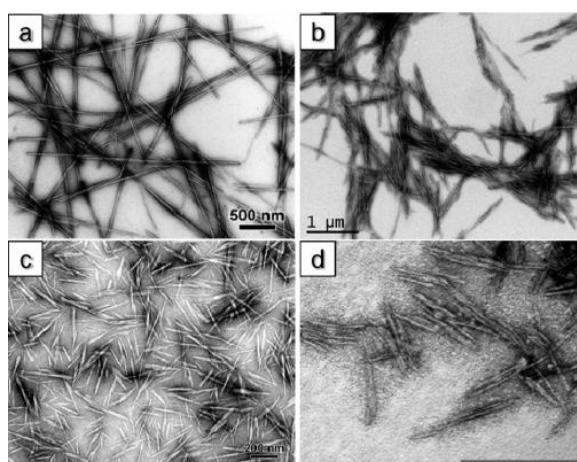


Figure 1.1 Transmission electron micrographs from a dilute suspension of CNC obtained from different sources: (a) tunicate,⁶ (b) bacterial cellulose,⁷ (c) ramie⁸ and (d) eucalyptus wood⁹.

Due to the hydrophilic character of cellulose nanocrystals, water is the preferred processing medium for solution blending because of their good dispersion and high stability in water, especially for cellulose nanocrystals prepared using sulfuric acid.¹⁰ Consequently, cellulose nanocrystals can easily be used as filler to reinforce hydrophilic polymers; however, when organic solvents are used as the blending medium and the matrix is a hydrophobic polymer the use of cellulose nanocrystals is

greatly restricted. Furthermore, the sulfate half-ester groups on the surface of cellulose nanocrystals, derived from hydrolysis with sulfuric acid, usually result in a mismatch between the thermal stability of cellulose nanocrystals and the thermoprocessing temperature. At this time, physical and chemical modifications are considered to regulate the chemical structure and hydrophilic/hydrophobic properties of the surface of cellulose nanocrystals.

1.1.2 Cellulose Nanofibrils (CNF)

As introduced by Turbak and co-workers in the 1980s,¹¹ the process for isolating cellulose nanofibrils (CNF) consists in the disintegration of cellulose fibers along their long axis. Simple mechanical methods in combination with enzymatic or chemical pretreatments are included in the preparation of CNF. Cellulosic fibers are disintegrated into their sub-structural fibrils having lengths in the micron scale and widths ranging from 10 to a few hundred nanometers depending on the nature of the native cellulose, pretreatment and disintegration conditions. The resulting aqueous suspensions exhibit gel-like characteristics in water with pseudoplastic and thixotropic properties even at low solid content. Three main technologies, namely homogenization, microfluidization and microgrinding, are widely used for the mechanical treatment. Other methods were also developed but they are not widely accepted and far from being amenable to scale up. It includes high-speed blending, cryocrushing, high-intensity ultrasonication,¹² and steam explosion.¹³ Using the above-mentioned technologies, CNF were prepared from numerous cellulosic sources including soft and hard woods,¹⁴ sugar beet pulp,¹⁵ banana,¹⁶ opuntia ficus-indica,¹⁷ potato,¹⁸ wheat straw,¹⁹ bamboo,²⁰ luffa cylindrica,²¹ and also from some seaweed.²² The morphological characteristics of the resulting CNF depend mainly on those of the original fibers. Generally, CNF obtained from primary cell wall fibers are longer and thinner than those obtained from secondary cell wall fibers. Examples of CNF TEM images are given in Figure 1.2.

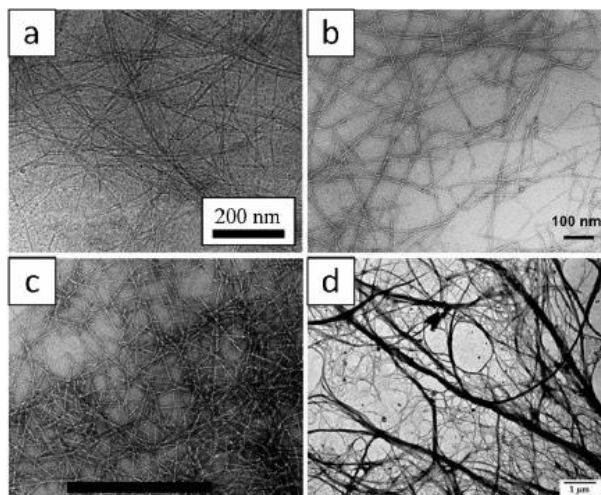


Figure 1.2 Transmission electron micrographs from a dilute suspension of CNF obtained from wood pulp using different pretreatments (a) enzymatic,²³ (b) TEMPO-mediated oxidation,²⁴ (c) carboxymethylation,²⁵ and from (d) *Opuntia ficus-indica*.¹⁷

1.1.3 Bacterial Cellulose (BC)

Besides being a dominant component of cell walls in plants, cellulose also exists extracellularly as synthesized cellulose fibers by several bacterial species.²⁶ Bacterial cellulose is mainly produced by the bacteria of *Acetobacter G. xylinus* species by cultivation in aqueous culture medium containing carbon and nitrogen sources during a time period of days. The resulting cellulosic network structure is in the form of a pellicle of randomly assembled ribbon shaped fibrils less than 100 nm wide that are in turn composed of a bundle of much finer nanofibrils (2-4 nm in diameter). These bundles are relatively straight, continuous and dimensionally uniform (Figure 1.3).

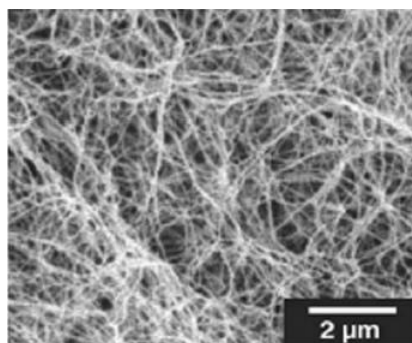


Figure 1.3 Scanning electron micrographs of a bacterial cellulose pellicle.²⁷

1.2 Structure and Properties of Nanocellulose

1.2.1 Surface Chemistry and Colloidal Stability

The colloidal stability of nanocellulose is the result of electrostatic repulsions due to the presence of charged groups at the surface of the particle. Conductometric titration and Zeta potential are the two commonly used methods to determine the surface or 'bulk' charge density of nanocellulose. The surface charge density of CNC can be tuned by varying the hydrolysis conditions, but a more accurate control of the surface charge density is commonly achieved by surface desulfation or postsulfation techniques using e.g. sodium hydroxide and chlorosulfonic acid (ClSO_3H), respectively.²⁸ In the case of CNF, the conductometric titration process can be challenging with the use of conventional titrants such as sodium hydroxide, due to their high surface area and ability to form a gel at high concentration and pH.²⁹ Further information on the surface charge and colloidal stability of nanocellulose can be obtained by measuring the zeta potential of the suspension.³⁰ CNC suspensions commonly feature zeta potential values between -20 and -50 mV, except for HCl hydrolyzed CNC, as these particles are not charged.²⁹

1.2.2 Specific Surface Area

When decreasing the size of a material, the specific surface area is expected to increase. The determination of the specific surface area from gas adsorption isotherms is often incorrect because of the irreversible aggregation of the nanoparticles upon drying. It can be estimated from the average geometrical dimensions of the nanoparticles, assuming a rod-like geometry and a density of 1.5 or $1.6 \text{ g}\cdot\text{cm}^{-3}$ for CNC. The values of the specific surface area were 51 and $533 \text{ m}^2\cdot\text{g}^{-1}$ for CNF and CNC, respectively, extracted from sisal fibers.³¹ A sharp increase is observed when the diameter drops below a value of 20 nm , which corresponds to the diameter range of CNC.³² This high specific area, coupled with the low concentration of the suspensions, allows the preparation of aerogels which can be used as porous templates, potentially useful in

various nano-applications. The aerogel network can be chemically modified to tune its wetting properties towards nonpolar liquids/oils. It can also be impregnated with different precursors, which can readily be transformed into functional nanoparticles along the CNF.

1.2.3 Aspect Ratio

An important parameter for cellulosic nanomaterials is the aspect ratio, which is defined as the ratio of the length to the width. It determines the anisotropic phase formation and reinforcing properties. It is indeed well-known that the mechanical percolation approach is highly relevant to describe the mechanical behavior of nanocellulose-based nanocomposites when prepared by casting/evaporation.^{32,33} This mechanism suggests the formation of a stiff continuous network of nanoparticles linked through hydrogen bonding, which leads to an unusual and outstanding reinforcing effect. Furthermore, this phenomenon is expected to occur only above a critical volume fraction of filler phase, defined as the percolation threshold, which in turn depends on the aspect ratio of the nanoparticle. In addition, it was shown by tensile tests performed on films prepared by water evaporation of a series of CNC suspensions that their tensile modulus increases when increasing the aspect ratio of the nanoparticles.³⁴ Films can also be prepared by dewatering process to analyze the tensile index. However, CNC and CNF cannot be utilized to make films by dewatering process due to the small size of the particles. Difficulties associated with the determination of the length make it challenging to assess its value for CNF. It is considered to be very high but strongly decreases when increasing the strength of oxidation for TEMPO-pretreated fibers.³⁵ For CNC, the aspect ratio is easier to determine and it is found to depend on both the source of cellulose and hydrolysis conditions. The aspect ratio varies between 10 for cotton and 67 for tunicin³² and can be higher than 100 for soy hulls³³.

1.2.4 Mechanical Properties

The mechanical modulus of nanocellulose is probably its main asset. Indeed, cellulose

is a ubiquitous structural polymer that confers its mechanical properties to higher plant cells. The tensile modulus of single cellulose I (native cellulose) crystal has been estimated both experimentally and theoretically. A broad range of values ranging between 56 and 220 GPa was reported with an average value of 130 GPa, with a tensile strength around 10 GPa.³⁶ As expected, the lower crystallinity of CNF results in a lower modulus, with an average value around 100 GPa.³⁶ Moreover, crystalline cellulose with a density around 1.5–1.6 g.cm⁻³ can be considered as a lightweight material. The specific tensile modulus, which is the ratio between the tensile modulus and the density, was estimated around 85 and 65 J.g⁻¹ for CNC and CNF, respectively, whereas it is around 25 J.g⁻¹ for steel.³⁷

1.2.5 Rheological Properties

The aqueous nanocellulose suspensions show a rheological behavior that can be described in terms of pseudoplastic and shear-thinning behavior.^{23,38} A rotational rheometer is the most commonly method for analyzing the rheology of nanocellulose. The nanocellulose suspensions are sheared between two plates to measure their viscosity and their viscoelastic response at low shear rates (commonly 0.001-100 s⁻¹). The rheological behavior of nanocellulose suspensions is influenced by the nanocellulose microstructure, the density of surface hydroxyl groups, the degree of dispersion and the interaction of the particles with the surrounding medium. Rheology can also be used as a complementary tool to determine the aspect ratio of nanocellulose³⁹ and to assess the quality of the nanocellulose dispersion. Typically, a poorly dispersed nanocellulose suspension would result in a decrease in viscosity due to limited particle-particle interaction at low shear rates.⁴⁰

1.2.6 Thermal Properties

When nanocellulose suspensions are dried, a film forms, which thermal expansion coefficient (TEC) is very low because of both its high crystallinity and strength of the nanocellulose network interactions.⁴¹ This low TEC of cellulose nanoparticles can be

used to reduce the TEC of polymer nanocomposite sheets if the strength of the network is strong enough to restrict the thermal expansion of the matrix. However, the low thermal stability of nanocellulose may limit their use and manufacturing conditions of its nanocomposites at high temperatures. This issue is particularly important for sulfuric acid-hydrolyzed CNC that exhibits a significantly reduced thermal stability compared with the raw starting material or other forms of nanocellulose. It is attributed to the sulfate ester groups that are introduced on the surface of the nanoparticles during the hydrolysis reaction.²⁸

1.2.7 Optical Properties

The optical properties of nanocellulose films can be measured by determining the light transmittance with a UV visible spectrometer in the wavelength range 200-1000 nm. CNF films can be optically transparent if the fibrils are small enough to densely packed, thus reducing the interstices between the fibrils to avoid light scattering.⁴² TEMPO-oxidized CNFs with diameters of 3–4 nm usually result in highly transparent films with transmittance values above 80%.⁴³ Films prepared by slow filtration, drying and compression are usually not optically transparent, but translucent due to a dense packing of the fibrils.⁴² CNCs display a lyotropic liquid crystalline behavior in water, caused by electrostatic repulsion forces between the negatively charged particles, which are indirectly characterized by a cholesteric pitch.⁴⁴ From a certain concentration threshold, a phase transition from an isotropic liquid phase to a chiral nematic phase is observed. The CNC self-organization is preserved by simple water evaporation, resulting in Bragg reflection of visible light if the pitch in the solid films approximates the wavelength of visible light.⁴⁵ Iridescent CNC films of different colors can be obtained by modifying the pitch by adding electrolytes to the CNC suspension, or varying the energy of the ultrasound/sonication treatment to disperse the particles in water.

1.2.8 Barrier Properties

In addition to excellent mechanical and optical properties, nanocellulose films feature good gas and liquid barrier properties due to their high crystallinity, their ability to form a dense percolating network and their high aspect ratio.³⁷ Generally, the addition of nanoparticles as filler or coating can significantly reduce the gas permeability of the substrate by increasing the tortuosity.⁴⁶ Very low oxygen transmission rates (OTR) can be achieved with neat nanocellulose films, with values as good as or even lower than OTR values for petroleum and bio-based polymers.⁴⁷ While nanocellulose films show reduced gas permeability in dry atmospheres, this property is often lost in moist atmosphere,⁴⁶ due to the plasticization and swelling of the fibrils through the adsorption of water molecules at high relative humidity. Strategies to improve the oxygen barrier of the films at high relative humidity can then involve the chemical surface modification of cellulose⁴⁸ or the preparation of composites, multilayer⁴⁹ or hybrid nanocellulose films.⁵⁰ However, it is worth noting that, although cellulose is a hydrophilic polymer, nanocellulose films still feature lower water vapor permeability than their macroscale counterpart.

1.3 Surface Modification of Nanocellulose

1.3.1 Physical Adsorption of Surfactants

Non-covalent surface modifications of nanocelluloses are typically achieved via adsorption of surfactants, oppositely charged entities or polyelectrolytes. Thus, these interactions with the nanocellulose substrate are ensured through hydrophilic affinity, electrostatic attractions, hydrogen bonds or van der Waals forces.

In order to obtain non-flocculated dispersion of CNC in non-polar solvents, the easiest approach is to cover the surface of the nanocrystals with surfactants bearing a polar head and long hydrophobic tail. With the simple mixing in solvent, non-covalent physical absorption of the surfactant molecules on the surface of nanocellulose will be a much more controllable and easy-operated process than delicate chemical

modification. Surfactants are usually amphiphilic organic compounds, containing both water-insoluble (oil-soluble) component as hydrophobic group (so-called tail) and water-soluble component as hydrophilic group (so-called head). The hydrophilic end of the surfactant molecule may adhere on the surface of nanocellulose, whereas the hydrophobic end may extend out providing a non-polar surface and lowering the surface tension of the nanoparticles. With this process, the ensuing surfactant-coated nanoparticles display reduced surface energy and improved dispersibility or compatibility with non-polar organic media.

Since the first report on the use of surfactant Beycostat NA (BNA) as stabilizing agent to prepare stable suspensions of CNC in nonpolar solvents,⁵¹ there were more studies focusing on the influence and property of BNA-modified CNC. BNA is a commercial anionic surfactant, and its chemical structure involves a phosphoric ester of polyoxyethylene nonylphenyl ether. The mixing ratio of surfactant and CNC should be cautiously controlled. A low amount of surfactant is not sufficient to obtain a good dispersion in organic solvents, whereas a too high amount of surfactant may induce self-aggregation of the nanoparticles during the mixing process (as shown in Table 1.1). Meanwhile, using small angle neutron scattering, it was observed that a surfactant layer 15 Å thick coated the surface of CNC, which indicated the effective adsorption of BNA and folded conformation of the surfactant molecule on the surface of the nanocrystals.⁵² In further studies, the properties of BNA-adsorbed CNC, such as morphology, self-assembling and chiral nematic property, were investigated with various techniques including AFM, TEM, and FESEM.⁵³ Particularly, the chiral nematic ordering of BNA-adsorbed CNC suspensions in cyclohexane with different concentrations was observed and discussed.⁵⁴ When using these surfactant-modified CNC as nanofiller to reinforce a polymeric matrix (such as PLA or PP), the presence of the surfactant on the surface of the nanocrystals was found to facilitate the dispersion of the nanofiller in the matrix and improve the nucleation effect towards crystallization of the matrix for ensuing materials.⁵⁵⁻⁵⁷

Table 1.1 Reactive conditions of adsorption of anionic, cationic and nonionic surfactants. (Γ is the grafting efficiency.)

Source	Surfactant	Solvent	Conditions	Γ	Ref.
Cotton	BNA	Toluene	BNA:CNC=4:1, pH=9	0.7	51
Tunicate	BNA	Toluene	BNA:CNC=4:1, pH=9	1.5	51
Tunicate	PEPNP	Toluene	—	0.2-1.5	52
MCC	Beycostat AB09	Chloroform	60 °C, 6 h	—	53
Cotton	BNA	Cyclohexane	BNA:CNC=4:1, pH=8	1.1	54
MCC	Beycostat AB09	H ₂ O	pH=7.5	—	55
Tunicate	BNA	Toluene	BNA:CNC=4:1, pH=8	—	57
Cotton/ Sisal/ Ramie	DODA-Br	H ₂ O	20°C, 15min	0.2-0.8	58
Whatman filter	sorbitan monostearate	THF	24h	—	59
MCC	tert-butanol	chloroform	solvent exchange	—	60

Different from the hydrophilic-hydrophobic mechanism for the absorption of common surfactants, cationic surfactants (such as DODA-Br) can be adsorbed on the surface of CNC through strong electrostatic interactions between the negative charge of the sulfate groups on H₂SO₄-hydrolyzed nanocrystals and the cationic charge of the surfactant. DODA is a cationic surfactant that has been widely used in films to investigate the adsorption and binding processes involving anionic polyelectrolytes at the air/water interface. Rojas et al. applied cationic surfactant DODA to modify the surface of CNC, and used this surfactant as the carrier to crosslink cellulose nanoparticles.⁵⁸ With Langmuir-Schaeffer (LS) technique, the precursor CNC-DODA complex was subsequently used to prepare monolayer films.

A nonionic surfactant, such as sorbitan monostearate, was also used to improve the dispersion of CNCs in organic solvents and to prevent their self-aggregation.⁵⁹ From the results of turbidity experiments performed on 0.3 and 0.6 wt% nanocrystal suspensions in THF, the surfactant concentration determined the stability of modified CNC in solvent. With high surfactant concentrations, the surfactant molecules self-

aggregate and probably did not adhere to the surface of nanocrystals, which probably caused the weak stress transfer effect when using CNC as reinforcing filler. In another study, as a small surfactant molecule, tert-butanol, was used to modify the surface of CNC.⁶⁰ It was reported that tert-butanol was able to limit the aggregation of the nanocrystals during the freeze-drying process, and promoted more loose condition and homogeneous dispersion in poly(lactic acid) (PLA) matrix.

1.3.2 TEMPO-mediated oxidation

TEMPO(2,2,6,6-Tetramethylpiperidine-1-oxyl)-mediated oxidation has been used to convert the hydroxymethyl groups on cellulose chains into carboxylic form. The use of this technique has been the subject of a number of reports since its introduction by de Nooy et al., who were the first to show that only the hydroxymethyl groups of polysaccharides were oxidized, while the secondary hydroxyls remained unaffected.⁶¹ Figure 1.4 depicts the TEMPO-mediated oxidation mechanism for cellulose molecules. The procedure for modification of CNC is carried out from the TEMPO/NaClO/NaBr system, with the control of the pH at a value of 10 to preserve the high oxidation efficiency.

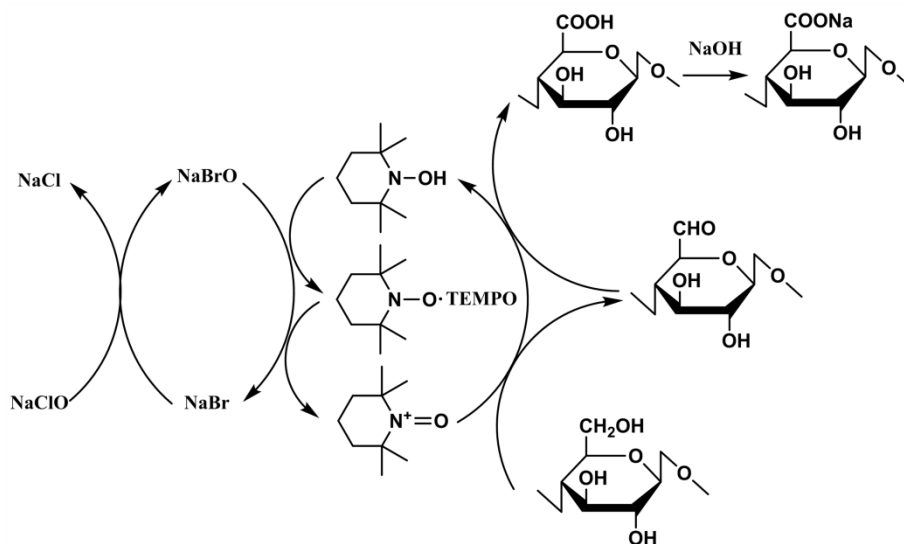


Figure 1.4 Scheme of the TEMPO-mediated oxidation mechanism of cellulose.

TEMPO-mediated oxidation of CNC obtained by HCl hydrolysis of cellulose fibers was first reported by Araki et al.^{62,63} The authors demonstrated that after TEMPO-

mediated oxidation, the CNC maintained their initial morphological integrity and formed a homogeneous suspension when dispersed in water. The presence of carboxyl groups imparted negative charges to the CNC surface and thus induced electrostatic stabilization. Montanari et al.⁶⁴ systematically investigated the degree of oxidation and size of surface carboxylated CNC prepared by TEMPO-mediated oxidation of cotton linters. The degree of oxidation (DO) was determined by conductometric titration as 0.24. During TEMPO-mediated oxidation, a decrease of the crystal size occurred, and the introduction of negative charges on the surface of the crystalline domains induced a better individualization and dispersion of the crystallites. Habibi et al.⁶⁵ performed TEMPO-mediated oxidation of CNC obtained from HCl hydrolysis of tunicate cellulose fibers and showed that TEMPO-mediated oxidation did not compromise the morphological integrity of CNC nor their native crystallinity. Based on the supramolecular structure, morphological attributes and crystallographic parameters of the oxidized CNC, these studies demonstrated that various degrees of oxidation could be predicted and achieved by using specific amounts of the primary oxidizing agent ratios.

In the case of CNF, TEMPO-mediated oxidation is mostly used as a cost-effective chemical treatment prior to the mechanical processing in order to facilitate the individualization of the nanofibrils. Indeed, after impairing their structural potential and softening their rigid structure by breaking the strong intra-fiber hydrogen bond networks, the TEMPO-oxidized cellulose fibers can be converted very easily, utilizing mechanical shearing discussed before (high speed blending, ultrasonication, high mechanical shearing, etc.), into highly crystalline individual nanofibers. This method has been reported for a variety of cellulosic fibers.⁶⁶ Isogai's group carried out pioneering work in this area as reported recently in a concise review.⁶⁷ With the most common TEMPO derivative, the optimal conditions reported are a pH of 10 and temperature ranging between 0 and 10 °C. These operating conditions usually yield cellulose nanofibers having 3-20 nm in width and a few microns in length depending

on the cellulosic raw material used.

1.3.3 Esterification

Owing to its ease and straightforwardness, the modification of hydroxyl groups present at the surface of nanocellulose through esterification is widely used. Among esterification reactions, acetylation of nanocellulose is the most widely studied. The use of pyridine as a solvent diluent in the heterogeneous acetylation of nanocellulose, using acetic anhydride and sulfuric acid as catalyst, seems to impact only slightly its morphological and crystalline structure even at 80 °C for 5 h.⁶⁸ The simultaneous occurrence of cellulose hydrolysis and acetylation of hydroxyl groups has also been reported. Fischer esterification of hydroxyl groups simultaneously with the hydrolysis of amorphous cellulose chains has been introduced as a viable one-pot reaction methodology that allows isolation of acetylated CNC in a single-step process.⁶⁹ However, a strict control of the degree of esterification using this method is quite tough. In a similar approach, Herrick et al.⁷⁰ have proposed in the early development of nanocellulose, the simultaneous acetylation of CNF during the mechanical shearing using as processing medium a mixture of acetic acid and acetic anhydride with sulfuric acid as catalyst. A similar one-step procedure aiming to esterify and defibrillate cellulose fibers was recently developed by Huang et al.⁷¹ The procedure involves ball milling of the fibers in organic solvents such as DMF or THF containing esterifying agents like chloride or anhydride derivatives leading to CNF with tunable properties. It is worth mentioning that acetylation was also suggested as a chemical pretreatment step prior to the mechanical processing to access CNF.⁷²

A novel and straightforward method for the surface acetylation of CNC by transesterification of vinyl acetate was proposed by Cetin et al.⁷³ The reaction was conducted in DMF at 95 °C using potassium carbonate as catalyst. The results analysis indicated that during the first stage of the reaction, only the surface of CNC was modified, while their dimensions and crystallinity remained intact. With increasing reaction duration, diffusion mechanisms controlled the rate, leading to higher levels of

acetylation, smaller dimensions, and lower crystallinity of modified CNC. In another study, the similar transesterification of CNF obtained through carboxymethylation to substitute carboxymethyl groups by hexyl moieties was reported using 1-hexanol as reactant and reaction medium, as well as in combination with sulfuric acid as catalyst.⁷⁴ The reaction was carried out at 105 °C for 72 h but did not show any regioselectivity because all hydroxyl groups were modified (Figure 1.5).

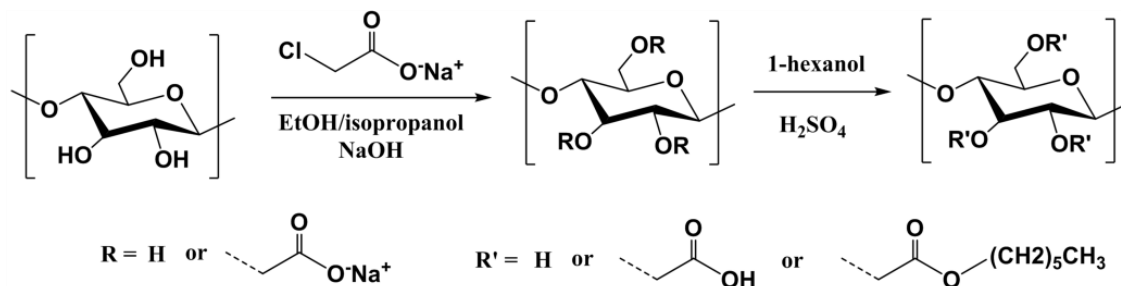


Figure 1.5 Transesterification modification of nanocellulose.

An environmentally friendly esterification modification route imparting high hydrophobicity to CNC was developed by Yuan et al.⁷⁵. The method used alkenyl succinic anhydride aqueous emulsions as a template, which were simply mixed with CNC aqueous suspensions, freeze dried, and the resulting solid was heated to 105 °C. With low reagent consumption and simple treatment procedures, highly hydrophobic modified CNC can be obtained. The acylated CNC can be dispersed in low-polarity solvents, i.e., DMSO ($\epsilon=46.45$) and 1,4-dioxane ($\epsilon=2.209$).

Menezes et al.⁷⁶ have reported the esterification of CNC by grafting organic acid chlorides presenting different lengths of the aliphatic chain. The reaction was conducted under reflux for 4 h using triethylamine (TEA) as catalyst and neutralizing agent for the in situ formed hydrochloric acid. The crystallinity of the particles was not altered by the chain grafting, but it was shown that covalently grafted chains were able to crystallize at the cellulose surface when using C18 agent. Berlioz et al.⁷⁷ have reported a highly efficient solvent-free synthetic method allowing an almost complete surface esterification of CNC, extracted from tunicate, leading to highly substituted CNC-esters. The reaction of fatty acids such as palmitoyl chloride was carried out at reduced

A mild silylation protocol was adapted to surface silylate CNF extracted from parenchymal cell cellulose with isopropyl dimethylchlorosilane. The silylated CNF maintained the same morphological features as that of the unmodified sample and were homogeneously dispersible in non-polar solvents providing stable suspensions that did not flocculate.⁷⁹ The rheological properties of their suspension in methyl oleate showed a marked shear thinning effect. Thus, by silylation, the CNF have acquired an inherent flexibility with the result that their suspensions present a rheological behavior equivalent to that of polymer solutions. Similarly, Anderson et al.⁸⁰ have reported the successful surface silylation of CNF with chlorodimethyl isopropylsilane. CNF obtained by disintegration of bleached softwood sulfite pulp in a homogenizer, was hydrophobically modified by surface silylation with chlorodimethyl isopropylsilane(CDMIPS). A moderate DS (between 0.6 and 1)⁸¹ stabilized water-in-oil emulsions.

Silylation was also attempted in order to tune the wetting properties towards non-polar liquids of pre-formed CNF-based aerogels. Perfluorodecyltrichlorosilane⁸² and octyltrichlorosilane⁸³ were grafted merely by a chemical vapor deposition method at elevated temperature. Owing to its simplicity silylation was also exploited as an intermediate step for further functionalization. Aminosilanes were first grafted onto CNC and served as reactive sites to covalently attach fluorescent moieties.⁸⁴ More recently, alkene thiol-functionalized silanes were also covalently grafted on CNF-based films and consequently clicked with appropriate moieties through thiol-ene click chemistry in Figure 1.7.⁸⁵

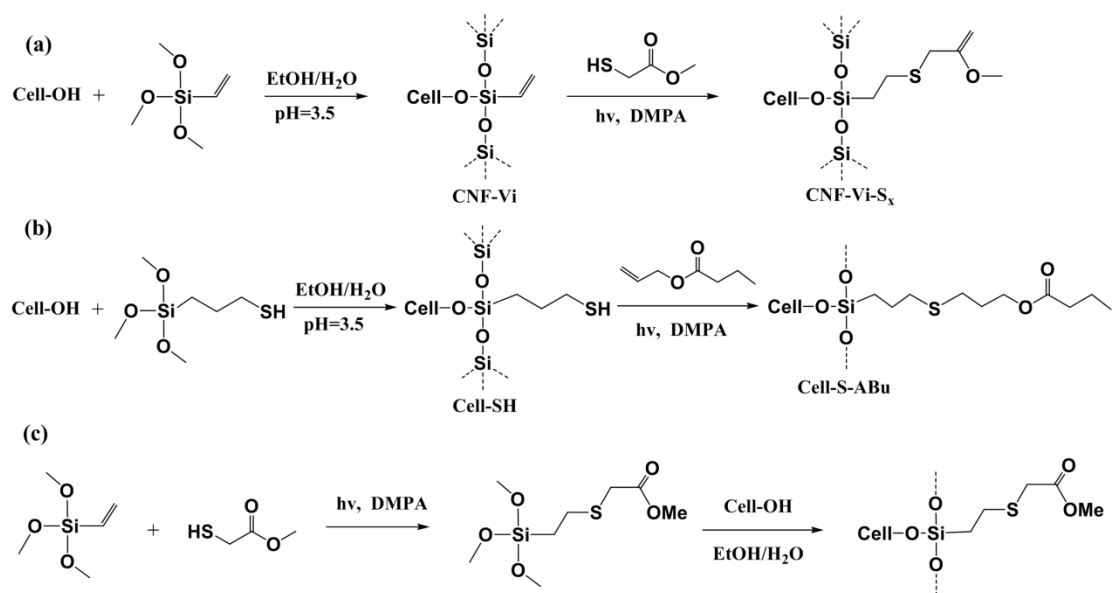


Figure 1.7 Scheme for the silylation of nanocellulose with vinyltrimethoxysilane (a), 3-mercaptopropyltrimethoxysilane (b), and trialkoxysilane (c).

1.3.5 Grafting onto

The “grafting onto” method involves attachment of pre-synthesized polymer chains, carrying reactive end groups, onto (modified) hydroxyl groups of the cellulose surface. Yet, steric hindrance can prevent optimal attachment during the grafting reaction because the polymer chains have to diffuse through the layer of already attached brushes to reach available reactive sites at the surface; hence, an unfavorable reduced surface grafting density is often obtained by using the “grafting onto” method. The case of poly(ethylene glycol) (PEG) or polyoxyethylene (PEO) grafted onto the surface of cellulose nanocrystals was widely studied because of the similar hydrophilic property and simple chemical structure of PEG. Three approaches were reported to combine PEG (or PEO) with CNC via the “grafting onto” strategy, as summarized in Figure 1.8. Araki et al. first reported the steric stabilization of TEMPO-mediated oxidized CNC suspensions by amine-terminated PEG grafting using a carbodiimide-catalyzed amidation procedure in water at room temperature.⁸⁶ By grafting PEG at a ratio of 0.2–0.3 g/g on CNC, the modified CNC showed drastically enhanced dispersion stability and ability to redisperse into either water or chloroform from the freeze-dried

state. On the basis of the chemical reaction between the hydroxyl and isocyanate groups, the polymeric chains of PEG can also be grafted onto the surface of CNC (through the covalent linkage with the isocyanate modified PEG agent).

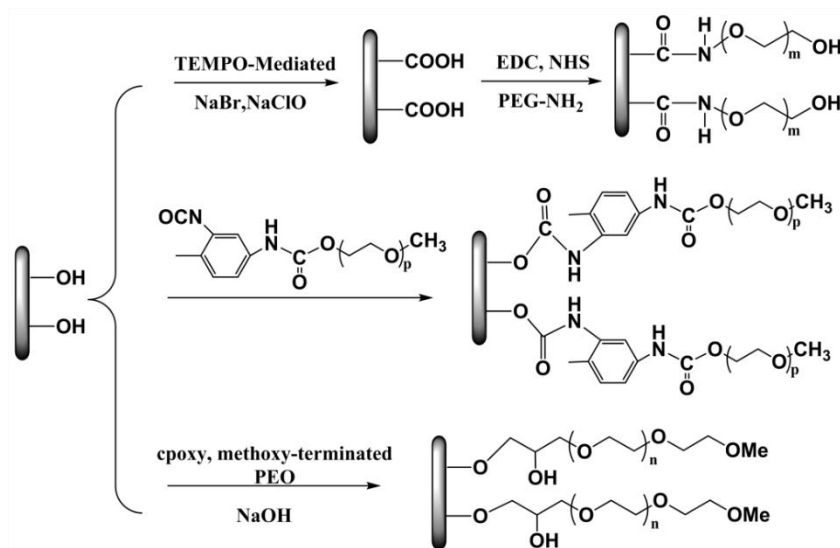


Figure 1.8 Different methods of introducing PEG/PEO chains on the surface of nanocellulose.

Kloser et al. reported a novel method to graft high molecular weight PEO on the surface of CNC, involving the reaction between epoxy and hydroxyl groups under alkaline conditions.⁸⁷ Figure 1.9 depicts this approach involving a two-step reaction, i.e., desulfation and grafting of epoxy-terminated PEO under alkaline conditions for grafting PEO onto the CNC surface. The CNC prepared by sulfuric acid hydrolysis were desulfated with sodium hydroxide, and then nucleophilic attack by the surface hydroxyl groups under strongly alkaline reaction conditions opened the epoxide ring of epoxy-terminated PEO to form a covalent ether linkage between CNC and PEO chains. The AFM images indicated that the whole process did not change the morphology or dimensions of CNC, and the grafted PEO chains successfully contributed to steric stabilization for good dispersion of CNC. The resultant PEO-grafted CNC suspension was stable for several months and no precipitation was observed.

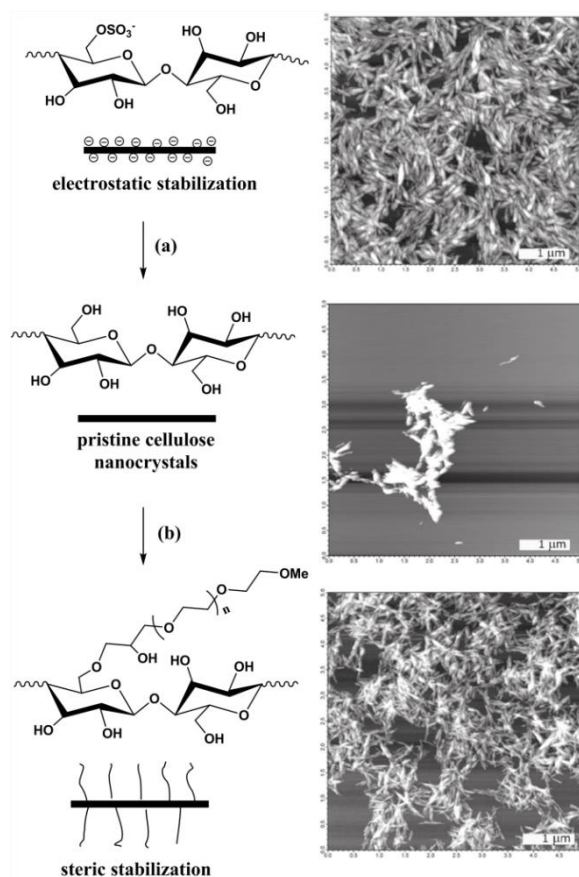


Figure 1.9 Schematic illustration for grafting PEO onto the CNC surface via desulfation reaction (a) and epoxy-terminated PEO grafting under alkaline condition (b), and the AFM images corresponding to the initial sulfated CNC and every products (the scale in the AFM images is $1 \mu\text{m}$)

Besides hydrophilic PEG, several hydrophobic polymers were also reported to be grafted onto the surface of CNC, as summarized in Table 1.2. The “grafting onto” approach was used by Ljungberg et al.⁸⁸ to graft maleated polypropylene (PPgMA), bearing 7.5 wt% of maleic anhydride groups, onto the surface of CNC extracted from tunicate. This esterification was carried out in toluene at $100 \text{ }^\circ\text{C}$ for 5 min. The resulting grafted nanocrystals showed very good compatibility and high adhesion when dispersed in a polypropylene matrix. Harrison et al.⁸⁹ and Azzam et al.⁹⁰ adopted the same approach using DMF as reaction medium to graft amine-terminated poly(styrene) (PS) or poly(tert-butyl acrylate) (Poly(TBA)) and Jeffamine copolymers, respectively, and the grafting efficiency seemed to be greater than that in water.

Table 1.2 Reactive conditions and grafting efficiency (GE) for the preparation of CNC/CNF grafted with polymeric chains using the “grafting onto” strategy.

Types of nanocellulose	Source of cellulose	Polymeric chain	Coupling agent	Solvent	Conditions	GE (%)	Ref.	
CNC	Whatman filter paper	PEG	carbodiimide	Water	R.T., 24 h, pH=7.5-8.0,	20	86	
	tunicate	PPgMA	—	Toluene	100 °C, 5 min	—	88	
	Whatman filter paper	PS	—	DMF	R.T, 16 h	56	89	
		Poly(TBA)	—		R.T, 13 h	60		
	Cotton	Jeffamine	—	—	Water	R.T, 24 h	30.1	90
					DMF	pH=7.5-8.0,	53.5	
Cotton	PEO	—	—	Water	65 °C , 6.5 h alkaline conditions	20-40	91	
Cotton	WPU	—	—	DMF	80 °C, 2 h, N ₂	45-57	92	
CNF	Ramie fibers	PCL10000	2,4-TDI	Toluene	80°C, N ₂ , 7d	56.3	93	
		PCL42500				53		

Isocyanation is the most popular method for termination and functionalization of end-groups in polymer chains, and hence it provides good precursors for surface “grafting onto”. The grafting of polycaprolactone (PCL) with different molecular weights on the surface of CNC has been achieved by using isocyanate-mediated coupling, which involves a three-step process as shown in Figure 1.10.⁹¹ The first step requires the reaction of phenylisocyanate with one functionality of the polymer. The second step requires the reaction of the modified polymer, having thus one protected functionality, with one isocyanate functionality of 2,4-TDI. During the third step, the unreacted second isocyanate functionality of 2,4-TDI is then able to react with the surface hydroxyl groups of CNC to graft the polymer chain onto the nanoparticle.⁹³ The reached grafting density was high enough that the grafted PCL chains were able to crystallize at the surface of CNC. Nevertheless, to reach a high grafting density the reaction was conducted for 7 days at 80 °C with continuous addition of the coupling agent and of the catalyst, as well as by using a high volume of toluene to ensure good dispersion. The same approach was implemented by Cao et al.,⁹² who reported isocyanate-catalyzed grafting of pre-synthesized water-borne polyurethane polymers via a one-pot process using DMF as reaction medium. These grafted-WPU chains were able to form a crystalline structure on the surface of CNC, and thus induce the crystallization of the matrix which created a co-continuous phase. The same approach was followed by Pei et al.⁹⁴ to prepare polyurethane-CNC nanocomposites with ultrahigh tensile strength and strain-to-failure with strongly improved modulus.

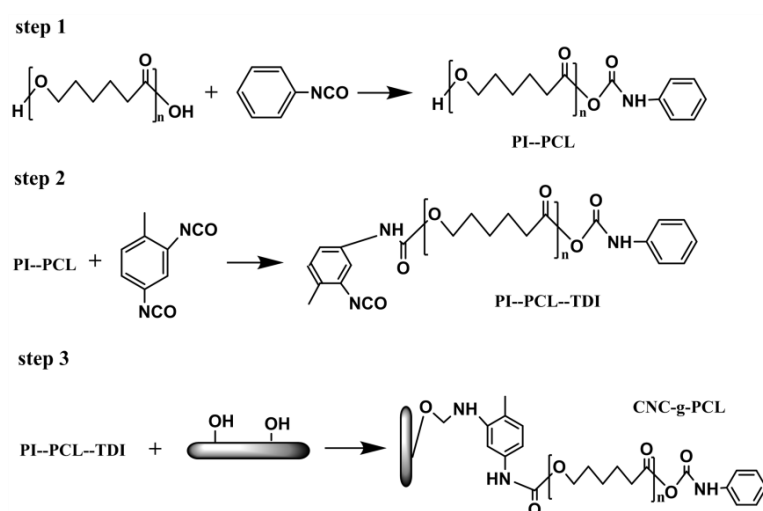


Figure 1.10 Three-step routine for the grafting of PCL onto the surface of CNC from the “grafting onto” strategy.

1.3.6 Grafting from

The “grafting from” approach can be implemented to increase the grafting density of the polymer brushes on the surface and to ensure their stability in different application conditions. In this method, polymer brushes can be grown in situ from nanocelluloses directly using the surface hydroxyl groups serving as initiating sites for ring opening polymerization (ROP) or the surface can be modified to introduce different initiator sites needed for controlled polymerization techniques such as atom transfer radical polymerization (ATRP) and other radical polymerization techniques.

1.3.6.1 Ring opening polymerization (ROP)

Ring opening polymerization (ROP), which was used to graft and polymerize cyclic monomers mainly lactones was first applied for the modification of CNC by Habibi et al.⁸ PCL was grafted by ROP on the CNC surface using stannous octoate ($\text{Sn}(\text{Oct})_2$) as catalyst and the reaction was conducted at 95 °C in toluene. Under these conditions CNC kept its original crystalline structure and morphology as confirmed during the modification reaction.⁹⁵ With a similar strategy, Chen et al.⁹⁶ and Lin et al.⁹⁷ conducted the grafting reactions under microwave irradiation to enhance the grafting efficiency and the CNC-g-PCL was incorporated into a PCL matrix by thermoforming. In this case, the long grafted PCL chains entangled with each other during the melting process of thermoforming and, hence, produced molded sheets with good mechanical strength. In order to overcome the use of metal-based catalysts, Labet and Thielemans⁹⁸ recently used citric acid, a benign naturally available organic acid, as catalyst. The possibility to exert control over the SI-ROP of PCL from CNC using a benign catalyst is a major step towards truly green materials, as the incorporation of potentially harmful metal catalysts in polymers is a continuous concern. Reaction conditions and grafting efficiency reported in the literature for the preparation of PCL-grafted CNC are summarized in Table 1.3. Recently Carlsson et al. reported the monitoring of CNC surface grafting with PCL by Quartz Crystal Microbalance, which provided a tool to regulate the polymerization reaction.⁹⁹

Table 1.3 Reactive conditions and grafting efficiency (GE) for the surface grafting of poly (caprolactone) (PCL) or poly (lactic acid) (PLA) on nanocellulose.

Nanocellulose	Source	Grafted polymer	Catalyst	Solvent	Reactive condition	GE (%)	Ref.
CNC	Ramie	PCL	Sn(Oct) ₂	Toluene	95 °C, 24 h	85	95
	Native linter	PCL	Sn(Oct) ₂	—	Microwave irradiation, 5 min	85	96,97
	Cotton wool	PCL	citric acid	—	120 °C, 24 h	58	98
	Ramie	PLLA	Sn(Oct) ₂	Toluene	80 °C, 24 h, N ₂	83	100
	—	PLA	Sn(Oct) ₂	Toluene	90 °C, 68 h, argon flow	60-70	101
	Ramie	PDLA	Sn(Oct) ₂	Toluene	80 °C, 24 h, N ₂	80	102
	Ramie	PCL/PLA	Sn(Oct) ₂	Toluene	80 °C, 48 h, N ₂	83	103
CNF		PCL300				98	
	Wood pulp	PCL600	Sn(Oct) ₂	—	95 °C, 18-20 h, argon flow	99	104
		PCL1200				95	
		PCL- short				22	
	Softwood	PCL-medium	Sn(Oct) ₂	Toluene	110 °C, 3-5 h, argon flow	70	105
	PCL-long				78		

Lönnerberg et al. have successfully achieved the surface grafting of CNF with PCL via ROP using $\text{Sn}(\text{Oct})_2$ as catalyst with a two-step procedure,¹⁰⁴ (i) CNF were dispersed in the monomer and the reaction was conducted at 95 °C without any solvent, and (ii) the reaction was performed in toluene where CNFs were previously dispersed.¹⁰⁵ The good reinforcing ability derived from the characteristic dimensions of CNF must be preserved during the grafting reaction. Great improvement in the dispersibility of CNF in organic solvents can be achieved after PCL grafting, and it was shown that longer graft lengths improved the stability of the suspensions.

Similar to the strategy followed in the case of PCL grafting at the surface of CNC, Goffin et al.¹⁰⁰ reported the grafting of poly(lactic acid) (PLA) chains from the surface of CNC by ROP. However, the grafted chains were suspected to be very short according to their crystallization behavior. Therefore, in order to achieve the molecular weight for grafted PLA chains, Braun et al.¹⁰¹ suggested the use of partially acetylated CNC, obtained through the Fischer esterification pathway, to control the grafting density. This well-designed approach for producing the materials is used to balance competing effects; blocking a fraction of the surface hydroxyl groups available for ring-opening polymerization initiation leads to high-molecular-weight chains covalently attached to the CNC surface. Significant enhancement of the mechanical performances was also obtained most probably induced by percolation of CNC-g-PLA network stabilized by stereo complexation. These results and a thorough comparison with their counterparts filled with PLA chains converge toward the contribution of the tiny stereo complexed PLA structure surrounding CNC. Efforts towards tuning this surface stereo complexation are underway to increase the size and amount of stereo complexed PLA around CNC.¹⁰²

In a particular work, Goffin et al.¹⁰³ employed ROP catalyzed by $\text{Sn}(\text{Oct})_2$ to graft successively PCL and then PLA from the surface of CNC (Figure 1.11). Despite prolonged reaction time under metal catalyzed ROP conditions, the morphology and crystalline structure of CNC were preserved. These CNC grafted with PCL-b-PLA copolymer showed distinct crystallization behavior and dispersion ability when blended with a mixture of immiscible PCL and PLA blend.

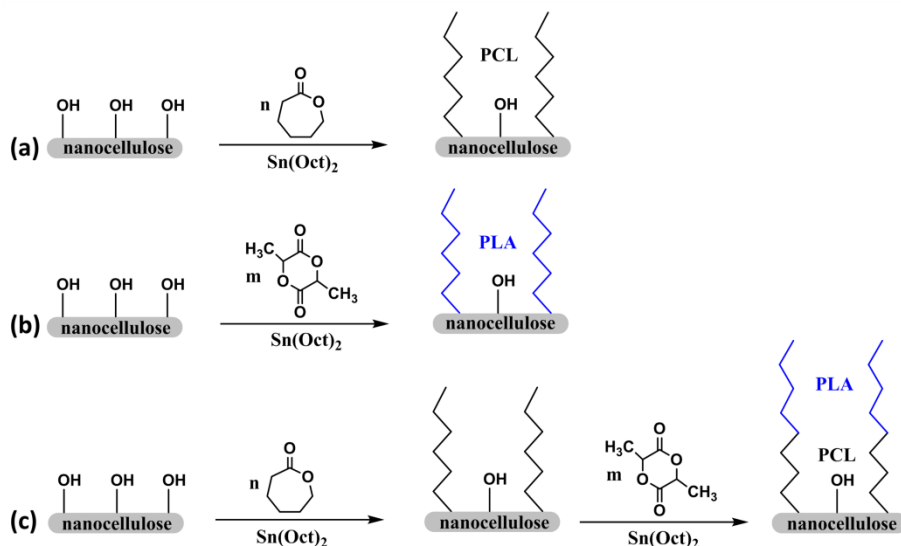


Figure 1.11 Chemical routines of surface grafting PCL (a), PLA (b), PCL-b-PLA (c) on nanocellulose from the ROP reaction.

1.3.6.2 Living radical polymerization (LRP)

Living radical polymerization (LRP), such as atom transfer radical polymerization (ATRP) and single electron transfer-living radical polymerization (SET-LR) can also be used for the surface polymer grafting on nanocellulose. Commonly, a two-step reaction is involved, which is the initial formation of initiating sites for LRP with the initiator immobilized on CNC, and the reaction of the initiator-modified nanoparticles with a monomer to induce polymerization. It has been proved that LRP is a versatile technique to synthesize well-defined polymers with high surface grafting density and low polydispersity on the surface of CNC. Copper-mediated LRP is generally chosen for its versatility with respect to monomer choice and ease of synthesis. Generally, two steps are involved in the chemical modification of grafting polymeric chains on CNC with LRP techniques, as shown in Figure 1.12. The first step is the initial formation of initiating sites for LRP, in which an initiator is immobilized on the nanoparticles, and the macromolecular initiator (CNC-Br is commonly used) can be obtained. It should be pointed out that 2-bromoisobutryl bromide (BriB) is always chosen for the esterification of nanocrystals and provides the initiating sites. To prevent the destruction of the crystalline structure of CNC, this reaction should be carefully performed at low temperature (sometimes in ice bath), which can dissipate superfluous heat. The second step involves the reaction of the initiator-modified nanoparticles with monomers (C=C alkene molecules) to induce the polymerization.

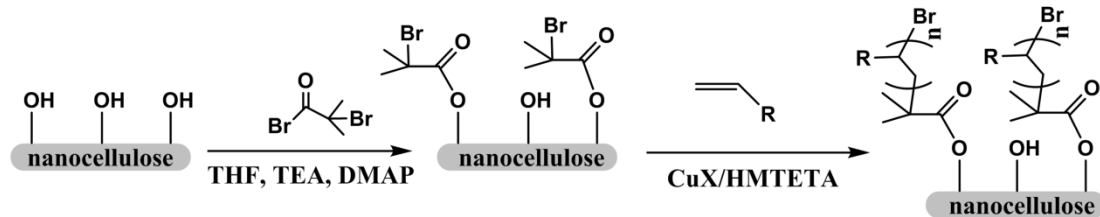


Figure 1.12 Common synthetic routes for grafting polyolefin chains on CNC with the technique of ATRP reaction.

Early reports on using SI-ATRP to graft polyolefin polymeric chains on CNC surface were published by Zhang et al. and involved polystyrene (PS),¹⁰⁶ poly [2-(N,N-dimethyl amino) ethyl methacrylate] (PDMAEMA),¹⁰⁷ and poly{6-[4-(4-methoxyphenylazo) phenoxy] hexyl methacrylate} (PMMAZO).¹⁰⁸ In these studies, the authors used 2-bromo-2-methylpropionyl bromide (Br-MPBr) as the initiator agent, which was attached to the hydroxyl groups of CNC by esterification in THF in the presence of 4-dimethylaminopyridine (DMAP) and triethylamine (TEA). The polymerization was then carried out in the presence of Cu(I)Br and 1,1,4,7,10,10-hexamethyltriethylenetetramine. All resulting polymer-grafted CNCs exhibited interesting liquid crystalline behaviors that are in some cases thermally sensitive. For example, CNC grafted with azo-polymer poly(MMAZO) exhibited both types of liquid crystal formation, thermotropic and lyotropic, as they showed smectic-to-nematic transition at 95°C and nematic-to-isotropic transition at 135°C, and exhibited analogous lyotropic liquid-crystalline phase behavior above 135°C. Another PDMAEMA-grafted CNC exhibited chiral nematic structure in lyotropic state. The results are consistent with the hypothesis of chiral interaction arising from the shape of the rods and not from the chiral character of the cellulose chain. The temperature-induced fingerprint texture changes of PDMAEMA-grafted CNC aqueous suspensions were investigated at various temperatures. It was a pity that the amount of bromine in the initiator-modified CNC was very low (only 0.6 wt%) in these studies, which restricted the subsequent grafting reaction. On the other hand, the issue of grafting polymeric chains with different lengths, which implied the controllable feature of ATRP, was not investigated.

By altering the extent of initiator surface modification through polymerization control, Morandi et al.¹⁰⁹ produced polystyrene(PS)-grafted CNC with varied grafting densities and different polymer brush lengths. Various grafting densities of PS on the surface of CNC were realized by controlling the final content of initiating sites under different

conditions (duration and temperature of BriB/CNC reactions). In the further study, a method of grafting a photosensitive moiety bearing initiating sites onto the surface of CNC was reported, followed by grafting PS chains with ATRP. Majoinen et al.¹¹⁰ reported an effective method of chemical vapor deposition (CVD) and continued esterification to improve the initiator density on CNC surface. The simple CVD pretreatment of BriB for CNC was conducted for 24 h at room temperature (5 wt% bromine content), which promoted the subsequent esterification to obtain more initiating sites (15 wt% bromine content). Whereafter, Zoppe et al.¹¹¹ reported the use of SI-SET-LRP to graft thermoresponsive poly(*N*-isopropylacrylamide) brushes from never-dried CNC under various conditions at room temperature, as shown in Figure 1.13. Accordingly, Cu(I) was rapidly disproportionated to Cu(0) and Cu(II) yielding simple catalyst removal. It was determined that when increasing initiator loading, increased molecular masses of polymer brushes were obtained. This effect could be explained by local heterogeneities shifting the SET-LRP equilibrium to the active state. Likewise, with increased monomer loading, increased molecular masses of resulting polymer brushes were obtained. Finally, the results presented are expected to provide the basis for the development of temperature-responsive materials based on cellulose nanocrystals.

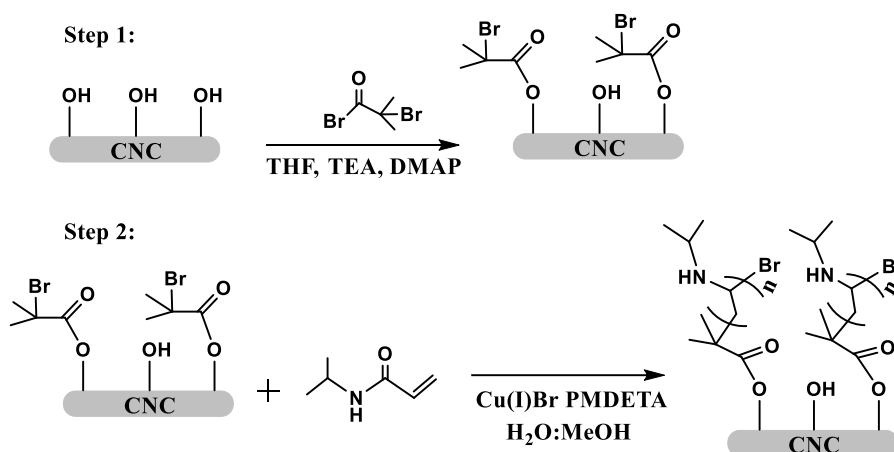


Figure 1.13 Synthetic routes for grafting polyolefin chains on CNC with the SET-LRP technique.

Examples can be found in the literature reporting the grafting of polymer brushes, i.e. poly(butyl acrylate) (PBA), from the surface of CNF through SI-ATRP.^{112,113} SI-ATRP of butyl acrylate (BA) on CNF was conducted to create controllable hydrophobic chains on CNF. The macroinitiator, CNF-Br, was prepared by the esterification of hydroxyl groups on CNF with 2-bromoisobutyrylbromide (BiBB); followed by ATRP of BA

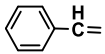
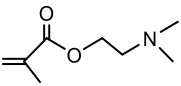
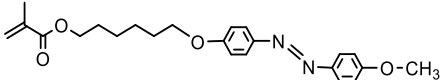
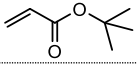
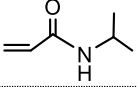
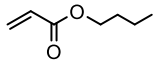
using two catalyst systems, Cu(I)Br/2,2'-bipyridine (BPY) and Cu(I)Br/pentamethyldiethylenetriamine (PMDETA). The results indicated that the PMDETA system exhibited relatively poor control over ATRP; whereas the BPY system produced PBA with tailored chain lengths and relatively narrow polydispersity but experienced a rather slow polymerization process. To optimize the polymerization with the Cu(I)Br/PMDETA system, several influencing factors were investigated, including the type of solvent, reaction temperature and the use of co-catalyst Cu(II)Br₂. Some studies exploited other approaches to graft polyolefin on the surface of CNC. Harrisson et al.⁸⁹ grafted PS and poly(*t*-butyl acrylate) (PtBA) chains on CNC via the carbodiimide-mediated amidation reaction between the terminal amine groups from polyolefin polymers and carboxylic acid groups on the surface of oxidized CNC.

With the method of HCl hydrolysis or saponification, grafted polyolefin chains can be cleaved from the surface of CNC, and the properties of grafted polymers, such as molecular weight (*M_n*) and polydispersity, can be carefully investigated by gel permeation chromatography (GPC) or size exclusion chromatography (SEC). As shown in Table 1.4, diverse monomers, reactive conditions and properties of grafted polyolefin chains on CNC have been used. Despite the advantages of controllability and high grafting density of surface-initiated LRP, there are some shortcomings for this technique, which are the inconvenience of experimental operation (with three freeze-pump-thaw or vacuum-nitrogen cycles) and rigorous reactive conditions of anaerobic circumstance.

1.4 End Modification of Nanocellulose

It is well known that the unidirectional parallel orientation of cellulose chains within elementary fibrils, occurring during biosynthesis and deposition, induces the formation of crystals having one side face with pendant hydroxyl groups known as the non-reducing end, and another front face with reducing end groups bearing hemiacetal functionality. The latter can be selectively exploited for chemical modification. In a pioneering work, Sipahi-Saglam et al.¹¹⁴ have demonstrated the feasibility of grafting groups or molecules on the hemiacetal groups of CNC end as sketched in Figure 1.14.

Table 1.4 Reactive conditions and properties of various grafted polymeric chains on nanocellulose from the LRP reactions.

Monomer	Polymeric chain	Reactive mechanism	Catalyst/ ligand	Solvent	Conditions	GE (%)	Grafted polymer (M_n)	PDI	Ref.
	PS	ATRP	Cu(I)Br/ HMTETA	—	110 °C, 12 h	68	74700	1.21	106
		ATRP	Cu(I)Br/ PMDETA	Toluene	30 °C/70 °C, 16 h/24 h	24%-40	2800-17800	1.09-1.13	109
	PDMAEMA	ATRP	Cu(I)Br/ HMTETA	CH ₃ OH	55 °C, 12 h	53	10200	1.38	107
	PMAZO	ATRP	Cu(I)Br/ HMTETA	Chlorobenzene	90 °C, 24 h	74.6	—	—	108
	PtBA/PAA	ATRP	Cu(I)Br/ PMDETA	DMF	75 °C	—	6200-36300	1.10	110
	P(NiPAAm)	SET-LRP	Cu(I)Br/ PMDETA	H ₂ O/MeOH	25 °C, 24 h	—	10630-42860	1.20	111
	PBA	ATRP	Cu(I)Br/ PMDETA	Toluene	90 °C, 24 h	83	9600	—	112
		ATRP	Cu(I)Br/ PMDETA	DMF/toluene/1- butanol	70 °C/90 °C/ 110 °C, 2-6 h	57	—	—	113
		ATRP	Cu(I)Br/ BPY	DMF/toluene/1- butanol	70 °C/90 °C/ 110 °C, 2-6 h	—	—	—	113

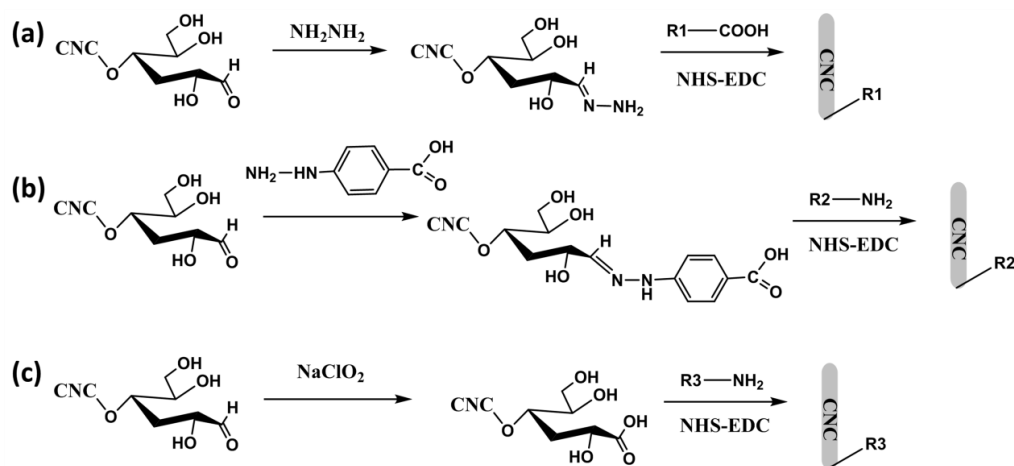


Figure 1.14 Three traditional end modification approaches on the hemiacetal groups of CNC.

Before the end modification reaction on CNC, the crystallites were chemically activated via hydrazone linkages at the reducing ends. Macromolecules, carrying reactive end groups, were attached to the reactive cellulose crystallites by coupling reaction. Amino-terminated polyethylene glycol and polydimethylsiloxane can be coupled to CNC carrying phenyl carboxylic functions at their front face. The cellulose-block-polydimethylsiloxane copolymer exhibits a pronounced tendency to form specific super-structures in slurries and films made from it. Alternatively, polyacrylamide was tethered from these hemiacetal units, after being modified with reactive azo initiators, by radical polymerization. Diverse reactive conditions and grafted molecules on the basis of the end hemiacetal of CNC were used and summarized in Table 1.5. Arcot et al.¹²³ and Lokanathan et al.¹²⁴ introduced a new way for topochemical thiolation of cellulose nanocrystals at their reducing ends by using a simple procedure involving initial carboxylation of the reducing end aldehyde groups followed by NHS-EDC-mediated activation and reaction with nucleophilic amine molecules bearing thiol termini as shown in Figure 1.15. The CNC aqueous dispersions ($10 \text{ mg} \cdot \text{mL}^{-1}$) at pH 9.2 were buffered with 0.1 M sodium carbonate buffer. The buffered CNC dispersions (10 mL) were placed in a water bath maintained at $70 \text{ }^\circ\text{C}$. A total of $150 \text{ } \mu\text{mol}$ of $\text{NH}_2(\text{CH}_2)_6\text{SH} \cdot \text{HCl}$ and 22.5 mmol of reducing agent (Ac) were added in three steps over a period of 3 days accompanied by stirring ($50 \text{ } \mu\text{mol}$ of $\text{NH}_2(\text{CH}_2)_6\text{SH} \cdot \text{HCl} + 7.5 \text{ mmol}$ of reducing agent $\cdot \text{day}^{-1}$ for 3 days). After 3 days the reaction mixture was cooled to room temperature, followed by addition of 10 mL of 3 M HCl to neutralize the excess reducing agent. The neutralized reaction mixture was dialyzed against distilled water, followed by addition of appropriate amounts of KCl salt so that the final dispersion was

2 M in KCl, and the resulting mixture was stirred overnight. After incubation with KCl, the reaction mixture was dialyzed against distilled water to remove electrolytes. The CNC-SH dispersion obtained from the final dialysis step was used for various characterization procedures.

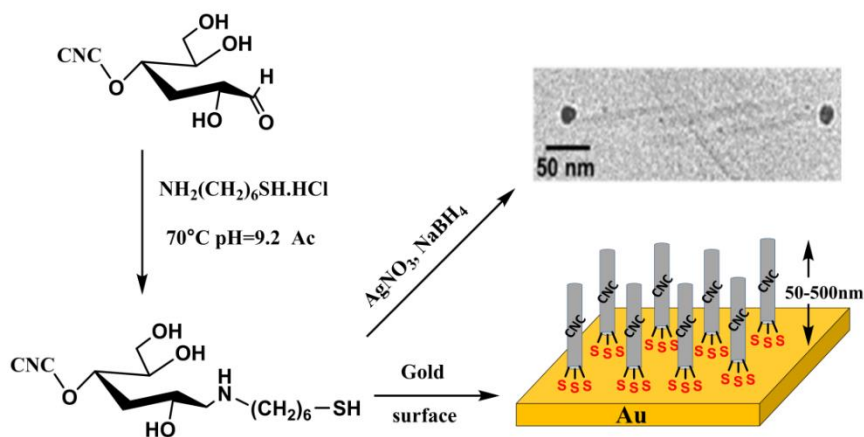


Figure 1.15 Common synthetic routes for topochemical functionalization of CNC nanorods with thiol end groups.

The successful specific thiolation of CNC was confirmed by imaging of tagged silver nanoparticles. The CNC-SH aqueous dispersions obtained from reductive amination were diluted using distilled water for a final CNC-SH concentration of $1 \text{ mg} \cdot \text{mL}^{-1}$. To 2 mL of diluted CNC-SH dispersion was added 200 μL of aqueous silver nitrate solution (10 mM), followed by addition of 2 mL of sodium borohydride (5 mM), and this final dispersion was used in the sample preparation procedure for cryo-TEM. CNC having a lateral dimension of 3-5 nm and a length of 50-500 nm incorporated the native crystalline structure with hydrogen bonded cellulose chains in the parallel configuration. This facilitates asymmetric, selective chemical modification of the reducing ends through reductive amination. Successful thiol functionalization was demonstrated using cryo transmission electron microscopy based on selective attachment of silver nanoparticles to the CNC-SH ends to form colloidal rod-sphere adducts. The promoted binding of CNC-SH on gold surfaces was shown by atomic force microscopy and quartz crystal microbalance, where the high dissipation suggested pronounced orientational mobility due to flexible joints at one rod end onto the surfaces. Joint flexibility was also demonstrated by bending and realignment of CNC-SH rods using a receding triple-phase evaporation front of a drying drop of water.

Table 1.5 Reactive conditions and grafted molecules on the basis of the end hemiacetal of CNC.

Pretreatment	Grafted molecule	Catalyst	Solvent	Reactive conditions	Ref.
4-hydrazinobenzoic acid	O,O-Bis(2-aminoethyl)-polyethylene glycol	Carbodiimide	H ₂ O	35 °C, 48 h, pH=9, R.T.	114
4-hydrazinobenzoic acid	3-aminopropyl-terminated polydimethylsiloxanes	Carbodiimide	H ₂ O	35 °C, 48 h, pH=9	114
4-cyanopentanoic dihydrazide	acrylamide	—	H ₂ O	60 °C, 48 h, N ₂	114
4-Hydrazinobenzoic acid	acrylamide	—	H ₂ O	70 °C, 48 h, N ₂	114
Sodium chlorite, acetic acid	6-amino-1-hexanethiol hydrochloride (NH ₂ -R-SH)	EDC, NHS	H ₂ O	70 °C, 72 h, pH=9.2	115
—	NH ₂ (CH ₂) ₆ SH·HCl	Sodium triacetoxyborohydride	H ₂ O	70 °C, 72 h, pH=9.2	116
Bis(triethylammonium) salt, acetic acid	Alexa Fluor 633	—	H ₂ O	R.T., 24 h , in the dark	117
—	7-hydrazino-4-methylcoumarin (HMC)	—	H ₂ O	25 °C, 24 h, in the dark.	118
—	7-amino-4-methylcoumarin (AMC)	—	H ₂ O	25 °C, 24 h, in the dark.	118

1.5 Functional Applications of Nanocellulose

1.5.1 Biological Scaffolds

Cell culture scaffolds are usually composed of a 3D porous network that can facilitate cell fusion, nutrient transport, and cellular waste metabolism.¹¹⁹ A wide range of hydrogel and aerogel scaffolds have been explored, such as collagen, peptides, alginates, chitosan, silk, hyaluronic acid, polyacrylamide, PEG, as well several synthetic polymers, which have been decorated with biofunctional side groups. They cover a wide range of physical and chemical properties. However, recently it has been emphasized that extracellular matrices are typically strain stiffening, where the stiffness increases upon imposed strain or loading of the gel.^{120–125} Nanocellulose hydrogels and aerogels at physiological conditions can provide a tunable platform technology for biomedical scaffolding, due to their unique mechanical and chemical properties, biocompatibility, low toxicity, and functionalities.

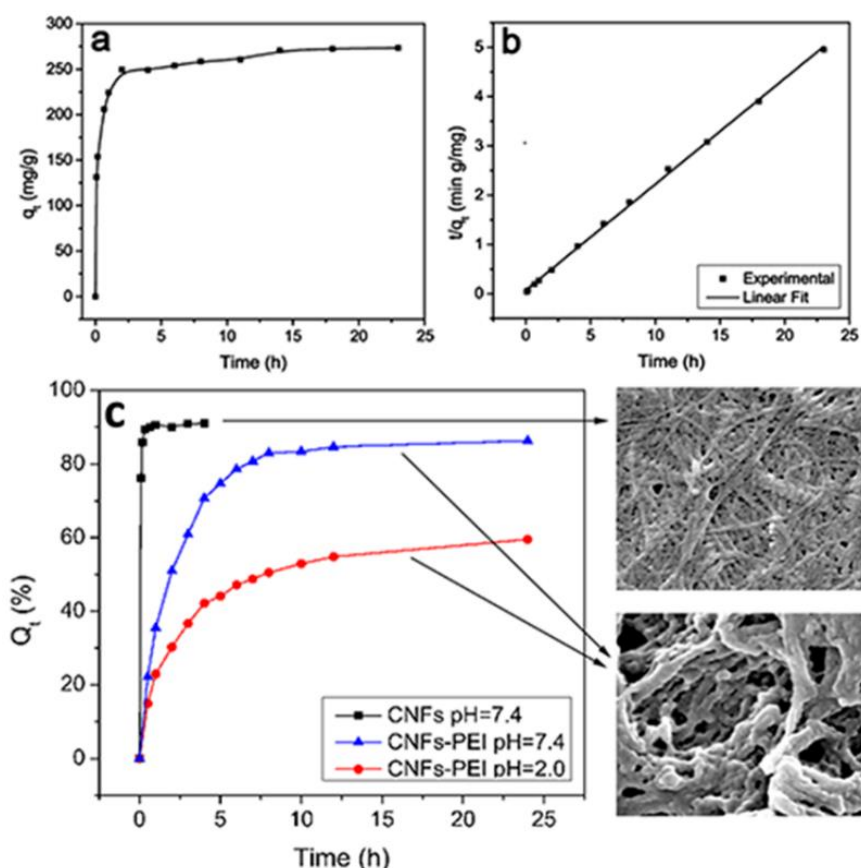


Figure 1.16 (a) Adsorption curves for CNFs-PEI aerogel and (b) linear fitting of NaSA adsorption data using the pseudo-second-order equation. (c) Sodium salicylate (NaSA) cumulative release curves with time for CNFs-PEI aerogel at different pH values.¹²⁶

Nanocellulose aerogels grafted with PEI (CNFs–PEI) have been manufactured as new drug carriers by freeze drying.¹²⁶ The drug loading and release properties of the aerogels were investigated using a model drug of water-soluble sodium salicylate (NaSA). The aerogels revealed an effective drug load capacity (287.39 mg g^{-1}) (Figure 1.16). In addition, controlled sustained release of sodium salicylate in the aerogel could be achieved by regulating the pH and temperature conditions during release, which was expected to be a new generation drug carrier. Cai et al. designed honeycomb aerogel microspheres using CNFs covalently crosslinked with epichlorohydrin resin without toxic solvents by spray freeze drying.¹²⁷ This unique ultralight aerogel presented an open porous structure with a low density (1.8 mg cm^{-3}) and a high water uptake capacity ($\approx 100 \text{ g g}^{-1}$). It was proved to be an excellent culture scaffold for cells even in a critical environment, owing to the openness of pores and enhanced mechanical properties provided by covalent crosslinking. Furthermore, some antibacterial nanoparticles (e.g., silver) can be mixed into the nanocellulose matrix to enhance the resistance and tolerance of the aerogel to bacteria, which can be developed as self-supporting wound dressings.^{128–130}

1.5.2 Thermal Insulation

The thermal transfer of a solid material is mainly divided into thermal conduction, thermal convection, and thermal radiation.¹³¹ When the pore size is larger than the average free path of the gas (70 nm), according to the Knudsen effect, the thermal conductivity of the nanocellulose aerogel will be affected as the porous structure can no longer restrict gas movement.¹³² Accordingly, it is necessary to adjust the pore size of the aerogel based on actual demands. Several strategies have been employed to achieve effective thermal insulation properties.

Kobayashi et al. explored a novel type of aerogel from liquid-crystalline nanocellulose with higher-order frameworks (Figure 1.17a).¹³³ They studied the relationship between aerogel density and thermal conductivity. When the aerogel density was 17 mg cm^{-3} , the lowest thermal conductivity was $18 \text{ mW m}^{-1} \text{ K}^{-1}$. For CNF aerogel, the thermal conductivity remained $18 \text{ mW m}^{-1} \text{ K}^{-1}$ even when increasing the density and reducing the porosity by compression, when compared with the uncompressed aerogel with $14 \text{ mW m}^{-1} \text{ K}^{-1}$, showing an excellent thermal insulation property.¹³⁴ To determine the thermal insulation effect of cotton CNF aerogel more intuitively, Qi et al. placed the

aerogel on a hot plate and a cold plate with temperatures of $\approx 70\text{ }^{\circ}\text{C}$ and $\approx 0\text{ }^{\circ}\text{C}$, respectively (Figure 1.17b).¹³⁵ The heat effectively stopped and diffused inside the aerogel network, allowing the aerogel to resist effects from different external environments without any obvious changes in shape and structure.

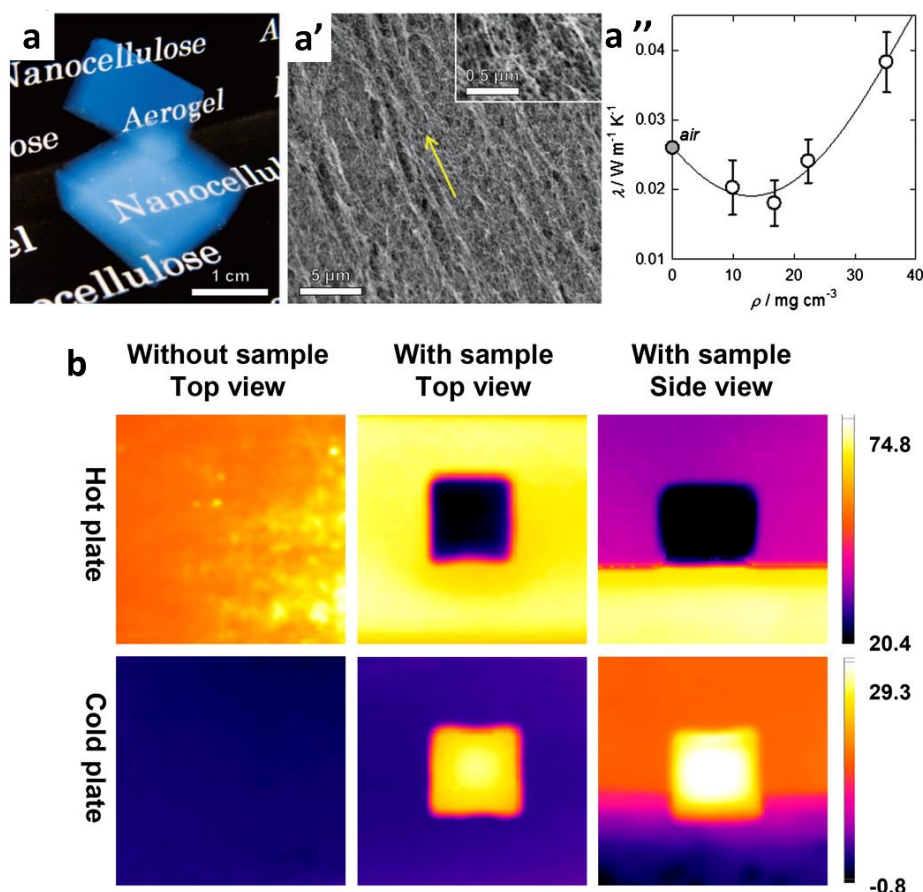


Figure 1.17 a) The ordered morphology of LC-NCell aerogels and the dependence of the thermal conductivity (λ) on the density (ρ) of the aerogel.¹³³ b) Thermographic images of cotton CNF aerogel under different environments. Reproduced with permission¹³⁵

1.5.3 Optical Functions

Various optical functions can be achieved using nanocelluloses. Probably, the most widely reported deals with cholesteric liquid crystallinity of CNC, which causes tunable iridescence, such as structural colors,^{165–167} and allows transferring such properties into other materials upon templating.^{139–142} Some berries also show structural colors due to chiral twisting of native cellulosic components.¹⁴³ The formation of chiral nematic phases of CNC was also studied in spherical confinement in emulsions to follow tactoid formation¹⁴⁴ or in case of microfluidic droplets demonstrating radial symmetric orientation of the CNC layers with angle-independent photonic properties.^{145,146} On the

other hand, one of the main efforts related to nanocelluloses has been to achieve transparency in films.^{42,147–149}

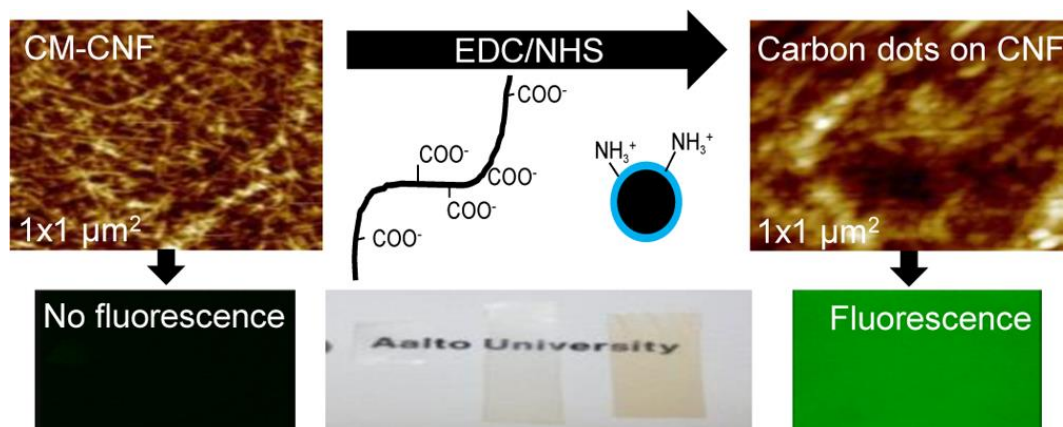


Figure 1.18 Optical functionalities based on nanocelluloses: CNF can be decorated with fluorescent carbon dots.¹⁵⁰

Carbon dots are roughly 1 nm fluorescent nanoparticles which were found upon purification of single wall carbon nanotubes.¹⁵¹ As they are nontoxic, they have potential application for biosensors, biomedical imaging, marker development, and anticounterfeiting. Cationic amine-coated carbon dots have been connected to TEMPO-CNF using EDC/NHS coupling chemistry (Figure 1.18).¹⁵⁰ In a follow up research, TEMPO-CNF was decorated with amine-coated carbon dots again using carbodiimide-assisted coupling chemistry and fluorescent adducts were observed. Cell viability tests suggest that the TEMPO-CNF decoration with amine-coated carbon dots improved the cytocompatibility and also enhanced their cellular association and internalization for both HeLa and RAW 264.7 cells after 4 and 24 h incubation.¹⁵²

1.5.4 Adsorption and Environmental Treatment

1.5.4.1 Adsorbents for heavy metal ions

Heavy metal ions, which are found in industrial effluents such as metal plating and paint manufacture, are considered as a serious threat to humans and the environment.¹⁵³ Polysaccharides and their derivatives showed high efficiency for removal of heavy metal ions from wastewater. The higher adsorption efficiency of polysaccharides can be attributed to high functionality, hydrophilicity and the highly reactive properties of the functional groups. Various polysaccharide adsorbents for the removal of heavy metals have been investigated and are shown in Table 1.6.

Table 1.6 Various polysaccharide-based adsorbents for the removal of heavy metals. q_{\max} corresponds to the maximum amount of pollutant that can be adsorbed per gram of adsorbent.

polysaccharide-based adsorbent	Heavy metal ion	Equilibrium adsorption conditions	q_{\max} (mmol g ⁻¹)	ref
CNC, CNF, ChNC	Ag (I)	pH = 6.39, 5.45, 6.63 T = 25 °C, t = 12 h	0.32 [CNC], 0.14 [CNF], 0.18 [ChNC]	154
Modified CNC	Pb (II), Cd (II), Ni (II)	pH = 6.0, T = 25 °C, t = 40 min	0.04 [Pb (II)], 0.09 [Cd (II)], 0.15 [Ni (II)]	155
Modified CNC	Cd (II), Pb (II)	pH = 6.5 [Cd (II)], pH = 5.5 [Pb (II)], T = 25 °C, t = 150 min	2.31 [Cd (II)] 1.77 [Pb (II)],	156
Modified CNC	Cd (II), Pb (II)	pH = 6.5 [Cd (II)], pH = 5.5 [Pb (II)], T = 25 °C, t = 5 min	3.07 [Cd (II)] 2.24 [Pb (II)],	156
Modified CNF	Ni (II), Zn (II), Cu (II), Cd (II)	pH = 5.0, T = 25 °C, t = 24 h	0.74 [Ni (II)], 1.61 [Zn (II)], 1.90 [Cu (II)], 2.06 [Cd (II)]	157
Carboxylated CNF	Cr (III), Ni (II), Cu (II), Zn (II)	pH = 6.2, T = 25 °C, t = 20 h	1.11 [Cr (III)], 0.83 [Ni (II)], 2.12 [Cu (II)], 1.01 [Zn (II)]	158
TEMPO-CNF	UO ₂ ²⁺	pH = 6.5, T = 25 °C, t = 2 h	0.62	159
Polymerized CNC	Pb (II), Ni (II), Cd (II), Cr (III)	pH = 6.5, T = 25 °C, t = 40 min	—	160,161
AMEO-modified CNF	Cu (II), Ni (II), Cd (II)	pH = 5.0, T = 25 °C, t = 160 min [Cu (II)], 8 min [Cd (II)], 35 min [Ni (II)]	3.15 [Cu (II)], 2.73 [Ni (II)], 4.19 [Cd (II)]	162
CHA-modified CNF	Cd (II), Ni (II)	pH = 5.0, T = 25 °C, t = 5 min	1.22 [Cd (II)], 2.02 [Ni (II)]	163
Carboxylated CNF	Pb (II), Hg (II), Ag (I), Cu (II)	T = 25 °C, t = 3 days	0.53 [Pb (II)], 0.78 [Hg (II)], 1.06 [Ag (I)], 2.38 [Cu (II)]	164
TEMPO-CNF	Cu (II)	pH = 5.0, T = 30 °C, t = 20 h	0.82	165
Phosphorylated CNC	Cu (II), Ag (I), Fe (III)	pH = 3.5 to 4.5, T = 25 °C, t = 12 h [Cu (II) & Fe (III)], t = 6 h [Ag (I)]	1.84 [Cu (II)], 1.26 [Ag (I)], 2.06 [Fe (III)]	166
Bisphosphonate CNC	V (V)	pH = 3, T = 25 °C, t = 24 h	1.98	167
Electrosterically CNC	Cu (II)	pH = 4.0, T = 25 °C, t = 210 s	2.91	168
Au-CNC composite	Hg (II)	pH = 7.0, T = 25 °C, t = 12 h	0.13	169
CNC nanocomposite	Co (II)	pH = 6.0, T = 30 °C, t = 120 min	5.95	170
CNC composite	Hg (II)	pH = 8.0, T = 30 °C, t = 60 min	1.19	171
FeNP-modified CNF	As (V)	pH = 2.0, T = 25 °C, t = 75 min	2.46	172
Carboxylated CNF	Pb (II)	pH = 4.5, T = 25 °C, t = 200 min	0.82	173
Sulfonated CNF	Pb (II)	pH = 5.0, T = 4 °C, t = 20 h	1.20	174

CNC, CNF and chitin nanocrystals (ChNC) were used to remove Ag (I), Cu (II) and Fe (III) from contaminated water.¹⁵⁴ CNC was produced by sulfuric acid hydrolysis, CNF was isolated from cellulose sludge in the acidic and alkaline pH, and ChNC was isolated from crab shell residue. The specific surface area of CNC, CNF and ChNC was 138 - 226, 146 - 219 and 76 - 86 m² g⁻¹, respectively. The maximum amount of pollutant that can be adsorbed per gram of adsorbent (q_{\max}) for CNC, CNF and ChNC for Ag (I) was 0.318, 0.143 and 0.183 mmol g⁻¹, respectively. Surface adsorption via electrostatic interactions was considered to be the prominent mechanism of heavy metal ion capture from wastewater. Surface-modified CNC was also used for the removal of Cd (II), Pb (II) and Ni (II).¹⁵⁵ The q_{\max} value for surface-modified CNC for Pb (II), Cd (II) and Ni (II) was 0.04, 0.09 and 0.15 mmol g⁻¹, respectively. Surface modification with more negatively charged groups significantly enhanced the removal efficiency of metal ions, which provided new ways for environmentally friendly remediation of heavy metals. The adsorbents could be regenerated by using 0.5 M HNO₃ after three adsorption cycles. Succinic anhydride-modified CNC (SCNC) was used for the adsorption of Cd (II) and Pb (II).¹⁵⁶ CNC was modified with succinic anhydride to get SCNC, then treated with saturated NaHCO₃ to obtain NaSCNC. The q_{\max} value for SCNC and NaSCNC was 465.1 and 344.8 mg g⁻¹ for Cd (II); 367.6 and 259.7 mg g⁻¹ for Pb (II), respectively. Carboxylated CNF extracted from pulp residue could be used as efficient adsorbent for the removal of Ni (II), Zn (II), Cu (II) and Cr (III) from aqueous solutions, while the q_{\max} value was 0.74, 1.61, 1.90 and 2.06 mmol g⁻¹, respectively.^{157,158} Negatively charged TEMPO-CNF was very effective to adsorb UO₂²⁺ from wastewater, while the q_{\max} value was 0.62 mmol g⁻¹.¹⁵⁹ The high specific surface area, surface charge density and hydrophilicity of TEMPO-CNF contributed to the high UO₂²⁺ adsorption efficiency.

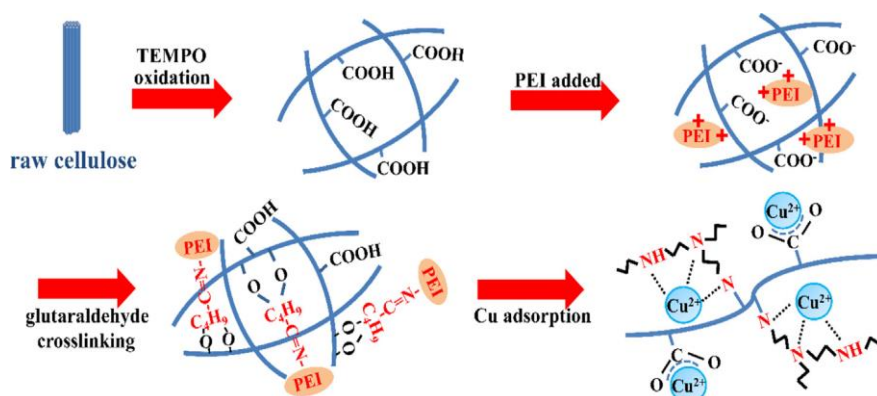


Figure 1.19 General chemical routes for the adsorption of Cu (II) by polyethylenimine (PEI) modified TEMPO-CNF.¹⁶⁵

Graft polymerization of CNC with monomeric acids introduced more negative carboxylate groups on the surface of CNC.^{160,161} Amination of CNC with acryl amide was responsible for the incorporation of NH_3^+ cationic ligands on the surface. Esterification of CNC with succinic anhydride led to an increase in the binding sites with positively charged metal ions. The q_{max} value for Cr (VI) and Cr (III) was 0.053 and 0.0055 mmol g^{-1} , respectively. Aminopropyltriethoxysilane (AMEO)-modified CNF was prepared for removal of Cu (II), Ni (II) and Cd (II), while the q_{max} value was 3.15, 2.73 and 4.19 mmol g^{-1} , respectively.¹⁶² The amino ($-\text{NH}_2$) and hydroxyl ($-\text{OH}$) groups contributed to the higher adsorption efficiency due to the free electron doublets of the nitrogen and oxygen atoms. Carbonated hydroxyapatite modified CNF was reported to remove Cd (II) and Ni (II) from aqueous solution, while the q_{max} value was 1.22 and 2.02 mmol g^{-1} , respectively.¹⁶³ The adsorption mechanism was mainly attributed to ionic interactions between adsorbates and modified CNF. The adsorption-desorption cycles proved that 0.01 M HNO_3 was a highly effective regenerant for the adsorption. Cross-linked polyvinyl alcohol CNF (PVA-CNF) hybrid aerogels were used for the removal of Pb (II), Hg (II), Ag (I) and Cu (II) from aqueous solutions, while the q_{max} value was 0.53, 0.78, 1.06 and 2.38 mmol g^{-1} , respectively.¹⁶⁴ PVA-CNF aerogels were hydrophobic and oleophilic after being treated with methyltrichlorosilane. Polyethylenimine (PEI)-modified TEMPO-CNF was reported for the removal of Cu (II), as shown in Figure 1.19.¹⁶⁵ The abundant carboxyl and amino functional groups were introduced onto CNF, which acted as active sites for the binding of Cu (II).

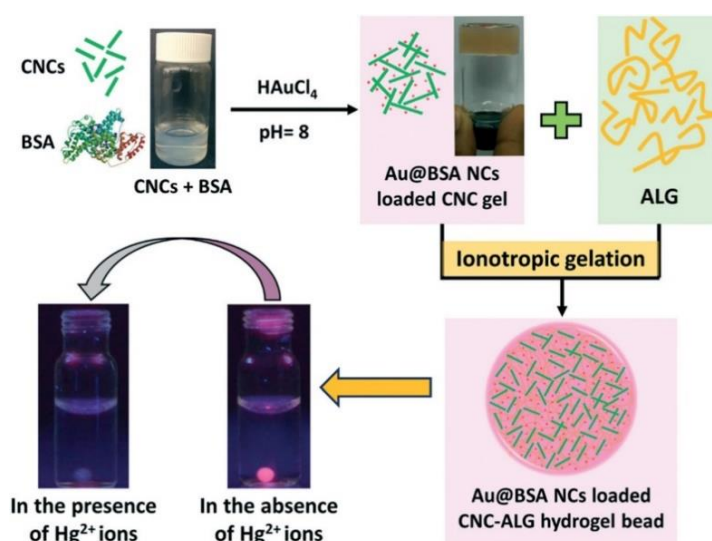


Figure 1.20 Schematic representation showing the preparation of CNC nanocomposites and its simultaneous sensing and scavenging of Hg^{2+} ions in water.¹⁶⁹

Enzymatically phosphorylated CNC was reported to remove Cu (II), Ag (I) and Fe (III), while q_{\max} value of 1.84, 1.26 and 2.06 mmol g⁻¹, respectively.¹⁶⁶ Phosphorylated CNC significantly improved the metal sorption capacity due to the high specific surface area. Bisphosphonate CNC was also used to remove vanadium (V) from aqueous solution, while the q_{\max} value was 1.98 mmol g⁻¹.¹⁶⁷ Electrosterically CNC (ECNC) was extracted from wood fibers through periodate/chlorite oxidation for removal of Cu (II).¹⁶⁸ During the adsorption, ECNC aggregated into star-like particles at low Cu (II) concentrations, and the aggregate morphology converted to raft-like particles at higher Cu (II) concentrations by the collapse between dicarboxylic cellulose chains and charge neutralization. The q_{\max} value for Cu (II) was 185 mg g⁻¹, which was attributed to the highly charged dicarboxylic cellulose chains. Luminescent CNC composite could simultaneously sense and scavenge heavy metal ions, specifically for Hg (II) in water, as shown in Figure 1.20.¹⁶⁹ Nanocomposites were constructed by introducing bovine serum albumin-protected gold nanoclusters into the CNC alginate hydrogel beads, while the q_{\max} value for Hg (II) was 0.13 mmol g⁻¹. A poly grafted CNC composite with multi carboxyl functional groups was developed for the removal of Co (II) and Hg (II) from aqueous solutions.^{170,171} The adsorbents could be effectively reused more than five cycles with 0.1 M HCl.

Magnetic iron nanoparticle-modified CNF was used for the removal of As (V), while the q_{\max} value was 2.46 mmol g⁻¹.¹⁷² The adsorbents could be effectively regenerated more than 98% after three cycles by 1 M NaOH solution. Magnetic hydrogels of carboxylated CNF were reported for removal of Pb (II), while the adsorption capacity was much higher than that of non-carboxylated CNF over the entire pH range.^{173,174} This could be attributed to the carboxyl groups on the carboxylated CNF surface, which significantly enhance the electrostatic interaction between the adsorbent and metal ions. Additionally, desorption experiments proved that the magnetic hydrogels could be easily regenerated with 0.01 M HNO₃ and the adsorption efficiency can be maintained more than 90% after four cycles.

1.5.4.2 Adsorbents for oil/water separation

Oil from petrochemical industries has become a serious concern, and absorbents based on organic and inorganic porous materials have been developed for oil/water separation. Among these absorbents, polysaccharide absorbents have gained increasing attention due to their unique properties and sustainable character, as shown in Table 1.7.

Table 1.7 Various polysaccharide-based absorbents for oil/water separation processes.

Polysaccharides-based adsorbent	Absorbent characteristics	Absorption capacity	ref
Carboxyl CNC aerogel	$\rho = 22.4 - 23.3 \text{ mg cm}^{-3}$, BET = 195 - 303 $\text{m}^2 \text{g}^{-1}$, P = 96.3-97.2%,	133 \pm 6 g g^{-1} (water), 54 \pm 6 g g^{-1} (dodecane), 99 \pm 8 g g^{-1} (ethanol), 34 \pm 4 g g^{-1} (toluene)	175
Hydrazine-CNC aerogel	$\rho = 5.6 \text{ mg cm}^{-3}$, BET = 250 \pm 80 $\text{m}^2 \text{g}^{-1}$, P = 99.6%,	160 \pm 10 g g^{-1} (water), 72 \pm 5 g g^{-1} (dodecane), 130 \pm 10 g g^{-1} (ethanol), 134 \pm 8 g g^{-1} (dimethyl sulfoxide)	176
Carboxylated-CNF/PVA aerogel	$\rho = 13 \text{ mg cm}^{-3}$, BET = 172 \pm 13 $\text{m}^2 \text{g}^{-1}$, $\theta = 150.3 \pm 1.2^\circ$, P = 98%,	44 - 96 g g^{-1} (oil and organic solvents)	173
Triethoxy (octyl) silane- CNF aerogel	$\rho = 1.7 - 8.1 \text{ mg cm}^{-3}$, BET = 10.9 $\text{m}^2 \text{g}^{-1}$, P = 99.5 - 99.9%	210 g g^{-1} (water), 375 g g^{-1} (chloroform), 139 - 356 g g^{-1} (non-polar liquids)	177
CNC scaffold composite	$\rho = 3.3 - 7.5 \text{ mg cm}^{-3}$, pore diameter = 0.1 - 10 μm	100 - 200 g g^{-1} (organic solvents)	178
Silylated tunicate CNC	BET = 73.23 $\text{m}^2 \text{g}^{-1}$, $\theta = 134.5$, P = 98.8%,	33 - 36 g g^{-1} (oil)	179
Methyltrimethoxysilane- CNF aerogel	$\rho = 5.07 - 17.3 \text{ mg cm}^{-3}$, BET = 3 - 25 $\text{m}^2 \text{g}^{-1}$, $\theta = 110 - 150^\circ$, P = 99%,	49 - 102 g g^{-1} (organic solvents)	180
TiO ₂ -CNF aerogel	$\rho = 20 - 30 \text{ mg cm}^{-3}$, P = 98%, $\theta = 90^\circ$	20 - 40 g g^{-1} (non-polar liquids)	181

ρ – density, P – Porosity, BET – specific surface area, θ – contact angle.

Hydrazine-carboxyl CNC aerogels were prepared and exhibited high elasticity and fast oil/water separation, with absorption capacity for water, dodecane, ethanol and toluene of 133, 54, 99 and 34 g g^{-1} , respectively.¹⁷⁵ Meanwhile, the results proved that the increased carboxyl groups contributed to the excellent mechanical properties and shape recovery ability. Chemically cross-linked CNC aerogels based on hydrazide and aldehyde-modified CNC were reported for oil/water separation.¹⁷⁶ The unique pore structure of the CNC aerogels contributed to the shape recovery ability. The absorption capacity of the CNC aerogels for water, dodecane, ethanol and dimethyl sulfoxide was 160, 72, 130 and 134 g g^{-1} , respectively. Cross-linked PVA-CNF hybrid aerogels were prepared for removing oil and organic solvents from wastewater.¹⁷³ The hydrophobic PVA-CNF aerogels exhibited excellent absorption capacity in the range of 44 - 96 g g^{-1} for various types of organic solvents (hexane, toluene, gasoline, chloroform) and oils

(pump oil, crude oil, diesel oil, corn oil). Hydrophobic CNF aerogels were also prepared through vapor deposition with triethoxyl silane for oil/water separation.^{177,178} The resulting aerogels exhibit ultra-light ($1.7 - 8.1 \text{ mg cm}^{-3}$) and ultra-porous (99.5 - 99.9%) features, which displayed excellent absorption capacity and good recyclability. The absorption capacity for water, chloroform, non-polar liquids was 210, 375, 139 - 356 g g^{-1} , respectively.

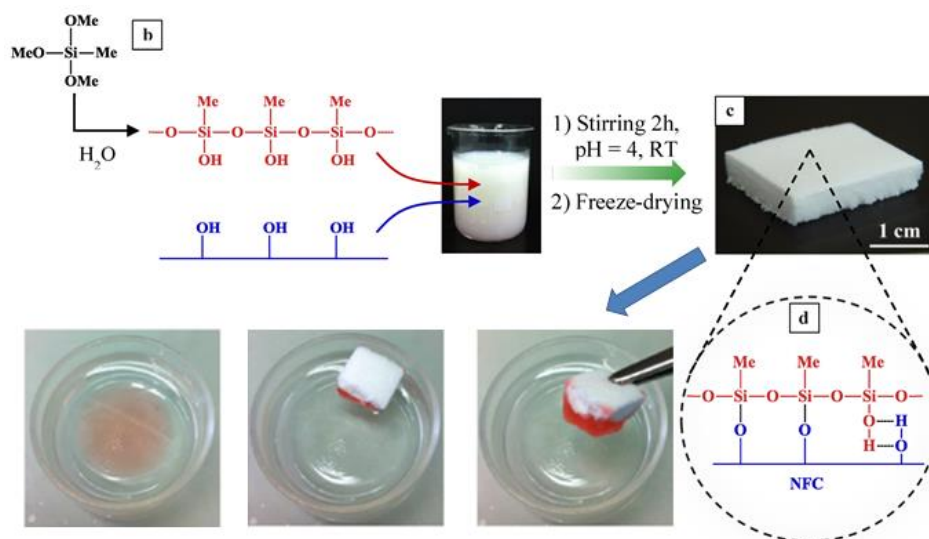


Figure 1.21 Schematic diagram showing the general scheme for the synthesis of silylated CNF sponges and their simultaneous use in the removal of red-colored dodecane spill from water.¹⁸⁰

Composite aerogels were fabricated from silylated tunicate CNC and red mud for oil/water separation.¹⁷⁹ The absorption capacity of these composite aerogels for oil and 2,4-dichlorophenol was 33 - 36 g g^{-1} and 5.5 - 6.0, respectively. A facile synthesis of hydrophobic and ultralight CNF aerogels was reported using a novel and efficient silylation process, as shown in Figure 1.21.¹⁸⁰ Compared with conventional inorganic porous materials, the shape recovery of silylated CNF aerogels was close to 96% after a compression strain of 50%, which displayed an excellent flexibility. On the basis of the hydrophobic properties, the aerogels were highly efficient in removing organic solvents from wastewater with an excellent selectivity and recyclability. The absorption capacity for oils (silicone oil, motor oil, mineral oil) and organic solvents (ethanol, acetone, dodecane, toluene) was 49 - 102 g g^{-1} . Highly porous CNF aerogels coated with titanium dioxide showed a selective oil-absorbing capacity, with absorption capacities in the range of 20 - 40 g g^{-1} for non-polar liquids and oils.¹⁸¹

1.5.5 Electrically Conducting Materials

Electrical functionalization of nanocelluloses can be achieved in several ways by dispersing electrically conductive components. In typical multicomponent materials, electrical percolation of the conducting component is pursued. In gels and aerogels, the mechanical percolation is inherent, and can lead to electrical percolation at low volume fractions due to double percolation. Therefore, it becomes particularly interesting to strive an electrically conducting component to an aerogel skeleton. Electrical conductivity was shown using CNF aerogels,¹⁸² which were dipped in polyaniline-dodecylbenzene sulphonate solution in toluene to coat the aerogel skeleton with a layer of conjugated polymer. This led to conducting aerogels with a very low geometric volume fraction of conjugated polymer due to the low density of the aerogel. Polyaniline can also be polymerized directly on TEMPO-oxidized CNF templates, catalyzed by laccase, thus leading to electrically conducting films.¹⁸³

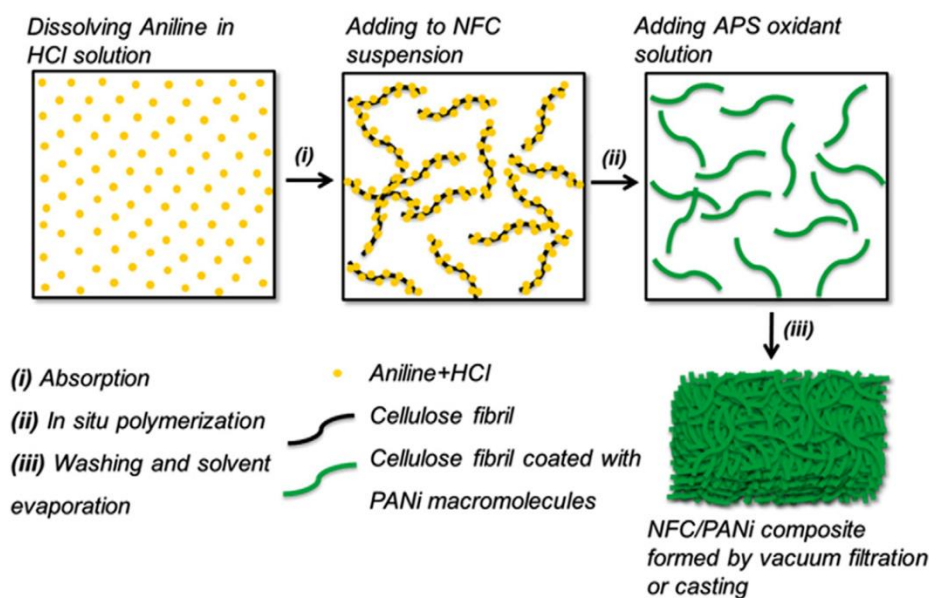


Figure 1.22 Schematics for in situ polymerization of polyaniline in CNF aqueous suspensions, followed by vacuum filtration or solvent casting and evaporation.¹⁸⁴

Higher conductivity values for polyaniline films were obtained by oxidative polymerization of aniline using ammonium persulfate in the presence of CNF dispersed in water (Figure 1.22).¹⁸⁴ This leads to relatively high conductivity of 1.8 S cm^{-1} for 80 wt% polyaniline loading and still moderate conductivity $2.9 \times 10^{-5} \text{ S cm}^{-1}$ for 5 wt% loading, where the mechanical properties are essentially the same as for pristine CNF. Reduced graphene oxide offers interaction sites that are compatible with CNF. Subsequent chemical reduction transfers graphene into the conducting state.

1.5.6 EMI Shielding

With the development of miniaturized and multifunctional electronic packaging, EMI has become an increasingly critical and intractable task to avoid undesirable EM energy generated by electronic components.¹⁸⁵ Generally, the EMI shielding performance is gradually enhanced with increasing electrical conductivity. However, high electrical conductivity is not the only criterion for EMI. For the mobile charge carriers to interact with the incoming EM field and for the porous structure to promote the multiple reflections, the adsorption of EM waves plays an important role. Compared with other 1D or 2D conducting composites, nanocellulose composite aerogels exhibited promising properties for EMI shielding by introducing novel conductive fillers (e.g., silver nanowires (AgNWs),¹⁸⁶ MXene^{187–189}), as they can combine advantages of nanocellulose, conductive fillers, and aerogels including i) biocompatibility, biodegradability, and chemical stability, ii) excellent electrical conductivity, and iii) ultralow density, large open pores, and ultrahigh SSA.

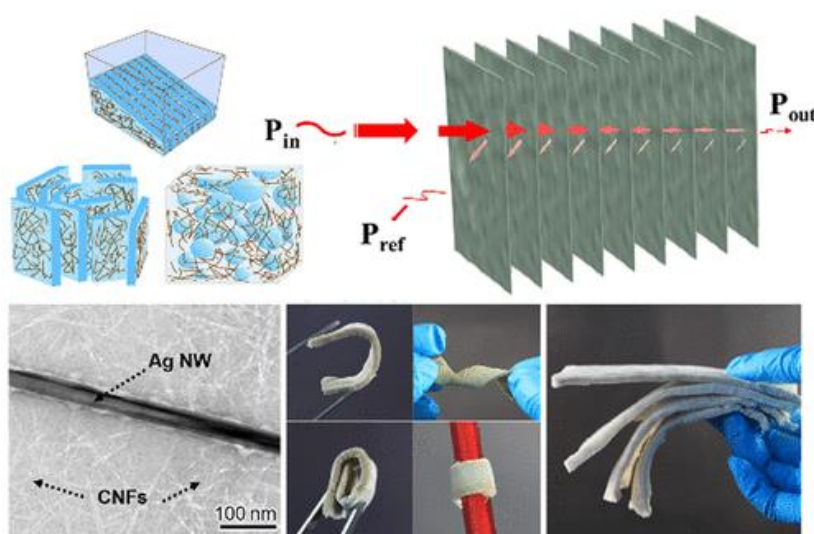


Figure 1.23 Lamellar and highly flexible unidirectional freeze-dried CNF/AgNW composite aerogel and its EMI shielding mechanism.¹⁸⁶

Recently, Zeng et al. assembled 1D AgNWs with a higher aspect ratio and electrical conductivity into CNF dispersions, forming ultralight and highly flexible CNF/AgNW composite aerogels via unidirectional freeze drying (Figure 1.23).¹⁸⁶ The lamellar, honeycomb-like porous structure, effective conductive network provided by AgNWs, and strong hydrogen bond interactions between CNFs and polyvinylpyrrolidone adsorbed on the AgNW surfaces endowed aerogels with a markedly high EMI shielding effectiveness (SE) of >70 dB. Fei et al. loaded zeolitic imidazolate framework-67 (ZIF-

67) into a continuous porous network of CNF aerogels and then annealed it to obtain Co/C@CNF aerogels.¹⁹⁰ The electrically conductive and magnetic aerogels exhibited excellent EMI SE owing to the enhanced magnetic loss and dielectric loss ability. Moreover, the interface impedance mismatch of aerogels has been improved, which was beneficial to reduce reflection loss and alleviate the undesired secondary pollution of EMI waves.

1.6 References

- (1) Filson, P. B.; Dawson-Andoh, B. E.; Schwegler-Berry, D. Enzymatic-Mediated Production of Cellulose Nanocrystals from Recycled Pulp. *Green Chem.* **2009**, *11* (11), 1808–1814.
- (2) Hayashi, N.; Kondo, T. Enzymatically Produced Nano-Ordered Elements Containing Cellulose I β Crystalline Domains of Cladophora Cellulose. In *Handbook of Polymer Nanocomposites. Processing, Performance and Application*; Springer, 2015; pp 1–14.
- (3) Nickerson, R. F.; Habrle, J. A. Cellulose Intercrystalline Structure. *Ind. Eng. Chem.* **1947**, *39* (11), 1507–1512.
- (4) Beck-Candanedo, S.; Roman, M.; Gray, D. G. Effect of Reaction Conditions on the Properties and Behavior of Wood Cellulose Nanocrystal Suspensions. *Biomacromolecules* **2005**, *6* (2), 1048–1054.
- (5) Hirota, M.; Tamura, N.; Saito, T.; Isogai, A. Water Dispersion of Cellulose II Nanocrystals Prepared by TEMPO-Mediated Oxidation of Mercerized Cellulose at PH 4.8. *Cellulose* **2010**, *17* (2), 279–288.
- (6) Elazzouzi-Hafraoui, S.; Nishiyama, Y.; Putaux, J.-L.; Heux, L.; Dubreuil, F.; Rochas, C. The Shape and Size Distribution of Crystalline Nanoparticles Prepared by Acid Hydrolysis of Native Cellulose. *Biomacromolecules* **2008**, *9* (1), 57–65.
- (7) Winter, H. T.; Cerclier, C.; Delorme, N.; Bizot, H.; Quemener, B.; Cathala, B. Improved Colloidal Stability of Bacterial Cellulose Nanocrystal Suspensions for the Elaboration of Spin-Coated Cellulose-Based Model Surfaces. *Biomacromolecules* **2010**, *11* (11), 3144–3151.
- (8) Habibi, Y.; Goffin, A.-L.; Schiltz, N.; Duquesne, E.; Dubois, P.; Dufresne, A. Bionanocomposites Based on Poly (ϵ -Caprolactone)-Grafted Cellulose Nanocrystals by Ring-Opening Polymerization. *J. Mater. Chem.* **2008**, *18* (41),

- 5002–5010.
- (9) de Mesquita, J. P.; Donnici, C. L.; Pereira, F. V. Biobased Nanocomposites from Layer-by-Layer Assembly of Cellulose Nanowhiskers with Chitosan. *Biomacromolecules* **2010**, *11* (2), 473–480.
 - (10) Siqueira, G.; Bras, J.; Follain, N.; Belbekhouche, S.; Marais, S.; Dufresne, A. Thermal and Mechanical Properties of Bio-Nanocomposites Reinforced by *Luffa Cylindrica* Cellulose Nanocrystals. *Carbohydr. Polym.* **2013**, *91* (2), 711–717.
 - (11) Turbak, A. F.; Snyder, F. W.; Sandberg, K. R. Microfibrillated Cellulose, a New Cellulose Product: Properties, Uses, and Commercial Potential. In *J Appl Polym Sci Appl Polym Symp*; 1983; Vol. 37, pp 815–827.
 - (12) Chen, W.; Yu, H.; Liu, Y.; Chen, P.; Zhang, M.; Hai, Y. Individualization of Cellulose Nanofibers from Wood Using High-Intensity Ultrasonication Combined with Chemical Pretreatments. *Carbohydr. Polym.* **2011**, *83* (4), 1804–1811.
 - (13) Abraham, E.; Deepa, B.; Pothan, L. A.; John, M.; Narine, S. S.; Thomas, S.; Anandjiwala, R. Physicomechanical Properties of Nanocomposites Based on Cellulose Nanofibre and Natural Rubber Latex. *Cellulose* **2013**, *20* (1), 417–427.
 - (14) Stelte, W.; Sanadi, A. R. Preparation and Characterization of Cellulose Nanofibers from Two Commercial Hardwood and Softwood Pulps. *Ind. Eng. Chem. Res.* **2009**, *48* (24), 11211–11219.
 - (15) Dinand, E.; Chanzy, H.; Vignon, R. M. Suspensions of Cellulose Microfibrils from Sugar Beet Pulp. *Food Hydrocoll.* **1999**, *13* (3), 275–283.
 - (16) Deepa, B.; Abraham, E.; Cherian, B. M.; Bismarck, A.; Blaker, J. J.; Pothan, L. A.; Leao, A. L.; De Souza, S. F.; Kottaisamy, M. Structure, Morphology and Thermal Characteristics of Banana Nano Fibers Obtained by Steam Explosion. *Bioresour. Technol.* **2011**, *102* (2), 1988–1997.
 - (17) Malainine, M. E.; Mahrouz, M.; Dufresne, A. Thermoplastic Nanocomposites Based on Cellulose Microfibrils from *Opuntia Ficus-Indica* Parenchyma Cell. *Compos. Sci. Technol.* **2005**, *65* (10), 1520–1526.
 - (18) Dufresne, A.; Dupeyre, D.; Vignon, M. R. Cellulose Microfibrils from Potato Tuber Cells: Processing and Characterization of Starch–Cellulose Microfibril Composites. *J. Appl. Polym. Sci.* **2000**, *76* (14), 2080–2092.

- (19) Kaushik, A.; Singh, M. Isolation and Characterization of Cellulose Nanofibrils from Wheat Straw Using Steam Explosion Coupled with High Shear Homogenization. *Carbohydr. Res.* **2011**, *346* (1), 76–85.
- (20) Chen, W.; Yu, H.; Liu, Y.; Hai, Y.; Zhang, M.; Chen, P. Isolation and Characterization of Cellulose Nanofibers from Four Plant Cellulose Fibers Using a Chemical-Ultrasonic Process. *Cellulose* **2011**, *18* (2), 433–442.
- (21) Siqueira, G.; Bras, J.; Dufresne, A. Luffa Cylindrica as a Lignocellulosic Source of Fiber, Microfibrillated Cellulose and Cellulose Nanocrystals. *BioResources* **2010**, *5* (2), 727–740.
- (22) Sundari, M. T.; Ramesh, A. Isolation and Characterization of Cellulose Nanofibers from the Aquatic Weed Water Hyacinth—Eichhornia Crassipes. *Carbohydr. Polym.* **2012**, *87* (2), 1701–1705.
- (23) Pääkkö, M.; Ankerfors, M.; Kosonen, H.; Nykänen, A.; Ahola, S.; Österberg, M.; Ruokolainen, J.; Laine, J.; Larsson, P. T.; Ikkala, O. Enzymatic Hydrolysis Combined with Mechanical Shearing and High-Pressure Homogenization for Nanoscale Cellulose Fibrils and Strong Gels. *Biomacromolecules* **2007**, *8* (6), 1934–1941.
- (24) Saito, T.; Kimura, S.; Nishiyama, Y.; Isogai, A. Cellulose Nanofibers Prepared by TEMPO-Mediated Oxidation of Native Cellulose. *Biomacromolecules* **2007**, *8* (8), 2485–2491.
- (25) Wågberg, L.; Decher, G.; Norgren, M.; Lindström, T.; Ankerfors, M.; Axnäs, K. The Build-up of Polyelectrolyte Multilayers of Microfibrillated Cellulose and Cationic Polyelectrolytes. *Langmuir* **2008**, *24* (3), 784–795.
- (26) Gatenholm, P.; Klemm, D. Bacterial Nanocellulose as a Renewable Material for Biomedical Applications. *MRS Bull.* **2010**, *35* (3), 208–213.
- (27) Nakagaito, A. N.; Iwamoto, S.; Yano, H. Bacterial Cellulose: The Ultimate Nano-Scalar Cellulose Morphology for the Production of High-Strength Composites. *Appl. Phys. A* **2005**, *80* (1), 93–97.
- (28) Lin, N.; Dufresne, A. Surface Chemistry, Morphological Analysis and Properties of Cellulose Nanocrystals with Graded Sulfation Degrees. *Nanoscale* **2014**, *6* (10), 5384–5393.
- (29) Foster, E. J.; Moon, R. J.; Agarwal, U. P.; Bortner, M. J.; Bras, J.; Camarero-Espinosa, S.; Chan, K. J.; Clift, M. J.; Cranston, E. D.; Eichhorn, S. J. Current Characterization Methods for Cellulose Nanomaterials. *Chem. Soc. Rev.* **2018**,

- 47 (8), 2609–2679.
- (30) Uetani, K.; Yano, H. Zeta Potential Time Dependence Reveals the Swelling Dynamics of Wood Cellulose Nanofibrils. *Langmuir* **2012**, *28* (1), 818–827.
- (31) Siqueira, G.; Bras, J.; Dufresne, A. New Process of Chemical Grafting of Cellulose Nanoparticles with a Long Chain Isocyanate. *Langmuir* **2010**, *26* (1), 402–411.
- (32) Dufresne, A. *Nanocellulose: From Nature to High Performance Tailored Materials*; Walter de Gruyter GmbH & Co KG, 2017.
- (33) Neto, W. P. F.; Mariano, M.; da Silva, I. S. V.; Silvério, H. A.; Putaux, J.-L.; Otaguro, H.; Pasquini, D.; Dufresne, A. Mechanical Properties of Natural Rubber Nanocomposites Reinforced with High Aspect Ratio Cellulose Nanocrystals Isolated from Soy Hulls. *Carbohydr. Polym.* **2016**, *153*, 143–152.
- (34) Bras, J.; Viet, D.; Bruzzese, C.; Dufresne, A. Correlation between Stiffness of Sheets Prepared from Cellulose Whiskers and Nanoparticles Dimensions. *Carbohydr. Polym.* **2011**, *84* (1), 211–215.
- (35) Benhamou, K.; Dufresne, A.; Magnin, A.; Mortha, G.; Kaddami, H. Control of Size and Viscoelastic Properties of Nanofibrillated Cellulose from Palm Tree by Varying the TEMPO-Mediated Oxidation Time. *Carbohydr. Polym.* **2014**, *99*, 74–83.
- (36) Dufresne, A. Cellulose Nanomaterial Reinforced Polymer Nanocomposites. *Curr. Opin. Colloid Interface Sci.* **2017**, *29*, 1–8.
- (37) Dufresne, A. Nanocellulose: A New Ageless Bionanomaterial. *Mater. Today* **2013**, *16* (6), 220–227.
- (38) Nechyporchuk, O.; Belgacem, M. N.; Pignon, F. Current Progress in Rheology of Cellulose Nanofibril Suspensions. *Biomacromolecules* **2016**, *17* (7), 2311–2320.
- (39) Boluk, Y.; Lahiji, R.; Zhao, L.; McDermott, M. T. Suspension Viscosities and Shape Parameter of Cellulose Nanocrystals (CNC). *Colloids Surf. Physicochem. Eng. Asp.* **2011**, *377* (1–3), 297–303.
- (40) Bröckel, U.; Meier, W.; Wagner, G. *Product Design and Engineering: Formulation of Gels and Pastes*; John Wiley & Sons, 2013.
- (41) Armstrong, M. *A Handbook of Human Resource Management Practice*; Kogan Page Publishers, 2006.
- (42) Nogi, M.; Iwamoto, S.; Nakagaito, A. N.; Yano, H. Optically Transparent

- Nanofiber Paper. *Adv. Mater.* **2009**, *21* (16), 1595–1598.
- (43) Fukuzumi, H.; Saito, T.; Iwata, T.; Kumamoto, Y.; Isogai, A. Transparent and High Gas Barrier Films of Cellulose Nanofibers Prepared by TEMPO-Mediated Oxidation. *Biomacromolecules* **2009**, *10* (1), 162–165.
- (44) Gray, D. G. Recent Advances in Chiral Nematic Structure and Iridescent Color of Cellulose Nanocrystal Films. *Nanomaterials* **2016**, *6* (11), 213.
- (45) Beck, S.; Bouchard, J.; Berry, R. Controlling the Reflection Wavelength of Iridescent Solid Films of Nanocrystalline Cellulose. *Biomacromolecules* **2011**, *12* (1), 167–172.
- (46) Nair, S. S.; Zhu, J. Y.; Deng, Y.; Ragauskas, A. J. High Performance Green Barriers Based on Nanocellulose. *Sustain. Chem. Process.* **2014**, *2* (1), 1–7.
- (47) Aulin, C. Novel Oil Resistant Cellulosic Materials, KTH, 2009.
- (48) Missoum, K.; Belgacem, M. N.; Bras, J. Nanofibrillated Cellulose Surface Modification: A Review. *Materials* **2013**, *6* (5), 1745–1766.
- (49) Dai, L.; Long, Z.; Chen, J.; An, X.; Cheng, D.; Khan, A.; Ni, Y. Robust Guar Gum/Cellulose Nanofibrils Multilayer Films with Good Barrier Properties. *ACS Appl. Mater. Interfaces* **2017**, *9* (6), 5477–5485.
- (50) Liu, A.; Walther, A.; Ikkala, O.; Belova, L.; Berglund, L. A. Clay Nanopaper with Tough Cellulose Nanofiber Matrix for Fire Retardancy and Gas Barrier Functions. *Biomacromolecules* **2011**, *12* (3), 633–641.
- (51) Heux, L.; Chauve, G.; Bonini, C. Nonflocculating and Chiral-Nematic Self-Ordering of Cellulose Microcrystals Suspensions in Nonpolar Solvents. *Langmuir* **2000**, *16* (21), 8210–8212.
- (52) Bonini, C.; Heux, L.; Cavail le, J.-Y.; Lindner, P.; Dewhurst, C.; Terech, P. Rodlike Cellulose Whiskers Coated with Surfactant: A Small-Angle Neutron Scattering Characterization. *Langmuir* **2002**, *18* (8), 3311–3314.
- (53) Kvien, I.; Tanem, B. S.; Oksman, K. Characterization of Cellulose Whiskers and Their Nanocomposites by Atomic Force and Electron Microscopy. *Biomacromolecules* **2005**, *6* (6), 3160–3165.
- (54) Elazzouzi-Hafraoui, S.; Putaux, J.-L.; Heux, L. Self-Assembling and Chiral Nematic Properties of Organophilic Cellulose Nanocrystals. *J. Phys. Chem. B* **2009**, *113* (32), 11069–11075.
- (55) Bondeson, D.; Oksman, K. Dispersion and Characteristics of Surfactant Modified Cellulose Whiskers Nanocomposites. *Compos. Interfaces* **2007**, *14*

- (7–9), 617–630.
- (56) Fortunati, E.; Armentano, I.; Zhou, Q.; Iannoni, A.; Saino, E.; Visai, L.; Berglund, L. A.; Kenny, J. M. Multifunctional Bionanocomposite Films of Poly (Lactic Acid), Cellulose Nanocrystals and Silver Nanoparticles. *Carbohydr. Polym.* **2012**, *87* (2), 1596–1605.
- (57) Ljungberg, N.; Cavallé, J.-Y.; Heux, L. Nanocomposites of Isotactic Polypropylene Reinforced with Rod-like Cellulose Whiskers. *Polymer* **2006**, *47* (18), 6285–6292.
- (58) Habibi, Y.; Hoeger, I.; Kelley, S. S.; Rojas, O. J. Development of Langmuir–Schaeffer Cellulose Nanocrystal Monolayers and Their Interfacial Behaviors. *Langmuir* **2010**, *26* (2), 990–1001.
- (59) Kim, H. J.; Shin, K. H.; Swanger, N. Burnout and Engagement: A Comparative Analysis Using the Big Five Personality Dimensions. *Int. J. Hosp. Manag.* **2009**, *28* (1), 96–104.
- (60) Petersson, L.; Kvien, I.; Oksman, K. Structure and Thermal Properties of Poly (Lactic Acid)/Cellulose Whiskers Nanocomposite Materials. *Compos. Sci. Technol.* **2007**, *67* (11–12), 2535–2544.
- (61) De Nooy, A. E. J.; Besemer, A. C.; Van Bekkum, H. Highly Selective TEMPO Mediated Oxidation of Primary Alcohol Groups in Polysaccharides. *Recl. Trav. Chim. Pays-Bas* **1994**, *113* (3), 165–166.
- (62) Lin, N.; Bruzzese, C.; Dufresne, A. TEMPO-Oxidized Nanocellulose Participating as Crosslinking Aid for Alginate-Based Sponges. *ACS Appl. Mater. Interfaces* **2012**, *4* (9), 4948–4959.
- (63) Araki, J.; Wada, M.; Kuga, S.; Okano, T. Birefringent Glassy Phase of a Cellulose Microcrystal Suspension. *Langmuir* **2000**, *16* (6), 2413–2415.
- (64) Montanari, S.; Roumani, M.; Heux, L.; Vignon, M. R. Topochemistry of Carboxylated Cellulose Nanocrystals Resulting from TEMPO-Mediated Oxidation. *Macromolecules* **2005**, *38* (5), 1665–1671.
- (65) Habibi, Y.; Chanzy, H.; Vignon, M. R. TEMPO-Mediated Surface Oxidation of Cellulose Whiskers. *Cellulose* **2006**, *13* (6), 679–687.
- (66) Besbes, I.; Alila, S.; Boufi, S. Nanofibrillated Cellulose from TEMPO-Oxidized Eucalyptus Fibres: Effect of the Carboxyl Content. *Carbohydr. Polym.* **2011**, *84* (3), 975–983.
- (67) Isogai, A.; Saito, T.; Fukuzumi, H. TEMPO-Oxidized Cellulose Nanofibers.

- nanoscale* **2011**, 3 (1), 71–85.
- (68) Lin, N.; Huang, J.; Chang, P. R.; Feng, J.; Yu, J. Surface Acetylation of Cellulose Nanocrystal and Its Reinforcing Function in Poly (Lactic Acid). *Carbohydr. Polym.* **2011**, 83 (4), 1834–1842.
- (69) Braun, B.; Dorgan, J. R. Single-Step Method for the Isolation and Surface Functionalization of Cellulosic Nanowhiskers. *Biomacromolecules* **2009**, 10 (2), 334–341.
- (70) Herrick, F. W.; Casebier, R. L.; Hamilton, J. K.; Sandberg, K. R. Microfibrillated Cellulose: Morphology and Accessibility. In *J. Appl. Polym. Sci.: Appl. Polym. Symp.; (United States)*; ITT Rayonier Inc., Shelton, WA, 1983; Vol. 37.
- (71) Huang, P.; Wu, M.; Kuga, S.; Wang, D.; Wu, D.; Huang, Y. One-step Dispersion of Cellulose Nanofibers by Mechanochemical Esterification in an Organic Solvent. *ChemSusChem* **2012**, 5 (12), 2319–2322.
- (72) Jonoobi, M.; Harun, J.; Mathew, A. P.; Hussein, M. Z. B.; Oksman, K. Preparation of Cellulose Nanofibers with Hydrophobic Surface Characteristics. *Cellulose* **2010**, 17 (2), 299–307.
- (73) Cetin, N. S.; Tingaut, P.; Özmen, N.; Henry, N.; Harper, D.; Dadmun, M.; Sebe, G. Acetylation of Cellulose Nanowhiskers with Vinyl Acetate under Moderate Conditions. *Macromol. Biosci.* **2009**, 9 (10), 997–1003.
- (74) Eyholzer, C.; Tingaut, P.; Zimmermann, T.; Oksman, K. Dispersion and Reinforcing Potential of Carboxymethylated Nanofibrillated Cellulose Powders Modified with 1-Hexanol in Extruded Poly (Lactic Acid)(PLA) Composites. *J. Polym. Environ.* **2012**, 20 (4), 1052–1062.
- (75) Yuan, H.; Nishiyama, Y.; Wada, M.; Kuga, S. Surface Acylation of Cellulose Whiskers by Drying Aqueous Emulsion. *Biomacromolecules* **2006**, 7 (3), 696–700.
- (76) De Menezes, A. J.; Siqueira, G.; Curvelo, A. A.; Dufresne, A. Extrusion and Characterization of Functionalized Cellulose Whiskers Reinforced Polyethylene Nanocomposites. *Polymer* **2009**, 50 (19), 4552–4563.
- (77) Berlioz, S.; Molina-Boisseau, S.; Nishiyama, Y.; Heux, L. Gas-Phase Surface Esterification of Cellulose Microfibrils and Whiskers. *Biomacromolecules* **2009**, 10 (8), 2144–2151.
- (78) Gousse, 77 C.; Chanzy, H.; Cerrada, M. L.; Fleury, E. Surface Silylation of

- Cellulose Microfibrils: Preparation and Rheological Properties. *Polymer* **2004**, *45* (5), 1569–1575.
- (79) Goussé, C.; Chanzy, H.; Excoffier, G.; Soubeyrand, L.; Fleury, E. Stable Suspensions of Partially Silylated Cellulose Whiskers Dispersed in Organic Solvents. *Polymer* **2002**, *43* (9), 2645–2651.
- (80) Andresen, M.; Johansson, L.-S.; Tanem, B. S.; Stenius, P. Properties and Characterization of Hydrophobized Microfibrillated Cellulose. *Cellulose* **2006**, *13* (6), 665–677.
- (81) Andresen, M.; Stenius, P. Water-in-oil Emulsions Stabilized by Hydrophobized Microfibrillated Cellulose. *J. Dispers. Sci. Technol.* **2007**, *28* (6), 837–844.
- (82) Aulin, C.; Netrval, J.; Wågberg, L.; Lindström, T. Aerogels from Nanofibrillated Cellulose with Tunable Oleophobicity. *Soft Matter* **2010**, *6* (14), 3298–3305.
- (83) Cervin, N. T.; Aulin, C.; Larsson, P. T.; Wågberg, L. Ultra Porous Nanocellulose Aerogels as Separation Medium for Mixtures of Oil/Water Liquids. *Cellulose* **2012**, *19* (2), 401–410.
- (84) Yang, Q.; Pan, X. A Facile Approach for Fabricating Fluorescent Cellulose. *J. Appl. Polym. Sci.* **2010**, *117* (6), 3639–3644.
- (85) Tingaut, P.; Hauert, R.; Zimmermann, T. Highly Efficient and Straightforward Functionalization of Cellulose Films with Thiol-Ene Click Chemistry. *J. Mater. Chem.* **2011**, *21* (40), 16066–16076.
- (86) Araki, J.; Wada, M.; Kuga, S. Steric Stabilization of a Cellulose Microcrystal Suspension by Poly (Ethylene Glycol) Grafting. *Langmuir* **2001**, *17* (1), 21–27.
- (87) Kloser, E.; Gray, D. G. Surface Grafting of Cellulose Nanocrystals with Poly (Ethylene Oxide) in Aqueous Media. *Langmuir* **2010**, *26* (16), 13450–13456.
- (88) Ljungberg, N.; Bonini, C.; Bortolussi, F.; Boisson, C.; Heux, L.; Cavaille, J.-Y. New Nanocomposite Materials Reinforced with Cellulose Whiskers in Atactic Polypropylene: Effect of Surface and Dispersion Characteristics. *Biomacromolecules* **2005**, *6* (5), 2732–2739.
- (89) Harrisson, S.; Drisko, G. L.; Malmstrom, E.; Hult, A.; Wooley, K. L. Hybrid Rigid/Soft and Biologic/Synthetic Materials: Polymers Grafted onto Cellulose Microcrystals. *Biomacromolecules* **2011**, *12* (4), 1214–1223.
- (90) Azzam, F.; Heux, L.; Putaux, J.-L.; Jean, B. Preparation by Grafting onto, Characterization, and Properties of Thermally Responsive Polymer-Decorated

- Cellulose Nanocrystals. *Biomacromolecules* **2010**, *11* (12), 3652–3659.
- (91) Habibi, Y.; Dufresne, A. Highly Filled Bionanocomposites from Functionalized Polysaccharide Nanocrystals. *Biomacromolecules* **2008**, *9* (7), 1974–1980.
- (92) Cao, X.; Habibi, Y.; Lucia, L. A. One-Pot Polymerization, Surface Grafting, and Processing of Waterborne Polyurethane-Cellulose Nanocrystal Nanocomposites. *J. Mater. Chem.* **2009**, *19* (38), 7137–7145.
- (93) Labet, M.; Thielemans, W.; Dufresne, A. Polymer Grafting onto Starch Nanocrystals. *Biomacromolecules* **2007**, *8* (9), 2916–2927.
- (94) Pei, A.; Malho, J.-M.; Ruokolainen, J.; Zhou, Q.; Berglund, L. A. Strong Nanocomposite Reinforcement Effects in Polyurethane Elastomer with Low Volume Fraction of Cellulose Nanocrystals. *Macromolecules* **2011**, *44* (11), 4422–4427.
- (95) Goffin, A.-L.; Raquez, J.-M.; Duquesne, E.; Siqueira, G.; Habibi, Y.; Dufresne, A.; Dubois, P. Poly (ϵ -Caprolactone) Based Nanocomposites Reinforced by Surface-Grafted Cellulose Nanowhiskers via Extrusion Processing: Morphology, Rheology, and Thermo-Mechanical Properties. *Polymer* **2011**, *52* (7), 1532–1538.
- (96) Chen, G.; Dufresne, A.; Huang, J.; Chang, P. R. A Novel Thermoformable Bionanocomposite Based on Cellulose Nanocrystal-graft-poly (E-caprolactone). *Macromol. Mater. Eng.* **2009**, *294* (1), 59–67.
- (97) Lin, N.; Chen, G.; Huang, J.; Dufresne, A.; Chang, P. R. Effects of Polymer-grafted Natural Nanocrystals on the Structure and Mechanical Properties of Poly (Lactic Acid): A Case of Cellulose Whisker-graft-polycaprolactone. *J. Appl. Polym. Sci.* **2009**, *113* (5), 3417–3425.
- (98) Labet, M.; Thielemans, W. Citric Acid as a Benign Alternative to Metal Catalysts for the Production of Cellulose-Grafted-Polycaprolactone Copolymers. *Polym. Chem.* **2012**, *3* (3), 679–684.
- (99) Carlsson, L.; Utsel, S.; Wågberg, L.; Malmström, E.; Carlmark, A. Surface-Initiated Ring-Opening Polymerization from Cellulose Model Surfaces Monitored by a Quartz Crystal Microbalance. *Soft Matter* **2012**, *8* (2), 512–517.
- (100) Goffin, A.-L.; Raquez, J.-M.; Duquesne, E.; Siqueira, G.; Habibi, Y.; Dufresne, A.; Dubois, P. From Interfacial Ring-Opening Polymerization to Melt Processing of Cellulose Nanowhisker-Filled Polylactide-Based Nanocomposites. *Biomacromolecules* **2011**, *12* (7), 2456–2465.

- (101) Braun, B.; Dorgan, J. R.; Hollingsworth, L. O. Supra-Molecular Ecobionanocomposites Based on Polylactide and Cellulosic Nanowhiskers: Synthesis and Properties. *Biomacromolecules* **2012**, *13* (7), 2013–2019.
- (102) Habibi, Y.; Aouadi, S.; Raquez, J.-M.; Dubois, P. Effects of Interfacial Stereocomplexation in Cellulose Nanocrystal-Filled Polylactide Nanocomposites. *Cellulose* **2013**, *20* (6), 2877–2885.
- (103) Goffin, A.-L.; Habibi, Y.; Raquez, J.-M.; Dubois, P. Polyester-Grafted Cellulose Nanowhiskers: A New Approach for Tuning the Microstructure of Immiscible Polyester Blends. *ACS Appl. Mater. Interfaces* **2012**, *4* (7), 3364–3371.
- (104) Lönnberg, H.; Fogelström, L.; Samir, M. A. S. A.; Berglund, L.; Malmström, E.; Hult, A. Surface Grafting of Microfibrillated Cellulose with Poly (ϵ -Caprolactone)–Synthesis and Characterization. *Eur. Polym. J.* **2008**, *44* (9), 2991–2997.
- (105) Lönnberg, H.; Larsson, K.; Lindstrom, T.; Hult, A.; Malmström, E. Synthesis of Polycaprolactone-Grafted Microfibrillated Cellulose for Use in Novel Bionanocomposites–Influence of the Graft Length on the Mechanical Properties. *ACS Appl. Mater. Interfaces* **2011**, *3* (5), 1426–1433.
- (106) Yi, J.; Xu, Q.; Zhang, X.; Zhang, H. Chiral-Nematic Self-Ordering of Rodlike Cellulose Nanocrystals Grafted with Poly (Styrene) in Both Thermotropic and Lyotropic States. *Polymer* **2008**, *49* (20), 4406–4412.
- (107) Yi, J.; Xu, Q.; Zhang, X.; Zhang, H. Temperature-Induced Chiral Nematic Phase Changes of Suspensions of Poly (N, N-Dimethylaminoethyl Methacrylate)-Grafted Cellulose Nanocrystals. *Cellulose* **2009**, *16* (6), 989–997.
- (108) Xu, Q.; Yi, J.; Zhang, X.; Zhang, H. A Novel Amphotropic Polymer Based on Cellulose Nanocrystals Grafted with Azo Polymers. *Eur. Polym. J.* **2008**, *44* (9), 2830–2837.
- (109) Morandi, G.; Heath, L.; Thielemans, W. Cellulose Nanocrystals Grafted with Polystyrene Chains through Surface-Initiated Atom Transfer Radical Polymerization (SI-ATRP). *Langmuir* **2009**, *25* (14), 8280–8286.
- (110) Majoinen, J.; Walther, A.; McKee, J. R.; Kontturi, E.; Aseyev, V.; Malho, J. M.; Ruokolainen, J.; Ikkala, O. Polyelectrolyte Brushes Grafted from Cellulose Nanocrystals Using Cu-Mediated Surface-Initiated Controlled Radical Polymerization. *Biomacromolecules* **2011**, *12* (8), 2997–3006.
- (111) Zoppe, J. O.; Habibi, Y.; Rojas, O. J.; Venditti, R. A.; Johansson, L.-S.;

- Efimenko, K.; Osterberg, M.; Laine, J. Poly (N-Isopropylacrylamide) Brushes Grafted from Cellulose Nanocrystals via Surface-Initiated Single-Electron Transfer Living Radical Polymerization. *Biomacromolecules* **2010**, *11* (10), 2683–2691.
- (112) Li, S.; Xiao, M.; Zheng, A.; Xiao, H. Cellulose Microfibrils Grafted with PBA via Surface-Initiated Atom Transfer Radical Polymerization for Biocomposite Reinforcement. *Biomacromolecules* **2011**, *12* (9), 3305–3312.
- (113) Xiao, M.; Li, S.; Chanklin, W.; Zheng, A.; Xiao, H. Surface-Initiated Atom Transfer Radical Polymerization of Butyl Acrylate on Cellulose Microfibrils. *Carbohydr. Polym.* **2011**, *83* (2), 512–519.
- (114) Sipahi-Sağlam, E.; Gelbrich, M.; Gruber, E. Topochemically Modified Cellulose. *Cellulose* **2003**, *10* (3), 237–250.
- (115) Arcot, L. R.; Lundahl, M.; Rojas, O. J.; Laine, J. Asymmetric Cellulose Nanocrystals: Thiolation of Reducing End Groups via NHS–EDC Coupling. *Cellulose* **2014**, *21* (6), 4209–4218.
- (116) Lokanathan, A. R.; Nykänen, A.; Seitsonen, J.; Johansson, L.-S.; Campbell, J.; Rojas, O. J.; Ikkala, O.; Laine, J. Cilia-Mimetic Hairy Surfaces Based on End-Immobilized Nanocellulose Colloidal Rods. *Biomacromolecules* **2013**, *14* (8), 2807–2813.
- (117) Colombo, L.; Zoia, L.; Violatto, M. B.; Previdi, S.; Talamini, L.; Sitia, L.; Nicotra, F.; Orlandi, M.; Salmona, M.; Recordati, C. Organ Distribution and Bone Tropism of Cellulose Nanocrystals in Living Mice. *Biomacromolecules* **2015**, *16* (9), 2862–2871.
- (118) Huang, J.-L.; Li, C.-J.; Gray, D. G. Cellulose Nanocrystals Incorporating Fluorescent Methylcoumarin Groups. *ACS Sustain. Chem. Eng.* **2013**, *1* (9), 1160–1164.
- (119) Lavoine, N.; Bergström, L. Nanocellulose-Based Foams and Aerogels: Processing, Properties, and Applications. *J. Mater. Chem. A* **2017**, *5* (31), 16105–16117.
- (120) Caliari, S. R.; Burdick, J. A. A Practical Guide to Hydrogels for Cell Culture. *Nat. Methods* **2016**, *13* (5), 405–414.
- (121) Place, E. S.; Evans, N. D.; Stevens, M. M. Complexity in Biomaterials for Tissue Engineering. *Nat. Mater.* **2009**, *8* (6), 457–470.
- (122) Discher, D. E.; Janmey, P.; Wang, Y. Tissue Cells Feel and Respond to the

- Stiffness of Their Substrate. *Science* **2005**, *310* (5751), 1139–1143.
- (123) Storm, C.; Pastore, J. J.; MacKintosh, F. C.; Lubensky, T. C.; Janmey, P. A. Nonlinear Elasticity in Biological Gels. *Nature* **2005**, *435* (7039), 191–194.
- (124) Jaspers, M.; Dennison, M.; Mabeoone, M. F.; MacKintosh, F. C.; Rowan, A. E.; Kouwer, P. H. Ultra-Responsive Soft Matter from Strain-Stiffening Hydrogels. *Nat. Commun.* **2014**, *5* (1), 1–8.
- (125) Jaspers, M.; Vaessen, S. L.; van Schayik, P.; Voerman, D.; Rowan, A. E.; Kouwer, P. H. Nonlinear Mechanics of Hybrid Polymer Networks That Mimic the Complex Mechanical Environment of Cells. *Nat. Commun.* **2017**, *8* (1), 1–10.
- (126) Zhao, J.; Lu, C.; He, X.; Zhang, X.; Zhang, W.; Zhang, X. Polyethylenimine-Grafted Cellulose Nanofibril Aerogels as Versatile Vehicles for Drug Delivery. *ACS Appl. Mater. Interfaces* **2015**, *7* (4), 2607–2615.
- (127) Cai, H.; Sharma, S.; Liu, W.; Mu, W.; Liu, W.; Zhang, X.; Deng, Y. Aerogel Microspheres from Natural Cellulose Nanofibrils and Their Application as Cell Culture Scaffold. *Biomacromolecules* **2014**, *15* (7), 2540–2547.
- (128) Zhou, S.; Wang, M.; Chen, X.; Xu, F. Facile Template Synthesis of Microfibrillated Cellulose/Polypyrrole/Silver Nanoparticles Hybrid Aerogels with Electrical Conductive and Pressure Responsive Properties. *Acs Sustain. Chem. Eng.* **2015**, *3* (12), 3346–3354.
- (129) Uddin, K. M.; Orelma, H.; Mohammadi, P.; Borghei, M.; Laine, J.; Linder, M.; Rojas, O. J. Retention of Lysozyme Activity by Physical Immobilization in Nanocellulose Aerogels and Antibacterial Effects. *Cellulose* **2017**, *24* (7), 2837–2848.
- (130) Xiong, R.; Lu, C.; Wang, Y.; Zhou, Z.; Zhang, X. Nanofibrillated Cellulose as the Support and Reductant for the Facile Synthesis of Fe₃O₄/Ag Nanocomposites with Catalytic and Antibacterial Activity. *J. Mater. Chem. A* **2013**, *1* (47), 14910–14918.
- (131) Poyraz, S.; Zhang, L.; Schroder, A.; Zhang, X. Ultrafast Microwave Welding/Reinforcing Approach at the Interface of Thermoplastic Materials. *ACS Appl. Mater. Interfaces* **2015**, *7* (40), 22469–22477.
- (132) Long, L.-Y.; Weng, Y.-X.; Wang, Y.-Z. Cellulose Aerogels: Synthesis, Applications, and Prospects. *Polymers* **2018**, *10* (6), 623.
- (133) Kobayashi, Y.; Saito, T.; Isogai, A. Aerogels with 3D Ordered Nanofiber

- Skeletons of Liquid-crystalline Nanocellulose Derivatives as Tough and Transparent Insulators. *Angew. Chem. Int. Ed.* **2014**, *53* (39), 10394–10397.
- (134) Chen, W.; Li, Q.; Wang, Y.; Yi, X.; Zeng, J.; Yu, H.; Liu, Y.; Li, J. Comparative Study of Aerogels Obtained from Differently Prepared Nanocellulose Fibers. *ChemSusChem* **2014**, *7* (1), 154–161.
- (135) Qi, J.; Xie, Y.; Liang, H.; Wang, Y.; Ge, T.; Song, Y.; Wang, M.; Li, Q.; Yu, H.; Fan, Z. Lightweight, Flexible, Thermally-Stable, and Thermally-Insulating Aerogels Derived from Cotton Nanofibrillated Cellulose. *ACS Sustain. Chem. Eng.* **2019**, *7* (10), 9202–9210.
- (136) Castro-Guerrero, C. F.; Gray, D. G. Chiral Nematic Phase Formation by Aqueous Suspensions of Cellulose Nanocrystals Prepared by Oxidation with Ammonium Persulfate. *Cellulose* **2014**, *21* (4), 2567–2577.
- (137) Lagerwall, J. P.; Schütz, C.; Salajkova, M.; Noh, J.; Park, J. H.; Scalia, G.; Bergström, L. Cellulose Nanocrystal-Based Materials: From Liquid Crystal Self-Assembly and Glass Formation to Multifunctional Thin Films. *NPG Asia Mater.* **2014**, *6* (1), e80–e80.
- (138) Dumanli, A. G.; Kamita, G.; Landman, J.; van der Kooij, H.; Glover, B. J.; Baumberg, J. J.; Steiner, U.; Vignolini, S. Controlled, Bio-inspired Self-assembly of Cellulose-based Chiral Reflectors. *Adv. Opt. Mater.* **2014**, *2* (7), 646–650.
- (139) Giese, M.; De Witt, J. C.; Shopsowitz, K. E.; Manning, A. P.; Dong, R. Y.; Michal, C. A.; Hamad, W. Y.; MacLachlan, M. J. Thermal Switching of the Reflection in Chiral Nematic Mesoporous Organosilica Films Infiltrated with Liquid Crystals. *ACS Appl. Mater. Interfaces* **2013**, *5* (15), 6854–6859.
- (140) Cheung, C. C.; Giese, M.; Kelly, J. A.; Hamad, W. Y.; MacLachlan, M. J. Iridescent Chiral Nematic Cellulose Nanocrystal/Polymer Composites Assembled in Organic Solvents. *ACS Macro Lett.* **2013**, *2* (11), 1016–1020.
- (141) Giese, M. ACS Macro Lett 2: 818 Khan MK. *Giese M Yu M Kelly JA Hamad WY MacLachlan MJ 2013 Angew Chem Int Ed* **2013**, *52*, 8921.
- (142) Giese, M.; Blusch, L. K.; Khan, M. K.; MacLachlan, M. J. Functional Materials from Cellulose-derived Liquid-crystal Templates. *Angew. Chem. Int. Ed.* **2015**, *54* (10), 2888–2910.
- (143) Vignolini, S.; Rudall, P. J.; Rowland, A. V.; Reed, A.; Moyroud, E.; Faden, R. B.; Baumberg, J. J.; Glover, B. J.; Steiner, U. Pointillist Structural Color in

- Pollia Fruit. *Proc. Natl. Acad. Sci.* **2012**, *109* (39), 15712–15715.
- (144) Wang, P.-X.; Hamad, W. Y.; MacLachlan, M. J. Polymer and Mesoporous Silica Microspheres with Chiral Nematic Order from Cellulose Nanocrystals. *Angew. Chem.* **2016**, *128* (40), 12648–12652.
- (145) Parker, R. M.; Frka-Petesic, B.; Guidetti, G.; Kamita, G.; Consani, G.; Abell, C.; Vignolini, S. Hierarchical Self-Assembly of Cellulose Nanocrystals in a Confined Geometry. *ACS Nano* **2016**, *10* (9), 8443–8449.
- (146) Li, Y.; Suen, J. J.-Y.; Prince, E.; Larin, E. M.; Klinkova, A.; Thérien-Aubin, H.; Zhu, S.; Yang, B.; Helmy, A. S.; Lavrentovich, O. D. Colloidal Cholesteric Liquid Crystal in Spherical Confinement. *Nat. Commun.* **2016**, *7* (1), 1–11.
- (147) Zhu, M.; Song, J.; Li, T.; Gong, A.; Wang, Y.; Dai, J.; Yao, Y.; Luo, W.; Henderson, D.; Hu, L. Highly Anisotropic, Highly Transparent Wood Composites. *Adv. Mater.* **2016**, *28* (26), 5181–5187.
- (148) Zhu, M.; Wang, Y.; Zhu, S.; Xu, L.; Jia, C.; Dai, J.; Song, J.; Yao, Y.; Wang, Y.; Li, Y. Anisotropic, Transparent Films with Aligned Cellulose Nanofibers. *Adv. Mater.* **2017**, *29* (21), 1606284.
- (149) Yao, K.; Huang, S.; Tang, H.; Xu, Y.; Buntkowsky, G.; Berglund, L. A.; Zhou, Q. Bioinspired Interface Engineering for Moisture Resistance in Nacre-Mimetic Cellulose Nanofibrils/Clay Nanocomposites. *ACS Appl. Mater. Interfaces* **2017**, *9* (23), 20169–20178.
- (150) Junka, K.; Guo, J.; Filpponen, I.; Laine, J.; Rojas, O. J. Modification of Cellulose Nanofibrils with Luminescent Carbon Dots. *Biomacromolecules* **2014**, *15* (3), 876–881.
- (151) Xu, X.; Ray, R.; Gu, Y.; Ploehn, H. J.; Gearheart, L.; Raker, K.; Scrivens, W. A. Electrophoretic Analysis and Purification of Fluorescent Single-Walled Carbon Nanotube Fragments. *J. Am. Chem. Soc.* **2004**, *126* (40), 12736–12737.
- (152) Guo, J.; Liu, D.; Filpponen, I.; Johansson, L.-S.; Malho, J.-M.; Quraishi, S.; Liebner, F.; Santos, H. A.; Rojas, O. J. Photoluminescent Hybrids of Cellulose Nanocrystals and Carbon Quantum Dots as Cytocompatible Probes for in Vitro Bioimaging. *Biomacromolecules* **2017**, *18* (7), 2045–2055.
- (153) O’Connell, D. W.; Birkinshaw, C.; O’Dwyer, T. F. Heavy Metal Adsorbents Prepared from the Modification of Cellulose: A Review. *Bioresour. Technol.* **2008**, *99* (15), 6709–6724.
- (154) Liu, P.; Sehaqui, H.; Tingaut, P.; Wichser, A.; Oksman, K.; Mathew, A. P.

- Cellulose and Chitin Nanomaterials for Capturing Silver Ions (Ag⁺) from Water via Surface Adsorption. *Cellulose* **2014**, *21* (1), 449–461.
- (155) Kardam, A.; Raj, K. R.; Srivastava, S.; Srivastava, M. M. Nanocellulose Fibers for Biosorption of Cadmium, Nickel, and Lead Ions from Aqueous Solution. *Clean Technol. Environ. Policy* **2014**, *16* (2), 385–393.
- (156) Yu, X.; Tong, S.; Ge, M.; Wu, L.; Zuo, J.; Cao, C.; Song, W. Adsorption of Heavy Metal Ions from Aqueous Solution by Carboxylated Cellulose Nanocrystals. *J. Environ. Sci.* **2013**, *25* (5), 933–943.
- (157) Hokkanen, S.; Repo, E.; Sillanpää, M. Removal of Heavy Metals from Aqueous Solutions by Succinic Anhydride Modified Mercerized Nanocellulose. *Chem. Eng. J.* **2013**, *223*, 40–47.
- (158) Sehaqui, H.; de Larraya, U. P.; Liu, P.; Pfenninger, N.; Mathew, A. P.; Zimmermann, T.; Tingaut, P. Enhancing Adsorption of Heavy Metal Ions onto Biobased Nanofibers from Waste Pulp Residues for Application in Wastewater Treatment. *Cellulose* **2014**, *21* (4), 2831–2844.
- (159) Ma, H.; Hsiao, B. S.; Chu, B. Ultrafine Cellulose Nanofibers as Efficient Adsorbents for Removal of UO₂²⁺ in Water. *ACS Macro Lett.* **2012**, *1* (1), 213–216.
- (160) Kardam, A.; ROHIT, R. K.; Srivastava, S. Novel Nano Cellulosic Fibers for Remediation of Heavy Metals from Synthetic Water. **2012**.
- (161) Srivastava, S.; Kardam, A.; Raj, K. R. Nanotech Reinforcement onto Cellulosic Fibers: Green Remediation of Toxic Metals. *Int. J. Green Nanotechnol.* **2012**, *4* (1), 46–53.
- (162) Hokkanen, S.; Repo, E.; Suopajarvi, T.; Liimatainen, H.; Niinimaa, J.; Sillanpää, M. Adsorption of Ni (II), Cu (II) and Cd (II) from Aqueous Solutions by Amino Modified Nanostructured Microfibrillated Cellulose. *Cellulose* **2014**, *21* (3), 1471–1487.
- (163) Hokkanen, S.; Repo, E.; Westholm, L. J.; Lou, S.; Sainio, T.; Sillanpää, M. Adsorption of Ni²⁺, Cd²⁺, PO₄³⁻ and NO₃⁻ from Aqueous Solutions by Nanostructured Microfibrillated Cellulose Modified with Carbonated Hydroxyapatite. *Chem. Eng. J.* **2014**, *252*, 64–74.
- (164) Kanel, S. R.; Manning, B.; Charlet, L.; Choi, H. Removal of Arsenic (III) from Groundwater by Nanoscale Zero-Valent Iron. *Environ. Sci. Technol.* **2005**, *39* (5), 1291–1298.

- (165) Zhang, N.; Zang, G.-L.; Shi, C.; Yu, H.-Q.; Sheng, G.-P. A Novel Adsorbent TEMPO-Mediated Oxidized Cellulose Nanofibrils Modified with PEI: Preparation, Characterization, and Application for Cu (II) Removal. *J. Hazard. Mater.* **2016**, *316*, 11–18.
- (166) Liu, P.; Borrell, P. F.; Božič, M.; Kokol, V.; Oksman, K.; Mathew, A. P. Nanocelluloses and Their Phosphorylated Derivatives for Selective Adsorption of Ag⁺, Cu²⁺ and Fe³⁺ from Industrial Effluents. *J. Hazard. Mater.* **2015**, *294*, 177–185.
- (167) Sirviö, J. A.; Hasa, T.; Leiviskä, T.; Liimatainen, H.; Hormi, O. Bisphosphonate Nanocellulose in the Removal of Vanadium (V) from Water. *Cellulose* **2016**, *23* (1), 689–697.
- (168) Sheikhi, A.; Safari, S.; Yang, H.; Van De Ven, T. G. Copper Removal Using Electrosterically Stabilized Nanocrystalline Cellulose. *ACS Appl. Mater. Interfaces* **2015**, *7* (21), 11301–11308.
- (169) Mohammed, N.; Baidya, A.; Murugesan, V.; Kumar, A. A.; Ganayee, M. A.; Mohanty, J. S.; Tam, K. C.; Pradeep, T. Diffusion-Controlled Simultaneous Sensing and Scavenging of Heavy Metal Ions in Water Using Atomically Precise Cluster–Cellulose Nanocrystal Composites. *ACS Sustain. Chem. Eng.* **2016**, *4* (11), 6167–6176.
- (170) Anirudhan, T. S.; Deepa, J. R.; Christa, J. Nanocellulose/Nanobentonite Composite Anchored with Multi-Carboxyl Functional Groups as an Adsorbent for the Effective Removal of Cobalt (II) from Nuclear Industry Wastewater Samples. *J. Colloid Interface Sci.* **2016**, *467*, 307–320.
- (171) Anirudhan, T. S.; Shainy, F. Effective Removal of Mercury (II) Ions from Chlor-Alkali Industrial Wastewater Using 2-Mercaptobenzamide Modified Itaconic Acid-Grafted-Magnetite Nanocellulose Composite. *J. Colloid Interface Sci.* **2015**, *456*, 22–31.
- (172) Hokkanen, S.; Repo, E.; Lou, S.; Sillanpää, M. Removal of Arsenic (V) by Magnetic Nanoparticle Activated Microfibrillated Cellulose. *Chem. Eng. J.* **2015**, *260*, 886–894.
- (173) Zheng, Q.; Cai, Z.; Gong, S. Green Synthesis of Polyvinyl Alcohol (PVA)–Cellulose Nanofibril (CNF) Hybrid Aerogels and Their Use as Superabsorbents. *J. Mater. Chem. A* **2014**, *2* (9), 3110–3118.
- (174) Zhou, Y.; Fu, S.; Zhang, L.; Zhan, H.; Levit, M. V. Use of Carboxylated

- Cellulose Nanofibrils-Filled Magnetic Chitosan Hydrogel Beads as Adsorbents for Pb (II). *Carbohydr. Polym.* **2014**, *101*, 75–82.
- (175) Ma, H.; Wang, S.; Meng, F.; Xu, X.; Huo, X. A Hydrazone-Carboxyl Ligand-Linked Cellulose Nanocrystal Aerogel with High Elasticity and Fast Oil/Water Separation. *Cellulose* **2017**, *24* (2), 797–809.
- (176) Yang, X.; Cranston, E. D. Chemically Cross-Linked Cellulose Nanocrystal Aerogels with Shape Recovery and Superabsorbent Properties. *Chem. Mater.* **2014**, *26* (20), 6016–6025.
- (177) Jiang, F.; Hsieh, Y.-L. Amphiphilic Superabsorbent Cellulose Nanofibril Aerogels. *J. Mater. Chem. A* **2014**, *2* (18), 6337–6342.
- (178) Abraham, E.; Weber, D. E.; Sharon, S.; Lapidot, S.; Shoseyov, O. Multifunctional Cellulosic Scaffolds from Modified Cellulose Nanocrystals. *ACS Appl. Mater. Interfaces* **2017**, *9* (3), 2010–2015.
- (179) Zhu, G.; Xu, H.; Dufresne, A.; Lin, N. High-Adsorption, Self-Extinguishing, Thermal, and Acoustic-Resistance Aerogels Based on Organic and Inorganic Waste Valorization from Cellulose Nanocrystals and Red Mud. *ACS Sustain. Chem. Eng.* **2018**, *6* (5), 7168–7180.
- (180) Zhang, Z.; Sèbe, G.; Rentsch, D.; Zimmermann, T.; Tingaut, P. Ultralightweight and Flexible Silylated Nanocellulose Sponges for the Selective Removal of Oil from Water. *Chem. Mater.* **2014**, *26* (8), 2659–2668.
- (181) Korhonen, J. T.; Kettunen, M.; Ras, R. H.; Ikkala, O. Hydrophobic Nanocellulose Aerogels as Floating, Sustainable, Reusable, and Recyclable Oil Absorbents. *ACS Appl. Mater. Interfaces* **2011**, *3* (6), 1813–1816.
- (182) Pääkkö, M.; Vapaavuori, J.; Silvennoinen, R.; Kosonen, H.; Ankerfors, M.; Lindström, T.; Berglund, L. A.; Ikkala, O. Long and Entangled Native Cellulose I Nanofibers Allow Flexible Aerogels and Hierarchically Porous Templates for Functionalities. *Soft Matter* **2008**, *4* (12), 2492–2499.
- (183) Leppänen, A.-S.; Xu, C.; Liu, J.; Wang, X.; Pesonen, M.; Willför, S. Anionic Polysaccharides as Templates for the Synthesis of Conducting Polyaniline and as Structural Matrix for Conducting Biocomposites. *Macromol. Rapid Commun.* **2013**, *34* (13), 1056–1061.
- (184) Luong, N. D.; Korhonen, J. T.; Soininen, A. J.; Ruokolainen, J.; Johansson, L.-S.; Seppälä, J. Processable Polyaniline Suspensions through in Situ Polymerization onto Nanocellulose. *Eur. Polym. J.* **2013**, *49* (2), 335–344.

- (185) Abbasi, H.; Antunes, M.; Velasco, J. I. Recent Advances in Carbon-Based Polymer Nanocomposites for Electromagnetic Interference Shielding. *Prog. Mater. Sci.* **2019**, *103*, 319–373.
- (186) Zeng, Z.; Wu, T.; Han, D.; Ren, Q.; Siqueira, G.; Nyström, G. Ultralight, Flexible, and Biomimetic Nanocellulose/Silver Nanowire Aerogels for Electromagnetic Interference Shielding. *ACS Nano* **2020**, *14* (3), 2927–2938.
- (187) Zeng, Z.; Wang, C.; Siqueira, G.; Han, D.; Huch, A.; Abdolhosseinzadeh, S.; Heier, J.; Nüesch, F.; Zhang, C.; Nyström, G. Nanocellulose-MXene Biomimetic Aerogels with Orientation-Tunable Electromagnetic Interference Shielding Performance. *Adv. Sci.* **2020**, *7* (15), 2000979.
- (188) Farooq, M.; Sipponen, M. H.; Seppälä, A.; Österberg, M. Eco-Friendly Flame-Retardant Cellulose Nanofibril Aerogels by Incorporating Sodium Bicarbonate. *ACS Appl. Mater. Interfaces* **2018**, *10* (32), 27407–27415.
- (189) Wang, D.; Peng, H.; Yu, B.; Zhou, K.; Pan, H.; Zhang, L.; Li, M.; Liu, M.; Tian, A.; Fu, S. Biomimetic Structural Cellulose Nanofiber Aerogels with Exceptional Mechanical, Flame-Retardant and Thermal-Insulating Properties. *Chem. Eng. J.* **2020**, *389*, 124449.
- (190) Fei, Y.; Liang, M.; Yan, L.; Chen, Y.; Zou, H. Co/C@ Cellulose Nanofiber Aerogel Derived from Metal-Organic Frameworks for Highly Efficient Electromagnetic Interference Shielding. *Chem. Eng. J.* **2020**, *392*, 124815.

CHAPTER 2.

**“Reinforcement of natural rubber by end-modified cellulose
nanofibrils and a thiol-ene click reaction”**

Table of contents – Chapter 2

Chapter 2. Synergistic reinforcing and cross-linking effect of thiol-ene-modified cellulose nanofibrils on natural rubber	93
Abstract.....	93
Keywords	93
2.1 Introduction.....	94
2.2 Experimental sections	96
2.2.1 Materials	96
2.2.2 CNF end modification via aldimine condensation.....	96
2.2.3 CNF end modification via carboxyamine condensation.....	97
2.2.4 Preparation of NR/CNF-x and NR/CNF-SH-x nanocomposites	97
2.2.5 Characterization	98
2.3 Results and discussion	100
2.3.1 Analysis of reducing end modification of CNF	100
2.3.2 Click reaction between CNF-SH-a and NR.....	104
2.3.3 Morphology of the nanocomposites.....	107
2.3.4 Mechanical properties of the nanocomposites.....	108
2.3.5 Successive tensile tests	110
2.3.6 Dynamic mechanical analysis.....	113
2.4 Conclusions.....	116
2.5 References.....	117

Chapter 2. Synergistic reinforcing and cross-linking effect of thiol-ene-modified cellulose nanofibrils on natural rubber

Ge Zhu, Alain Dufresne*

Univ. Grenoble Alpes, CNRS, Grenoble INP, LGP2, F-38000, Grenoble, France

* Corresponding author: Alain Dufresne (alain.dufresne@pagora.grenoble-inp.fr)

Abstract

In order to achieve a synergistic reinforcing and cross-linking effect across the interface between hydrophilic nanocellulose and a hydrophobic rubber matrix, active thiol groups (-SH) were introduced at the reducing end of CNF while retaining the hydroxyl (-OH) on the surface, thus forming a stable percolation network in the nanocomposites. The nanocomposites were obtained by casting/evaporation a mixture of dispersed modified CNF and NR in latex form, in which covalent cross-links were formed between the thiol groups and double bonds of the NR matrix via photochemically initiated thiol-ene reaction. The strong interfacial interaction between the NR matrix and the end-modified CNF was characterized by Fourier-transform infrared (FTIR) spectroscopy. The structural and mechanical properties of the nanocomposites were evaluated by scanning electron microscopy (SEM), dynamic mechanical analysis (DMA) and mechanical tensile tests. Compared to neat NR, the nanocomposite reinforced with 10 wt% modified CNF showed significantly higher values of tensile strength (from 0.33 MPa to 5.83 MPa), Young's modulus (from 0.48 MPa to 45.25 MPa) and toughness (from 2.63 MJ m⁻³ to 22.24 MJ m⁻³). This highly efficient method is environmentally friendly and uses renewable materials. It can also be used for reinforcing other rubbers.

Keywords

Cellulose nanofibril, End modification, Thiol-ene reaction, Interfacial interaction, Mechanical properties

2.1 Introduction

Polymer nanocomposites consisting of a nanoscale reinforcing filler and polymer matrix have attracted researchers' great interest in the last few decades.¹⁻⁶ The nanofiller helps to achieve better properties at lower volume fractions due to their large specific surface area compared to micrometer size particles. By using nanofillers (such as silica, carbon nanotubes, clay and graphene),⁷⁻⁹ stronger reinforcement effects have been achieved in natural rubber (NR) composites. Among the potential nanofillers, nanocellulose, consisting of nanosized cellulose-based particles, is an elongated nanomaterial with high aspect ratio and high crystallinity. It has been widely studied due to its excellent mechanical properties, biocompatibility, renewability, sustainability and abundance.

NR is one of the most important elastic materials in daily applications due to its excellent strength, resilience, flexibility and elasticity.¹⁰⁻¹⁵ However, unfilled NR exhibits poor mechanical properties in terms of stiffness, so the incorporation of a nanofiller into NR matrix is often required.¹⁶⁻¹⁸ Smyth¹⁶ and Pasquini¹⁷ et al. studied the reinforcing effect of cellulose nanocrystals (CNCs) on natural rubber and found that the performance of the obtained nanocomposites mainly depended on the properties of CNC, since the higher the aspect ratio, the better the reinforcing effect. Meanwhile, it was found that the formation of a rigid percolation network over a certain filler content greatly enhanced the reinforcement of the NR matrix.^{19,20}

However, the increase in the mechanical properties of the nanocomposites by adding nanocellulose was still not very obvious and far from expectation due to inadequate interfacial interaction between nanocellulose and NR matrix. The nanocellulose surface contains a large number of hydroxyl groups, so the interfacial compatibility between hydrophilic nanocellulose and hydrophobic rubber matrix is poor and leads to aggregation of nanocellulose in the NR matrix. This insufficient interfacial adhesion between both components does not effectively transfer the stress from the continuous

phase to the filler under mechanical loading. In order to improve the compatibility and enhance the interfacial adhesion between nanocellulose and the NR matrix, Kanoth et al. introduced sulfhydryl groups (-SH) on the surface of CNC and achieved reinforcement and cross-linking between the NR matrix and modified CNC by thiol-ene reaction.²¹ Goetz et al.^{22,23} used poly(methyl vinyl ether-co-maleic acid)-polyethylene glycol as a matrix and nanocellulose as a cross-linking agent to prepare cross-linked nanocomposites via the esterification reaction. The nanocellulose is trapped in the cross-linking network which prevents its aggregation, and the nanocomposite shows excellent mechanical properties. Therefore, the dispersion of the nanofiller within the host polymer matrix and the interfacial interactions between the nanofiller and the matrix are key properties for improving the properties of the nanocomposite. However, these strategies consume surface hydroxyl groups which are the basis of the exceptional reinforcing effect of these nanoparticles via the establishment of a nanofiller percolating network.

Here, we chose high aspect ratio cellulose nanofibrils (CNFs) as reinforcing nanofiller but also as cross-linking agent after end modification. In order to achieve the synergistic effect of strengthening and cross-linking across the interface, active thiol groups (-SH) were introduced at the reducing end of CNF, while retaining the hydroxyl (-OH) groups on the surface, giving CNFs the possibility to interact with each other and thus forming a stable percolating network in the nanocomposites. The nanocomposites were obtained by casting/evaporation a mixture of dispersed modified CNF and NR in latex form, in which covalent cross-links were formed between the thiol groups and double bonds of the NR matrix via photochemically initiated thiol-ene reaction. With this design, it was possible to achieve both the formation of a percolation network and strong interfacial interactions between the nanofiller and the NR matrix, which should improve the strength and modulus while retaining the high ductility of the nanocomposites. The strong interfacial interaction between the NR matrix and the end-modified CNF was characterized by Fourier-transform infrared (FTIR) spectroscopy. The structural and

mechanical properties of the nanocomposites were evaluated by scanning electron microscopy (SEM), dynamic mechanical analysis (DMA) and mechanical tensile tests.

2.2 Experimental sections

2.2.1 Materials

The natural rubber (NR) latex with 60 wt% solid content was supplied by Centrotrade Deutschland GmbH (Eschborn, Germany). Cellulose nanofibril (CNF) aqueous suspension (CNF, 3 wt%) was obtained from CTP (Centre Technique du Papier, Grenoble). It was isolated from strongly refined bleached birch pulp using an enzymatic pretreatment and a final homogenization step. 6-Amino-1-hexanethiol hydrochloride (AHH), 2-hydroxy-4-(2-hydroxyethoxy)-2-methylpropiophenone (Irgacure 2959), 1-[3-(dimethylamino)propyl]-3-ethylcarbodiimide methiodide (EDC), N-hydroxysuccinimide (NHS), sodium triacetoxyborohydride (Ac), and sodium chlorite (NaClO_2) were purchased from Sigma Aldrich. Potassium chloride (KCl), sodium carbonate anhydrous (Na_2CO_3), acetic acid, hydrochloric acid (HCl), silver nitrate (AgNO_3), sodium borohydride (NaNH_4), and sulfuric acid (H_2SO_4 , 98%) were purchased from Roth and used as received.

2.2.2 CNF end modification via aldimine condensation

The pH of CNF aqueous dispersions (10 mg/mL) was regulated to 9.2 with Na_2CO_3 buffer solution in oil bath at 70°C. $\text{NH}_2(\text{CH}_2)_6\text{SH}\cdot\text{HCl}$ (0.3 mmol) and reducing agent Ac (45 mmol) were dissolved in distilled water and added into the CNF suspension by magnetic stirring under the protection of nitrogen for 3 days. After reaction, the dispersion was cooled to room temperature. Then 20 mL of 3 M HCl solution was added to neutralize the excess reducing agent (Ac), and the neutralized suspension was dialyzed against distilled water for 5 days. Then the KCl solution was added under magnetic stirring for 24h. After incubation treatment, the CNF-SH-a suspension was obtained by dialysis against distilled water to remove electrolytes.

2.2.3 CNF end modification via carboxyamine condensation

The end aldehyde groups of CNF were first converted into carboxyl groups ($-\text{COOH}$).²⁴ NaClO_2 solution (250 mM) was added to the CNF aqueous suspension (10 mg mL^{-1}) at room temperature for 20 h, the pH of the aqueous suspension was regulated to 3.5 by acetic acid, and it was followed by dialysis against distilled water to remove excess reactants. The resulting CNF-COOH suspension with carboxyl ends was used for further modification. The pH of the CNF-COOH suspension (5 mg/mL) was adjusted to 7.0, then NHS (0.3 mmol) and EDC (3 mmol) were added under the protection of nitrogen. Following, the pH of the suspension was adjusted to 6.5, and desired amounts of KCl (1 M) solution were added to increase the ionic strength. Then the carboxyamine reaction started with the addition of $\text{NH}_2(\text{CH}_2)_6\text{SH}\cdot\text{HCl}$ (3 mmol) under a pH of 9.2 (regulation by 0.1 M Na_2CO_3 buffer) at room temperature. After the 2 h incubation, the resulting CNF with end-thiol (CNF-SH-b) was obtained by dialysis against distilled water to remove the unreacted reagents.

2.2.4 Preparation of NR/CNF-x and NR/CNF-SH-x nanocomposites

The nanocomposites were prepared by mixing the two aqueous dispersions and casting/evaporation. The desired amount of pristine CNF or end-modified CNF-SH and NR latex was first mixed uniformly. Then the photoinitiator (Irgacure 2959, 2 wt%) was added into the mixture suspension under magnetic stirring for 3 h. Next, the uniform mixture suspension was exposed to UV irradiation (365 nm) to initiate the click reaction between NR matrix and CNF-SH under controlled intensity and distance for 30 min. Finally, the mixture suspension was poured into PTFE molds (diameter = 100 cm) at 45°C overnight to get the nanocomposites by water evaporation. Two kinds of composites were prepared and codified as NR/CNF-x and NR/CNF-SH-x with various CNF or CNF-SH contents ($x = 0, 2, 5, 8, 10, 15 \text{ wt} \%$). The CNF and CNF-SH contents were based on the total solid content.

2.2.5 Characterization

Elemental analysis (EA) was performed to trace the content of nitrogen (N %) and sulfur (S %) elements after modification with elemental analyzer (Elemental Analysis system, GmbH). X-ray photoelectron spectroscopy (XPS) experiments were carried out on a Thermo Fisher spectrometer.

The Zeta potential of CNF and CNF-SH suspensions was measured with Zetasizer Nano instrument (Malvern). Fourier-transform infrared spectroscopy (FTIR) measurements were performed on a Perkin Elmer Spectrum 65 spectrometer in the range 4000-600 cm^{-1} . Solid-state NMR analysis was performed on a Bruker AVANCE 400 NMR spectrometer with a 4 mm CP-MAS probe at 12 000 Hz spinning speed and 6 s relaxation delays. Thermogravimetric analysis (TGA) curves were recorded from 25°C to 600°C (10°C/min) under nitrogen atmosphere. X-ray diffraction (XRD) (Bruker, Germany) was performed by Cu $K\alpha$ radiation at 40 KV. The diffraction angle (2θ) was varied from 5 to 45° with a rate of 0.02°/s. The Segal method was used to calculate the crystallinity index from XRD data.²⁵

The CNF suspension was negatively stained with a 2 wt% uranyl acetate solution, and samples were observed with a transmission electron microscope (JEOL JEM 2100-Plus) at 200 kV. For the CNF-SH suspension, a silver-staining technique was used to identify the reducing end modification by in situ growth method. The silver nitrate solution (1 mL, 1 mM) was added to the CNF-SH suspension (10 mL, 1 mg mL^{-1}) under magnetic stirring for 30 min. Then sodium borohydride solution (10 mL, 5 mM) was added under magnetic stirring for 24h. The resulting suspension was prepared for TEM.

The cross-linking density was determined as follows. Five weighed samples (m_0) were each immersed in an airtight container of toluene at room temperature. The swollen samples were then periodically taken out and immediately weighed on an analytical balance (m_1) after wiping up with filter paper until a constant weight was obtained. The cross-linking density (ν) was calculated by the Flory-Rehner equation.^{26,27}

$$v = -\frac{\ln(1-V_{nr})+V_{nr}+xV_{nr}^2}{V_t(V_{nr}^{1/3}-\frac{V_{nr}}{2})} \quad (1)$$

$$V_{nr} = \frac{\frac{m_{nr}}{\rho_{nr}}}{\frac{m_t}{\rho_t} + \frac{m_{nr}}{\rho_{nr}}} \quad (2)$$

where x and V_t are the interaction parameter and molar volume of toluene ($x = 0.39$, $V_t = 106.2 \text{ cm}^3/\text{mol}$), respectively. m_{nr} and ρ_{nr} are the weight and density of natural rubber ($\rho_{nr} = 0.93 \text{ g/cm}^3$), respectively. m_t and ρ_t are the weight and density of toluene ($\rho_s = 0.865 \text{ g/cm}^3$), respectively.

The network structure constructed with CNF in the NR nanocomposites was identified by scanning electron microscopy (SEM) (Quanta 200 FEI). The NR/CNF nanocomposites were put in liquid nitrogen for a few minutes and fractured.

The mechanical properties of NR/CNF and NR/CNF-SH nanocomposites were measured in tensile mode (Instron 5567, USA) with a 100 N load cell. The measurements were performed at a strain rate of 100 mm/min. The sample dimensions were $18 \times 6 \times 0.6 \text{ mm}^3$, and the results were averaged on five measurements. The toughness of the nanocomposites was calculated from the area under the stress-strain curve before rupture.

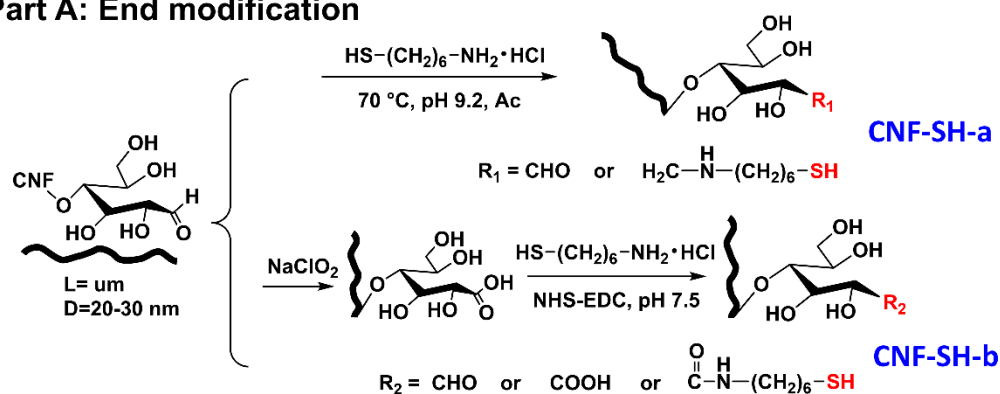
Successive tensile tests were carried out to investigate the energy dissipation of nanocomposites using Instron 5567. At the beginning of each experiment, the sample was first stretched under a load of 0.5 N. Then, the experiment consisted in stretching the sample up to a given elongation $\Delta L_1 = 10 \text{ mm}$ (cycle 1), then releasing the force down to 0.5 N, and stretching again up to $\Delta L_2 = 2\Delta L_1$ (cycle 2). This procedure was repeated with increasing elongation $\Delta L_i = i\Delta L_1$ until the rupture of the sample. The tensile modulus E_i and the shrinkage r_i were determined for each successive cycle.

Dynamic mechanical analysis (DMA, TA, USA) was carried out from -100 to $100 \text{ }^\circ\text{C}$ at $5 \text{ }^\circ\text{C min}^{-1}$ in tensile mode. The strain amplitude and frequency were 0.05% and 1 Hz, respectively.

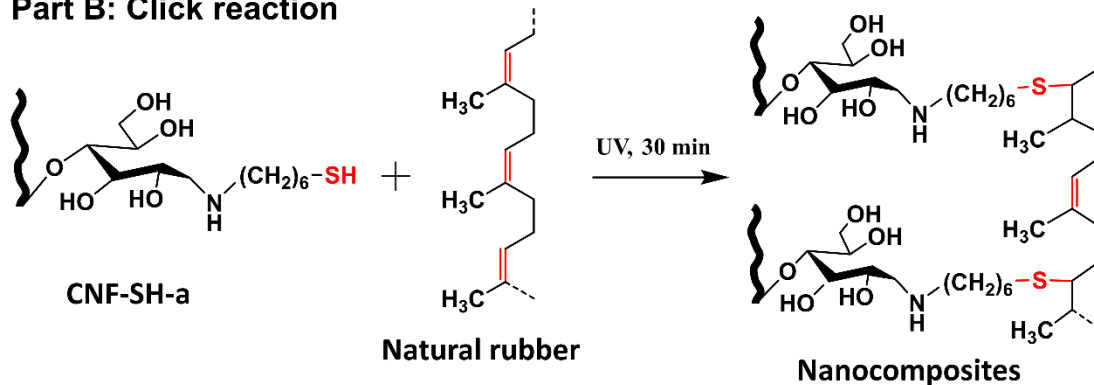
2.3 Results and discussion

The main objectives of this work were the preparation of reducing end modified CNF and the development of nanocomposites by reactive compounding between reducing end modified CNF and NR matrix. As shown in Scheme 1, the aim of the reducing end modification was to introduce active thiol groups ($-SH$) at the reducing ends of CNF, while being able to retain the surface hydroxyl groups ($-OH$). Subsequently, covalently cross-linked nanocomposites were prepared by click reaction between the $-SH$ groups on the end modified CNF-SH and unsaturated bonds ($-C=C-$) of the NR matrix via UV radiation.

Part A: End modification



Part B: Click reaction



Scheme 1 Reducing end modification of CNF and preparation of nanocomposites.

2.3.1 Analysis of reducing end modification of CNF

In this study, two strategies were designed to achieve end modification of CNF, including aldimine condensation (CNF-SH-a) and carboxyamine condensation (CNF-SH-b), as shown in Scheme 1 (Part A). For the chemical reaction mechanism of CNF-

SH-a, the active end aldehyde groups were easily nucleophilically attacked by the primary amino group, inducing aldimine condensation. This reaction initially formed a covalent linkage through the generation of an unstable $-C=N-$ group, which was then reduced by Ac to form a stable $-C-N-$ group, resulting in the CNF-SH-a terminal modification. Regarding the chemical reaction mechanism for CNF-SH-b, the CNF end aldehyde group was oxidized to carboxyl group by NaClO_2 solution, and then combined with EDC catalyst to form O-acylisourea active intermediate, which was converted into active NHS-CNF-ester product under NHS catalysis. Finally, the nucleophilic attack by the primary amino group and the cleavage of NHS-CNF-ester occurred to obtain end modified CNF-SH-b.

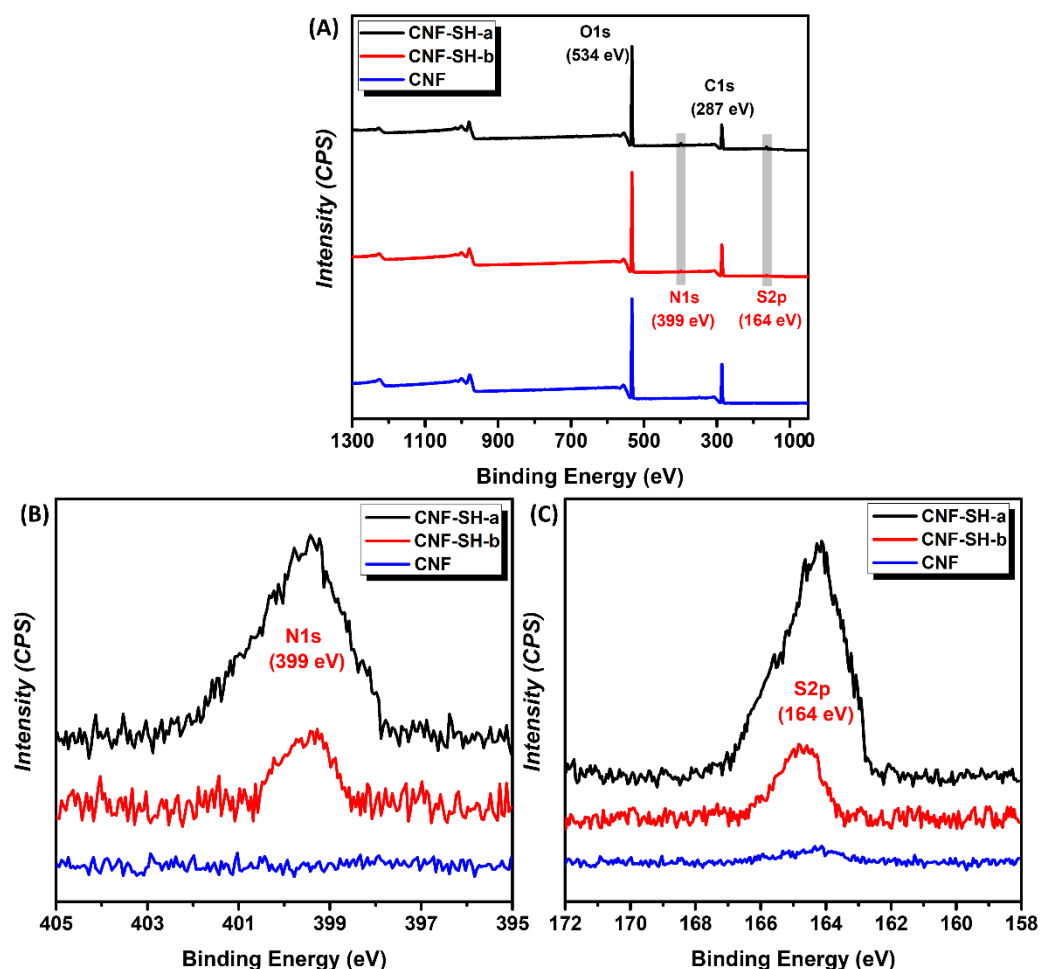


Figure 2.1 XPS spectra for CNF, CNF-SH-a and CNF-SH-b (A), N1s (B) and S2p (C) spectra.

Table 2.1 Elemental analysis results (C/H/N/S) for pristine CNF and end-modified CNF.

Samples	C (wt%)	H (wt%)	N (wt%)	S (wt%)
CNF	43.34 ± 0.39	6.45 ± 0.33	0.00 ± 0.02	0.00 ± 0.05
CNF-SH-a	41.56 ± 0.47	6.19 ± 0.41	0.14 ± 0.07	0.16 ± 0.04
CNF-SH-b	42.98 ± 0.23	6.38 ± 0.25	0.04 ± 0.02	0.05 ± 0.03

Compared to surface modifications, the end modification of CNF has relatively few active sites. XPS and elemental analysis were used to track the changes in sulfur and nitrogen elements. As shown in Figure 2.1A, the typical characteristic signals of O1s (534 eV) and C1s (287 eV) can be observed in the XPS spectrum for CNF before and after end modification. At the same time, characteristic peaks of N1s (399 eV) and S2p (164 eV) were observed in the end-modified CNF-SH spectrum, which is consistent with the results of elemental analysis (Table 2.1), which proved that the thiol group (-SH) was successfully grafted to the reducing end of CNF. It is worth noting that elemental analysis results show that the nitrogen and sulfur content in CNF-SH-a was higher than that of CNF-SH-b; the peak intensity for N1s and S2p for CNF-SH-a in the XPS characteristic element spectrum was also stronger than that of CNF-SH-b (Figure 2.1B, C), indicating that CNF-SH-a has a higher grafting efficiency than CNF-SH-b.

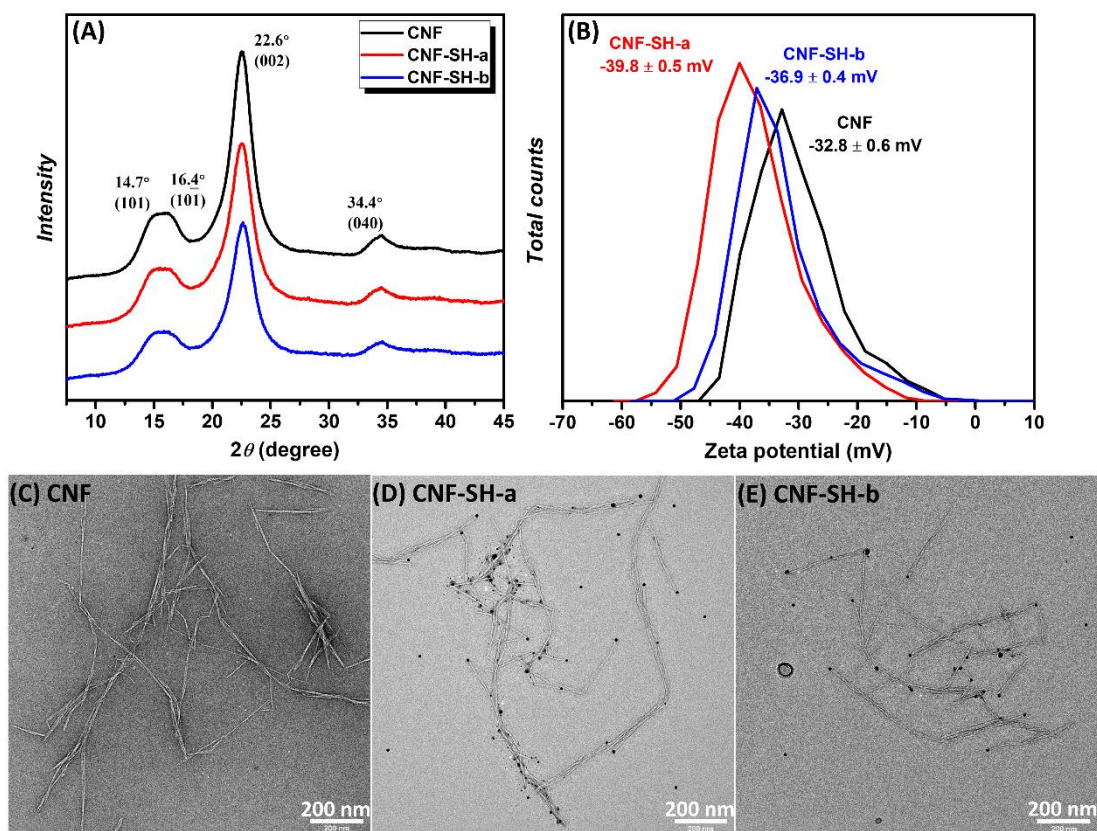


Figure 2.2 (A) XRD spectrum and (B) Zeta potential for CNF before and after modification; TEM images for (C) pristine CNF, negatively silver nanoparticle-stained (D) CNF-SH-a and (E) CNF-SH-b.

The crystalline properties and zeta potential value for CNF before and after end modification were investigated. As shown in Figure 2.2A, the XRD pattern for pristine CNF and modified CNF (CNF-SH-a and CNF-SH-b) showed typical cellulose I crystalline characteristic peaks. According to Segal formula,²⁸ the crystalline index for pristine CNF, CNF-SH-a and CNF-SH-b was 72.8%, 66.8% and 65.7%, respectively, which indicates that the end modification process did not significantly impair the original crystalline structure of CNF. Zeta potential measurements were used to prove the stability of the suspension before and after modification. It is considered that a zeta potential value lower than -30 or over 30 mV provides adequate repulsive force to achieve colloidal physical stability.²⁹ As shown in Figure 2.2B, end-modified CNF-SH-a and CNF-SH-b maintained a high zeta potential absolute value (-39.8 mV and -36.9 mV, respectively), which shows its good dispersibility ability.

After end modification, sulfur atoms were successfully grafted on the reducing end of CNF. According to the well-known spontaneous reaction between silver nanoparticles and sulfur, the regioselective labeling of CNF-SH with silver nanoparticles via a σ - π coordinate bond^{30,31} could prove the reducing end modification. From Figure 2.2C-E, CNF, CNF-SH-a and CNF-SH-b maintained a fibrous morphology and good dispersibility, as expected from zeta potential measurements. Furthermore, most of CNF-SH were labeled with several silver nanoparticles located on one end of CNF-SH by the in-situ growth strategy. These results provide visual evidence of the successful modification of the reducing end of CNF. In agreement with XPS and EA results, it was observed that the amount of silver nanoparticles labeling on CNF-SH-a is significantly higher than for CNF-SH-b, indicating that the grafting efficiency of the former is higher than the latter.

2.3.2 Click reaction between CNF-SH-a and NR

End-modified CNF-SH-a with -SH groups could react with the unsaturated double bond (-C=C-) of NR matrix under UV radiation to achieve a reactive compound. To demonstrate the chemical reaction between CNF-SH-a and NR matrix, the reaction mixture consisting of NR matrix and CNF-SH-a (2:1 w/w) was purified after 30 min of UV radiation under stirring. The mixture was prepared by continuous centrifugation and washing with acetone to completely remove unreacted NR component and the purified product was conditioned at 40°C in an oven overnight. For comparison, purified NR/CNF was also subjected to the same treatment.

As shown in Figure 2.3A, compared to the FTIR spectra of pristine NR and CNF, the purified NR/CNF-SH-a mixture exhibits an out-of-plane bending vibrational peak assigned to =C-H for the alkene group on NR matrix at 836 cm⁻¹.³² However, the FTIR spectrum for the purified NR/CNF mixture was essentially identical to pristine CNF with no new peak appearing. Furthermore, the characteristic peaks were observed in the solid-state NMR spectrum of purified NR/CNF-SH-a mixture, corresponding to C1'

(33ppm), C4' (27ppm) and C5' (23ppm) in the chemical structure of isoprene.³³ Combining FTIR and ¹³C ssNMR results, it is shown that the covalent bond formed by the click reaction between the end-modified CNF-SH-a and NR corresponds to a strong interaction, so that successive centrifugation and washing steps cannot remove the NR component covalently bonded to CNF-SH-a, and the characteristic peaks belonging to NR were observed in the FTIR and ssNMR spectra of the purified NR/CNF-SH-a mixture. The interaction between NR and unmodified CNF is weak in the NR/CNF mixture and therefore the free NR component can be easily removed during the purification process.

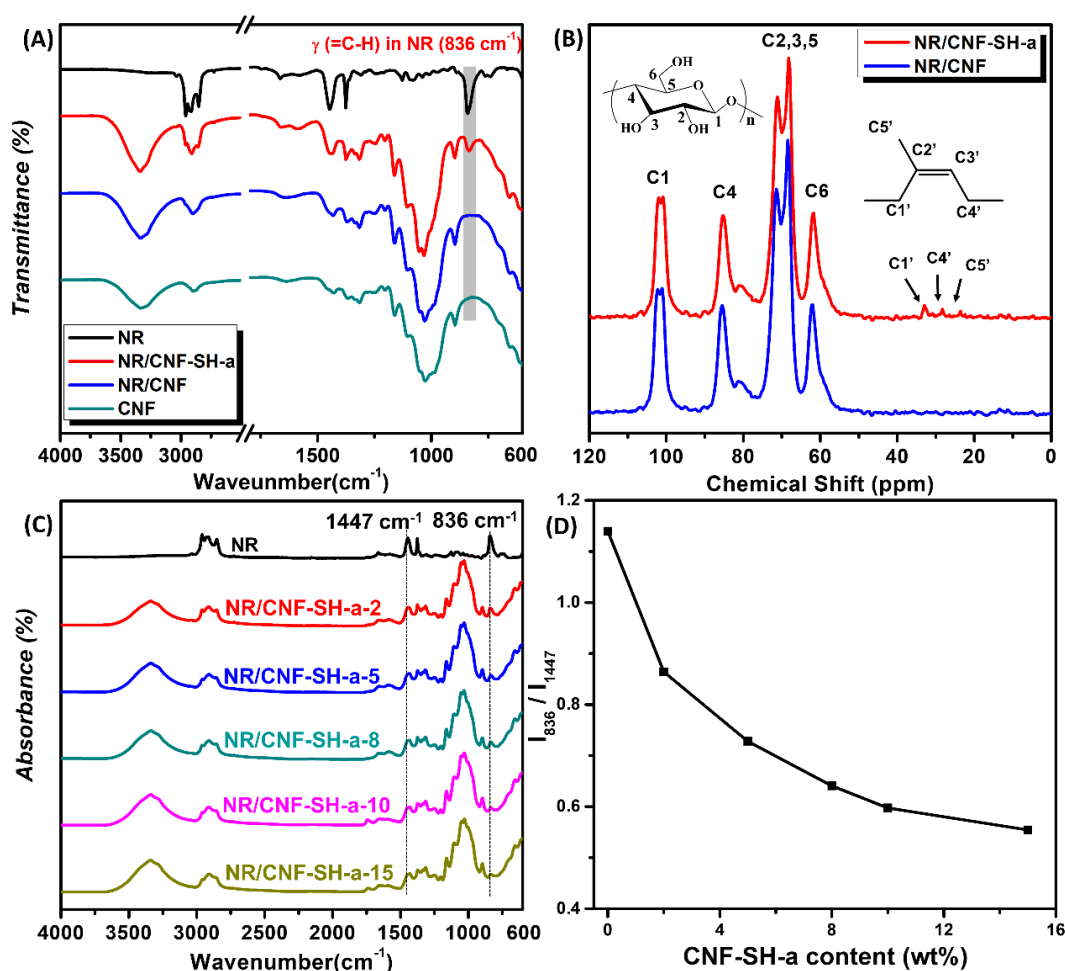


Figure 2.3 (A) FTIR spectra for NR, NR/CNF-SH-a (2:1 w/w), NR/CNF (2:1 w/w) and pristine CNF; (B) ¹³C solid-state NMR spectra for NR/CNF-SH-a (2:1 w/w) and NR/CNF (2:1 w/w). (C) FTIR spectra for the nanocomposites with different CNF-SH-a contents; (D) Evolution of I₈₃₆/I₁₄₄₇ as a function of CNF-SH-a content.

The interfacial interaction between CNF-SH-a and NR matrix in the nanocomposites was investigated by FTIR, as shown in Figure 2.3C. The peak at 836 cm^{-1} was assigned to the =C-H out-of-plane bending vibration of the alkene group. Compared to neat NR, the intensity of the peak at 836 cm^{-1} for the nanocomposites decreased when increasing the CNF-SH-a content, attributed to the click reaction between the double bond in the NR chain and the -SH group of CNF-SH-a. To further explore the chemical reaction between CNF-SH-a and NR matrix, the C-H bending vibration of the methyl group at 1447 cm^{-1} was chosen as a comparison to normalize the intensity of the =C-H peak at 836 cm^{-1} by integrating the area of the two peaks in the spectra of the nanocomposites (I_{836}/I_{1447}). The I_{836}/I_{1447} value decreased from 1.14 to 0.55, when increasing the CNF-SH-a content from 0 to 15 wt%, as shown in Figure 2.3D. These results demonstrate that covalent bonds are formed and controlled between the thiol group of CNF-SH-a and the unsaturated double bond in the NR matrix.

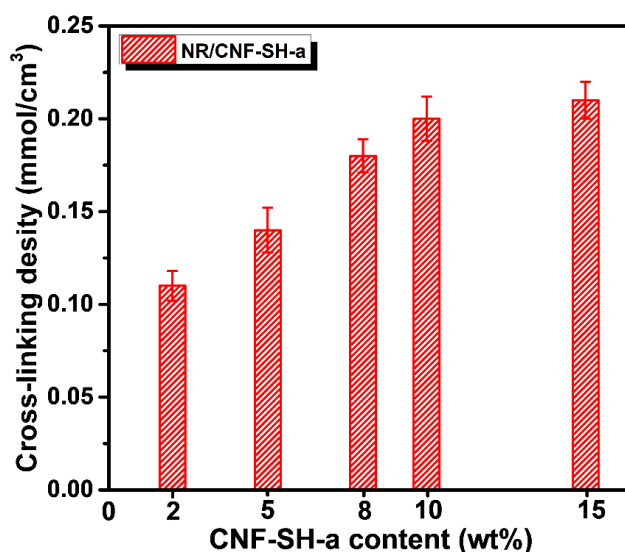


Figure 2.4 Cross-linking density of the nanocomposites with different CNF-SH-a contents.

The cross-linking density was calculated by the solvent swelling measurement method using the Flory-Rehner equation. As shown in Figure 2.4, The cross-linking density of NR/CNF-SH-a-x nanocomposites increases when increasing the CNF-SH-a content, which is consistent with the results of FTIR analysis. Compared with NR/CNF-SH-a-2

(0.11 mmol/cm³), NR/CNF-SH-a-15 nanocomposite exhibits a higher cross-linking density (0.21 mmol/cm³). The results indicate that the improvement of interfacial interaction in the nanocomposites may contribute to increase the cross-linking density. The strong interfacial interaction between CNF-SH-a and NR matrix through click chemistry resulted in a tight bond between the filler and the matrix, effectively binding the polymer chains together. The greatly increased proportion of rigid phase in the matrix³⁴ slows down the penetration of the solvent into the matrix, thereby reducing the solvent adsorption and swelling of the NR/CNF-SH-a nanocomposites.

2.3.3 Morphology of the nanocomposites

The fractured surface for neat NR and nanocomposites reinforced with 5 wt% CNF-SH-a or CNF were observed by SEM to evaluate the compatibility between the filler and NR matrix. As shown in Figure 2.5A,D), a smooth and uniform morphology was observed for unfilled NR. CNF-SH-a was homogeneously dispersed in the NR matrix without significant aggregation (Figure 2.5B,E) due to the introduction of relatively long NR chains at the end of CNF-SH-a via click reaction, which weakened the hydrophilic character and hydrogen-bonding tendency of CNF-SH-a. Furthermore, no gaps or voids were found in the NR/CNF-SH-a-5 nanocomposites, indicating good interfacial compatibility between CNF-SH-a and NR matrix. The good interfacial compatibility was mainly attributed to the strong interaction between CNF-SH-a and NR matrix via click reaction. However, a significant micro-phase separation (two layers: one rougher phase and another smoother phase) was observed for NR/CNF-5 nanocomposites. The rougher phase possibly corresponded to the aggregation of unmodified CNF at the bottom of the PTFE molds during water evaporation. The simple physical compounding of hydrophilic CNF and hydrophobic NR matrix resulted in poor interfacial compatibility and significant micro-phase separation for the NR/CNF-5 nanocomposite. Therefore, the good interfacial compatibility for CNF-SH-a reinforced materials is expected to greatly improve the properties of the resulting nanocomposites.³⁵

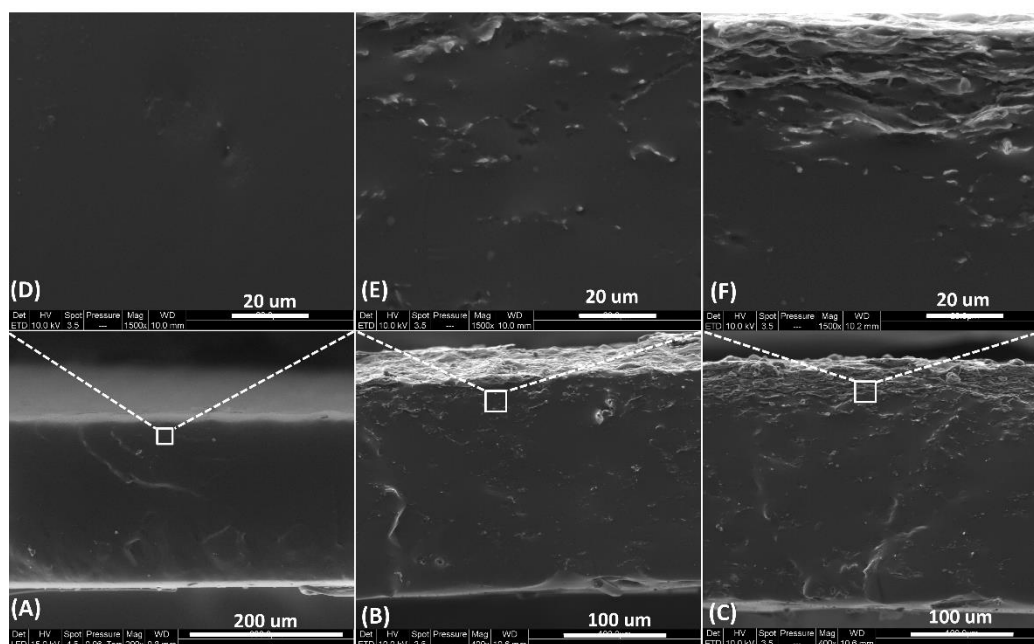


Figure 2.5 SEM of fractured surfaces for (A, D) neat NR, (B, E) NR/CNF-SH-a-5 and (C, F) NR/CNF-5 with different magnifications. The regions delimited by white rectangles in (A, B and C) images correspond to the lower face of the composite films, which are in contact with the PTFE mold during water evaporation.

2.3.4 Mechanical properties of the nanocomposites

The mechanical properties of NR/CNF and NR/CNF-SH-a nanocomposites were characterized by tensile tests. Typical stress-strain curves for the nanocomposites and pure NR are shown in Figure 2.6, and the tensile properties are collected in Table 2.2. Compared to neat NR, the modulus and tensile strength of the nanocomposites increased significantly with the addition of CNF and CNF-SH-a. The tensile strength for NR/CNF-SH-a-10 (5.83 MPa) was 17.6 times higher than that of neat NR (0.33 MPa) and 1.67 times higher than that of NR/CNF-SH-10 (3.48 MPa). Meanwhile, the Young's modulus for NR/CNF-SH-a-10 (45.25 MPa) was 94.3 times higher than that of neat NR (0.48 MPa) and 1.27 times higher than that of NR/CNF-SH-10 (35.55 MPa). The elongation at break of the nanocomposites decreased when increasing the CNF and CNF-SH content, in line with previous studies.^{36,37}

Table 2.2 Tensile properties data for NR/CNF and NR/CNF-SH-a nanocomposites.

Samples	Strength	Young's modulus	Elongation at break	Toughness
	MPa	MPa	%	MJ m ⁻³
NR	0.33±0.09	0.48±0.13	1099±32	2.63±0.23
NR/CNF-2	0.67±0.12	0.81±0.14	841±25	3.35±0.34
NR/CNF-5	1.42±0.35	7.75±1.07	681±38	7.16±0.38
NR/CNF-8	2.71±0.37	22.9±1.89	574±20	10.82±0.44
NR/CNF-10	3.48±0.41	35.55±2.65	447±23	12.51±0.53
NR/CNF-15	4.76±0.37	56.08±3.67	241±14	10.12±0.76
NR/CNF-SH-a-2	0.81±0.15	1.68±0.26	994±31	5.01±0.28
NR/CNF-SH-a-5	1.99±0.23	8.81±1.14	718±19	9.89±0.78
NR/CNF-SH-a-8	4.51±0.34	36.03±3.54	647±19	19.73±0.95
NR/CNF-SH-a-10	5.83±0.31	45.25±4.34	543±21	22.24±0.45
NR/CNF-SH-a-15	7.23±0.42	89.45±5.65	369±28	22.83±0.88

This is mainly attributed to the fact that the entangled CNF network expected to form within the NR matrix provides higher stiffness at the expense of ductility. Meanwhile, the strong interfacial interaction between NR and CNF-SH via click reaction held the matrix and filler more tightly and restricted the movement of NR chain segments. The toughness of the nanocomposites increased when increasing CNF and CNF-SH-a content. For 15% CNF content, the toughness decreased due to the aggregation of CNF in the NR matrix, which is consistent with SEM observations. The toughness of NR/CNF-SH-a-10 (22.24 MJ m⁻³) was 8.45 times higher than that of neat NR (2.63 MJ m⁻³) and 1.78 times higher than that of NR/CNF-SH-10 (12.51 MJ m⁻³). Therefore, for a given CNF content, a lower degradation of the ductility of the material is observed for CNF-SH-a based nanocomposites. These results indicate the synergistic effect of the rigid CNF-SH-a reinforcement together with cross-linking at the filler-matrix interface.

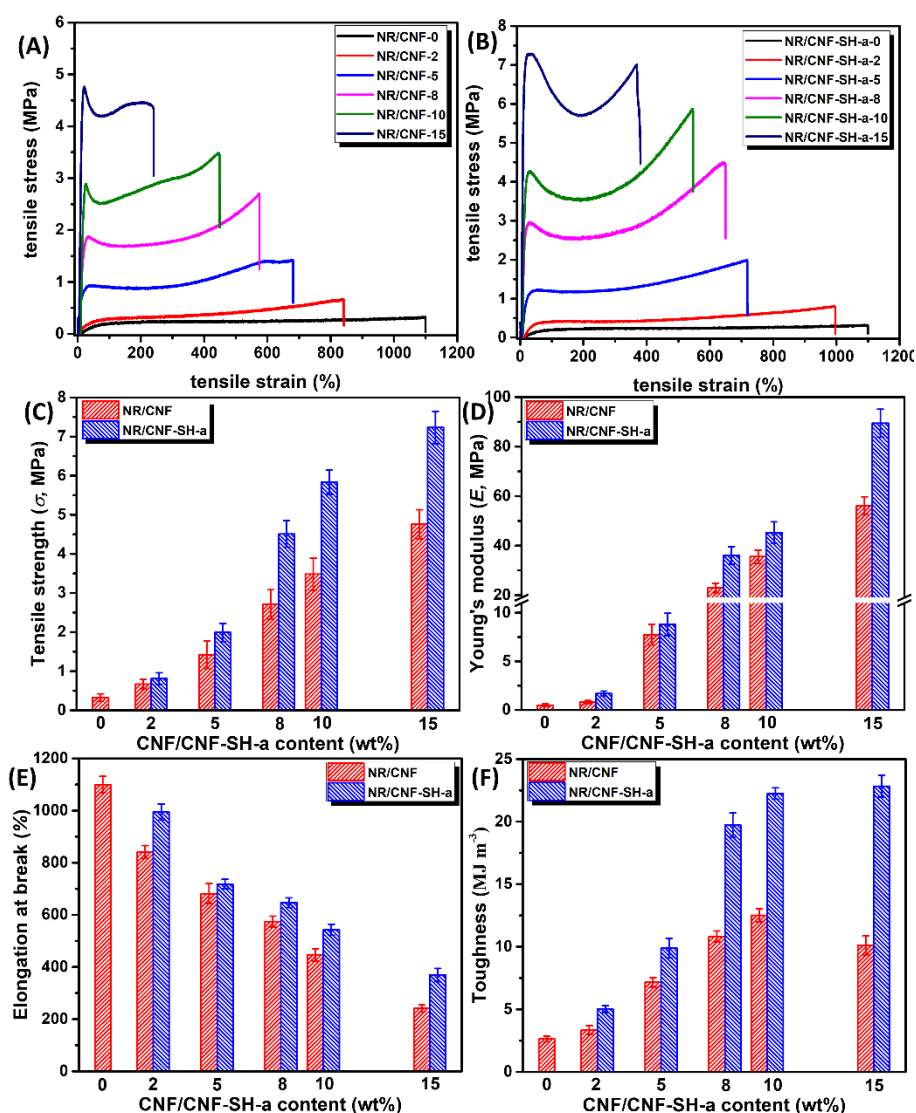


Figure 2.6 Stress-strain curves for (A) NR/CNF nanocomposites, and (B) NR/CNF-SH-a nanocomposites. Evolution of (C) the tensile strength, (D) Young's modulus, (E) elongation at break and (F) toughness as a function of filler content for neat NR and nanocomposites (the error bars are standard deviations).

2.3.5 Successive tensile tests

The stress-strain curves obtained from the successive tensile tests applied to the nanocomposites are shown in Figure 2.7A,B. During the successive tensile tests, the positive stretch curve and the negative recovery curve were not superimposed. Meanwhile, a residual elongation was induced for each cycle, which is due to the entropic nature of the strain and the involvement of the viscoelastic component to the

total compliance. It is worth noting that it is mainly influenced by the experimental stretching rate and temperature, and it is strongly time-dependent.^{38,39} For subsequent cycles, the nanocomposites could be stretched to an elongation above their elastic limit, since the rubber was unvulcanized.

Table 2.3 Tensile modulus (E_i , MPa) and shrinkage (r_i , %) determined for nanocomposites during successive tensile tests.

Sample	E_1	E_2	E_3	E_4	E_5	E_6	E_7	E_8	E_9	E_{10}	E_{11}
NR	0.49	0.41	0.39	0.35	0.31	0.26	0.22	0.15	0.10	0.08	0.05
NR/CNF-2	0.93	0.86	0.8	0.75	0.58	0.48	0.37	0.3	0.22	-	-
NR/CNF-SH-a-2	1.81	1.44	1.04	0.7	0.53	0.43	0.37	0.31	0.17	-	-
NR/CNF-5	6.41	3.13	2.45	1.64	1.06	0.79	0.24	-	-	-	-
NR/CNF-SH-a-5	9.11	6.23	5.01	4.97	3.26	1.86	1.12	0.84	-	-	-
Sample	r_1	r_2	r_3	r_4	r_5	r_6	r_7	r_8	r_9	r_{10}	r_{11}
NR	66	141	209	278	354	419	482	550	598	655	726
NR/CNF-2	61	132	205	273	348	406	465	541	-	-	-
NR/CNF-SH-a-2	67	139	209	281	350	415	475	547	-	-	-
NR/CNF-5	55	121	188	252	310	363	-	-	-	-	-
NR/CNF-SH-a-5	57	129	196	262	324	393	449	-	-	-	-

The shrinkage r_i of the nanocomposites was determined by the difference between the elongation and the residual elongation retained at the end of each cycle. The evolution of the tensile modulus E_i and shrinkage r_i during the successive cycles is plotted in three-dimensional diagram (Fig. 7C,D, respectively). For all samples, the tensile modulus showed a continuous decreasing trend during successive cycles, where the higher the nanocellulose contents was, the stronger the modulus drop was, as shown in Table 2.3. During the first successive tensile tests, the decrease in modulus of the nanocomposites could be attributed to the gradual breakdown of the continuous nanocellulose network. We also observed that the tensile modulus of the nanocomposites was higher than that of neat NR for a given cycle, while the modulus increased with increasing nanocellulose content, which is consistent with tensile test results, as well as DMA experiments that will be reported latter.

Regardless of the sample, residual elongation was observed from the first stretching cycle, while shrinkage increases during successive tensile tests. These data suggest that the viscous flow in the samples decreases for each successive stretching cycle, while the elastic recovery component increases. For a given cycle, the shrinkage of the nanocomposites was lower than that of the neat NR matrix. In addition, the nanocomposites reinforced with CNF-SH-a exhibit higher shrinkage than that of CNF in a given cycle. This indicated that CNF-SH-a induces a more elastic behavior of the nanocomposite while reducing its viscoelasticity, demonstrating the interaction between CNF-SH-a and NR matrix.

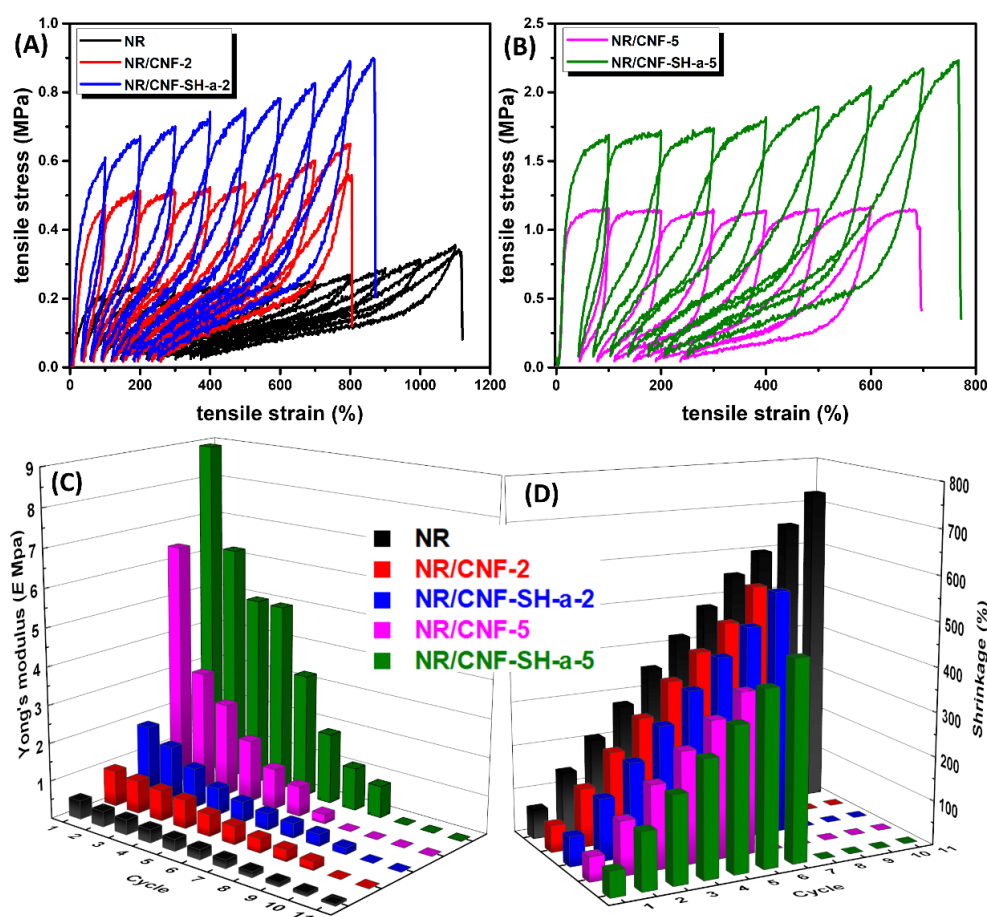


Figure 2.7 Stress-strain curves recorded during successive tensile tests for (A) NR, NR/CNF-2, and NR/CNF-SH-a-2 nanocomposites; (B) NR/CNF-5, NR/CNF-SH-a-5 nanocomposites; and evolution of (C) the tensile modulus E_i and (D) the shrinkage r_i measured during each cycle i for NR/CNF and NR/CNF-SH-a nanocomposites.

2.3.6 Dynamic mechanical analysis

Typical dynamic mechanical curves for the isochronal evolution of the tensile storage modulus (E') and loss factor ($\tan \delta$) as a function of temperature for pure NR, NR/CNF-5, NR/CNF-10, NR/CNF-SH-a-5 and NR/CNF-SH-a-10 nanocomposites are shown in Figure 2.8. At low temperature, E' remains roughly constant around 3 GPa (Figure 2.8A). It is due to the fact that in the glassy state, molecular motions are largely restricted to vibration and short-range rotational motions. Increasing the CNF content successively increased the E' value. This sort of modulus enhancement, even below the glass transition temperature, is good evidence for the strong reinforcing tendency of CNF in the NR matrix. A sharp modulus drop over about three decades is observed for all samples around -55°C , which corresponds to the relaxation process associated to the glass transition of the NR matrix. This modulus drop is linked to an energy dissipation phenomenon displayed through the concomitant increase of the loss factor where $\tan \delta$ passes through a maximum (Figure 2.8B). This relaxation process involves cooperative motions of long chain sequences. Above T_g , the modulus becomes roughly constant and corresponds to the rubbery modulus. In this temperature range, the impact of the filler on the stiffness of the material appears more distinctly, due to the greater difference in the modulus of the two components. A higher reinforcing effect is observed for CNF-SH-a based nanocomposites compared to CNF based nanocomposites, probably because of stronger interactions between the filler and the matrix via click reaction, which increased the effective volume fraction of the rigid phase and led to the formation of a bound matrix material around the filler.

Compared to neat NR, the T_g of both nanocomposite materials showed a slight shift towards higher temperatures, as shown in Figure 2.8B. $\tan \delta$ for neat NR exhibits a maximum at -56.4°C , while it is -54.3°C and -51.5°C for NR/CNF-10 and NR/CNF-SH-a-10 nanocomposites, respectively. This is mainly attributed to the restricted segmental movement due to strong interaction between the filler and the matrix. Meanwhile, the increased cross-linking density also led to an increase of T_g . As the

filler content increased, the magnitude of the damping peak associated to the glass transition for both nanocomposites decreased, probably due to the covalent bonds formed between the filler and the NR chain segment molecules, which greatly restricted the movement of the NR chains. These results suggest that strong covalent links exist at the composite interface for NR/CNF-SH-a nanocomposites, while a denser cross-linked NR network would give a stronger reinforcement effect of CNF-SH-a in the rubbery state.

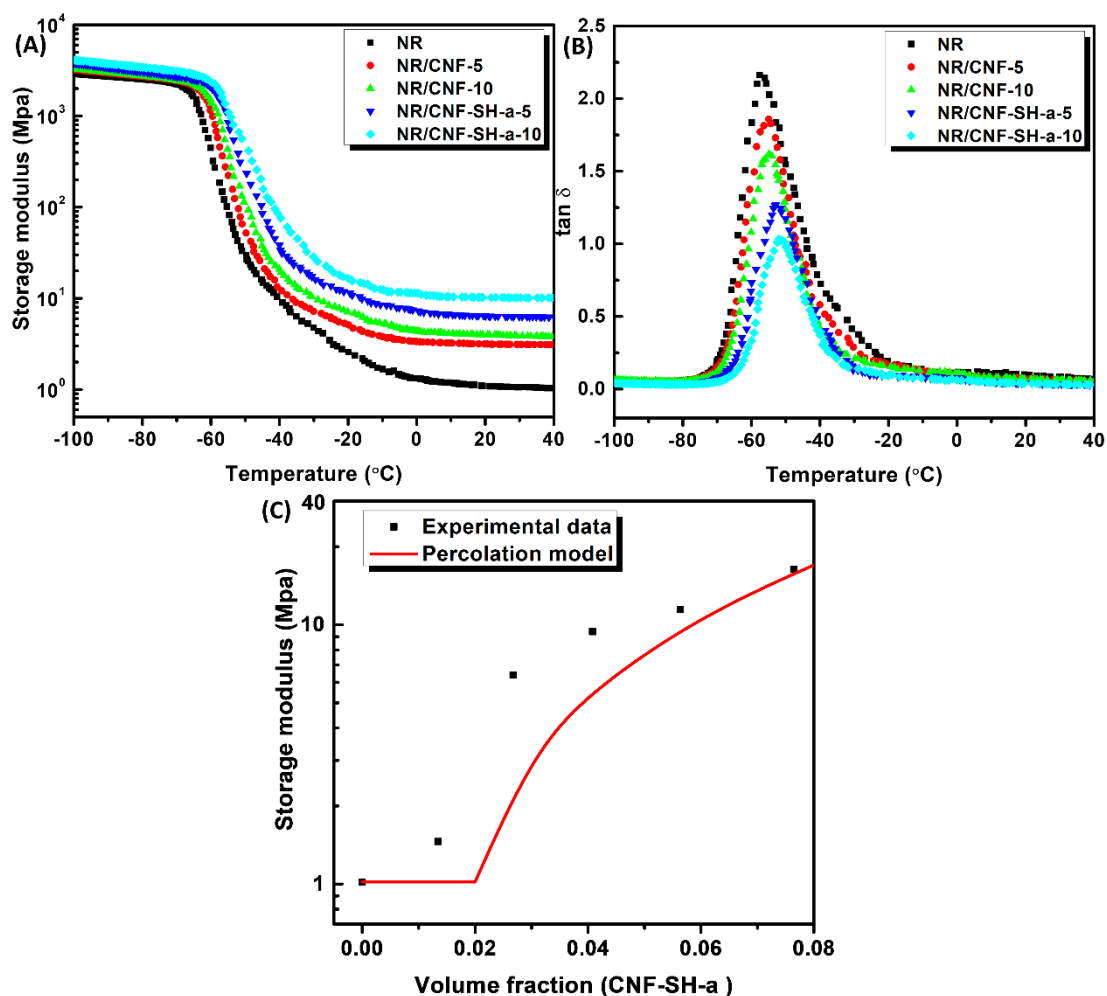


Figure 2.8 Typical dynamic mechanical analysis isochronal curves: (A) tensile storage modulus (E') and (B) loss factor ($\tan \delta$) vs. temperature for neat NR, NR/CNF-5, NR/CNF-10, NR/CNF-SH-a-5 and NR/CNF-SH-a-10 nanocomposites. (C) Evolution of the predicted and experimental modulus for CNF-SH-a nanocomposites vs. CNF-SH-a volume fraction at 25 $^{\circ}\text{C}$.

Table 2.4 Experimental (DMA at 25°C) and predicted (Takayanagi model) storage modulus value for NR/CNF-SH-a nanocomposites.

Sample	Filler volume fraction	Experimental	Predicted
		MPa	MPa
NR	0	1.02	–
NR/CNF-SH-a-2	0.0128	1.46	1.02
NR/CNF-SH-a-5	0.0325	6.41	3.69
NR/CNF-SH-a-8	0.0527	8.41	8.78
NR/CNF-SH-a-10	0.0663	11.45	12.72
NR/CNF-SH-a-15	0.101	16.38	24.37

This high reinforcement effect could be attributed to the formation of a continuous rigid three-dimensional percolation network structure by hydrogen bonds, which has been extensively discussed in the literature and is well predicted by the percolation approach adapted to the Takayanagi model.^{40,41}

$$E' = \frac{(1-2\psi+\psi X_r)E_r'E_s'+(1-\psi X_r)\psi E_r'^2}{(1-X_r)E_r'+(X_r-\psi)E_s'} \quad (3)$$

$$\psi = X_r \left(\frac{X_r - X_c}{1 - X_c} \right)^{0.4} \quad (4)$$

$$X_c = \frac{0.7}{f} \quad (5)$$

where E_r' is the storage modulus of the rigid filler network; E_s' is the storage modulus of neat NR; X_r is the volume fraction of CNF-SH-a in the nanocomposite; X_c is the volume fraction of CNF-SH-a at the percolation threshold; ψ is the volume fraction of CNF-SH-a contributing to the percolation network; f is the aspect ratio of CNF-SH-a, which was estimated to 34.8 according to TEM observations by software of NanoScope Analysis 1.5. The density of NR and CNF-SH-a was 0.96 and 1.5 g cm⁻³, respectively.

The comparison between predicted and experimental modulus it classically used to evaluate the dispersion state of the filler within the polymer matrix and the formation of a percolating network in the nanocomposite. At sufficiently high temperatures, i.e. above T_g of the NR matrix, the modulus of CNF-SH-a (0.65 GPa^{42,43}) is much higher

than that of the NR matrix (1.02 MPa, according to DMA results). Thus, Eq. 3 can be simplified and the storage modulus of the nanocomposite is just the product of the volume fraction of CNF-SH-a contributing to the percolation network (ψ) and modulus of the percolation rigid CNF-SH-a network.^{44,45}

$$E' = \psi * E'_r \quad (6)$$

Based on the above equation, the calculated percolation threshold of CNF-SH-a was 2.01 vol%, which is around 3.1 wt%. From Figure 2.8C and Table 2.4, it is obvious that for the nanocomposite reinforced with 5 wt% CNF-SH-a percolating network effectively formed. The end-modification allows CNFs to not only retain the original crystal structure and size, but also preserves the surface hydroxyl group, which serve as the driving force for hydrogen bonding and are the basis for rigid network formation.⁴⁶ It significantly improved the dispersion and storage modulus of the nanocomposite.

2.4 Conclusions

We have demonstrated a novel concept for the development of rubbery nanocomposites based on the synergistic effect of cellulose nanofibrils used as a biobased reinforcement, which also possess cross-linking sites for covalent coupling to the natural rubber elastomer matrix. Reducing end-modified CNFs bearing -SH groups (CNF-SH-a) were successfully prepared by aldimine condensation at one end of CNF with 6-Amino-1-hexanethiol hydrochloride. CNF-SH-a showed improved hydrophobicity and good dispersibility in hydrophobic medium. Nanocomposite films with homogeneous dispersion of CNF-SH-a in NR matrix were prepared by a casting/evaporation method. The cross-link density of the NR/CNF-SH-a sample was confirmed to significantly increase when increasing CNF-SH-a content. This is due to the covalent cross-links formed at the filler-matrix interface photochemically initiated by thiol-ene reaction. The NR nanocomposite reinforced with 10 wt%/CNF-SH-a showed significantly higher values of tensile strength (from 0.33 MPa to 5.83 MPa), Young's modulus (from 0.48

MPa to 45.25 MPa) and toughness (from 2.63 MJ m⁻³ to 22.24 MJ m⁻³) compared to neat NR nanocomposites. As the present concept is general in material synthesis and design, we foresee that this green method to reinforce NR matrix with end-modified CNF-SH will have the potential application in textile, printing, automobile and machinery manufacturing fields.

Acknowledgements

This work was supported by the China Scholarship Council (CSC) under Grant No. 201806950016. LGP2 is part of the LabEx Tec 21 (Investissements d’Avenir—Grant Agreement No. ANR-11-LABX-0030) and of the PolyNat Carnot Institute (Investissements d’Avenir—Grant Agreement No. ANR-16-CARN-0025-01).

2.5 References

- (1) Liff, S. M.; Kumar, N.; McKinley, G. H. High-Performance Elastomeric Nanocomposites via Solvent-Exchange Processing. *Nat. Mater.* **2007**, *6* (1), 76–83.
- (2) Papageorgiou, D. G.; Kinloch, I. A.; Young, R. J. Graphene/Elastomer Nanocomposites. *Carbon* **2015**, *95*, 460–484.
- (3) Fu, L.; Wu, F.; Xu, C.; Cao, T.; Wang, R.; Guo, S. Anisotropic Shape Memory Behaviors of Polylactic Acid/Citric Acid–Bentonite Composite with a Gradient Filler Concentration in Thickness Direction. *Ind. Eng. Chem. Res.* **2018**, *57* (18), 6265–6274.
- (4) Cao, J.; Zhang, X.; Lu, C.; Luo, Y.; Zhang, X. Self-Healing Sensors Based on Dual Noncovalent Network Elastomer for Human Motion Monitoring. *Macromol. Rapid Commun.* **2017**, *38*. <https://doi.org/10.1002/marc.201700406>.
- (5) Ma, L.-F.; Bao, R.-Y.; Dou, R.; Liu, Z.-Y.; Yang, W.; Xie, B.-H.; Yang, M.-B.; Fu, Q. A High-Performance Temperature Sensitive TPV/CB Elastomeric Composite with Balanced Electrical and Mechanical Properties via PF-Induced Dynamic Vulcanization. *J. Mater. Chem. A* **2014**, *2* (40), 16989–16996.

- (6) Chen, Y.; Huang, X.; Gong, Z.; Xu, C.; Mou, W. Fabrication of High Performance Magnetic Rubber from NBR and Fe₃O₄ via in Situ Compatibilization with Zinc Dimethacrylate. *Ind. Eng. Chem. Res.* **2017**, *56* (1), 183–190.
- (7) Cao, L.; Huang, J.; Chen, Y. Dual Cross-Linked Epoxidized Natural Rubber Reinforced by Tunicate Cellulose Nanocrystals with Improved Strength and Extensibility. *ACS Sustain. Chem. Eng.* **2018**, *6* (11), 14802–14811.
- (8) Cao, L.; Fan, J.; Huang, J.; Chen, Y. A Robust and Stretchable Cross-Linked Rubber Network with Recyclable and Self-Healable Capabilities Based on Dynamic Covalent Bonds. *J. Mater. Chem. A* **2019**, *7* (9), 4922–4933.
- (9) Jardin, J. M.; Zhang, Z.; Hu, G.; Tam, K. C.; Mekonnen, T. H. Reinforcement of Rubber Nanocomposite Thin Sheets by Percolation of Pristine Cellulose Nanocrystals. *Int. J. Biol. Macromol.* **2020**, *152*, 428–436.
- (10) Xu, C.; Zheng, Z.; Wu, W.; Wang, Z.; Fu, L. Dynamically Vulcanized PP/EPDM Blends with Balanced Stiffness and Toughness via in-Situ Compatibilization of MAA and Excess ZnO Nanoparticles: Preparation, Structure and Properties. *Compos. Part B Eng.* **2019**, *160*, 147–157.
- (11) Xu, C.; Cui, R.; Fu, L.; Lin, B. Recyclable and Heat-Healable Epoxidized Natural Rubber/Bentonite Composites. *Compos. Sci. Technol.* **2018**, *167*, 421–430.
- (12) Xu, C.; Wu, W.; Zheng, Z.; Wang, Z.; Nie, J. Design of Shape-Memory Materials Based on Sea-Island Structured EPDM/PP TPVs via in-Situ Compatibilization of Methacrylic Acid and Excess Zinc Oxide Nanoparticles. *Compos. Sci. Technol.* **2018**, *167*, 431–439.
- (13) Liu, Y.; Cao, L.; Yuan, D.; Chen, Y. Design of Super-Tough Co-Continuous PLA/NR/SiO₂ TPVs with Balanced Stiffness-Toughness Based on Reinforced Rubber and Interfacial Compatibilization. *Compos. Sci. Technol.* **2018**, *165*, 231–239.

- (14) Gan, L.; Dong, M.; Han, Y.; Xiao, Y.; Yang, L.; Huang, J. Connection-Improved Conductive Network of Carbon Nanotubes in a Rubber Cross-Link Network. *ACS Appl. Mater. Interfaces* **2018**, *10* (21), 18213–18219.
- (15) Chen, Y.; Wang, W.; Yuan, D.; Xu, C.; Cao, L.; Liang, X. Bio-Based PLA/NR-PMMA/NR Ternary Thermoplastic Vulcanizates with Balanced Stiffness and Toughness: “Soft–Hard” Core–Shell Continuous Rubber Phase, in Situ Compatibilization, and Properties. *ACS Sustain. Chem. Eng.* **2018**, *6* (5), 6488–6496.
- (16) Smyth, M.; García, A.; Rader, C.; Foster, E. J.; Bras, J. Extraction and Process Analysis of High Aspect Ratio Cellulose Nanocrystals from Corn (*Zea Mays*) Agricultural Residue. *Ind. Crops Prod.* **2017**, *108*, 257–266.
- (17) Pasquini, D.; de Moraes Teixeira, E.; da Silva Curvelo, A. A.; Belgacem, M. N.; Dufresne, A. Extraction of Cellulose Whiskers from Cassava Bagasse and Their Applications as Reinforcing Agent in Natural Rubber. *Ind. Crops Prod.* **2010**, *32* (3), 486–490.
- (18) Wu, X.; Lu, C.; Zhang, X.; Zhou, Z. Conductive Natural Rubber/Carbon Black Nanocomposites via Cellulose Nanowhisker Templated Assembly: Tailored Hierarchical Structure Leading to Synergistic Property Enhancements. *J Mater Chem A* **2015**, *3*. <https://doi.org/10.1039/C5TA02601F>.
- (19) Peng, C.; Yang, Q.; Zhao, W.; Ren, J.; Yu, Q.; Hu, Y.; Zhang, X. Relationship between Interface Chemistry and Reinforcement in Polybutadiene/Cellulose Nanocrystal Nanocomposites. *Compos. Sci. Technol.* **2019**, *177*, 103–110.
- (20) Tao, H.; Dufresne, A.; Lin, N. Double-Network Formation and Mechanical Enhancement of Reducing End-Modified Cellulose Nanocrystals to the Thermoplastic Elastomer Based on Click Reaction and Bulk Cross-Linking. *Macromolecules* **2019**, *52* (15), 5894–5906.
- (21) Parambath Kanoth, B.; Claudino, M.; Johansson, M.; Berglund, L. A.; Zhou, Q. Biocomposites from Natural Rubber: Synergistic Effects of Functionalized

- Cellulose Nanocrystals as Both Reinforcing and Cross-Linking Agents via Free-Radical Thiol–Ene Chemistry. *ACS Appl. Mater. Interfaces* **2015**, *7* (30), 16303–16310.
- (22) Goetz, L.; Foston, M.; Mathew, A. P.; Oksman, K.; Ragauskas, A. J. Poly (Methyl Vinyl Ether-Co-Maleic Acid)– Polyethylene Glycol Nanocomposites Cross-Linked in Situ with Cellulose Nanowhiskers. *Biomacromolecules* **2010**, *11* (10), 2660–2666.
- (23) Goetz, L.; Mathew, A.; Oksman, K.; Gatenholm, P.; Ragauskas, A. J. A Novel Nanocomposite Film Prepared from Crosslinked Cellulosic Whiskers. *Carbohydr. Polym.* **2009**, *75* (1), 85–89.
- (24) Arcot, L. R.; Lundahl, M.; Rojas, O. J.; Laine, J. Asymmetric Cellulose Nanocrystals: Thiolation of Reducing End Groups via NHS–EDC Coupling. *Cellulose* **2014**, *21* (6), 4209–4218.
- (25) Zhu, G.; Xu, H.; Dufresne, A.; Lin, N. High-Adsorption, Self-Extinguishing, Thermal, and Acoustic-Resistance Aerogels Based on Organic and Inorganic Waste Valorization from Cellulose Nanocrystals and Red Mud. *ACS Sustain. Chem. Eng.* **2018**, *6* (5), 7168–7180.
- (26) Flory, P. J.; Rehner Jr, J. Statistical Mechanics of Cross-linked Polymer Networks I. Rubberlike Elasticity. *J. Chem. Phys.* **1943**, *11* (11), 512–520.
- (27) Jiang, M.; Zhang, J.; Wang, Y.; Ahmad, I.; Guo, X.; Cao, L.; Chen, Y.; Gan, L.; Huang, J. Covalent-Bond-Forming Method to Reinforce Rubber with Cellulose Nanocrystal Based on the Thiol-Ene Click Reaction. *Compos. Commun.* **2021**, *27*, 100865.
- (28) Zhu, G.; Chen, Z.; Wu, B.; Lin, N. Dual-Enhancement Effect of Electrostatic Adsorption and Chemical Crosslinking for Nanocellulose-Based Aerogels. *Ind. Crops Prod.* **2019**, *139*, 111580.
- (29) Joseph, E.; Singhvi, G. Multifunctional Nanocrystals for Cancer Therapy: A Potential Nanocarrier. *Nanomater. Drug Deliv. Ther.* **2019**, 91–116.

- (30) Ning, Y.; Xie, H.; Xing, H.; Deng, W.; Yang, D. Comparison of Self-Assembled Monolayers of N-Alkanethiols and Phenylthioureas on the Surface of Gold. *Surf. Interface Anal.* **1996**, *24* (9), 667–670.
- (31) Ulman, A. Formation and Structure of Self-Assembled Monolayers. *Chem. Rev.* **1996**, *96* (4), 1533–1554.
- (32) Neto, W. P. F.; Mariano, M.; da Silva, I. S. V.; Silvério, H. A.; Putaux, J.-L.; Otaguro, H.; Pasquini, D.; Dufresne, A. Mechanical Properties of Natural Rubber Nanocomposites Reinforced with High Aspect Ratio Cellulose Nanocrystals Isolated from Soy Hulls. *Carbohydr. Polym.* **2016**, *153*, 143–152.
- (33) Kawahara, S.; Chaikumpollert, O.; Sakurai, S.; Yamamoto, Y.; Akabori, K. Crosslinking Junctions of Vulcanized Natural Rubber Analyzed by Solid-State NMR Spectroscopy Equipped with Field-Gradient-Magic Angle Spinning Probe. *Polymer* **2009**, *50* (7), 1626–1631.
- (34) Tang, L.; Weder, C. Cellulose Whisker/Epoxy Resin Nanocomposites. *ACS Appl. Mater. Interfaces* **2010**, *2* (4), 1073–1080.
- (35) Cao, L.; Yuan, D.; Fu, X.; Chen, Y. Green Method to Reinforce Natural Rubber with Tunicate Cellulose Nanocrystals via One-Pot Reaction. *Cellulose* **2018**, *25* (8), 4551–4563.
- (36) Cao, X.; Xu, C.; Wang, Y.; Liu, Y.; Liu, Y.; Chen, Y. New Nanocomposite Materials Reinforced with Cellulose Nanocrystals in Nitrile Rubber. *Polym. Test.* **2013**, *32* (5), 819–826.
- (37) Cao, X.; Xu, C.; Liu, Y.; Chen, Y. Preparation and Properties of Carboxylated Styrene-Butadiene Rubber/Cellulose Nanocrystals Composites. *Carbohydr. Polym.* **2013**, *92* (1), 69–76.
- (38) Angellier, H.; Molina-Boisseau, S.; Dufresne, A. Mechanical Properties of Waxy Maize Starch Nanocrystal Reinforced Natural Rubber. *Macromolecules* **2005**, *38* (22), 9161–9170.
- (39) Bendahou, A.; Kaddami, H.; Dufresne, A. Investigation on the Effect of

- Cellulosic Nanoparticles' Morphology on the Properties of Natural Rubber Based Nanocomposites. *Eur. Polym. J.* **2010**, *46* (4), 609–620.
- (40) Azizi Samir, M. A. S.; Alloin, F.; Dufresne, A. Review of Recent Research into Cellulosic Whiskers, Their Properties and Their Application in Nanocomposite Field. *Biomacromolecules* **2005**, *6* (2), 612–626.
- (41) Bras, J.; Hassan, M. L.; Bruzesse, C.; Hassan, E. A.; El-Wakil, N. A.; Dufresne, A. Mechanical, Barrier, and Biodegradability Properties of Bagasse Cellulose Whiskers Reinforced Natural Rubber Nanocomposites. *Ind. Crops Prod.* **2010**, *32* (3), 627–633.
- (42) Shanmuganathan, K.; Capadona, J. R.; Rowan, S. J.; Weder, C. Bio-Inspired Mechanically-Adaptive Nanocomposites Derived from Cotton Cellulose Whiskers. *J. Mater. Chem.* **2010**, *20* (1), 180–186.
- (43) Capadona, J. R.; Van Den Berg, O.; Capadona, L. A.; Schroeter, M.; Rowan, S. J.; Tyler, D. J.; Weder, C. A Versatile Approach for the Processing of Polymer Nanocomposites with Self-Assembled Nanofibre Templates. *Nat. Nanotechnol.* **2007**, *2* (12), 765–769.
- (44) Dufresne, A. *Nanocellulose: From Nature to High Performance Tailored Materials*; Walter de Gruyter GmbH & Co KG, 2017.
- (45) Bettaieb, F.; Khiari, R.; Dufresne, A.; Mhenni, M. F.; Belgacem, M. N. Mechanical and Thermal Properties of Posidonia Oceanica Cellulose Nanocrystal Reinforced Polymer. *Carbohydr. Polym.* **2015**, *123*, 99–104.
- (46) Fox, J. D.; Capadona, J. R.; Marasco, P. D.; Rowan, S. J. Bioinspired Water-Enhanced Mechanical Gradient Nanocomposite Films That Mimic the Architecture and Properties of the Squid Beak. *J. Am. Chem. Soc.* **2013**, *135* (13), 5167–5174.

CHAPTER 3.

“Cellulose nanocrystal-mediated assembly of graphene oxide in natural rubber nanocomposites with high electrical conductivity”

Table of contents – Chapter 3

Chapter 3. Cellulose nanocrystal-mediated assembly of graphene oxide in natural rubber nanocomposites with high electrical conductivity	127
Abstract	127
Keywords	127
3.1 Introduction	128
3.2 Experimental	129
3.2.1 Materials	129
3.2.2 Preparation of CNC/GO nanohybrids.....	129
3.2.3 Preparation of NR/CNC/GO and NR/GO Composites.....	130
3.2.4 Characterization.....	130
3.3 Results and Discussion.....	131
3.3.1 Morphology and Thermal Stability	132
3.3.2 Zeta potential	134
3.3.3 FTIR spectra	135
3.3.4 SEM	136
3.3.5 Electrical Conductivity	137
3.3.6 Mechanical property	138
3.4 Conclusions.....	139
3.5 References.....	140

Chapter 3. Cellulose nanocrystal-mediated assembly of graphene oxide in natural rubber nanocomposites with high electrical conductivity

Ge Zhu, Laura Giraldo Isaza, Alain Dufresne*

Univ. Grenoble Alpes, CNRS, Grenoble INP, LGP2, F-38000, Grenoble, France

Abstract

This study reports a green and powerful strategy for preparing cellulose nanocrystal (CNC)/graphene oxide (GO)/natural rubber (NR) nanocomposites hosting a 3D hierarchical conductive network. Due to good dispersibility and amphiphilic nature of CNC, well dispersed CNC/GO nanohybrids were prepared. Hydrogen bonding interactions between CNC and GO greatly enhanced the stability of the CNC/GO nanohybrids. CNC/GO nanohybrids were introduced into NR latex under sonication and the mixture was cast and evaporated. Self-assembled CNC/GO nanohybrids preferentially dispersed in the interstice between latex microspheres allowing the construction of a 3D hierarchical conductive network. By combining strong hydrogen bonds and 3D conductive network, both the electrical conductivity and mechanical properties (tensile strength and modulus) have been significantly improved. The electrical conductivity of the nanocomposite with 4 wt% GO and 5 wt% CNC exhibited an increase of 9 orders of magnitude compared to the nanocomposite with only 4 wt% GO. Meanwhile, the electrical percolation threshold was 3-fold lower than for NR/GO composites.

Keywords

Cellulose nanocrystals; Natural rubber; Graphene oxide; Self-assembly; 3D hierarchical nanostructure

3.1 Introduction

Rubber-based conductive polymer composites are important materials for applications such as electromagnetic shielding, antistatic materials, pressure-sensitive sensors, overcurrent devices, etc. Conductive composites are commonly prepared by adding a conductive filler, such as carbon nanotubes,¹ carbon black,² graphene,³ or metal nanoparticles⁴ or an intrinsically conductive polymer^{5–10} to a polymer matrix. Solution mixing, melt blending and in-situ polymerization are generally used to fabricate conductive composites.¹¹ However, it requires high conductive filler contents to form a continuous conductive network, which result in the deterioration of the mechanical properties, processing difficulty and high production cost.^{12–15} Hence, the development of highly conductive composites having a low percolation threshold, good processability and adequate mechanical properties, has become a critical issue. Graphene oxide (GO) consists of a monolayered carbon material with a hexagonal lattice structure. It is recognized as an attractive component due to its excellent thermal conductivity, electronic properties, high surface area, strength and Young's modulus.^{16–18} Graphene oxide-based conductive composites have many potential applications in different sectors, such as antistatic sealing rings, stretchable conductors, electromagnetic shielding devices, etc. Nevertheless, graphene oxide readily forms irreversible aggregates in water attributed to intermolecular $\pi - \pi$ stacking attraction forces.^{19–22} The poor dispersion of GO in aqueous suspension is always a negative factor to reach optimal properties. Therefore, obtaining a well-dispersed GO suspension is a necessary condition for the development of highly electrically conductive GO composites with good mechanical properties.

Cellulose nanocrystals (CNCs) consist of elongated rod-like nanomaterials that can be extracted from natural cellulosic fibers by acid hydrolysis. They have been particularly considered for a wide range of applications owing to attractive properties such as tunable surface chemistry, high aspect ratio, stiffness, environmental sustainability, etc. Because of these attractive properties, CNC can be used as stabilizer and template for conductive fillers, enabling the formation of a 3D hierarchical conductive structure in a latex polymer matrix, such as natural rubber (NR), by a self-assembly method in liquid medium.^{23–25} By combining a low percolation threshold due to the elongated structure of these nanomaterials and the high mechanical strength intrinsic to crystallized cellulose, composites with a 3D hierarchical network structure can be

obtained.^{26–30} Several authors^{8,23} reported that CNC can be decorated with a thin conductive polymer layer and ensuing modified nanoparticles can be used to decrease the percolation threshold of conductive composites.

In this article, we report an easily implementable and efficient strategy to prepare NR/CNC/GO nanocomposites hosting a 3D hierarchical multiscale conductive network based on a CNC-assisted latex assembly approach. CNC can significantly improve the dispersion of GO in aqueous medium through the formation of CNC/GO nanohybrids. The prepared CNC/GO nanohybrids can be associated with NR latex by a simple casting/evaporation method. The latex microspheres act as impenetrable domains during the film formation due to their high viscosity and condition the formation of a continuous 3D connected CNC/GO network. A self-organized NR/CNC/GO nanocomposite exhibiting low electrical percolation thresholds, high electrical conductivity and good mechanical properties was successfully constructed following this approach. These highly attractive properties can find applications in stretchable electronics, wearable sensors, energy storage, etc.

3.2 Experimental

3.2.1 Materials

Whatman filter paper was used as the source of native cotton fibers for the preparation of CNC. Sulfuric acid (H₂SO₄, 98%), graphene oxide (GO), sodium hydroxide (NaOH) and uranyl acetate were purchased from Sigma-Aldrich and used without further treatment. The natural rubber (NR) latex with a solid content of 60 wt% was kindly provided by Corrie MacColl Deutschland GmbH (Germany).

3.2.2 Preparation of CNC/GO nanohybrids.

Firstly, the Whatman filter paper was purified with NaOH solution (2 wt%) for 12 h. Cellulose nanocrystals (CNC) were classically prepared by selective acid hydrolysis with H₂SO₄ from purified Whatman filter paper, according to a well-known protocol.³¹ Acid hydrolysis was performed using 65 wt% H₂SO₄ and conducted at 45°C for 45 min under mechanical stirring (IKA, EUROSTAR 20 digital). The suspension was then washed by successive centrifugations (Sigma, 6-16KS) at 8,000 rpm for 5 min, allowing the removal of part of the excess acid and water-soluble fragments. Dialysis against distilled water was subsequently carried out for 5 days to remove any free acid molecule

from the dispersion. The ensuing aqueous suspension contained homogeneously dispersed CNC, and its average solid content was 0.98 wt% as measured in triplicate.

An ultrasonically assisted mixing process was implemented to prepare the CNC/GO nanohybrids. For this, a desired amount of GO was added to the well-dispersed CNC aqueous suspension, and the mixture was dispersed with ultrasonic energy of 5 kJ/g CNC with 250 Watt sonication probe (Sonifier 250, Branson, USA) at 50% of maximum energy during 15 min resulting in a uniform CNC/GO nanohybrid suspension.

3.2.3 Preparation of NR/CNC/GO and NR/GO Composites.

For preparing the NR/CNC/GO nanocomposites, a given amount of CNC/GO nanohybrid suspended in water was added to the NR latex under magnetic stirring (IKA, C-MAG HS 7) for 1h until a uniform mixture was formed. Then, this mixture was degassed at room temperature and under vacuum for 30 min to remove bubbles, and finally cast in PTFE molds before evaporation at 45°C overnight to obtain solid composite films. A similar procedure was used to prepare CNC-free NR/GO nanocomposites. Both sets of composites were labeled as NR/CNC/GO-x and NR/GO-x with x corresponding to the GO content (0, 1, 2, 4, 6, 8, 10, 15 wt%), which was based on the total solid content. It was varied from 0 to 15 wt%. For all composites containing CNC, the CNC content was fixed at 5 wt% based on the total solid content, and this information was therefore not recorded for the sample codification.

3.2.4 Characterization

Both the morphology and dimensions of CNC were characterized by atomic force microscopy (AFM) (O-TESPA tip, Bruker, USA). The CNC suspension (~0.01 wt. %) was ultrasonically dispersed for 10 min before being deposited on a mica substrate. The nanoparticle-loaded substrate was imaged in tapping mode with a Nanoscope IIIa microscope. The morphology of GO and CNC/GO nanohybrids was observed by transmission electronic microscopy (TEM) (JEOL, JEM 2100-Plus). Diluted GO and CNC/GO nanohybrid aqueous suspensions were submitted to a sonication treatment for 30 min to disperse the aggregates. The well-dispersed GO and CNC/GO nanohybrids were directly deposited on a copper grid for further TEM observation.

Zeta potential of CNC, neat GO and CNC/GO nanohybrid suspensions was quantified with Zetasizer Nano instrument (Nano ZS, Malvern). Fourier-transform infrared (FTIR)

spectroscopy spectra were recorded on a Nicolet 6700 spectrophotometer (USA) in the range 4000-600 cm^{-1} by the transmission method. KBr pellets were prepared by mixing and milling KBr and the sample (99: 1 wt%), then sintered under a pressure of 10 t/m^2 for 1 min. Both pure KBr and KBr pellets with the samples were dried in an oven (1 h, 105°C). For thermogravimetric analysis (TGA) (Perkin Elmer) a heating scan was performed from 25°C to 600°C using a heating rate of 10°C/min under nitrogen atmosphere. X-ray diffraction (XRD) analysis (Bruker, Germany) was carried out with Cu K α radiation ($\lambda = 0.154 \text{ nm}$). Voltage/intensity conditions were 40 kV/60 mA and the diffraction angle (2θ) was varied from 5 to 45° with a scan rate of 0.02°/s. For calculating the crystallinity index of the nanocrystals from XRD data the Segal method was implemented.³²

Scanning electron microscopy (SEM) observations were performed on a Quanta 200 FEI device (Everhart-Thornley detector) with an accelerating voltage of 1.0 kV. Coating of the sample with gold using a sputter coater was carried out before observing its cross-section. The electrical conductivity for all samples ($18 \times 6 \times 0.5 \text{ mm}^3$) was measured using a CYL-RM300 four-probe resistivity instrument (JANDEL, UK) with 2 mm distance between two copper electrodes. All the electrical resistivity measurements were performed five times at different positions on the sample to obtain accurate results. The mechanical properties of the composites were measured in tensile mode using a testing machine (Instron 5567, USA). The load cell had a 0.5 N capacity and the strain rate was 100 mm/min. The sample dimensions were $18 \times 6 \times 0.5 \text{ mm}^3$, and the results were averaged on five measurements.

3.3 Results and Discussion

The preparation strategy for NR/CNC/GO and NR/GO nanocomposites developed in this study is illustrated in Figure 3.1. The CNC suspension was stabilized by electrostatic repulsion interactions due to the partially charged sulfate ester groups introduced during the sulfuric acid hydrolysis step.³³ However, irreversible aggregation and poor dispersion of graphene oxide in water was observed, which are attributed to intermolecular $\pi - \pi$ stacking attractive forces.^{19,34} When GO and CNC suspensions were mixed uniformly under magnetic stirring and sonication, amphiphilic CNCs self-assembled onto the surface of GO nanosheets to form a well-dispersed CNC/GO nanohybrid. It can be attributed to enhanced stability of the CNC/GO nanohybrids,

which results from expected hydrogen bonding interaction between hydroxyl groups from CNC surface and oxygen-containing groups borne by GO. Then, the CNC/GO nanohybrids were mixed with the NR latex under magnetic stirring and the mixture was finally cast and evaporated to obtain solid nanocomposite films. The CNC/GO self-assembled nanohybrids can disperse in a controlled manner in the space formed between NR latex microspheres, which lead to the formation of NR/CNC/GO nanocomposites with a 3D hierarchical conducting network structure.

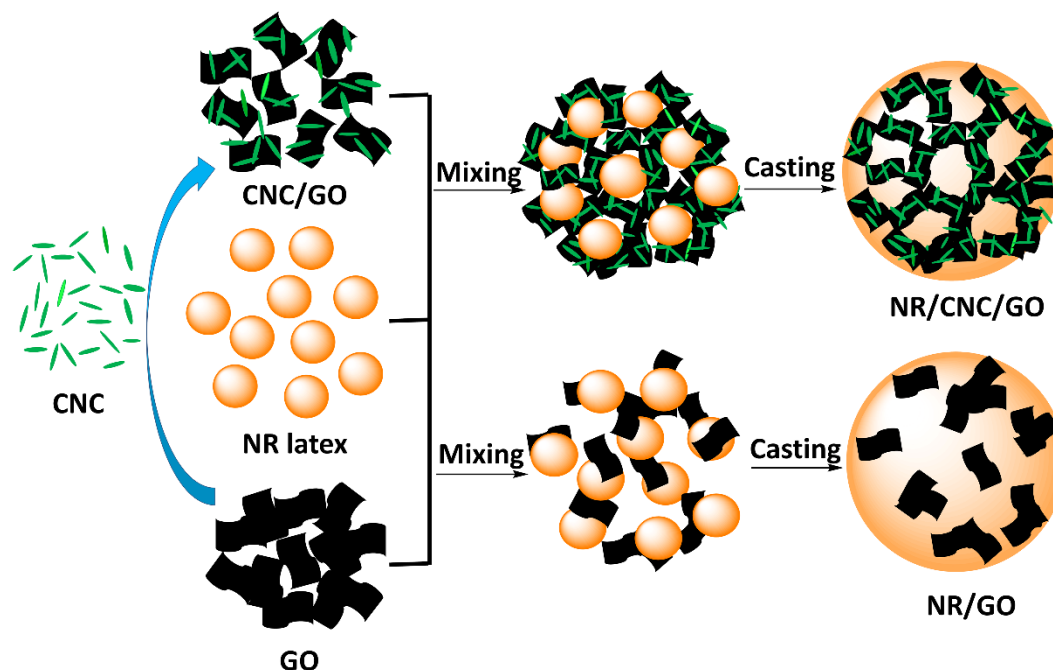


Figure 3.1 Schematic illustration for the preparation of NR/CNC/GO and NR/GO nanocomposites with 3D conductive network.

3.3.1 Morphology and Thermal Stability

The morphology and dimensions of CNC were characterized by AFM at different observation scales. As shown in Figure 3.2A,B, the CNC exhibits a typical rod-like morphology with nanoparticles 100-300 nm long and 10-20 nm wide. Electrostatic repulsion interactions among the nanoparticles promoted the dispersion of CNC in the aqueous suspension and well-individualized nanoparticles are observed.³⁵ The sheet-like morphology of GO was observed by TEM observation (Figure 3.2C). When comparing the aspect of GO nanosheets in CNC/GO nanohybrids (Figure 3.2D) with the aspect of neat GO (Figure 3.2C), weaker dispersion and stronger aggregation is observed for the latter. Figure 3.2 D illustrates that the added CNC self-assembled on the GO layers exhibiting a veined CNC/GO structure. This is an indication that CNC

can act as a stabilizer for GO, enhancing its stabilization in water and preventing aggregation between the graphene layers. It conditions a good dispersion of the CNC/GO nanohybrids prone to form a 3D continuous conductive network. The crystalline structure and thermal stability of CNC were characterized by XRD analysis and TGA, respectively, and the results are shown in Figure 3.3. The XRD spectrum reveals the typical cellulose I crystalline features with diffraction peaks located at $2\theta = 14.7^\circ$, 16.4° , 22.6° and 34.4° , ascribed to the planes of $1\bar{1}0$, 110 , 002 and 040 , respectively. The crystallinity index was 85.9 wt %.

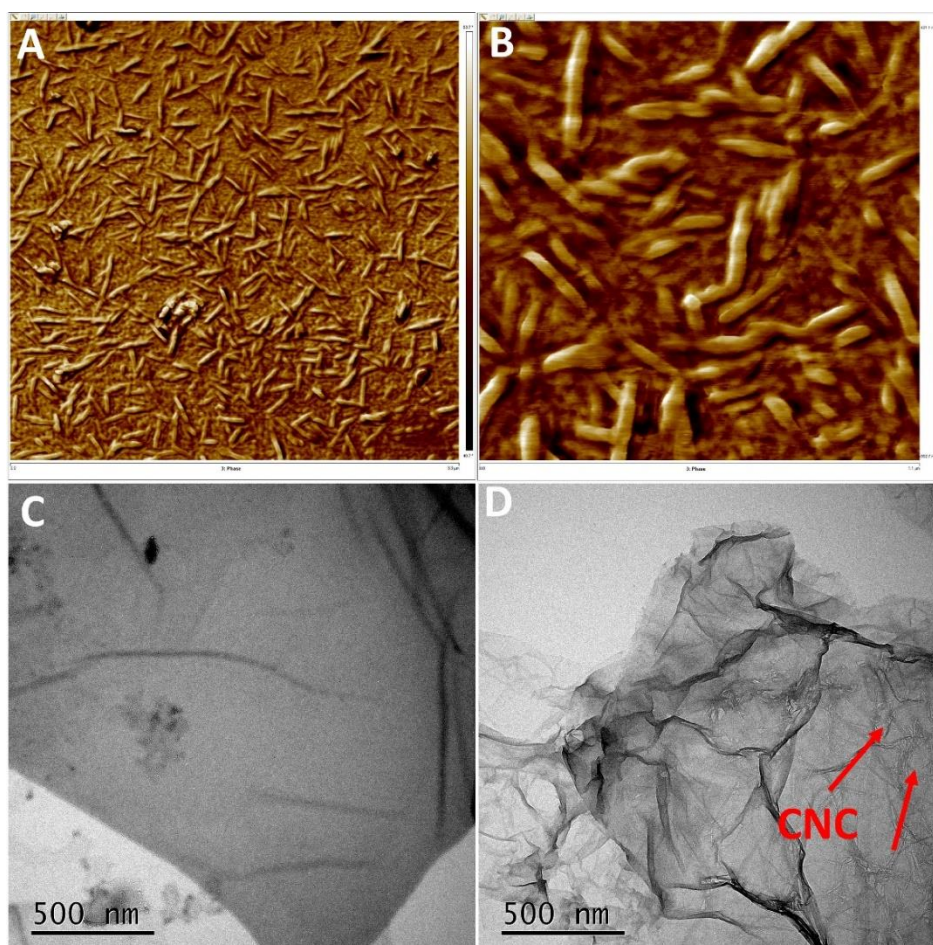


Figure 3.2 AFM images for CNC (A, B) at different observation scales (images A: $3.3 \times 3.3 \mu\text{m}$; image B: $1.1 \times 1.1 \mu\text{m}$); TEM images for GO (C) and CNC/GO nanohybrids (D).

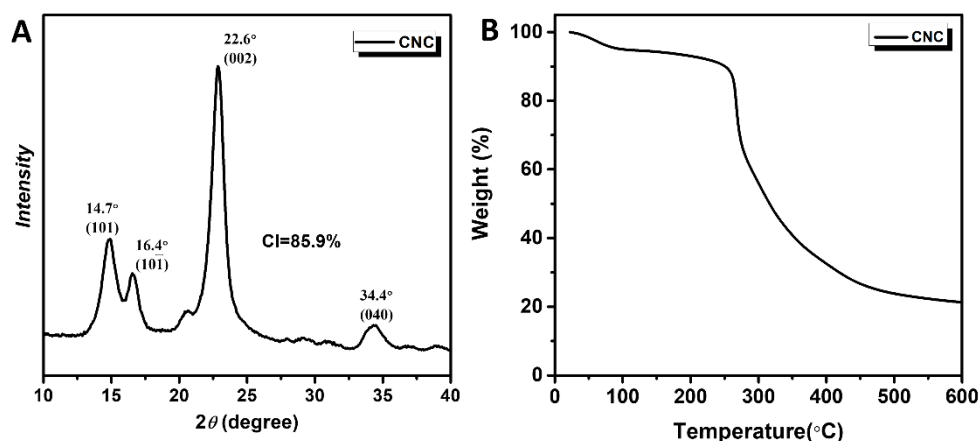


Figure 3.3 XRD spectrum (A) and TGA thermogram (B) for CNC.

3.3.2 Zeta potential

Zeta (ξ) potential is a crucial parameter to evaluate the stability of nanoparticles suspended in a liquid medium. A high Zeta potential in absolute value is an indication of a good dispersibility of the suspension. Typically, a suspension with a ξ potential absolute value higher than 30 mV is solely stabilized by electrostatic repulsions.^{36,37} Figure 3.4A shows the Zeta potential values for CNC, GO and CNC/GO nanohybrid suspensions. The aspect of the suspensions before and after standing for 24 h, which can be correlated with their Zeta potential value, is also reported in Figure 3.4B,C. The Zeta potential for the CNC suspension was -49.3 mV and it exhibited excellent stability even after standing for 24 h. The Zeta-potential for neat GO aqueous suspension was -6.3 mV. The GO nanosheets can therefore easily aggregate resulting in their precipitation to the bottom of the flask, leaving a transparent solution on top. When adding CNC to the GO dispersion, the Zeta potential of the CNC/GO nanohybrid suspension was -44.7 mV and a well-dispersed suspension was observed even after standing for 24 h. These results clearly demonstrated that CNC can effectively stabilize the GO suspension.

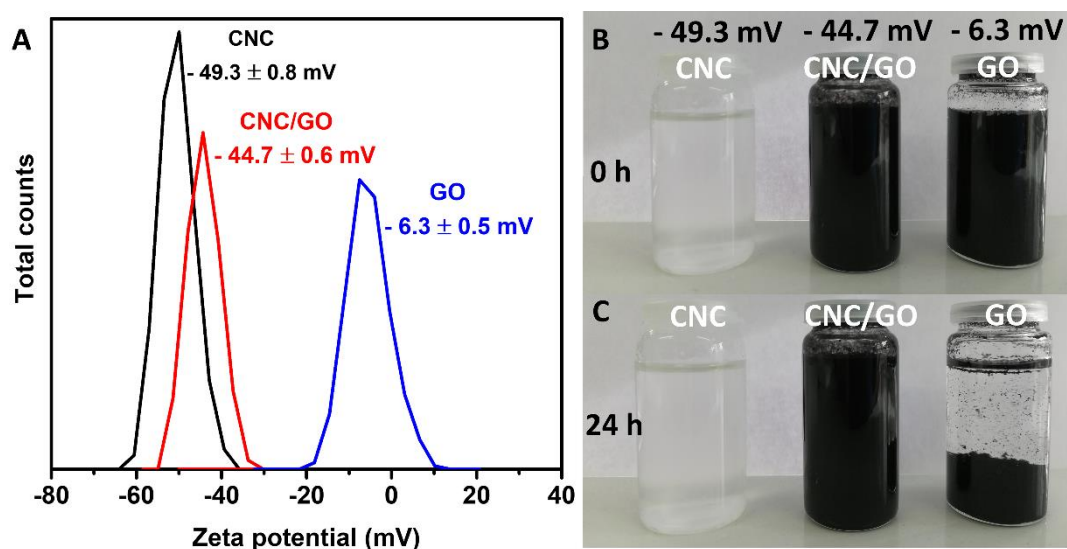


Figure 3.4 Zeta potential value (A) and digital camera images for CNC, GO and CNC/GO nanohybrid suspension before (B) and after (C) standing for 24 h.

3.3.3 FTIR spectra

Figure 3.5 presents the FTIR spectra for CNC, GO and CNC/GO nanohybrids. The FTIR spectrum corresponding to CNC shows peaks at 2910 and 1365 cm^{-1} , which can be assigned to C-H stretching and bending vibrations, respectively. The broad band at 3358 cm^{-1} is associated with OH bonds from hydroxyl groups. The band at 1645 cm^{-1} is representative of the H-O-H bending of absorbed water.^{38,39} The strong bands at 1058 - 1160 cm^{-1} are attributed to the C-O-C pyranose ring skeletal vibration.⁴⁰ For the GO spectrum, the band at 3445 corresponds to the stretching of OH bonds from hydroxyl groups. The band at 1716 cm^{-1} is associated to the C=O carbonyl stretching.⁴¹⁻⁴³ For the CNC/GO hybrids, the magnitude of the band at 3332 cm^{-1} drastically decreased, and it shifted to lower wavenumbers compared to CNC (3358 cm^{-1}) and GO (3445 cm^{-1}). These results confirmed that strong interfacial interactions occurred in the CNC/GO hybrids.³⁷ It can be ascribed to hydrogen bonding interaction between the hydroxyl surface groups from CNC and oxygen-containing groups borne by GO.⁴⁴

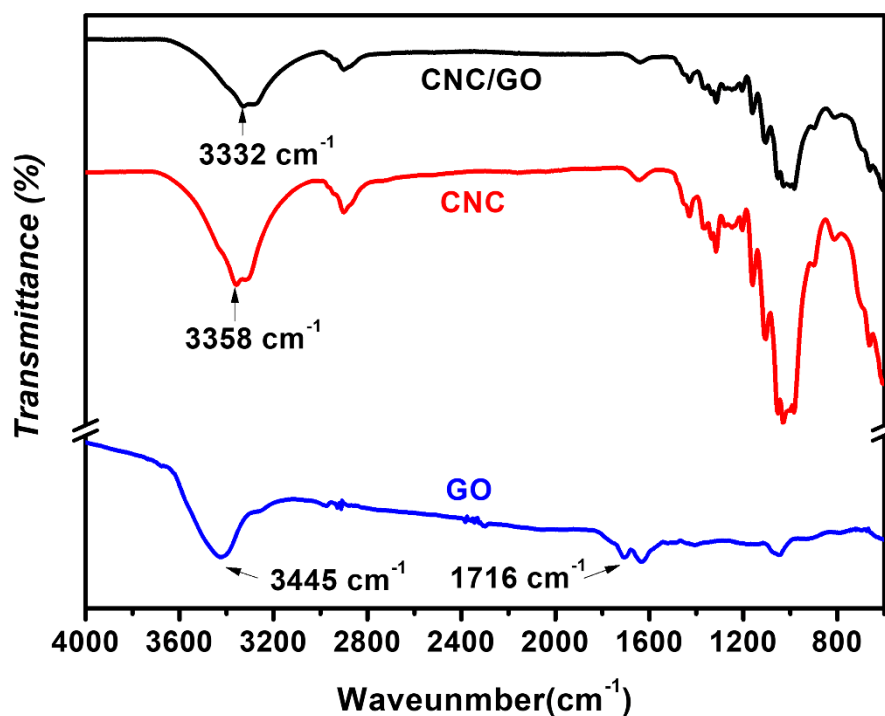


Figure 3.5 FTIR spectra for pristine CNC, neat GO and CNC/GO nanohybrids.

3.3.4 SEM

In order to observe and verify the hypothesis of the formation of a 3D conductive structure induced by the CNC/GO nanohybrids within the NR matrix, the surface of the fractured NR/CNC/GO nanocomposite films was characterized by SEM, as shown in Figure 3.6. The uniform porous network skeleton existed in the NR/CNC/GO-4 nanocomposite containing 4 wt% GO (Figure 3.6C), suggesting that the 3D network structure was formed during the casting process. As a comparison, the morphology of pure NR and NR/GO-4 nanocomposite films were also characterized (Figure 3.6A,B). Obviously, neat NR exhibits a smooth fracture surface. For the NR/GO-4 nanocomposite, the aggregated GO nanosheets are clearly observed. These observations demonstrate that the observed uniform porous network can be properly attributed to the well-dispersed CNC/GO nanohybrids within the NR matrix. The selective localization of the nanohybrid material between the NR microspheres results from the excluded volume that they create. The formation of this 3D network structure is expected to condition and hopefully improve both the electrical conductivity and mechanical properties of NR/CNC/GO nanocomposites.

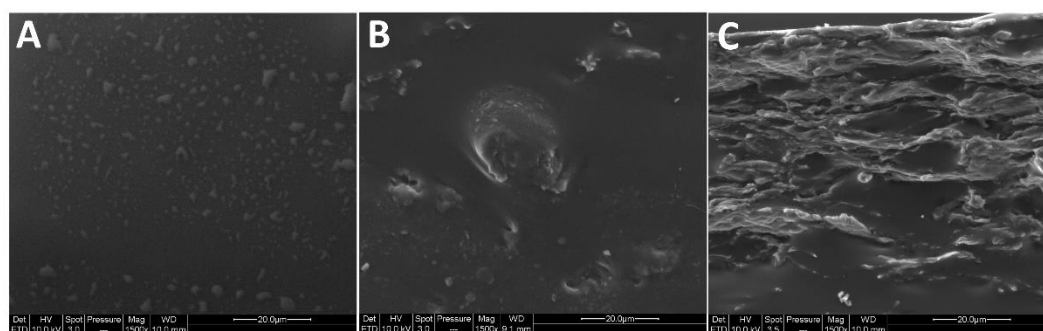


Figure 3.6 SEM images from the fractured surface for neat NR (A), NR/GO-4 nanocomposite (B) and NR/CNC/GO-4 nanocomposite (C).

3.3.5 Electrical Conductivity

The value of the electrical conductivity for NR/GO and NR/CNC/GO nanocomposites according to their GO content is shown in Figure 3.7. NR/CNC/GO nanocomposites exhibit a much higher electrical conductivity compared to NR/GO nanocomposites, regardless of the GO content. Moreover, for a critical content of conductive charge, a transition from an insulator to a conductor state is observed, which corresponds to the well-known electrical percolation threshold. This electrical percolation threshold is much lower for NR/CNC/GO nanocomposites (1.8 wt%) compared to NR/GO nanocomposites (5.6 wt%). It is approximately 3-fold lower for the formers. The value of the electrical conductivity for the NR/CNC/GO-4 nanocomposite (the material composed of 5 wt% CNC and 4 wt% GO) was 3.24×10^{-4} S/m. It is 9 orders of magnitude higher than that for the NR/GO-4 nanocomposite (3.15×10^{-13} S/m) (the CNC-free material load with 4 wt% GO). This improvement in electrical conductivity can be attributed to the CNC/GO self-assembly and to the formation of the 3D conductive structure within the NR matrix.

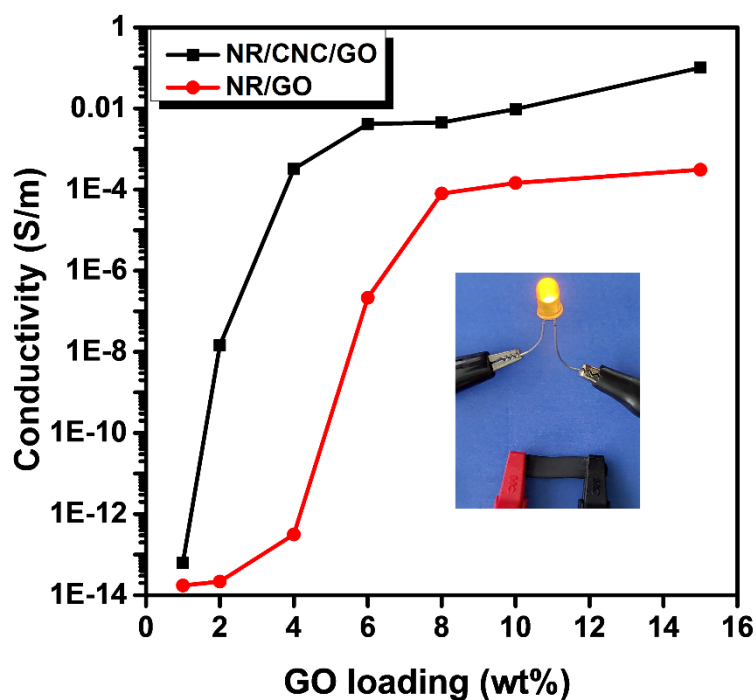


Figure 3.7 Evolution of the electrical conductivity for NR/GO and NR/CNC/GO nanocomposites as a function of GO content.

3.3.6 Mechanical property

Figure 3.8A presents the stress-strain curves for pure NR, NR/GO and NR/CNC/GO nanocomposites. Data collected from these stress-strain curves are plotted in Figure 3.8B-D, for the tensile strength, Young's modulus and elongation at break, respectively as a function of the GO content. Both the strength and Young's modulus significantly increase by increasing the nanoparticle content, while the elongation at break decreases. Compared to NR/GO samples, NR/CNC/GO samples exhibit significantly higher tensile strength and Young's modulus values. The tensile strength for NR/CNC/GO-10 (3.21 MPa) was increased by 646% compared to neat NR (0.43 MPa), while the tensile strength for NR/GO-10 (1.07 MPa) was increased by 149% (Figure 3.8B). Meanwhile, the Young's modulus (Figure 3.8C) for NR/CNC/GO-10 was 10.65 MPa, which is 21.7 times higher than that for neat NR (0.49 MPa) and 8.8 times higher compared to NR/GO-10 (1.21 MPa). However, when comparing NR/GO and NR/CNC/GO materials with neat NR, a decrease in the elongation at break is observed, which is a typical phenomenon for filled composites. The results demonstrate that the 3D hierarchical conductive network consisting of CNC and GO plays a crucial role in effectively reducing the electrical percolation threshold and enhancing at the same time the structural stability of the composite.

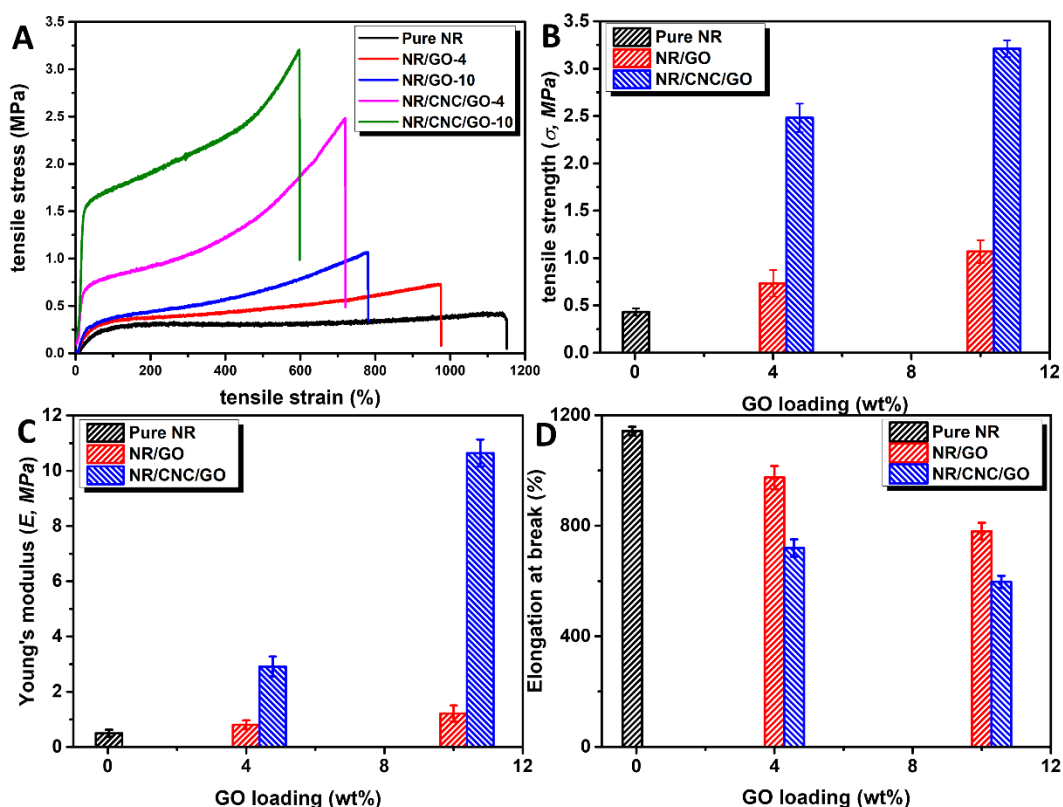


Figure 3.8 Stress-strain curves (A), tensile strength (B), Young's modulus (C) and elongation at break (D) for neat NR, NR/GO nanocomposites and NR/CNC/GO nanocomposites (the error bars are standard deviation).

3.4 Conclusions

In this work, we report a simple, effective, easily implementable and environmentally friendly water-based approach for preparing NR/CNC/GO nanocomposites. This approach is based on the formation of a 3D hierarchical conductive network structure through CNC-assisted self-assembly of graphene oxide in NR latex. The formation of this conductive network structure significantly enhanced the electrical conductivity and lowers the electrical percolation threshold of the composites. The electrical conductivity percolation threshold for NR/CNC/GO nanocomposites was 3-fold lower than that of NR/GO nanocomposites. Moreover, the electrical conductivity for NR/CNC/GO-4 nanocomposite (sample with 4 wt% GO) was 9 orders of magnitude higher than that of NR/GO-4 nanocomposite (CNC-free sample with 4 wt% GO). CNC played a critical role in assisting the formation of a 3D assembled conductive structure and enhancing the structure robustness as a rigid template as shown by the improvement in the tensile strength and Young's modulus. This unique combination of high electrical conductivity and mechanical properties makes the developed NR/CNC/GO

nanocomposites strong candidates for applications in stretchable electronics, wearable sensors and energy storage.

3.5 References

- (1) Shin, M. K.; Oh, J.; Lima, M.; Kozlov, M. E.; Kim, S. J.; Baughman, R. H. Elastomeric Conductive Composites Based on Carbon Nanotube Forests. *Advanced materials* **2010**, *22* (24), 2663–2667.
- (2) Ma, P.-C.; Liu, M.-Y.; Zhang, H.; Wang, S.-Q.; Wang, R.; Wang, K.; Wong, Y.-K.; Tang, B.-Z.; Hong, S.-H.; Paik, K.-W. Enhanced Electrical Conductivity of Nanocomposites Containing Hybrid Fillers of Carbon Nanotubes and Carbon Black. *ACS applied materials & interfaces* **2009**, *1* (5), 1090–1096.
- (3) Maiti, S.; Shrivastava, N. K.; Suin, S.; Khatua, B. B. Polystyrene/MWCNT/Graphite Nanoplate Nanocomposites: Efficient Electromagnetic Interference Shielding Material through Graphite Nanoplate–MWCNT–Graphite Nanoplate Networking. *ACS applied materials & interfaces* **2013**, *5* (11), 4712–4724.
- (4) Mahendia, S.; Tomar, A. K.; Kumar, S. Electrical Conductivity and Dielectric Spectroscopic Studies of PVA–Ag Nanocomposite Films. *Journal of Alloys and Compounds* **2010**, *508* (2), 406–411.
- (5) Chen, D.; Miao, Y.-E.; Liu, T. Electrically Conductive Polyaniline/Polyimide Nanofiber Membranes Prepared via a Combination of Electrospinning and Subsequent in Situ Polymerization Growth. *ACS applied materials & interfaces* **2013**, *5* (4), 1206–1212.
- (6) Romo-Urbe, A.; Arizmendi, L.; Romero-Guzmán, M. E.; Sepulveda-Guzmán, S.; Cruz-Silva, R. Electrospun Nylon Nanofibers as Effective Reinforcement to Polyaniline Membranes. *ACS applied materials & interfaces* **2009**, *1* (11), 2502–2508.
- (7) Silva, M. J.; Sanches, A. O.; Medeiros, E. S.; Mattoso, L. H. C.; McMahan, C. M.; Malmonge, J. A. Nanocomposites of Natural Rubber and Polyaniline-Modified Cellulose Nanofibrils. *Journal of Thermal Analysis and Calorimetry* **2014**, *117* (1), 387–392.
- (8) Tkalya, E.; Ghislandi, M.; Thielemans, W.; van der Schoot, P.; de With, G.; Koning, C. Cellulose Nanowhiskers Templating in Conductive Polymer

- Nanocomposites Reduces Electrical Percolation Threshold 5-Fold. *ACS Macro Letters* **2013**, 2 (2), 157–163.
- (9) Zhang, X.; He, Q.; Gu, H.; Colorado, H. A.; Wei, S.; Guo, Z. Flame-Retardant Electrical Conductive Nanopolymers Based on Bisphenol F Epoxy Resin Reinforced with Nano Polyanilines. *ACS applied materials & interfaces* **2013**, 5 (3), 898–910.
- (10) Shi, Z.; Zang, S.; Jiang, F.; Huang, L.; Lu, D.; Ma, Y.; Yang, G. In Situ Nano-Assembly of Bacterial Cellulose–Polyaniline Composites. *Rsc Advances* **2012**, 2 (3), 1040–1046.
- (11) Liao, K.-H.; Qian, Y.; Macosko, C. W. Ultralow Percolation Graphene/Polyurethane Acrylate Nanocomposites. *Polymer* **2012**, 53 (17), 3756–3761.
- (12) Mao, C.; Zhu, Y.; Jiang, W. Design of Electrical Conductive Composites: Tuning the Morphology to Improve the Electrical Properties of Graphene Filled Immiscible Polymer Blends. *ACS applied materials & interfaces* **2012**, 4 (10), 5281–5286.
- (13) Qi, X.-Y.; Yan, D.; Jiang, Z.; Cao, Y.-K.; Yu, Z.-Z.; Yavari, F.; Koratkar, N. Enhanced Electrical Conductivity in Polystyrene Nanocomposites at Ultra-Low Graphene Content. *ACS applied materials & interfaces* **2011**, 3 (8), 3130–3133.
- (14) Etika, K. C.; Liu, L.; Hess, L. A.; Grunlan, J. C. The Influence of Synergistic Stabilization of Carbon Black and Clay on the Electrical and Mechanical Properties of Epoxy Composites. *Carbon* **2009**, 47 (13), 3128–3136.
- (15) Liu, L.; Grunlan, J. C. Clay Assisted Dispersion of Carbon Nanotubes in Conductive Epoxy Nanocomposites. *Advanced Functional Materials* **2007**, 17 (14), 2343–2348.
- (16) Geim, A. K.; Novoselov, K. S. The Rise of Graphene, *Nature Materials*, 6. **2007**.
- (17) Lee, C.; Wei, X.; Kysar, J. W.; Hone, J. Measurement of the Elastic Properties and Intrinsic Strength of Monolayer Graphene. *science* **2008**, 321 (5887), 385–388.
- (18) Naeimi, H.; Golestanzadeh, M. Highly Sulfonated Graphene and Graphene Oxide Nanosheets as Heterogeneous Nanocatalysts in Green Synthesis of Bisphenolic Antioxidants under Solvent Free Conditions. *RSC Advances* **2014**, 4 (99), 56475–56488.

- (19) Li, D.; Müller, M. B.; Gilje, S.; Kaner, R. B.; Wallace, G. G. Processable Aqueous Dispersions of Graphene Nanosheets. *Nature nanotechnology* **2008**, *3* (2), 101–105.
- (20) Huang, X.; Qi, X.; Boey, F.; Zhang, H. Graphene-Based Composites. *Chemical Society Reviews* **2012**, *41* (2), 666–686.
- (21) Kuilla, T.; Bhadra, S.; Yao, D.; Kim, N. H.; Bose, S.; Lee, J. H. Recent Advances in Graphene Based Polymer Composites. *Progress in polymer science* **2010**, *35* (11), 1350–1375.
- (22) Wang, M.; Duan, X.; Xu, Y.; Duan, X. Functional Three-Dimensional Graphene/Polymer Composites. *ACS nano* **2016**, *10* (8), 7231–7247.
- (23) Wu, X.; Lu, C.; Xu, H.; Zhang, X.; Zhou, Z. Biotemplate Synthesis of Polyaniline@ Cellulose Nanowhiskers/Natural Rubber Nanocomposites with 3D Hierarchical Multiscale Structure and Improved Electrical Conductivity. *ACS applied materials & interfaces* **2014**, *6* (23), 21078–21085.
- (24) Zhang, X.; Wu, X.; Lu, C.; Zhou, Z. Dialysis-Free and in Situ Doping Synthesis of Polypyrrole@ Cellulose Nanowhiskers Nanohybrid for Preparation of Conductive Nanocomposites with Enhanced Properties. *ACS Sustainable Chemistry & Engineering* **2015**, *3* (4), 675–682.
- (25) Cao, J.; Zhang, X.; Wu, X.; Wang, S.; Lu, C. Cellulose Nanocrystals Mediated Assembly of Graphene in Rubber Composites for Chemical Sensing Applications. *Carbohydrate Polymers* **2015**, *140*. <https://doi.org/10.1016/j.carbpol.2015.12.042>.
- (26) Potts, J. R.; Shankar, O.; Du, L.; Ruoff, R. S. Processing–Morphology–Property Relationships and Composite Theory Analysis of Reduced Graphene Oxide/Natural Rubber Nanocomposites. *Macromolecules* **2012**, *45* (15), 6045–6055.
- (27) Scherillo, G.; Lavorgna, M.; Buonocore, G. G.; Zhan, Y. H.; Xia, H. S.; Mensitieri, G.; Ambrosio, L. Tailoring Assembly of Reduced Graphene Oxide Nanosheets to Control Gas Barrier Properties of Natural Rubber Nanocomposites. *ACS applied materials & interfaces* **2014**, *6* (4), 2230–2234.
- (28) Tian, M.; Ma, Q.; Li, X.; Zhang, L.; Nishi, T.; Ning, N. High Performance Dielectric Composites by Latex Compounding of Graphene Oxide-Encapsulated Carbon Nanosphere Hybrids with XNBR. *Journal of Materials Chemistry A* **2014**, *2* (29), 11144–11154.

- (29) Yan, D.-X.; Pang, H.; Li, B.; Vajtai, R.; Xu, L.; Ren, P.-G.; Wang, J.-H.; Li, Z.-M. Structured Reduced Graphene Oxide/Polymer Composites for Ultra-efficient Electromagnetic Interference Shielding. *Advanced Functional Materials* **2015**, 25 (4), 559–566.
- (30) Yoonessi, M.; Gaier, J. R. Highly Conductive Multifunctional Graphene Polycarbonate Nanocomposites. *Acs Nano* **2010**, 4 (12), 7211–7220.
- (31) Zhu, G.; Chen, Z.; Wu, B.; Lin, N. Dual-Enhancement Effect of Electrostatic Adsorption and Chemical Crosslinking for Nanocellulose-Based Aerogels. *Industrial Crops and Products* **2019**, 139, 111580.
- (32) Zhu, G.; Dufresne, A.; Lin, N. Humidity-Sensitive and Conductive Nanopapers from Plant-Derived Proteins with a Synergistic Effect of Platelet-like Starch Nanocrystals and Sheet-like Graphene. *ACS Sustainable Chemistry & Engineering* **2017**, 5 (10), 9431–9440.
- (33) Wu, X.; Lu, C.; Zhang, W.; Yuan, G.; Xiong, R.; Zhang, X. A Novel Reagentless Approach for Synthesizing Cellulose Nanocrystal-Supported Palladium Nanoparticles with Enhanced Catalytic Performance. *Journal of Materials Chemistry A* **2013**, 1 (30), 8645–8652.
- (34) Peng, Z.; Feng, C.; Luo, Y.; Li, Y.; Kong, L. X. Self-Assembled Natural Rubber/Multi-Walled Carbon Nanotube Composites Using Latex Compounding Techniques. *Carbon* **2010**, 48 (15), 4497–4503.
- (35) Araki, J. Electrostatic or Steric?—Preparations and Characterizations of Well-Dispersed Systems Containing Rod-like Nanowhiskers of Crystalline Polysaccharides. *Soft Matter* **2013**, 9 (16), 4125–4141.
- (36) Cabuk, M.; Alan, Y.; Yavuz, M.; Unal, H. I. Synthesis, Characterization and Antimicrobial Activity of Biodegradable Conducting Polypyrrole-Graft-Chitosan Copolymer. *Applied Surface Science* **2014**, 318, 168–175.
- (37) Du, W.-L.; Niu, S.-S.; Xu, Y.-L.; Xu, Z.-R.; Fan, C.-L. Antibacterial Activity of Chitosan Tripolyphosphate Nanoparticles Loaded with Various Metal Ions. *Carbohydrate polymers* **2009**, 75 (3), 385–389.
- (38) El Miri, N.; Abdelouahdi, K.; Barakat, A.; Zahouily, M.; Fihri, A.; Solhy, A.; El Achaby, M. Bio-Nanocomposite Films Reinforced with Cellulose Nanocrystals: Rheology of Film-Forming Solutions, Transparency, Water Vapor Barrier and Tensile Properties of Films. *Carbohydrate Polymers* **2015**, 129, 156–167.

- (39) Valentini, L.; Cardinali, M.; Fortunati, E.; Torre, L.; Kenny, J. M. A Novel Method to Prepare Conductive Nanocrystalline Cellulose/Graphene Oxide Composite Films. *Materials Letters* **2013**, *105*, 4–7.
- (40) Hu, W.; Liu, S.; Chen, S.; Wang, H. Preparation and Properties of Photochromic Bacterial Cellulose Nanofibrous Membranes. *Cellulose* **2011**, *18* (3), 655–661.
- (41) El Achaby, M.; Essamlali, Y.; El Miri, N.; Snik, A.; Abdelouahdi, K.; Fihri, A.; Zahouily, M.; Solhy, A. Graphene Oxide Reinforced Chitosan/Polyvinylpyrrolidone Polymer Bio-nanocomposites. *Journal of Applied Polymer Science* **2014**, *131* (22).
- (42) El Achaby, M.; Arrakhiz, F. Z.; Vaudreuil, S.; Essassi, E. M.; Qaiss, A. Piezoelectric β -Polymorph Formation and Properties Enhancement in Graphene Oxide–PVDF Nanocomposite Films. *Applied Surface Science* **2012**, *258* (19), 7668–7677.
- (43) El Achaby, M.; Arrakhiz, F.-E.; Vaudreuil, S.; el Kacem Qaiss, A.; Bousmina, M.; Fassi-Fehri, O. Mechanical, Thermal, and Rheological Properties of Graphene-based Polypropylene Nanocomposites Prepared by Melt Mixing. *Polymer composites* **2012**, *33* (5), 733–744.
- (44) El Miri, N.; El Achaby, M.; Fihri, A.; Larzek, M.; Zahouily, M.; Abdelouahdi, K.; Barakat, A.; Solhy, A. Synergistic Effect of Cellulose Nanocrystals/Graphene Oxide Nanosheets as Functional Hybrid Nanofiller for Enhancing Properties of PVA Nanocomposites. *Carbohydrate polymers* **2016**, *137*, 239–248.

CHAPTER 4.

“Multifunctional Nanocellulose/Carbon Nanotubes Composite Aerogels for High-efficiency Electromagnetic Interference Shielding”

Table of contents – Chapter 4

Chapter 4. Multifunctional Nanocellulose/Carbon Nanotubes Composite Aerogels for High-efficiency Electromagnetic Interference Shielding	149
Abstract	149
Keywords	149
4.1 Introduction.....	150
4.2 Experimental Section	152
4.2.1 Materials	152
4.2.2 Chemical functionalization of CNC with GTMAC	152
4.2.3 Preparation of nanocellulose-CNTs composite aerogels	153
4.2.4 Nanocellulose chemical and morphological analysis	153
4.2.5 Nanocellulose-based aerogels characterization	154
4.3 Results and Discussion	156
4.3.1 Synthesis of cationic cellulose nanocrystals.....	156
4.3.2 Nanocellulose chemical and morphological analysis	157
4.3.3 Characterization of nanocellulose-CNT aerogels	162
4.3.4 Electrical conductivity	166
4.3.5 Mechanical properties	168
4.3.6. EMI shielding Performance	170
4.4 Conclusions.....	173
4.5 References.....	174

Chapter 4. Multifunctional Nanocellulose/Carbon Nanotubes Composite Aerogels for High-efficiency Electromagnetic Interference Shielding

Ge Zhu, [†] Laura Giraldo Isaza, [†] Bai Huang, ^{†§} Alain Dufresne ^{†*}

[†] University Grenoble Alpes, CNRS, Grenoble INP, LGP2, 38000, Grenoble, France

[§] School of Materials Science and Engineering, South China University of Technology, Wushan Road, Tianhe District, Guangzhou, Guangdong, 510640, P. R. China

Abstract

Biobased specialized components have emerged as a promising trend to limit the use of petroleum derivatives. Conversely, the current use of electronic systems has conditioned the emission of electromagnetic waves, which interfere with high-precision devices and harm human health. Thus, robust, ultralight, and conductive nanocellulose-based aerogels paired with carbon nanotubes appear as an electromagnetic interference (EMI) shielding biomaterial to reduce the dispersion of microwaves emitted or received from a device. This study proposes a reliable aerogel system to deflect radiation by integrating TEMPO-oxidized cellulose nanofibrils (TCNF), cationic cellulose nanocrystals (CCNC), and sodium alginate (SA), with carbon nanotubes (CNTs) at various concentrations. After inducing gelation, the aerogels were obtained by freeze drying. According to Zeta potential and FTIR analysis data of nanocellulose, the aerogel frame was induced by electrostatic attraction and hydrogen bonds between the cellulosic matrix and the nanofillers. Finally, lightweight (density < 0.075 g/cm³), highly porous (porosity > 95.47%), conductive (up to 26.2 S/m), mechanically resistant, and EMI protective aerogels were obtained, proving their potential to be used as green and lightweight shielding elements against electromagnetic radiation.

Keywords

Nanocellulose; Nanocellulose cationization; Aerogels; Carbon nanotubes; EMI shielding.

4.1 Introduction

Lignocellulosic biomass is a byproduct derived from the agriculture and forestry industries, characterized by its renewability, biodegradability, availability, and elevated generation.¹ Thereby, it is the most abundant organic resource worldwide, with a yield around 200 billion annually.² According to its great potential, accessibility, carbon-neutral character and versatility, biomass can be processed to generate green energy, chemicals, and materials within a biorefinery scheme,³ offsetting the use of fossil-based components. Biomass has a complex structure, composed of cellulose (33-51 wt%), enclosed in a compact frame formed by hemicellulose (19-34 wt%), and lignin (20-30 wt%).⁴ The composition of the heteromatrix differs according to the biomass source, though, cellulose is its major constituent, referred to as the most abundant natural polymer on Earth.⁵ In general, cellulose is the integral module of natural fibers, consisting of cellulose set into larger units, known as microfibrils.⁶ These are composed of a string of nano-sized cellulose fragments, nanocellulose. Hence, nanocellulose integrates the relevant features of native cellulose with high crystallinity, hydrophilicity, high specific surface area, thermal stability, and remarkable mechanical properties.⁷

Notably, the tendency of developing a material scheme based on renewable and organic sources restricts the reliability on petroleum derivatives and sets new perspectives regarding sustainable specialized applications.⁸ For instance, biosourced nanostructured components have evolved to improve the performance of a material with multifunctional properties and green attributes.⁸ Advancements in electronics information, communication networks, power systems, and biomedical devices,⁹ condition the propagation of magnetic and electronic fields. The diffusion of electromagnetic waves can lead to disruptions in high precision circuits by electromagnetic induction, coupling, or conduction.¹⁰ This can limit operative accuracy and cause malfunctioning of essential appliances, like communications, radars, military protection, navigation systems, hospital instruments, and energy transmission lines,¹¹ which also restricts the progress of the electronic industry.

Additionally, electromagnetic radiation has been presumably related; although not scientifically proven, to negative health effects, such as nervous system affectations in children,¹² headaches, anxiety, suicide and depression, nausea, fatigue, cataracts, and cancer.¹³ Thereupon, due to the harmful character of electromagnetic radiations, the introduction of electromagnetic interference (EMI) shielding materials in electronic

devices is decisive to minimize microwave release into the environment and its receptivity from other devices.¹¹ Thus, EMI shielding modules require a high porosity and elevated specific surface area to interact with radiation, while demonstrating a low density, cost-effective manufacture, and conformed by a non-conductive matrix receptive to be coupled with a conductive nanofiller.^{14,15}

Accordingly, nanocellulose-based elements have shown good results in dispersing electromagnetic radiation.^{16,17} However, their associated price, and technical factors concerning humidity sensitivity, shelf life, high density, mechanical performance, and thermal stability,¹⁶ limit further progress. Regarding this, nanocellulose aerogel; a porous ultralight solid, has been referred as a solution for EMI shielding, compiling with an ultralow density, high porosity, low cost of production, and adaptability for surface functionalization.^{5,18–20} As stated, nanocellulose-based aerogels provide an option for protection against EMI. Nevertheless, the composition of ultralight, robust, and conductive aerogels is restricted by the mechanical strength of nanocellulose, and its limited dispersibility to form a consistent structure.²¹ Consequently, conductive nanofillers can serve as a supporting frame.²² Their synergy with nanocellulose promotes a high electrical conductivity, improved mechanical performance, and interfacial polarization in electromagnetic fields,²¹ resulting in a higher EMI shielding capacity for aerogels. Carbon nanotubes (CNTs) are known for their strength, durability, electrical conductivity, thermal conductivity, and lightweight properties,²³ which have potentiated their prospect as a precursor for EMI shielding items. Then, the formation of percolative networks of nanocellulose paired with carbon nanotubes, is a new approach for conductive aerogels.²⁰ Within this perspective, the interaction forces between carbon nanotubes and nanocellulose are a relevant factor for the formation of aerogels, and they determine their conductivity and final EMI shielding capacity.^{20,24}

In this study, a coactive chemical modification of cellulose nanocrystals paired with physical ionic reinforcement of a nanocellulose matrix is proposed to enhance the formation of a cohesive cellulose frame. This work reveals effective CNC cationization to improve electrostatic interaction with anionic nanofibrils and complementary precursors to form a consistent cellulose substructure through simple but practical electrostatic interactions. Then, CNT integration is promoted by electrostatic adhesion and H-bonding, which undergoes gelation and freeze-drying to form nanocellulose-CNTs aerogels. CNTs are introduced as a nanofiller, using their surface electrical

charge, to improve the EMI shielding potential of the aerogel structure. As part of the nanocellulose-CNTs aerogel formation process, the underlying interaction between nanocellulose and CNTs in the composite is investigated. Additionally, this effective coupling will be evaluated in aerogels in terms of a suitable conductive pathway in aerogels to promote an efficient EMI protection. This simple, effective, and environmentally friendly scheme produces aerogels with low density (density < 0.075 g/cm³), highly porous (porosity > 95.47%), conductive (up to 26.2 S/m), mechanically resistant that exhibit practical EMI shielding efficiency above 39.8 dB. This indicates that these aerogels can potentially be used as a lightweight, environmentally friendly EMI shielding material.

4.2 Experimental Section

4.2.1 Materials

Cellulose nanocrystal (CNC) (10.4 wt%) and TEMPO-oxidized cellulose nanofibril suspension (TCNF) (2.23 wt%) were purchased from The University of Maine. Sodium alginate (SA), glycidyltrimethylammonium chloride (GTMAC), and multiwall carbon nanotubes (CNTs) were supplied by Sigma Aldrich, and sodium hydroxide (NaOH, 98%) was provided by Carl Roth, all used without any treatment. Unless otherwise stated, all other reagents were of analytical grade and used directly as received without further purification.

4.2.2 Chemical functionalization of CNC with GTMAC

Cationization of H₂SO₄-hydrolyzed CNC was induced by GTMAC; employing NaOH as a catalyst, with a protocol adjusted from Rol et al.²⁵ and Saini et al.²⁶ Initially, CNC was activated with NaOH solution (5 wt%) at 65°C during 30 min. Afterwards, 4 mol/mol AGU of GTMAC were added dropwise, with the reaction lasting 6 h at 65°C under mechanical stirring. The composition was precipitated in 95% ethanol and centrifuged at 10,000 rpm for 15 min to remove free GTMAC. Finally, cationic CNC (CCNC) was dialyzed against distilled water for 5 days. The obtained CCNC suspension was taken to freeze drying (Christ & Alpha, 2-4 LSCplus) for two days to obtain CCNC powder.

4.2.3 Preparation of nanocellulose-CNTs composite aerogels

For nanocellulose aerogels, the anionic TCNF suspension was added into the cationic CCNC suspension under magnetic stirring for 1 h. To stabilize the nanoparticles, the desired amount of sodium alginate (SA) solution was slowly added into the composite suspension under magnetic stirring for 1 h to achieve a stable dispersion. Due to the opposite charges of TCNF and CCNC suspensions, the direct complexation of TCNF with CCNC leads to flocculation and sedimentation, so the introduction of sodium alginate greatly improves the dispersion and stability of the suspension.²⁷ According to our previous study, the weight ratios and compositions of the TCNF/CCNC/SA suspension was controlled as 4: 4: 2 (w/w/w).

For nanocellulose-CNTs aerogels, in order to stabilize the CNT nanoparticles, a 2.23 wt% aqueous TCNF suspension was magnetically combined with CNTs powder to get a stable TCNF/CNTs suspension in a 3:7 (w/w) ratio. Then the aerogels were prepared from stable CCNC, SA, and TCNF/CNTs suspension following the same steps as described above. The aerogel suspension was formed by electrostatic adsorption between the desired amount of anionic TCNF/CNTs suspension and cationic CCNC suspension, then adding anionic SA to strengthen the interaction under magnetic stirring. Finally, the composite suspension was poured into cylindrical molds and frozen overnight. To conclude, the molds were taken to freeze drying at $-60\text{ }^{\circ}\text{C}$ and 0.098 atm (Christ & Alpha, 2-4 LSCplus) for three days. In the nanocellulose-CNTs aerogel, the relative mass fraction of TCNF/CCNC/SA remained constant (4/4/2, w/w/w) with a varying CNT content of 0, 2, 5, 10, 15, 20 and 30 wt%, which was based on the total solid content. In agreement with previous reports, the densities of the different components ρ_{TCNF} , ρ_{CCNC} , ρ_{SA} and ρ_{CNT} are assumed to be equal to , 1.46 g/cm³,²⁸ 1.54 g/cm³,²⁹ 1.64 g/cm³,²⁹ and 2.1 g/cm³,³⁰ respectively. The CNT weight contents were converted to volume contents using the density of CNT and nanocellulose. The CNT volume contents were calculated to be 0, 0.08, 0.22, 0.44, 0.68, 0.89 and 1.20 vol%, coded as CA, CA-0.08, CA-0.22, CA-0.44, CA-0.68, CA-0.89 and CA-1.20 vol%, respectively.

4.2.4 Nanocellulose chemical and morphological analysis

Nanocellulose analysis was conducted for CNC, CCNC and TCNF. The modification process related to the presence specific functional groups on nanocellulose was

identified by Fourier-transform infrared spectroscopy (FTIR). The spectra were recorded on a Spectrum 65 FT-IR instrument (PerkinElmer), in the range of 4000-400 cm^{-1} .

Solid-state NMR analysis was carried out to characterize the surface cationic CCNC through a Bruker AVANCE 400 NMR spectrometer at 12 000 Hz spinning speed by a 4 mm CP-MAS probe. Elemental analysis (EA) was used to track the nitrogen (N %) element of cationic CCNC through elemental analyzer (Elemental Analysis system, GmbH).

The surface charge of nanocellulose samples allows to define the subsequent electrostatic interactions. Zeta potential was quantified with a Zetasizer Pro device (Malvern Panalytical), using a DTS1070 cell, with water as dispersant, and setting 3 measuring rounds with no intermediate pause.

For thermogravimetric analysis (TGA), a heating scan was performed from 25 °C to 600 °C at a heating rate of 10 °C/min, under N₂ atmosphere using a Mettler Toledo TGA/DSC 3+ star instrument.

The crystalline properties were analyzed by X-ray diffraction (XRD), carried out with a D8 Advance X-ray Bruker diffractometer, with Cu K α radiation (λ : 0.154 nm). The voltage and intensity conditions were 40 kV and 60 mA, respectively, and the diffraction angle (2θ) was varied between 5° and 40° at a rate of 0.02°/sec. In line with the Segal height peak method, the crystallinity index of nanocellulose samples can be calculated by **Equation 1**.³¹ Specifically, I_{am} is the intensity of the valley located at $2\theta \approx 20^\circ$, and I_{002} is the maximum intensity of the main crystalline peak of cellulose I located at $2\theta \approx 22.6^\circ$.

$$CI = \left(1 - \frac{I_{am}}{I_{002}}\right) \times 100 \quad (1)$$

4.2.5 Nanocellulose-based aerogels characterization

The specific surface area and pore characteristics of the aerogels were determined by Brunauer-Emmett-Teller method using nitrogen adsorption-desorption Micrometrics TriStar II 3020 apparatus.

The apparent density (ρ_a), skeletal density (ρ_s), and porosity (p) were estimated based on the aerogel weight and dimensions, according to Equation 2-4, respectively.

$$\rho_a = \frac{m}{\pi r^2 h} \quad (2)$$

$$\rho_s = \frac{1}{\frac{w_{TCNF}}{\rho_{TCNF}} + \frac{w_{CCNC}}{\rho_{CCNC}} + \frac{w_{SA}}{\rho_{SA}} + \frac{w_{CNTs}}{\rho_{CNTs}}} \quad (3)$$

$$p(\%) = 1 - \frac{\rho_a}{\rho_s} \quad (4)$$

Where m , h , and r are the mass, height, and radius of the composite aerogels, respectively, considering their cylindrical shape. Moreover, w_{TCNF} , w_{CCNC} , w_{SA} and w_{CNTs} are the weight fractions of TCNF, CCNC, SA and CNT components in the aerogels, respectively.

The shrinkage of the aerogels was established after freeze-drying, using electronic caliper measurement. The volume reduction percentage (S (vol%)) was calculated using Equation 5.

$$S \text{ (vol\%)} = 1 - \frac{V_1}{V_2} \quad (5)$$

Where V_1 is the volume of the aerogel after the freeze-drying, and V_2 is the volume of the mold for preparing the aerogel.

To study the porosity topography and cross-sectional morphology of the aerogels, representative samples were frozen in liquid nitrogen and carefully sliced. They were then coated with gold using a sputter coater and observed by Scanning Electron Microscopy (SEM), employing a FEI ESEM Quanta 200 microscope at 1.0 kV voltage.

Compression tests were performed to evaluate the mechanical properties of aerogels, and thus their suitability for load bearing applications, on an Instron 3365 universal testing system, equipped with a 500 N load cell with two flat-surface compression stages. The compression strain was configured at 50% on the cylindrical aerogel sample at a rate of 10 mm/min. The compression strength, modulus and toughness were estimated from the recorded stress-strain curves.

Electrical conductivity, which promotes the reduction of incoming or outgoing electromagnetic radiation, was measured for all samples using a RM3000 conductivity test unit (JANDEL), with a four-point measurement in the aerogel. For each sample, measurements were performed five times at different positions to obtain accurate results.

The EMI shielding efficiency validates the diffusion of electromagnetic radiation by the composite aerogels with thickness and diameter of 2 and 15 mm, respectively. It

was explored by the Agilent vector network analyzer (E5071C), in the X band frequency range of 8.2-12.4 GHz at room temperature. The scattering parameters of S11 and S21 were used to evaluate the transmission coefficient (T), absorption coefficient (A) and reflection coefficient (R), where $T+A+R=1$. EMI shielding performance included the total EMI shielding effect (SE_{total}), absorption shielding effect (SE_A) and reflection shielding effect (SE_R).

4.3 Results and Discussion

4.3.1 Synthesis of cationic cellulose nanocrystals

Etherification of CNCs was achieved by alkaline hydrolysis. A basic medium activates hydroxyl groups on cellulose and cleaves the sulfate half-ester groups to ensure a pure cationic modification.³² In parallel, GTMAC agent forms reactive epoxy functional groups. Finally, a nucleophilic reaction between alkali groups on CNC and GTMAC epoxy groups results in CNC-GTMAC, as shown in Figure 4.1. In this reaction, the characteristics of the aqueous medium and the GTMAC/CNC molar ratio are relevant parameters. Besides the cationization reaction, hydrolysis of GTMAC can occur, creating a competition.³³ CNC cationization is desirable, and hydrolysis of GTMAC should be limited. Hence, at higher water contents, GTMAC hydrolysis prevails, limiting GTMAC availability for cationization, due to the formation of undesirable diols, which ultimately minimize the efficiency of the reaction.^{32,33}

Further, GTMAC/anhydroglucose unit (AGU) molar ratio impacts the cationic substitution of CNC. The cationization efficiency decreases with a higher GTMAC/AGU molar ratio. For a lower molar ratio, the limited availability of GTMAC provides insufficient substitution of hydroxyl groups, although this creates an excess of GTMAC hydroxyl groups, which prioritizes etherification over hydrolysis, improving the reaction efficiency. On the contrary, the degree of substitution increases with a higher molar ratio, but GTMAC is hydrolyzed more, reducing the efficiency.³³ Possibly, non-reactive GTMAC groups might be hydrolyzed to yield quaternary ammonium diols, which form a stable H-bond not easily removed during dialysis. Thereby, it is very likely that some quaternary ammonium groups are not covalently bonded to CNC,³² not allowing complete cationization of CNC.

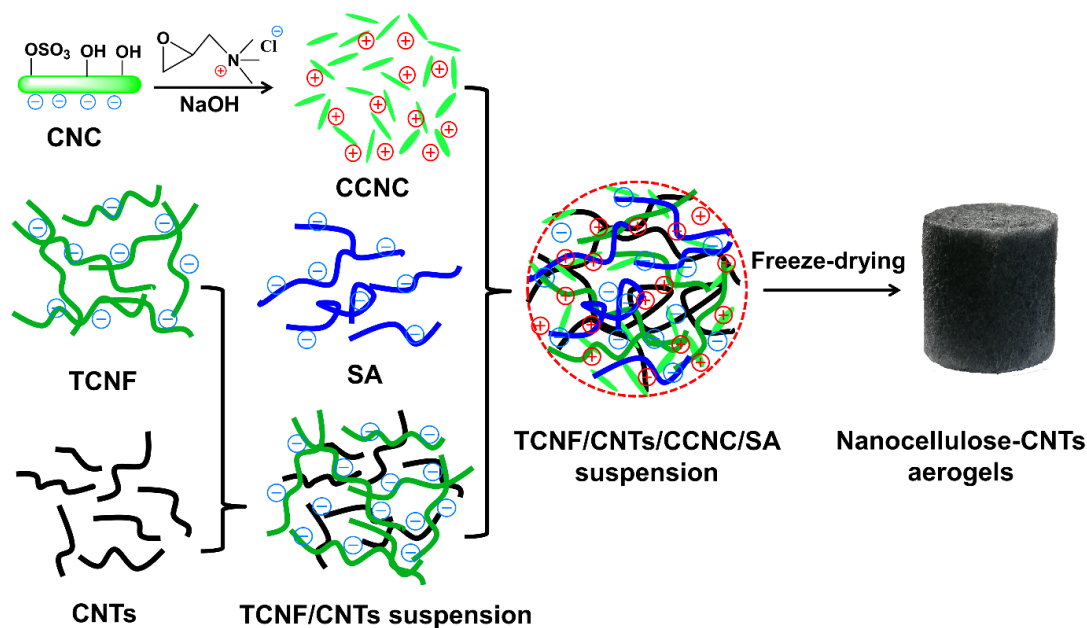


Figure 4.1 Schematic for the preparation of nanocellulose-CNT aerogels.

4.3.2 Nanocellulose chemical and morphological analysis

This analysis allows characterizing the surface charge of nanocellulose, which is related to the physical stability of the nanosuspension. Thus, a Zeta potential value lower than -30 or over 30 mV provides sufficient repulsive forces to achieve adequate colloidal physical stability.³⁴ Similarly, the electrokinetic potential indicates the effective ion concentration on the outer frame of nanocellulose, which according to Coulomb's law, dictates the electrostatic attraction dynamics in an aerogel precursor dispersion. Figure 4.2A shows the Zeta potential results for CNC, TCNF, CCNC, CNT/water and TCNF/CNT suspensions. Owing to H_2SO_4 hydrolysis, sulfate groups end up being chemically linked to CNC,³⁵ conferring a negative charge with a ZP value of -51.3 ± 0.8 mV. For CCNC, negative hydroxyl groups are converted into positive quaternary ammonium groups,^{36,37} as indicated by the ZP value ($+31.9 \pm 0.5$ mV). For TCNF, carboxyl groups are induced on nanofibrils,³⁸ resulting in a ZP of -55.7 ± 0.6 mV. The dispersibility of the suspension is closely related to the Zeta potential value. When CNTs are dispersed into water, they aggregate easily and rapidly settle to the bottom of the flask with a transparent liquid top layer, which has ZP value of 2.9 ± 0.1 mV, as shown in Figure 4.2B,C. When CNTs are dispersed in the TCNF suspension, the TCNF/CNT suspension maintains good dispersion stability even after standing for 24 h with a ZP value of -45.6 ± 0.9 mV. These results clearly indicate that TCNF can effectively assist dispersing CNTs in the suspension.

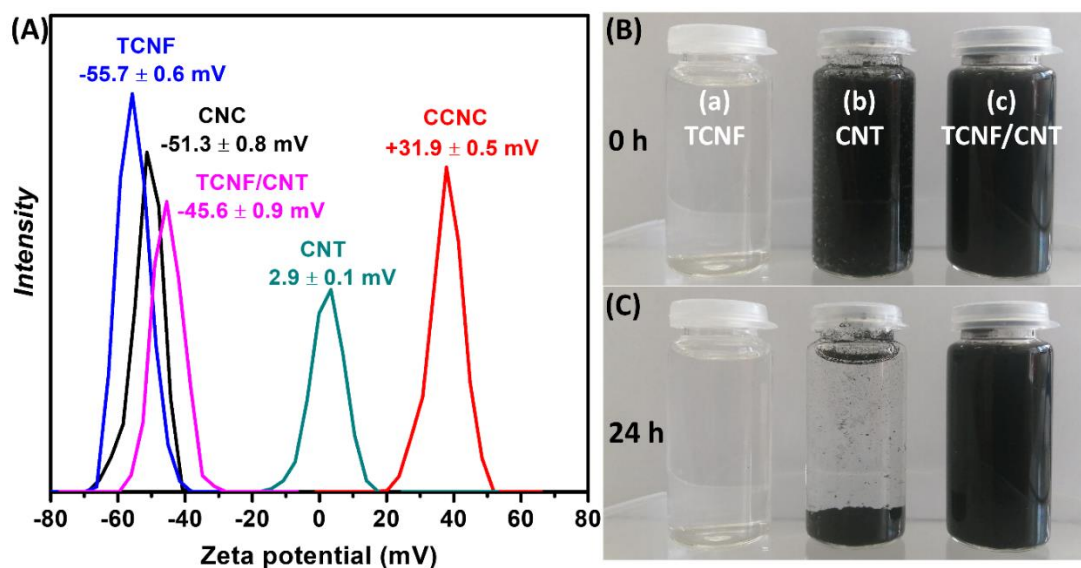


Figure 4.2 Zeta potential for CNC, CCNC, TCNF, CNT and TCNF/CNT suspensions (A), and digital camera images for TCNF, CNT and TCNF/CNT suspensions standing for 0 h (B) and 24 h (C).

Specifically, TCNF and CCNC suspensions exhibit high electrical charge,³⁴ which confer good stability due to electrostatic repulsion, making them less prone to aggregation and particle size increase. This finding validates the use of highly charged nanocellulose compositions for aerogel processing, as a high colloidal stability is important to maintain an elevated specific surface area and porosity of the final aerogel.³⁹ Moreover, cationic CNC in complement with anionic TCNF conform an oppositely charged nanocellulose matrix, in which the electrostatic forces balance to get an over-all net attraction between the particles. Precisely, this state enhances the destabilization of the primary dispersion into a colloidal gel,³⁹ which can serve as a consistent basis for the formation of the nanocellulose network. Furthermore, adding sodium alginate enhances the electrostatic repulsion, resulting in a highly dispersed suspension.

FTIR is used to characterize the external chemical modifications of nanocellulose. Figure 4.3A shows the FTIR spectra for CNC, CCNC, and TCNF, related to the regular pattern of cellulose I. Concretely, common CNC and TCNF vibrations are displayed: OH⁻ signals from 3000 to 3700 cm⁻¹, C-H stretching at 2910 cm⁻¹, O-H bending due to moisture found at 1640 cm⁻¹, carboxyl groups (COO⁻) stretching peak at 1614 cm⁻¹, O-C-H and H-C-H in-plane bending at 1427 cm⁻¹, C-H deformation at 1367 cm⁻¹, C-O-C asymmetric stretching from 1203 to 1157 cm⁻¹, glucose ring stretching at 1108

cm^{-1} , an absorption signal ranging from 1030 to 1153 cm^{-1} attributed to the ether bonds, and a band between 800 and 891 cm^{-1} assigned to C–H bond of the glucosidic bond between the glucose units.^{32,40} The insertion of the quaternary GTMAC agent used for CNC cationization was confirmed. Specifically, an increase in the intensity of the ether band, and a weaker OH^- vibration peak, indicate the consumption of OH^- groups and formation of new ether groups during cationization.³² Correspondingly, TCNF exhibits a prominent peak at 1614 cm^{-1} , related to the stretching of COONa carboxyl groups.³⁷ In detail, the underlying mechanism of TEMPO treatment involves the selective oxidation of C6 primary OH^- into carboxylate groups, precisely to COONa when the pH is basic.³⁸ Altogether, COONa and OH^- groups in TCNF are responsive to form H-bonds with CNTs,⁴¹ due to the OH^- groups reported on their surface.⁴² Thus, a justification for the co-solubility of CNTs in TCNF suspension for the stabilized suspension, includes the disruption of intramolecular H-bonds of nanocellulose by OH^- groups, and the formation of H-bonds between TCNF and CNTs.⁴² Hence, the prepared TCNF-CNTs dispersion involves a chemical association, with the negative charge of TCNF. Thereafter, the precursor suspension (CCNC, TCNF/CNF, and SA) undergoes gelation by a physical method, based on electrostatic interactions between the negative TCNF/CNT dispersion and the positively charged CCNC suspension.¹⁸ Besides, another conceivable mechanism can be by hydrogen bonds between COOH and OH^- groups distributed on CCNC and SA.

The success of the cationic modification of CNC can be demonstrated by comparing the NMR spectra of CNC and CCNC, as shown in Figure 4.3B. The characteristic chemical shifts of the cellulose carbon in the NMR spectra for CNC and CCNC correspond to C1 (101 ppm), C2, 3, 5 (68-71 ppm), C4 crystalline (85 ppm), and C6 (62 ppm), respectively.⁴³ The additional chemical shift located at 51 ppm in the NMR spectrum of CCNC corresponds to $-\text{CH}_3$ of the quaternary ammonium group, proving the success of the cationic modification. During the cationization modification process, about 23.9% of the surface hydroxyl groups of CNC were replaced by quaternary ammonium groups through tracking the content of nitrogen (N %) element, as shown in Table 4.1.

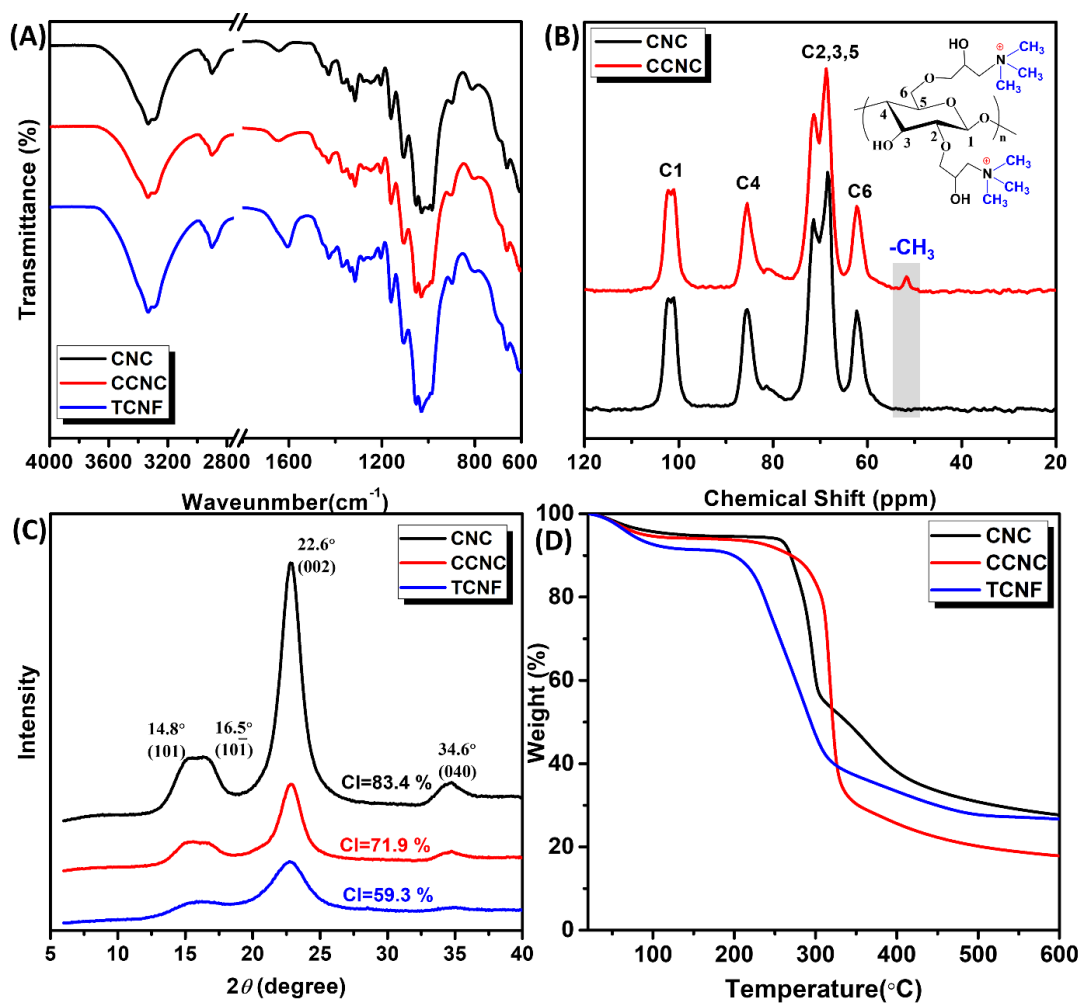


Figure 4.3 FTIR spectra (A), solid-state NMR spectra (B), XRD patterns (C) and TGA curves (D) for CNC, CCNC and TCNF.

Table 4.1 Elemental analysis results for CNC and CCNC

Sample	C (%)	H (%)	S (%)	N (%)	$n_{\text{surface-OH}}$ mmol/g	Toughness (kJ m ⁻³)
CNC	40.85	6.38	1.85	0	1.554	—
CCNC	43.38	6.87	0.42	0.52		23.9%

XRD patterns shown in Figure 4.3C reveal the periodic atomic arrangements, used to evaluate the crystalline features of nanocellulose, as its crystallinity index (CI). They exhibited cellulose I diffraction peaks at $2\theta = 14.7^\circ$ (101), 16.5° ($10\bar{1}$), 22.6° (002), and 34.6° (040), in agreement with reported data.^{32,37} The CI of CNC, CCNC and TCNF is 83.4%, 71.9% and 59.3, respectively. The decrease in CI can be attributed to the surface modification of nanocellulose. Nevertheless, surface alteration does not result in any

significant change in XRD signals, indicating that cationic and oxidizing agents do not affect the crystal structure of CNC or CNF, limiting the changes only to the surface.³² Unlike other types of cellulose, nanocellulose exhibits a higher degree of crystallinity and larger aspect ratio. In this sense, the mentioned conditions are related to a limited shrinkage rate, and high modulus for the aerogel fabrication process.⁵ Henceforth, these properties will be evaluated in aerogels, and discussed on the basis of the reduced crystalline state of CCNC and TCNF.

TGA experiments can reflect the effects of nanocellulose modification on its thermal characteristics, as shown in Figure 4.3D. Notably, the thermal degradation of CNC includes dehydration, depolymerization, and decomposition of glycosyl units.⁴⁴ The first shift denotes humidity loss, from 100 to 150 °C due to evaporation of physically bound moisture. Further, at 150 °C, removal of sulfate groups initiates with a weight loss of about 5-8%.³² Then, cellulose degradation occurs over a temperature range of 280-450 °C, representing a mass loss around 42.46-61.63%.³² Ultimately, this cycle leaves nearly 30% nanocellulose residue. The TGA curve corresponding to CNC is altered by the substitution of surface groups, denoting changes in thermal stability. The thermogram for CCNC follows the trend of CNC, however, it is shifted towards higher temperatures, marking an improvement in thermal resistance. In fact, the decomposition stage (150 to 200 °C) is limited by the removal of carboxyl groups during the alkaline pretreatment, which negatively impact the thermal stability.⁴⁰ Also, GTMAC substituents with quaternary ammonium groups and additional oxygen content, enhance thermal combustion at higher temperatures (above 350 °C),⁴⁴ yielding a lower char residue. Finally, the removal of sulfate ions during ester substitution prevents early thermal degradation. Contrarily, TCNF degrades at lower temperature (200-340 °C). This observation is related to a smaller fiber size, resulting in a higher specific surface area with more accessible sites.⁴⁵ Furthermore, possible lignin contamination induces thermal decomposition at 200-340 °C, reducing thermal stability.⁴⁶ Likewise, the presence of carboxyl groups, which are known to have limited heat resistance, compromises the thermal degradation of TCNF. Ultimately, as a result of TEMPO oxidation, it is possible that a reduction in the degree of polymerization could lead to lower decomposition temperature.⁴⁵

AFM has been used to evaluate the morphology, size, and dispersion of CNC, CCNC, and TCNF. As shown in Figure 4.4A,a, individual CNC has a rod-like morphology with

diameter of 14 ± 3 nm and 185 ± 22 nm in length. Hence, it is expected that quaternary ammonium groups related to GTMAC substituents, induce a higher positive charge on CNC, forming a homogeneous dispersion in aqueous medium by electrostatic repulsion. It appears that attraction forces (H-bonds among OH^- and OH^- /quaternary ammonium groups) and repulsion forces (electrostatic repulsion between quaternary ammonium cations) counteract each other, setting a particular state with scattered crystals. Thus, the degree of substitution could affect this factor, as it determines the level of positive charges chemically grafted onto CNC. Specially, for CCNC the nanocrystal morphology is maintained, demonstrating that cationization only compromises the surface charge, with a width of 11 ± 3 nm and a length of 181 ± 23 nm (Figure 4.4B,b). It is observed that TCNF are composed of semi-flexible chains of ultrahigh aspect ratio (Figure 4.4C,c).

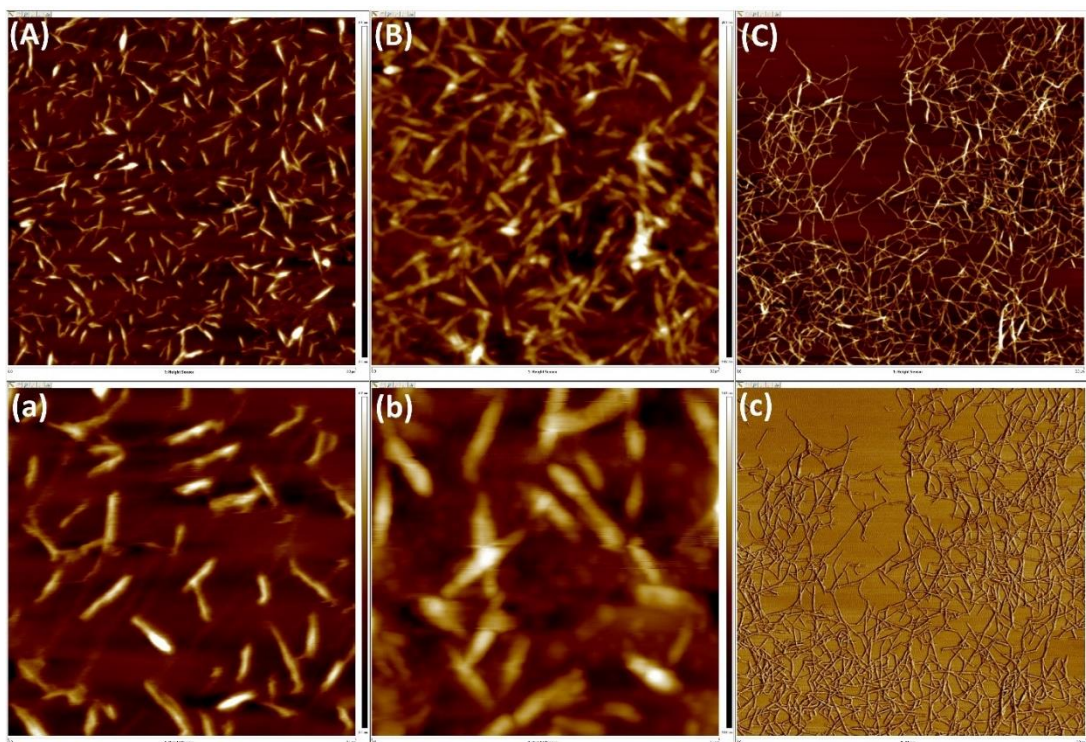


Figure 4.4 AFM images for CNC (A: 3.3×3.3 μm , a: 1.1×1.1 μm), CCNC (B: 3.3×3.3 μm , b: 1.1×1.1 μm), TCNF (C, c: 3.3×3.3 μm) at different observation scales.

4.3.3 Characterization of nanocellulose-CNT aerogels

Following the previously described preparation sequence, the obtained aerogels are shown in Figure 4.5. They exhibit a continuous solid network, apparent high porosity, lightness, and nanostructured frame. Regarding the dispersion and drying constraint to obtain a porous element, using oppositely charged nanocelluloses allowed for

appropriate dispersion of CCNC and TCNF to limit the formation of aggregates, and strong electrostatic interaction to build a strong frame that was not greatly affected by the freeze-drying process. Particularly, aerogels were prepared considering different CNT volume contents.

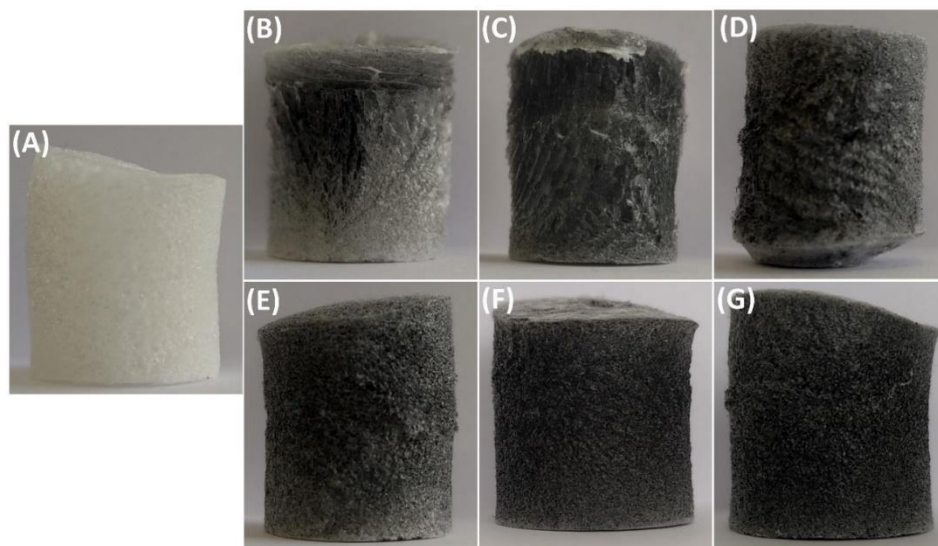


Figure 4.5 Digital images of nanocellulose-CNT aerogels: (A) CA, (B) CA-0.08, (C) CA-0.22, (D) CA-0.44, (E) CA-0.68, (F) CA-0.89, (G) CA-1.2.

To a large extent, both density and porosity depend on the initial solid concentration, dispersion expansion for aerogel network formation, and shrinkage during solvent removal. Expressly, shrinkage changes the density, morphology, and specific surface area, compromising the physical stability, external interactions, and porosity of aerogels.⁴⁷ This shrinkage factor depends on the type of polysaccharide used, its concentration, dispersion medium, and solvent exchange dynamic during drying.⁴⁷ Accordingly, density, porosity, and shrinkage results, are detailed in Table 4.2. The density values are within the range of values reported in the literature.⁵ More precisely, the nanocellulose aerogels have a density of 0.058 g/cm^3 , which increases with CNT content by increasing mass and maintaining volume. In contrast to some studies reporting nanocellulose aerogels paired with CNTs, the nanocellulose-CNT elements exhibit a reduced density,^{48–50} but the results are higher than for most nanocellulose-based aerogels.^{51–53} This can be attributed to the addition of an anionic polymer (SA), and the dispersion of CNTs with TCNF.

Table 4.2 Properties of aerogel samples.

Sample (vol %)	Density (ρ_a) (g/cm ³)	Porosity (%)	Shrinkage (%)	Strength (MPa)	Young's modulus (MPa)	Toughness (kJ m ⁻³)
CA	0.058	96.21	9.74	0.36±0.011	13.8±0.39	146.1±5.98
CA-0.08	0.059	96.12	10.41	0.37±0.021	14.39±0.72	152.5±7.61
CA-0.22	0.063	95.92	10.61	0.41±0.014	15.76±0.39	154.6±6.42
CA-0.44	0.066	95.77	11.91	0.45±0.023	16.4±0.52	179.1±12.52
CA-0.68	0.068	95.71	10.19	0.53±0.013	16.83±0.64	205.5±9.44
CA-0.89	0.072	95.54	12.19	0.55±0.016	15.44±0.77	218.4±8.47
CA-1.20	0.075	95.47	11.67	0.6±0.018	16.33±0.69	220.8±11.03

In terms of porosity, this property ranges from 95.45% to 96.21%. Furthermore, it is inversely proportional to the CNT content, thus, increasing the CNT volume limits the pore distribution, since more CNTs induce higher pore filling and restrict their size. In addition, the porous frame is maintained through freeze-drying, which prevents adhesion caused by the solvent surface tension and collapse of the internal network structure due to capillary action of the solid matrix.⁵⁴ Hence, this technique prevents capillary pressure during drying, and preserves the pores of the aerogel.

From BET analysis, the specific surface area of CA, CA-0.22 and CA-0.89 samples is 80.4 m²/g, 78.3 m²/g and 75.2 m²/g, respectively. This validates that the addition of CNTs increases the pore volume, therefore affecting the porosity and limiting the specific surface area.⁵³ This may be induced by water expansion during hydrogel freezing, which internally expands the composite, and then, during freeze-drying, while ice sublimates, the porous frame is shaped. However, CNTs counteract this phase, thus, the expansion is more restricted with higher content, and the pore size and surface area are smaller.⁴⁸

The aerogel shrinkage follows the data reported for nanocellulose based aerogels (9% to 12%), demonstrating that the gel does not significantly shrink during drying. Remarkably, the shrinkage depends on the nanocellulose concentration, gelation and drying mechanisms, and type of solvent.⁴⁷ The low shrinkage is due to the flexibility and adaptability of nanocellulose; however, gelation and nanocellulose concentration

are obvious constraints. Explicitly, the applied physical crosslinking can lead to a less cohesive nanocellulose dispersion, as some nanocellulose sections end up not being linked to each other. Additionally, with a higher CNT percentage in the aerogels, the amount of nanocellulose is limited, which restricts its reinforcing effect.^{6,55}

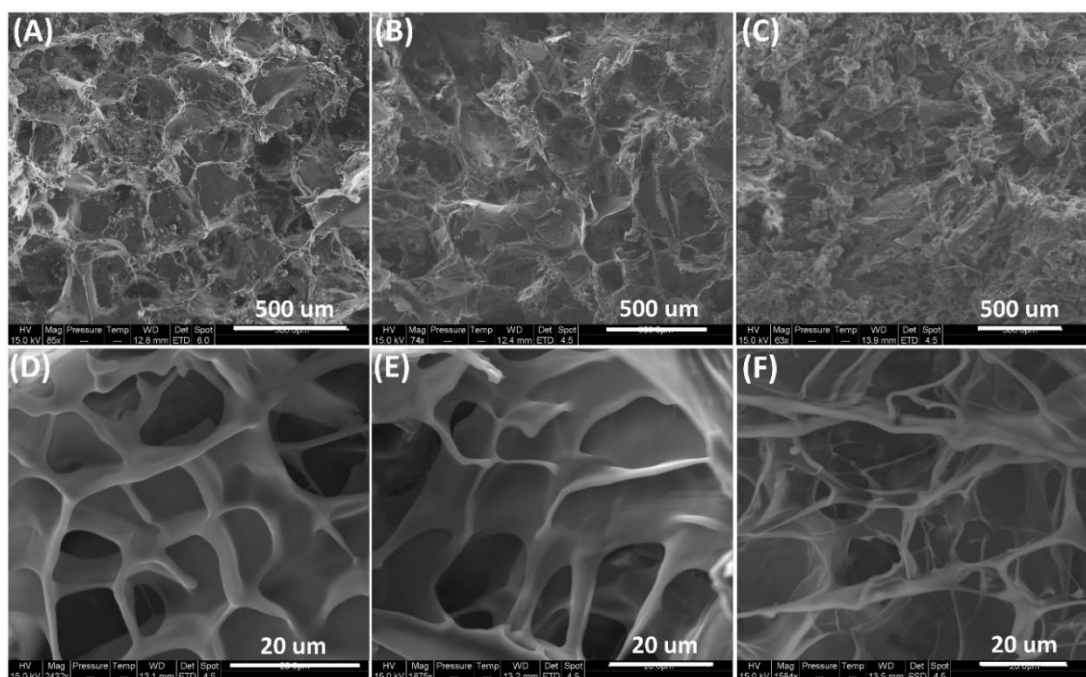


Figure 4.6 SEM images for CA (A, D), CA-0.22 (B, E) and CA-0.89 (C, F) aerogels at different observation scales.

CA, CA-0.22, and CA-0.89 aerogels were characterized to evaluate the progressive internal changes when increasing the CNT content, and to analyze the level of interaction between nanocellulose and CNTs. Figure 4.6 shows that all aerogels exhibit an oriented and interconnected three-dimensional porous structure, a critical factor for structural stability and improved mechanical properties.³⁷ Notably, the images are related to the porous patterns associated with the applied freeze-drying technique.³³ Moreover, the parallel distribution and heterogeneous appearance of the pores are due to the slow cooling to which the aerogels were submitted, as a low solidification rate results in large pores, abnormal structure, and solvent segregation after ice-sublimation during freeze-drying.³³

Considering the variation in CNT volume content, the neat nanocellulose sample showed smooth pore walls due to fibrous frame, uniform dispersion, and interaction in the nanocellulose matrix. Conversely, the cross-section is less porous with higher nanofiller loading. Specially, CNTs are relatively well dispersed, implying their

unification with the nanocellulose fibers, thus reducing the pore size. As the section turns smoother and more compact, there is a better compatibility between nanocellulose and CNTs. In this sense, a uniform distribution of CNTs proves their adequate adsorption by the negatively charged TCNF in the primary suspension, and then with the CCNC and SA composition, promoted by physical crosslinking through electrostatic interactions and H-bonds.

Likewise, the decrease in pore size can be attributed to the accumulation of CNTs at the pore boundary.⁵⁶ The drying mechanism highlights another reason, as CNTs are prone to form films along the pores via freeze drying.⁵⁶ These arguments can support the porosity limitation, as formerly calculated. Despite the homogeneous interaction between nanocellulose and CNTs, few film-like elements can be seen among the fibers, specifically in high CNT content aerogels. This may be due to the aggregation of CNTs during dispersion in the nanocellulose matrix, promoting low nanocellulose dispersion, resulting in concentrated bundles, which are then pressed during freeze-drying to form films.⁵⁰

4.3.4 Electrical conductivity

Electrical conductivity is a critical property in EMI shielding, as it determines the absorption and reflection of incident electromagnetic radiation.²⁴ As stated previously, nanocellulose-CNT aerogels exhibit high porosity, which promotes a multireflection mechanism for EMI attenuation based on the interaction of charge carriers in the shield with the electromagnetic fields of radiation.¹⁶ Reflection is facilitated in many directions due to the high specific surface area of the aerogels, increasing the EMI shielding effectiveness. In complement, absorption is another pathway for EMI dissipation, conditioned by the relationship between the electric dipoles in the aerogels and the electromagnetic field of the radiation.¹⁶ Concretely, CNTs provide an effective electrical dipole due to their high dielectric constant. Hence, the conductivity allows estimating an active absorption mechanism for electromagnetic wave depletion in aerogels, which will be further confirmed by EMI shielding capacity analysis.

Electrical resistivity quantifies the opposition to an electric current flow, the inverse to conductivity. It is worth noting that nanocellulose itself is not a conductor, although it serves as a substrate for conductive composites. Thus, neat nanocellulose aerogels exhibit high resistivity and low conductivity. Mainly, for low CNT contents, the

nanofiller is dispersed, hence a conductive network has not been formed and the electric charge cannot flow effectively. By increasing the CNT content, the conductivity improves significantly, as reflected in Figure 4.7A.

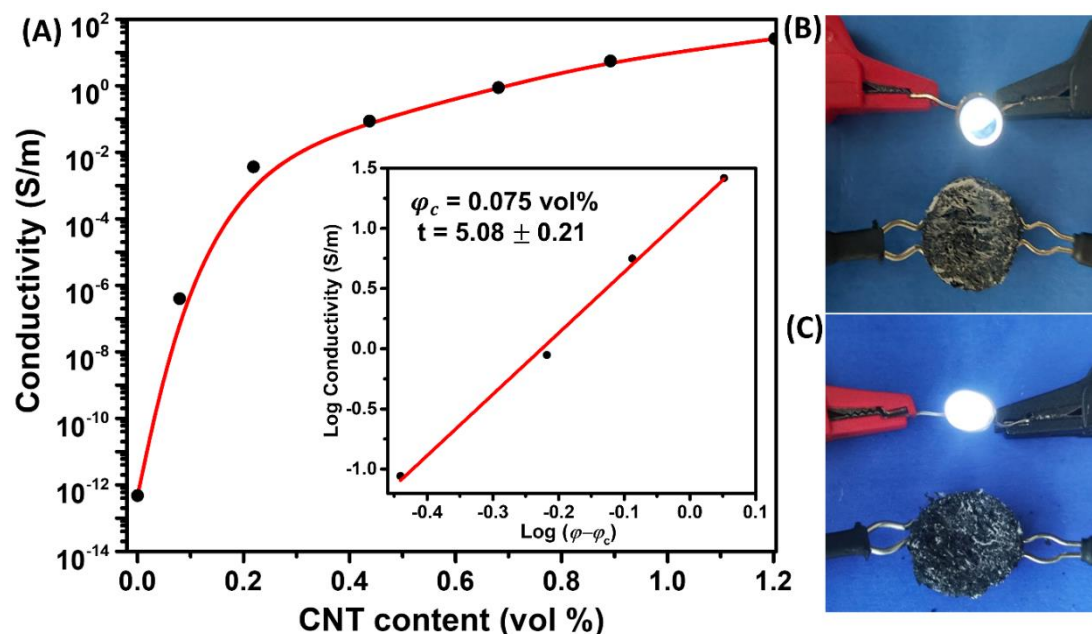


Figure 4.7 Electrical conductivity for composite aerogels with different CNT contents (A). The inset shows the evolution of log conductivity vs. $\log(\varphi - \varphi_c)$ used to determine the critical volume content = 0.075 vol% and exponent $t = 2.75$. Composite aerogels CA-0.22 (B) and CA-0.89 (C) lighting a LED device.

According to statistical percolation theory, the conductivity (σ) in a composite depends on the volume fraction of conductive fillers (φ).⁵⁷ In this case, the conductivity increases sharply when the nanofiller content exceeds the percolation threshold, implying that conductive lines start forming. Thus, the critical volume fraction (φ_c) represents the best linear fit of the $\log(\sigma)$ versus $\log(\varphi - \varphi_c)$ plot. As shown in the inset of Figure 4.7A, below 0.075 vol.%, the aerogels exhibit insulating ability with high resistivity, as the dispersed nanotubes cannot form a conductive network. Above this critical value, CNTs are integrated to the cellulose fibers inside the aerogel frame, forming an interconnected electric grid, which enhances the conductivity due to the inserted charge carriers, inducing a metal-like conducting behavior.^{52,58} The aerogels could be connected to a circuit that turned on a LED lamp at a constant voltage of 9 V (Figure 4.7B,C).

The conductivity value is higher than that found in the literature for cellulose-functionalized CNT based composite aerogels.^{49,59,60} This could be related to an

efficient and cohesive CNT interaction, which further proves that the dispersion of the nanofiller in the cellulose matrix by physical interactions is uniform. Moreover, the percolation threshold value is achieved at a very low concentration, attributed to the interlocking ability of carbon nanotubes, which ensures an electrically conductive pathway even at low contents.

4.3.5 Mechanical properties

The mechanical properties are used to evaluate the ability of aerogels to withstand a specific stress, as EMI shielding materials are required to sustain a considerable load during practical application.^{24,61} Table 4.2 shows the Young's modulus, compression strength and toughness values of the aerogels, while Figure 4.8A displays typical stress-strain curves. The stress-strain curves prove the trend of an open-cell foam: elastic behavior at low strain (<10%), cell collapse associated to stress reduction at medium strains (15-40%), and plastic stiffening at high strain (>40%).⁶² It can be deduced that the main deformation (<50%), is caused by bending and pore collapse. Under low compression strain, all aerogels have similar modulus, however, after the onset of plastic deformation, the stress increases according to the reinforcing capacity of the nanoparticles. In line with the increase in CNT content, the aerogels show a higher compression toughness (Figure 4.8B). The compression strength and modulus of aerogels are shown in the Table 4.2. The higher toughness supported by the material may be due to strong interactions between nanocellulose and CNTs based on physical interactions, ascribed to the crosslinking mechanism. In addition, due to the recognized mechanical impedance of CNTs, the strength of these composites can be credited to a good dispersion of CNTs in the nanocellulose matrix.

The specific Young's modulus values of CNT-cellulose aerogels are higher than that of the various cellulose aerogels (Figure 4.8C and Table 4.3). This is most probably due to the formation of strong electrostatic interactions between cationic CCNC and anionic TCNF promoting the stability of the aerogel structure. Also, the modulus is limited by the CNT content.⁵⁰ Although CNTs are known for their high brittleness, they can enhance the mechanical properties of aerogels.⁶³ In this case, more CNTs reduce the surface energy which limits the bonding loading conditions, turning the aerogels with a higher CNT content into more flexible elements.

Table 4.3 Comparison of specific modulus (modulus divided by density) of various cellulose aerogels.

Samples	Density (g/cm ³)	Specific modulus (Mpa g ⁻¹ cm ³)	Ref.
RC aerogels	0.129	45.74	64
	0.173	34.63	
	0.209	27.77	
	0.217	29.91	
CNT/WPU	0.032	6.25	65
	0.053	20.76	
	0.12	52.34	
CNF	0.0198	36.73	66
	0.0204	47.52	
	0.0202	72.73	
	0.022	20.54	
CNT/PLLA	03	54.12	67
CNT/CNF	0.01	41.76	68
	0.015	34.43	
	0.022	30.46	
	0.054	10.23	
CNT matrix/interface	0.047	119.15	61
	0.057	61.43	
	0.064	73.42	
	0.075	124.56	
CNT/cellulose aerogel	0.063	250.56	This work
	0.068	247.51	
	0.072	214.49	

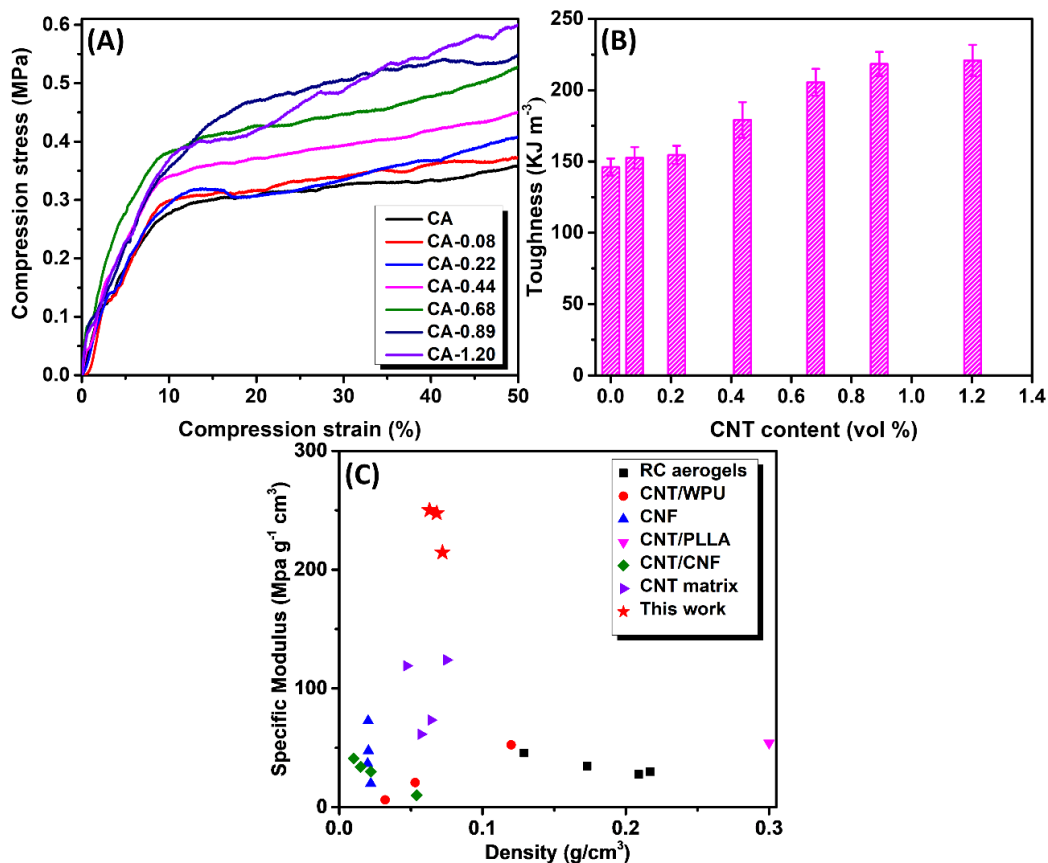


Figure 4.8 (A) Compression stress vs strain curves for nanocellulose-CNT aerogels, (B) evolution of the toughness for nanocellulose-CNT aerogels. (C) Comparison of specific modulus (Young's modulus divided by density) between other reported lightweight porous materials and this work.

4.3.6. EMI shielding Performance

The EMI shielding efficiency (EMI-SE) of nanocellulose-CNT aerogels was measured to determine their ability to shield electromagnetic waves through reflection and absorption mechanisms. Typically, an active EMI shielding aerogel has three functions: reflection (SE_R), absorption (SE_A), and multiple reflections.^{24,69} Reflection occurs at the surface level through the interaction of electromagnetic radiation with charge carriers, determined by the alignment of incident waves and electric or magnetic dipoles. Absorption involves wave dissipation across the aerogel. Particularly, reflection and absorption depend on the conductivity of the medium, despite these multiple reflections ascribed to radiation bending and scattering due to inner interfaces, they are neglected since the total EMI-SE is higher than 10 dB.²⁴

Accordingly, the total shielding efficiency considers the sum of reflection and absorption.¹⁵ The EMI shielding efficiencies are displayed in the frequency range from 8.2 to 12.4 GHz in Figure 4.9. It can be clearly observed that both samples exhibit a weak frequency dependence in the measured region.^{49,70} The SE_{Total} value for CA-0.22 is 27.5 dB, and it is 39.8 dB for CA-0.89, above the limit for practical applications.⁷⁰ Analyzing the results, it appears that higher CNT loading enhances the depletion of induced EM waves. With a higher conductive content, the interaction between CNT charge carriers and incoming EM waves is improved. Besides, the high interface area simplifies the reflection mechanism. In addition, a broader CNT distribution ensures more stable relationships between the electric dipoles in the aerogels and the electromagnetic field of inflowing radiation, and conditions a more stable EMI-SE absorption pathway.

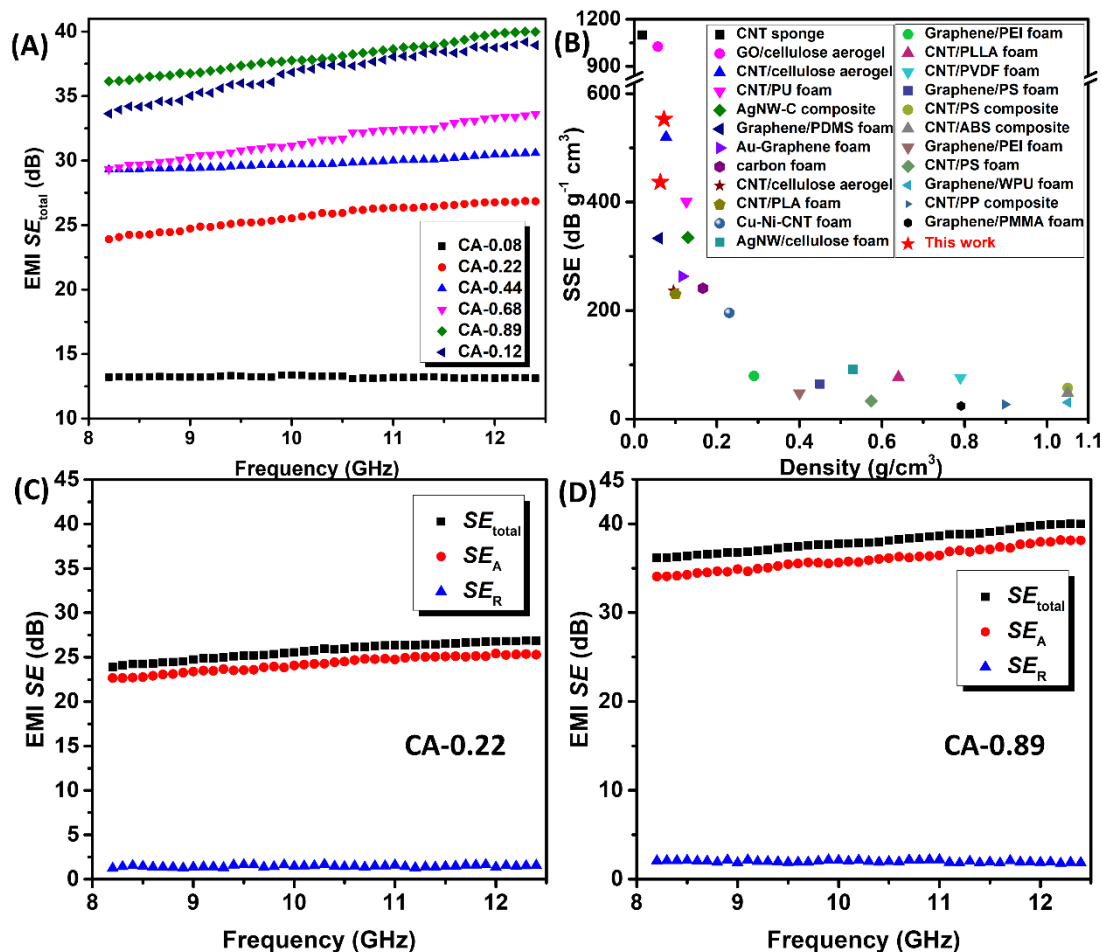


Figure 4.9 (A) EMI shielding efficiency (SE_T) of the aerogel samples with various CNT contents. (B) Comparison of the specific SE (SSE) of various previously reported foams, sponges, and aerogels. EMI shielding efficiency (SE_T , SE_R , and SE_A) for CA-0.22 aerogel (C) and CA-0.89 (D) aerogel.

Table 4.4 Comparisons of EMI shielding efficiency of various foams, sponges, and aerogels.

Samples	Density (g/cm ³)	EMI SE (dB)	SSE (dB g ⁻¹ cm ³)	Ref.
Graphene/PS foam	0.450	29	64.4	71
Graphene/PEI foam	0.29	23	79.3	72
Graphene/PDMS foam	0.060	19.98	333	73
Graphene/PMMA foam	0.792	19	23.9	74
Graphene/PEI foam	0.40	19	47.5	75
GO/cellulose aerogel	0.0569	58.4	1026	76
Graphene/WPU composite	1.05	32	30.5	77
CNT/PS foam	0.574	19	33.1	78
CNT/PU foam	0.126	50.5	400.8	79
CNT/PLA foam	0.1	23	230	80
CNT/PLLA foam	0.64	23	77	67
CNT/PVDF foam	0.79	57	76	81
CNT sponge	0.02	22	1100	82
CNT/PS composite	1.05	60	57.1	83
CNT/PP composite	0.898	24	26.7	84
CNT/ABS composite	1.05	50	47.6	85
CNT/cellulose aerogel	0.077	40	519.5	61
CNT/cellulose aerogel	0.095	22.5	236.8	49
AgNW/cellulose foam	0.53	48.6	91.7	86
AgNW-C composite	0.13	43.5	334.6	87
Cu-Ni-CNT foam	0.23	45	195.6	88
Au-Graphene foam	0.116	30.5	262.9	89
Commercial carbon foam	0.166	40	240.9	90
CNT/cellulose aerogel	0.063	27.5	436.5	This work
CNT/cellulose aerogel	0.072	39.8	552.7	This work

Considering the EMI shielding and aerogel density, the specific SE (SSE, EMI SE divided by density) vs. CNT volume content is summarized to represent the EMI shielding performance (Figure 4.9B). The SSE value for CA-0.22 and CA-0.89 was

estimated to be 436.5 and 537.5 dB cm³ g⁻¹, respectively, which is highly competitive compared with most previously published porous materials with relative CNTs loading (Table 4.4). This may be due to the integrated nanocellulose-CNT matrix, which forms a stable conductive network allowing the aerogel to properly interact with the incident electromagnetic radiation. Remarkably, the favorable shielding efficiency can be related to the low density and porosity of the aerogels, complemented with a good thermal stability attributed to the nanocellulose network. This creates a stable and reliable protection against electromagnetic waves caused by the synergy of promoted electron hopping, induce multiple polarization centers, assembled magnetic resonance, and equivalent wedge effect of the aerogel's porous surface and interior.⁹¹ The SSE of CNT sponge⁸² and graphene oxide/cellulose aerogel⁹² (Figure 4.9B) are higher than our work, but their application is limited by their weak physical properties.

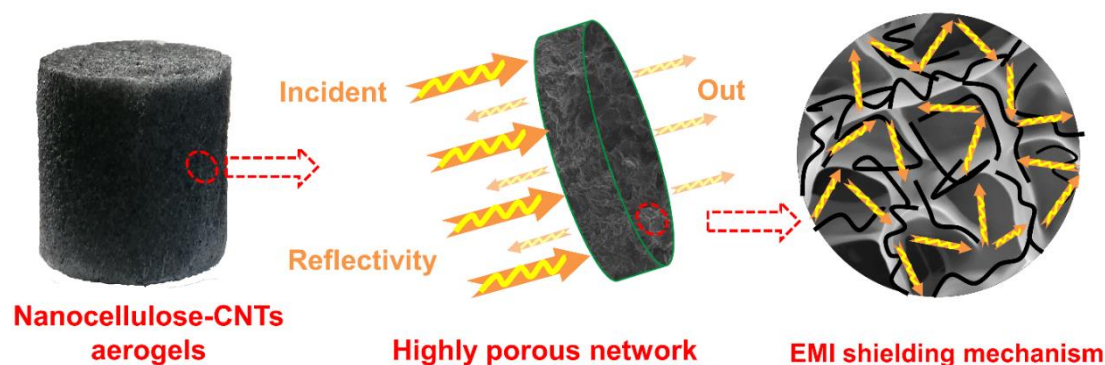


Figure 4.10 Electromagnetic microwave dissipation in the nanocellulose-CNT composite aerogel.

Based on these results, absorption is the main shielding mechanism for the X-band frequency range. As a consequence of the high porosity of the composite aerogels, electromagnetic microwaves can penetrate with low reflectivity.⁹³ Then, they are trapped in the pores, where they are attenuated and scattered by the CNT layer, until being absorbed and dissipated as heat, as shown in Figure 4.10.

4.4 Conclusions

In conclusion, this work reveals effective CNC cationization to improve electrostatic interaction with anionic nanofibrils and complementary precursors to form a consistent cellulose substructure through simple but practical electrostatic interactions. Then, CNT integration is promoted by electrostatic adhesion and H-bonding, which undergoes gelation and freeze-drying to form nanocellulose-CNTs aerogels. This

simple, effective, and environmentally friendly scheme produces aerogels with low density (density < 0.075 g/cm³), highly porous (porosity > 95.47%), conductive (up to 26.2 S/m), mechanically resistant that exhibit practical EMI shielding efficiency above 39.8 dB. This indicates that these aerogels can potentially be used as a lightweight, environmentally friendly EMI shielding material.

Acknowledgement

This work was supported by the China Scholarship Council (CSC) under Grant No. 201806950016 and by the Labex TEC 21 (Investissements d’Avenir - grant agreement n°ANR-11-LABX-0030). LGP2 is part of the LabEx Tec 21 (Investissements d’Avenir - grant agreement n°ANR-11-LABX-0030) and of the PolyNat Carnot Institut (Investissements d’Avenir - grant agreement n°ANR-11-CARN-030-01).

4.5 References

- (1) Phitsuwan, P.; Sakka, K.; Ratanakhanokchai, K. Improvement of Lignocellulosic Biomass in Planta: A Review of Feedstocks, Biomass Recalcitrance, and Strategic Manipulation of Ideal Plants Designed for Ethanol Production and Processability. *Biomass and Bioenergy* **2013**, *58*, 390–405.
- (2) Xu, N.; Liu, S.; Xin, F.; Zhou, J.; Jia, H.; Xu, J.; Jiang, M.; Dong, W. Biomethane Production from Lignocellulose: Biomass Recalcitrance and Its Impacts on Anaerobic Digestion. *Frontiers in bioengineering and biotechnology* **2019**, *7*, 191.
- (3) Shuttleworth, P. S.; Parker, H. L.; Hunt, A. J.; Budarin, V. L.; Matharu, A. S.; Clark, J. H. Applications of Nanoparticles in Biomass Conversion to Chemicals and Fuels. *Green Chemistry* **2014**, *16* (2), 573–584.
- (4) Lee, H. V.; Hamid, S. B. A.; Zain, S. K. Conversion of Lignocellulosic Biomass to Nanocellulose: Structure and Chemical Process. *The Scientific World Journal* **2014**, *2014*.
- (5) Long, L.-Y.; Weng, Y.-X.; Wang, Y.-Z. Cellulose Aerogels: Synthesis, Applications, and Prospects. *Polymers* **2018**, *10* (6), 623.
- (6) Lavoine, N.; Bergström, L. Nanocellulose-Based Foams and Aerogels: Processing, Properties, and Applications. *Journal of Materials Chemistry A* **2017**, *5* (31), 16105–16117.

- (7) Huang, P.; Wang, C.; Huang, Y.; Wu, M. Structure and Properties of Cellulose Nanofibrils. *Nanocellulose: From Fundamentals to Advanced Materials* **2019**, 53–80.
- (8) Muhd Julkapli, N.; Bagheri, S. Nanocellulose as a Green and Sustainable Emerging Material in Energy Applications: A Review. *Polymers for Advanced Technologies* **2017**, 28 (12), 1583–1594.
- (9) Hirose, M.; Tachikawa, K.; Ozaki, M.; Umezawa, N.; Shinbo, T.; Kokubo, K.; Kobayashi, H. X-ray Radiation Causes Electromagnetic Interference in Implantable Cardiac Pacemakers. *Pacing and clinical electrophysiology* **2010**, 33 (10), 1174–1181.
- (10) Jiang, D.; Murugadoss, V.; Wang, Y.; Lin, J.; Ding, T.; Wang, Z.; Shao, Q.; Wang, C.; Liu, H.; Lu, N. Electromagnetic Interference Shielding Polymers and Nanocomposites-a Review. *Polymer Reviews* **2019**, 59 (2), 280–337.
- (11) Tong, X. C. *Advanced Materials and Design for Electromagnetic Interference Shielding*; CRC press, 2016.
- (12) Moon, J.-H. Health Effects of Electromagnetic Fields on Children. *Clinical and experimental pediatrics* **2020**, 63 (11), 422.
- (13) Lin, J. C. *Electromagnetic Fields in Biological Systems*; Taylor & Francis, 2012.
- (14) Chung, D. D. L. Materials for Electromagnetic Interference Shielding. *Materials Chemistry and Physics* **2020**, 255, 123587. <https://doi.org/10.1016/j.matchemphys.2020.123587>.
- (15) Liao, S.-Y.; Wang, X.-Y.; Li, X.-M.; Wan, Y.-J.; Zhao, T.; Hu, Y.-G.; Zhu, P.-L.; Sun, R.; Wong, C.-P. Flexible Liquid Metal/Cellulose Nanofiber Composites Film with Excellent Thermal Reliability for Highly Efficient and Broadband EMI Shielding. *Chemical Engineering Journal* **2021**, 422, 129962.
- (16) Nizam, P. A.; Gopakumar, D. A.; Pottathara, Y. B.; Pasquini, D.; Nzihou, A.; Thomas, S. Nanocellulose-Based Composites: Fundamentals and Applications in Electronics. In *Nanocellulose Based Composites for Electronics*; Elsevier, 2021; pp 15–29.
- (17) Vazhayal, L.; Wilson, P.; Prabhakaran, K. Waste to Wealth: Lightweight, Mechanically Strong and Conductive Carbon Aerogels from Waste Tissue Paper for Electromagnetic Shielding and CO₂ Adsorption. *Chemical Engineering Journal* **2020**, 381, 122628.

- (18) Chen, Y.; Zhang, L.; Yang, Y.; Pang, B.; Xu, W.; Duan, G.; Jiang, S.; Zhang, K. Recent Progress on Nanocellulose Aerogels: Preparation, Modification, Composite Fabrication, Applications. *Advanced Materials* **2021**, *33* (11), 2005569.
- (19) Nita, L. E.; Ghilan, A.; Rusu, A. G.; Neamtu, I.; Chiriac, A. P. New Trends in Bio-Based Aerogels. *Pharmaceutics* **2020**, *12* (5), 449.
- (20) Pai, A. R.; Paoloni, C.; Thomas, S. Nanocellulose-Based Sustainable Microwave Absorbers to Stifle Electromagnetic Pollution. In *Nanocellulose Based Composites for Electronics*; Elsevier, 2021; pp 237–258.
- (21) Zeng, Z.; Wu, T.; Han, D.; Ren, Q.; Siqueira, G.; Nyström, G. Ultralight, Flexible, and Biomimetic Nanocellulose/Silver Nanowire Aerogels for Electromagnetic Interference Shielding. *ACS nano* **2020**, *14* (3), 2927–2938.
- (22) Wan, Y.-J.; Zhu, P.-L.; Yu, S.-H.; Sun, R.; Wong, C.-P.; Liao, W.-H. Ultralight, Super-Elastic and Volume-Preserving Cellulose Fiber/Graphene Aerogel for High-Performance Electromagnetic Interference Shielding. *Carbon* **2017**, *115*, 629–639.
- (23) O'connell, M. J. *Carbon Nanotubes: Properties and Applications*; CRC press, 2018.
- (24) Anju, V. P. Nanocellulose-Based Composites for EMI Shielding Applications. In *Nanocellulose Based Composites for Electronics*; Elsevier, 2021; pp 125–161.
- (25) Rol, F.; Saini, S.; Meyer, V.; Petit-Conil, M.; Bras, J. Production of Cationic Nanofibrils of Cellulose by Twin-Screw Extrusion. *Industrial crops and products* **2019**, *137*, 81–88.
- (26) Saini, S.; Falco, Ç. Y.; Belgacem, M. N.; Bras, J. Surface Cationized Cellulose Nanofibrils for the Production of Contact Active Antimicrobial Surfaces. *Carbohydrate polymers* **2016**, *135*, 239–247.
- (27) Lin, N.; Dufresne, A. Surface Chemistry, Morphological Analysis and Properties of Cellulose Nanocrystals with Graded Sulfation Degrees. *Nanoscale* **2014**, *6* (10), 5384–5393.
- (28) Wicklein, B.; Kocjan, A.; Salazar-Alvarez, G.; Carosio, F.; Camino, G.; Antonietti, M.; Bergström, L. Thermally Insulating and Fire-Retardant Lightweight Anisotropic Foams Based on Nanocellulose and Graphene Oxide. *Nature nanotechnology* **2015**, *10* (3), 277–283.

- (29) Naseri, N.; Deepa, B.; Mathew, A. P.; Oksman, K.; Girandon, L. Nanocellulose-Based Interpenetrating Polymer Network (IPN) Hydrogels for Cartilage Applications. *Biomacromolecules* **2016**, *17* (11), 3714–3723.
- (30) Cui, C.-H.; Yan, D.-X.; Pang, H.; Jia, L.-C.; Xu, X.; Yang, S.; Xu, J.-Z.; Li, Z.-M. A High Heat-Resistance Bioplastic Foam with Efficient Electromagnetic Interference Shielding. *Chemical Engineering Journal* **2017**, *323*, 29–36.
- (31) Le Gars, M.; Roger, P.; Belgacem, N.; Bras, J. Role of Solvent Exchange in Dispersion of Cellulose Nanocrystals and Their Esterification Using Fatty Acids as Solvents. *Cellulose* **2020**, *27* (8), 4319–4336.
- (32) Morantes, D.; Muñoz, E.; Kam, D.; Shoseyov, O. Highly Charged Cellulose Nanocrystals Applied as a Water Treatment Flocculant. *Nanomaterials* **2019**, *9* (2), 272.
- (33) Zaman, A.; Huang, F.; Jiang, M.; Wei, W.; Zhou, Z. Preparation, Properties, and Applications of Natural Cellulosic Aerogels: A Review. *Energy and Built Environment* **2020**, *1* (1), 60–76.
- (34) Joseph, E.; Singhvi, G. Multifunctional Nanocrystals for Cancer Therapy: A Potential Nanocarrier. *Nanomaterials for drug delivery and therapy* **2019**, 91–116.
- (35) De France, K. J.; Hoare, T.; Cranston, E. D. Review of Hydrogels and Aerogels Containing Nanocellulose. *Chemistry of Materials* **2017**, *29* (11), 4609–4631.
- (36) Wang, M.; Yu, T.; Tan, L.; Li, W.; Wei, W.; Jiang, M.; Liu, D.; Zhou, Z. An Eco-Friendly Approach to Preparing Cellulose Nanocrystals by Precisely Controlling the Dissolution of Natural Cellulose in TBAH/H₂O Solvent. *Cellulose* **2020**, *27* (16), 9311–9324.
- (37) Zhu, G.; Chen, Z.; Wu, B.; Lin, N. Dual-Enhancement Effect of Electrostatic Adsorption and Chemical Crosslinking for Nanocellulose-Based Aerogels. *Industrial Crops and Products* **2019**, *139*, 111580.
- (38) Patiño-Masó, J.; Serra-Parareda, F.; Tarrés, Q.; Mutjé, P.; Espinach, F. X.; Delgado-Aguilar, M. TEMPO-Oxidized Cellulose Nanofibers: A Potential Bio-Based Superabsorbent for Diaper Production. *Nanomaterials (Basel)* **2019**, *9* (9), 1271. <https://doi.org/10.3390/nano9091271>.
- (39) Matter, F.; Luna, A. L.; Niederberger, M. From Colloidal Dispersions to Aerogels: How to Master Nanoparticle Gelation. *Nano Today* **2020**, *30*, 100827. <https://doi.org/10.1016/j.nantod.2019.100827>.

- (40) Li, M.-C.; Mei, C.; Xu, X.; Lee, S.; Wu, Q. Cationic Surface Modification of Cellulose Nanocrystals: Toward Tailoring Dispersion and Interface in Carboxymethyl Cellulose Films. *Polymer* **2016**, *107*, 200–210.
- (41) Huang, H.-D.; Liu, C.-Y.; Zhang, L.-Q.; Zhong, G.-J.; Li, Z.-M. Simultaneous Reinforcement and Toughening of Carbon Nanotube/Cellulose Conductive Nanocomposite Films by Interfacial Hydrogen Bonding. *ACS Sustainable Chemistry & Engineering* **2015**, *3* (2), 317–324.
- (42) Adsul, M. G.; Rey, D. A.; Gokhale, D. V. Combined Strategy for the Dispersion/Dissolution of Single Walled Carbon Nanotubes and Cellulose in Water. *Journal of Materials Chemistry* **2011**, *21* (7), 2054–2056.
- (43) Silva, L. S.; Lima, L. C.; Silva, F. C.; Matos, J. M. E.; Santos, M. R. M.; Júnior, L. S. S.; Sousa, K. S.; da Silva Filho, E. C. Dye Anionic Sorption in Aqueous Solution onto a Cellulose Surface Chemically Modified with Aminoethanethiol. *Chemical Engineering Journal* **2013**, *218*, 89–98.
- (44) Abraham, E.; Kam, D.; Nevo, Y.; Slattegard, R.; Rivkin, A.; Lapidot, S.; Shoseyov, O. Highly Modified Cellulose Nanocrystals and Formation of Epoxy-Nanocrystalline Cellulose (CNC) Nanocomposites. *ACS applied materials & interfaces* **2016**, *8* (41), 28086–28095.
- (45) Mahendra, I. P.; Wirjosentono, B.; Ismail, H.; Mendez, J. A. Thermal and Morphology Properties of Cellulose Nanofiber from TEMPO-Oxidized Lower Part of Empty Fruit Bunches (LEFB). *Open Chemistry* **2019**, *17* (1), 526–536.
- (46) Mahendra, I. P.; Wirjosentono, B.; Tamrin, T.; Ismail, H.; Mendez, J. A.; Causin, V. The Effect of Nanocrystalline Cellulose and TEMPO-Oxidized Nanocellulose on the Compatibility of Polypropylene/Cyclic Natural Rubber Blends. *Journal of Thermoplastic Composite Materials* **2020**, 0892705720959129.
- (47) Budtova, T. Cellulose II Aerogels: A Review. *Cellulose* **2019**, *26* (1), 81–121.
- (48) Gnanaseelan, M.; Chen, Y.; Luo, J.; Krause, B.; Pionteck, J.; Pötschke, P.; Qi, H. Cellulose-Carbon Nanotube Composite Aerogels as Novel Thermoelectric Materials. *Composites Science and Technology* **2018**, *163*, 133–140.
- (49) Huang, H.-D.; Liu, C.-Y.; Zhou, D.; Jiang, X.; Zhong, G.-J.; Yan, D.-X.; Li, Z.-M. Cellulose Composite Aerogel for Highly Efficient Electromagnetic Interference Shielding. *Journal of Materials Chemistry A* **2015**, *3* (9), 4983–4991.

- (50) Qi, H.; Mäder, E.; Liu, J. Electrically Conductive Aerogels Composed of Cellulose and Carbon Nanotubes. *Journal of Materials Chemistry A* **2013**, *1* (34), 9714–9720.
- (51) Du, X.; Qiu, J.; Deng, S.; Du, Z.; Cheng, X.; Wang, H. Alkylated Nanofibrillated Cellulose/Carbon Nanotubes Aerogels Supported Form-Stable Phase Change Composites with Improved n-Alkanes Loading Capacity and Thermal Conductivity. *ACS applied materials & interfaces* **2020**, *12* (5), 5695–5703.
- (52) Hosseini, H.; Kokabi, M.; Mousavi, S. M. Conductive Bacterial Cellulose/Multiwall Carbon Nanotubes Nanocomposite Aerogel as a Potentially Flexible Lightweight Strain Sensor. *Carbohydrate polymers* **2018**, *201*, 228–235.
- (53) Hajian, A.; Fu, Q.; Berglund, L. A. Recyclable and Superelastic Aerogels Based on Carbon Nanotubes and Carboxymethyl Cellulose. *Composites Science and Technology* **2018**, *159*, 1–10.
- (54) Sun, Y.; Chu, Y.; Wu, W.; Xiao, H. Nanocellulose-Based Lightweight Porous Materials: A Review. *Carbohydrate Polymers* **2020**, 117489.
- (55) Hoepfner, S.; Ratke, L.; Milow, B. Synthesis and Characterisation of Nanofibrillar Cellulose Aerogels. *Cellulose* **2008**, *15* (1), 121–129.
- (56) Muthuraj, R.; Sachan, A.; Castro, M.; Feller, J.-F.; Seantier, B.; Grohens, Y. Vapor and Pressure Sensors Based on Cellulose Nanofibers and Carbon Nanotubes Aerogel with Thermoelectric Properties. *Journal of Renewable Materials* **2018**, *6* (3), 277–287.
- (57) Koga, H.; Saito, T.; Kitaoka, T.; Nogi, M.; Suganuma, K.; Isogai, A. Transparent, Conductive, and Printable Composites Consisting of TEMPO-Oxidized Nanocellulose and Carbon Nanotube. *Biomacromolecules* **2013**, *14* (4), 1160–1165.
- (58) Sun, F.; Liu, W.; Dong, Z.; Deng, Y. Underwater Superoleophobicity Cellulose Nanofibril Aerogel through Regioselective Sulfonation for Oil/Water Separation. *Chemical Engineering Journal* **2017**, *330*, 774–782.
- (59) Chen, Y.; Liu, Y.; Li, Y.; Qi, H. Highly Sensitive, Flexible, Stable, and Hydrophobic Biofoam Based on Wheat Flour for Multifunctional Sensor and Adjustable EMI Shielding Applications. *ACS Applied Materials & Interfaces* **2021**.

- (60) Chen, Y.; Pötschke, P.; Pionteck, J.; Voit, B.; Qi, H. Multifunctional Cellulose/RGO/Fe₃O₄ Composite Aerogels for Electromagnetic Interference Shielding. *ACS applied materials & interfaces* **2020**, *12* (19), 22088–22098.
- (61) Zhang, L.-Q.; Yang, S.-G.; Li, L.; Yang, B.; Huang, H.-D.; Yan, D.-X.; Zhong, G.-J.; Xu, L.; Li, Z.-M. Ultralight Cellulose Porous Composites with Manipulated Porous Structure and Carbon Nanotube Distribution for Promising Electromagnetic Interference Shielding. *ACS applied materials & interfaces* **2018**, *10* (46), 40156–40167.
- (62) Yang, X.; Shi, K.; Zhitomirsky, I.; Cranston, E. D. Cellulose Nanocrystal Aerogels as Universal 3D Lightweight Substrates for Supercapacitor Materials. *Advanced Materials* **2015**, *27* (40), 6104–6109.
- (63) Shishehbor, M.; Pouranian, M. R. Tuning the Mechanical and Adhesion Properties of Carbon Nanotubes Using Aligned Cellulose Wrap (Cellulose Nanotube): A Molecular Dynamics Study. *Nanomaterials* **2020**, *10* (1), 154.
- (64) Liu, C.-Y.; Zhong, G.-J.; Huang, H.-D.; Li, Z.-M. Phase Assembly-Induced Transition of Three Dimensional Nanofibril- to Sheet-Networks in Porous Cellulose with Tunable Properties. *Cellulose* **2014**, *21* (1), 383–394. <https://doi.org/10.1007/s10570-013-0096-z>.
- (65) Zeng, Z.; Jin, H.; Chen, M.; Li, W.; Zhou, L.; Xue, X.; Zhang, Z. Microstructure Design of Lightweight, Flexible, and High Electromagnetic Shielding Porous Multiwalled Carbon Nanotube/Polymer Composites. *Small* **2017**, *13* (34), 1701388.
- (66) Sehaqui, H.; Salajkova, M.; Zhou, Q.; Berglund, L. A. Mechanical Performance Tailoring of Tough Ultra-High Porosity Foams Prepared from Cellulose I Nanofiber Suspensions. *Soft Matter* **2010**, *6* (8), 1824–1832. <https://doi.org/10.1039/b927505c>.
- (67) Kuang, T.; Chang, L.; Chen, F.; Sheng, Y.; Fu, D.; Peng, X. Facile Preparation of Lightweight High-Strength Biodegradable Polymer/Multi-Walled Carbon Nanotubes Nanocomposite Foams for Electromagnetic Interference Shielding. *Carbon* **2016**, *105*, 305–313.
- (68) Wang, M.; Anoshkin, I. V.; Nasibulin, A. G.; Korhonen, J. T.; Seitsonen, J.; Pere, J.; Kauppinen, E. I.; Ras, R. H.; Ikkala, O. Modifying Native Nanocellulose Aerogels with Carbon Nanotubes for Mechanoresponsive Conductivity and Pressure Sensing. *Advanced materials* **2013**, *25* (17), 2428–2432.

- (69) Li, E.; Pan, Y.; Wang, C.; Liu, C.; Shen, C.; Pan, C.; Liu, X. Multifunctional and Superhydrophobic Cellulose Composite Paper for Electromagnetic Shielding, Hydraulic Triboelectric Nanogenerator and Joule Heating Applications. *Chemical Engineering Journal* **2021**, *420*, 129864.
- (70) Zhou, Z.-H.; Liang, Y.; Huang, H.-D.; Li, L.; Yang, B.; Li, M.-Z.; Yan, D.-X.; Lei, J.; Li, Z.-M. Structuring Dense Three-Dimensional Sheet-like Skeleton Networks in Biomass-Derived Carbon Aerogels for Efficient Electromagnetic Interference Shielding. *Carbon* **2019**, *152*, 316–324.
- (71) Yan, D.-X.; Ren, P.-G.; Pang, H.; Fu, Q.; Yang, M.-B.; Li, Z.-M. Efficient Electromagnetic Interference Shielding of Lightweight Graphene/Polystyrene Composite. *Journal of Materials Chemistry* **2012**, *22* (36), 18772–18774.
- (72) Ling, J.; Zhai, W.; Feng, W.; Shen, B.; Zhang, J.; Zheng, W. G. Facile Preparation of Lightweight Microcellular Polyetherimide/Graphene Composite Foams for Electromagnetic Interference Shielding. *ACS applied materials & interfaces* **2013**, *5* (7), 2677–2684.
- (73) Chen, Z.; Xu, C.; Ma, C.; Ren, W.; Cheng, H.-M. Lightweight and Flexible Graphene Foam Composites for High-performance Electromagnetic Interference Shielding. *Advanced materials* **2013**, *25* (9), 1296–1300.
- (74) Zhang, H.-B.; Yan, Q.; Zheng, W.-G.; He, Z.; Yu, Z.-Z. Tough Graphene–Polymer Microcellular Foams for Electromagnetic Interference Shielding. *ACS applied materials & interfaces* **2011**, *3* (3), 918–924.
- (75) Shen, B.; Zhai, W.; Tao, M.; Ling, J.; Zheng, W. Lightweight, Multifunctional Polyetherimide/Graphene@ Fe₃O₄ Composite Foams for Shielding of Electromagnetic Pollution. *ACS applied materials & interfaces* **2013**, *5* (21), 11383–11391.
- (76) Wan, C.; Li, J. Graphene Oxide/Cellulose Aerogels Nanocomposite: Preparation, Pyrolysis, and Application for Electromagnetic Interference Shielding. *Carbohydrate polymers* **2016**, *150*, 172–179.
- (77) Hsiao, S.-T.; Ma, C.-C. M.; Tien, H.-W.; Liao, W.-H.; Wang, Y.-S.; Li, S.-M.; Huang, Y.-C. Using a Non-Covalent Modification to Prepare a High Electromagnetic Interference Shielding Performance Graphene Nanosheet/Water-Borne Polyurethane Composite. *Carbon* **2013**, *60*, 57–66.

- (78) Yang, Y.; Gupta, M. C.; Dudley, K. L.; Lawrence, R. W. Novel Carbon Nanotube- Polystyrene Foam Composites for Electromagnetic Interference Shielding. *Nano letters* **2005**, 5 (11), 2131–2134.
- (79) Zeng, Z.; Jin, H.; Chen, M.; Li, W.; Zhou, L.; Zhang, Z. Lightweight and Anisotropic Porous MWCNT/WPU Composites for Ultrahigh Performance Electromagnetic Interference Shielding. *Advanced Functional Materials* **2016**, 26 (2), 303–310.
- (80) Cui, C.-H.; Yan, D.-X.; Pang, H.; Jia, L.-C.; Xu, X.; Yang, S.; Xu, J.-Z.; Li, Z.-M. A High Heat-Resistance Bioplastic Foam with Efficient Electromagnetic Interference Shielding. *Chemical Engineering Journal* **2017**, 323, 29–36.
- (81) Wang, H.; Zheng, K.; Zhang, X.; Ding, X.; Zhang, Z.; Bao, C.; Guo, L.; Chen, L.; Tian, X. 3D Network Porous Polymeric Composites with Outstanding Electromagnetic Interference Shielding. *Composites Science and Technology* **2016**, 125, 22–29.
- (82) Crespo, M.; González, M.; Elías, A. L.; Pulickal Rajukumar, L.; Baselga, J.; Terrones, M.; Pozuelo, J. Ultra-light Carbon Nanotube Sponge as an Efficient Electromagnetic Shielding Material in the GHz Range. *physica status solidi (RRL)–Rapid Research Letters* **2014**, 8 (8), 698–704.
- (83) Arjmand, M.; Apperley, T.; Okoniewski, M.; Sundararaj, U. Comparative Study of Electromagnetic Interference Shielding Properties of Injection Molded versus Compression Molded Multi-Walled Carbon Nanotube/Polystyrene Composites. *Carbon* **2012**, 50 (14), 5126–5134.
- (84) Al-Saleh, M. H.; Sundararaj, U. Electromagnetic Interference Shielding Mechanisms of CNT/Polymer Composites. *Carbon* **2009**, 47 (7), 1738–1746.
- (85) Al-Saleh, M. H.; Saadeh, W. H.; Sundararaj, U. EMI Shielding Effectiveness of Carbon Based Nanostructured Polymeric Materials: A Comparative Study. *Carbon* **2013**, 60, 146–156.
- (86) Lee, T.-W.; Lee, S.-E.; Jeong, Y. G. Highly Effective Electromagnetic Interference Shielding Materials Based on Silver Nanowire/Cellulose Papers. *ACS applied materials & interfaces* **2016**, 8 (20), 13123–13132.
- (87) Yuan, Y.; Sun, X.; Yang, M.; Xu, F.; Lin, Z.; Zhao, X.; Ding, Y.; Li, J.; Yin, W.; Peng, Q. Stiff, Thermally Stable and Highly Anisotropic Wood-Derived Carbon Composite Monoliths for Electromagnetic Interference Shielding. *ACS applied materials & interfaces* **2017**, 9 (25), 21371–21381.

- (88) Ji, K.; Zhao, H.; Zhang, J.; Chen, J.; Dai, Z. Fabrication and Electromagnetic Interference Shielding Performance of Open-Cell Foam of a Cu–Ni Alloy Integrated with CNTs. *Applied Surface Science* **2014**, *311*, 351–356.
- (89) Sun, Y.; Luo, S.; Sun, H.; Zeng, W.; Ling, C.; Chen, D.; Chan, V.; Liao, K. Engineering Closed-Cell Structure in Lightweight and Flexible Carbon Foam Composite for High-Efficient Electromagnetic Interference Shielding. *Carbon* **2018**, *136*, 299–308.
- (90) Moglie, F.; Micheli, D.; Laurenzi, S.; Marchetti, M.; Primiani, V. M. Electromagnetic Shielding Performance of Carbon Foams. *Carbon* **2012**, *50* (5), 1972–1980.
- (91) Wang, X.-X.; Shu, J.-C.; Cao, W.-Q.; Zhang, M.; Yuan, J.; Cao, M.-S. Eco-Mimetic Nanoarchitecture for Green EMI Shielding. *Chemical Engineering Journal* **2019**, *369*, 1068–1077.
- (92) Wan, C.; Li, J. Graphene Oxide/Cellulose Aerogels Nanocomposite: Preparation, Pyrolysis, and Application for Electromagnetic Interference Shielding. *Carbohydrate polymers* **2016**, *150*, 172–179.
- (93) Fei, Y.; Liang, M.; Yan, L.; Chen, Y.; Zou, H. Co/C@ Cellulose Nanofiber Aerogel Derived from Metal-Organic Frameworks for Highly Efficient Electromagnetic Interference Shielding. *Chemical Engineering Journal* **2020**, *392*, 124815.

General conclusions and perspectives

The main objective of this thesis was to investigate the properties of nanocellulose and its application in nanocomposites and advanced functional materials.

In Chapter 1, the current status of research on nanocellulose has been reviewed, focusing on its physical and chemical properties, surface modification and applications as functional nanomaterial.

The research work introduced in chapter 2 originated from the following question: ‘How to improve the compatibility and enhance the interfacial adhesion between nanocellulose and a natural rubber matrix while preserving the surface hydroxyl groups beneficial for mechanical reinforcement?’ The nanocellulose surface exhibits a large number of hydroxyl groups, so the interfacial compatibility between the hydrophilic nanocellulose and the hydrophobic rubber matrix is poor and leads to aggregation of nanocellulose in the natural rubber matrix. Moreover, the insufficient interfacial adhesion between both components does not allow for effective stress transfer from the continuous phase to the filler under mechanical loading. We have demonstrated a novel concept for biobased rubbery nanocomposites, i.e., the synergistic effect of biobased reinforcing CNF-SH nanoparticles, which also possess cross-linking sites for covalent coupling to the natural rubber elastomer network. Two strategies were designed to implement the end modification of CNF, including aldimine condensation (CNF-SH-a) and carboxyamine condensation (CNF-SH-b). Elemental analysis results show that the nitrogen and sulfur content in CNF-SH-a was higher than that of CNF-SH-b; the peak intensity for N1s and S2p in CNF-SH-a in the XPS characteristic element spectrum was stronger than that of CNF-SH-b, the amount of silver nanoparticles labeled on CNF-SH-a was significantly higher than for CNF-SH-b in TEM images, indicating that the grafting efficiency of the former may be higher than that of the latter. Combining FTIR and ^{13}C ssNMR results, it was shown that covalent bonds are formed and controlled between the thiol group of CNF-SH-a and the unsaturated double bond in the NR matrix. CNF-SH-a showed improved hydrophobicity and good dispersibility

in hydrophobic medium. Nanocomposite films with homogeneous dispersion of CNF-SH-a in NR matrix were prepared by a casting/evaporation method. The cross-linking density of the NR/CNF-SH-a sample was confirmed to significantly increase when increasing the CNF-SH-a content. This is due to the covalent cross-links formed at the filler-matrix interface photochemically initiated by thiol-ene reactions. The NR/CNF-SH-a-10 nanocomposite showed significantly higher values of tensile strength (5.83 ± 0.31 MPa), Young's modulus (45.25 ± 4.34 MPa), and elongation at break ($543 \pm 21\%$) compared to neat NR and NR/CNF nanocomposites. As the present concept is general in material synthesis and design, we foresee that this green method for reinforcing NR matrix with end modified CNF-SH can have potential application in textile, printing, automobile and machinery manufacturing fields.

Chapter 3 focused on the development of highly conductive composites with low percolation threshold, good processability and adequate mechanical properties. Solution mixing, melt blending and in-situ polymerization are generally used to fabricate conductive composites. However, these methods require high conductive filler contents to form a continuous conductive network, resulting in the deterioration of the mechanical properties, processing difficulty and high production cost. We reported an easily implementable and efficient strategy to prepare NR/CNC/GO nanocomposites hosting a 3D hierarchical multiscale conductive network based on a CNC-assisted latex assembly approach. CNC can significantly improve the dispersion of GO in aqueous medium through the formation of CNC/GO nanohybrids. The prepared CNC/GO nanohybrids can be associated with NR latex by a simple casting/evaporation method. The latex microspheres act as impenetrable domains during the film formation due to their high viscosity and condition the formation of a continuous 3D connected CNC/GO network. The Zeta potential of the CNC/GO nanohybrid suspension was -44.7 mV and a well-dispersed suspension was observed even after standing for 24 h. These results clearly demonstrated that CNC can effectively stabilize the GO suspension. The FTIR results confirmed that strong interfacial interactions occurred in the CNC/GO hybrids.

It can be ascribed to hydrogen bonding interaction between the surface hydroxyl groups from CNC and oxygen-containing groups borne by GO. SEM observations highlight a uniform 3D porous network structure that was probably formed within the NR matrix during the casting process. The formation of this conductive network structure significantly enhanced the electrical conductivity and lowered the electrical percolation threshold of the composites. The electrical conductivity percolation threshold for NR/CNC/GO nanocomposites was 3-fold lower than that of NR/GO nanocomposites. Moreover, the electrical conductivity for NR/CNC/GO-4 nanocomposite (sample with 4 wt% GO) was 9 orders of magnitude higher than that of NR/GO-4 nanocomposite (CNC-free sample with 4 wt% GO). CNC played a key role in assisting the formation of a 3D assembled conductive structure and enhancing the robustness of the structure as a rigid template, as shown by the improved tensile strength and Young's modulus. This unique combination of high electrical conductivity and good mechanical properties makes the developed NR/CNC/GO nanocomposites strong candidates for applications in stretchable electronics, wearable sensors and energy storage.

Specialized biobased components have emerged as a promising trend to limit the use of petroleum derivatives. Conversely, the current use of electronic systems has conditioned the emission of electromagnetic waves, which interfere with high-precision devices and harm human health. Thus, robust, ultralight, and conductive nanocellulose-based aerogels combined with carbon nanotubes appear as a promising electromagnetic interference (EMI) shielding biomaterial to reduce the dispersion of microwaves emitted or received from a device. In chapter 4, we proposed a reliable aerogel system for deflecting radiation by integrating Tempo-oxidized cellulose nanofibrils (TCNF), cationic cellulose nanocrystals (CCNC), and sodium alginate (SA), with carbon nanotubes (CNTs) at various concentrations. After inducing gelation, the aerogels were obtained by freeze drying. After surface cationization, the surface hydroxyl groups of CNC were converted to positive quaternary ammonium groups, as indicated by the zeta-potential result ($+31.9 \pm 0.5$ mV) for CCNC. Specifically, TCNF and CCNC

suspensions exhibit high electrical charges, which confer them good stability due to electrostatic repulsion, making them less prone to aggregation and particle size increase. This finding validates the use of highly charged nanocellulose compositions for aerogel processing, as high colloidal stability is important to maintain high specific surface area and porosity of the final aerogel. In addition, cationic CNC complementing anionic TCNF form a nanocellulose matrix with opposite charges, in which the electrostatic forces balance to achieve an overall net attraction between the particles. According to Zeta potential and FTIR analysis data of nanocellulose, the aerogel structure was induced by electrostatic attraction and H-bonds between the cellulosic matrix and the nanofiller. Finally, lightweight (density < 73.05 mg/cm³), highly porous (porosity > 96.38%), conductive (up to 71,43 S/cm), mechanically resistant, and EMI protective aerogels (EMI shielding efficiency > 20 dB) were obtained, proving their potential to be used as green and lightweight shielding elements against electromagnetic radiation.

To complement the research presented in this thesis, some research topics may also be carried out in future work.

In chapter 2:

1. How to improve the grafting efficiency of CNF end functions and further characterized the successful end modification?
2. How to improve the cross-linking density of CNF-SH with the rubber matrix?
3. Further characterization of the interaction between nanocellulose and the NR matrix deserves to be conducted.
4. Cellulose II nanofibrils with antiparallel arrangement of cellulose chains could be used. What would be the impact on the cross-linking and the structure of the material?

In chapter 3:

1. A more direct and clearer characterization of the CNC distribution in the NR matrix could be implemented.

2. Further characterization would be desirable to clarify the hydrogen bonding interactions between CNC and graphene oxide.
3. It would be interesting to prepare flexible wearable sensor materials from the developed materials that have shown excellent mechanical properties and sensitive response.

In Chapter 4:

1. Different methods of cationic modification of CNC could be investigated.
2. The physical or chemical cross-linking of the prepared aerogels can be considered to further increase their mechanical properties.
3. Due to the excellent mechanical properties and electrical conductivity of the developed aerogels, it can be extended to multifunctional sensor applications.

Extended French Abstract – Résumé en Français

La cellulose est la ressource polymère renouvelable à structure amphiphile la plus répandue dans la biosphère, avec une production annuelle d'environ $7,5 \times 10^{10}$ tonnes.¹ Ses principales sources sont les suivantes : (i) les résidus agricoles (tiges de maïs, bagasse, coques de noix de coco, paille de riz, épis de maïs, enveloppes de blé, balles de riz et résidus d'huile de palme) ; (ii) le bois ; (iii) les déchets alimentaires ; (iv) les cultures ; et (v) les déchets de papier et de carton.²⁻⁴ Cette ressource pratiquement illimitée de cellulose durable fournit un matériau doté d'excellentes propriétés physiques et chimiques qui peut être utilisé dans un large éventail d'applications.⁵ Dans l'industrie, la cellulose est largement utilisée dans le papier, les textiles, les explosifs et les fibres alimentaires.⁶ La cellulose contient à la fois des régions cristallines et amorphes, et la nanocellulose, la forme nanométrique de la cellulose, peut être préparée par un procédé mécanique ou chimique, qui peut être combiné à un traitement enzymatique. L'unité répétitive de la chaîne de cellulose est un dimère de D-glucose. L'extrémité de chaque chaîne de cellulose contient un groupe hémiacétal, qui confère une asymétrie dans la direction de la chaîne de cellulose.

La nanocellulose présente plusieurs des excellentes propriétés de la cellulose, notamment la biocompatibilité, la faible densité, la non-toxicité et la biodégradabilité. Elle possède également des propriétés distinctives telles qu'une capacité de renforcement élevée, une résistance mécanique et des propriétés d'auto-assemblage ajustables en milieu aqueux, principalement attribuées à la taille, la forme, la chimie de surface, le facteur de forme élevé et la haute cristallinité uniques de ces nanoparticules.⁷ Le terme "nanocellulose" inclut différents nanomatériaux à base de cellulose dont les propriétés chimiques et physiques varient souvent en fonction de leur source, mais surtout de leur méthode d'extraction : nanocristal de cellulose (CNC), nanofibrilles de cellulose (CNF) et nanocellulose bactérienne (BNC). Le CNC et les CNF sont obtenus par des méthodes descendantes, impliquant respectivement un traitement chimique ou

mécanique. Le cisaillement mécanique ou l'hydrolyse acide vont d'abord affaiblir et détruire les domaines amorphes et les plus petites régions cristallines pour produire la nanocellulose souhaitée. Le CNC est un fragment hautement cristallin en forme de bâtonnet obtenu par hydrolyse acide jusqu'à l'échelle nanométrique. Les CNF peut être obtenu par cisaillement mécanique des fibres cellulosiques, généralement précédé d'une hydrolyse acide contrôlée, ou d'un prétraitement chimique ou enzymatique, ce qui permet de réduire la consommation énergétique associée à ce traitement. Elle présente des structures et une chimie de surface différentes, selon la méthode de production, et est généralement plus longue que le CNC, à l'échelle du micron.⁷ La BNC est obtenue par une méthode ascendante, en utilisant des cultures bactériennes pour synthétiser la nanocellulose. D'autres noms pour les matériaux de nanocellulose peuvent être trouvés dans la littérature, incluant cellulose nanofibrillée, cellulose microfibrillée, nanofibrilles de cellulose, nanowhiskers de cellulose, trichites (ou whiskers) de cellulose et cellulose nanocristalline.

Au XXI^e siècle, la demande en nourriture, en eau et en énergie explose en raison de la croissance de la population mondiale et du développement économique rapide. La société devrait s'appuyer davantage sur les ressources renouvelables de la biomasse pour répondre à cette demande croissante. Le développement durable de la société devrait se concentrer davantage sur les produits recyclables, facilement dégradables, respectueux de l'environnement et présentant peu de risques pour la santé et la sécurité. Grâce à son module de Young de 100-130 GPa, à sa grande surface spécifique et à sa haute cristallinité, la nanocellulose devrait être utilisée pour la fabrication et le développement de diverses nouvelles applications utiles à faible impact environnemental et social.⁸ La nanocellulose est dérivée de la biomasse qui est une ressource renouvelable et abondante et est considérée comme une bonne alternative au pétrole comme source de biocarburants et de divers produits chimiques. La nanocellulose peut désormais être produite industriellement, et sa capacité de production peut atteindre plusieurs tonnes par jour.⁹

La modification chimique de surface est très importante pour la fonctionnalité et la facilité de mise en forme des nanocomposites, c'est pourquoi nous nous concentrons sur le grand nombre de modifications de surface actuelles dans le chapitre 1. Les propriétés de surface de la nanocellulose peuvent être facilement ajustées par des méthodes de modification physique et chimique.¹⁰⁻¹² La nanocellulose modifiée en surface est une excellente plateforme qui peut être ajustée en fonction de différents objectifs. Les larges applications de la nanocellulose sont limitées par sa faible dispersabilité dans les solvants non polaires, son incompatibilité et sa faible adhésion interfaciale aux substrats hydrophobes. Pour résoudre ce problème, les chercheurs ont tenté de modifier la surface et la structure de la nanocellulose, en ciblant principalement la modification physique et chimique des groupes hydroxyle pendants de la surface (-OH).

La nanocellulose a des applications très diverses dans de nombreux domaines interdisciplinaires. Lorsque la nanocellulose est entrelacée, des nanocomposites aux propriétés mécaniques et à la porosité élevées peuvent être obtenus, comme le nanopapier, les films de nanocellulose, les aérogels et les hydrogels. Son application peut être étendue à la fabrication du papier, à l'assainissement de l'environnement, à la biologie, à la médecine, à l'optoélectronique et aux applications d'ingénierie.¹³⁻¹⁶ La nanocellulose peut être utilisée pour renforcer les nanocomposites en raison de la formation d'un réseau continu solide dans la matrice avec une rigidité et une résistance à la traction élevées.^{17,18} Le développement et l'application de composites polymères rigides renforcés par la nanocellulose à partir de ressources renouvelables ont attiré l'attention du monde académique et de l'industrie. Avec la sensibilisation croissante du public au respect de l'environnement et à la durabilité, la nanocellulose est appelée à jouer un rôle important dans les applications commerciales.

L'objectif principal de cette thèse était d'étudier les propriétés de la nanocellulose et son application dans les nanocomposites et les matériaux fonctionnels avancés.

Le chapitre 1 présente l'état actuel de la recherche sur la nanocellulose, en mettant l'accent sur ses propriétés physiques et chimiques, la modification de sa surface et ses applications en tant que nanomatériau fonctionnel.

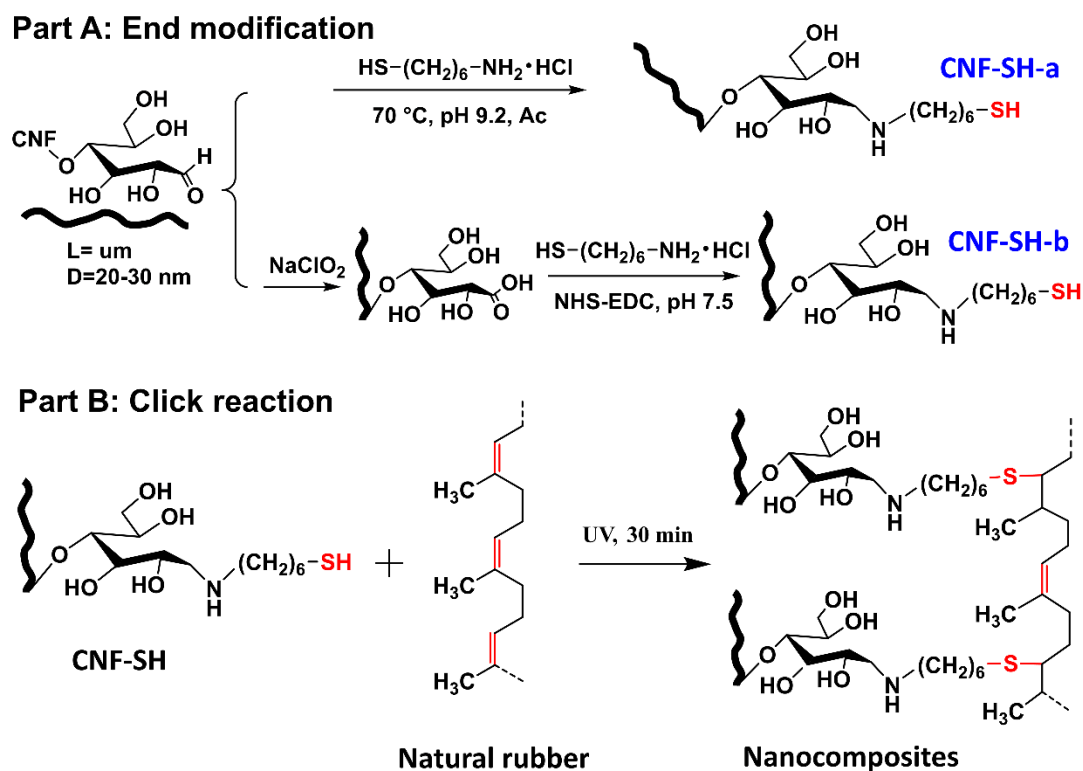


Figure 1. Modification de l'extrémité réductrice des CNF et préparation des nanocomposites.

Le travail de recherche présenté dans le chapitre 2 est né de la question suivante : "Comment améliorer la compatibilité et renforcer l'adhésion interfaciale entre la nanocellulose et une matrice de caoutchouc naturel tout en préservant les groupes hydroxyles de surface bénéfiques pour le renforcement mécanique ?". Pour améliorer la compatibilité interfaciale entre la nanocellulose hydrophile et la matrice de caoutchouc hydrophobe, nous avons développé un nouveau concept pour les nanocomposites à base de caoutchoucs biosourcés, c'est-à-dire l'effet synergique des nanoparticules CNF-SH de renforcement biosourcées, qui possèdent également des sites de réticulation pour un couplage covalent au réseau élastomère du caoutchouc naturel. Deux stratégies ont été conçues pour mettre en œuvre la modification finale des CNF, notamment la condensation d'aldimine (CNF-SH-a) et la condensation de carboxyamine (CNF-SH-b), comme le montre la figure 1. L'analyse élémentaire, les résultats XPS et TEM ont indiqué que l'efficacité de greffage du CNF-SH-a peut être supérieure à celle du CNF-SH-b. En combinant les résultats FTIR et ^{13}C ssNMR, il a

été démontré que des liaisons covalentes sont formées et contrôlées entre le groupe thiol de CNF-SH-a et la double liaison insaturée de la matrice NR. Nous avons montré que la densité de réticulation de l'échantillon NR/CNF-SH-a augmente de manière significative lorsque la teneur en CNF-SH-a augmente. Le nanocomposite NR/CNF-SH-a-10 a montré des valeurs significativement plus élevées de résistance à la traction (de 0,33 MPa à 5,83 MPa), de module de Young (de 0,48 MPa à 45,25 MPa) et de déformation à rupture (de 2,63 MJ m⁻³ à 0,45 MJ.m⁻³) par rapport aux nanocomposites NR/CNF. Comme ce concept est général dans la synthèse et la conception des matériaux, nous prévoyons que cette méthode verte pour renforcer la matrice de NR avec des CNF-SH modifiés peut avoir des applications potentielles dans les domaines du textile, de l'impression, de l'automobile et de la fabrication de machines.

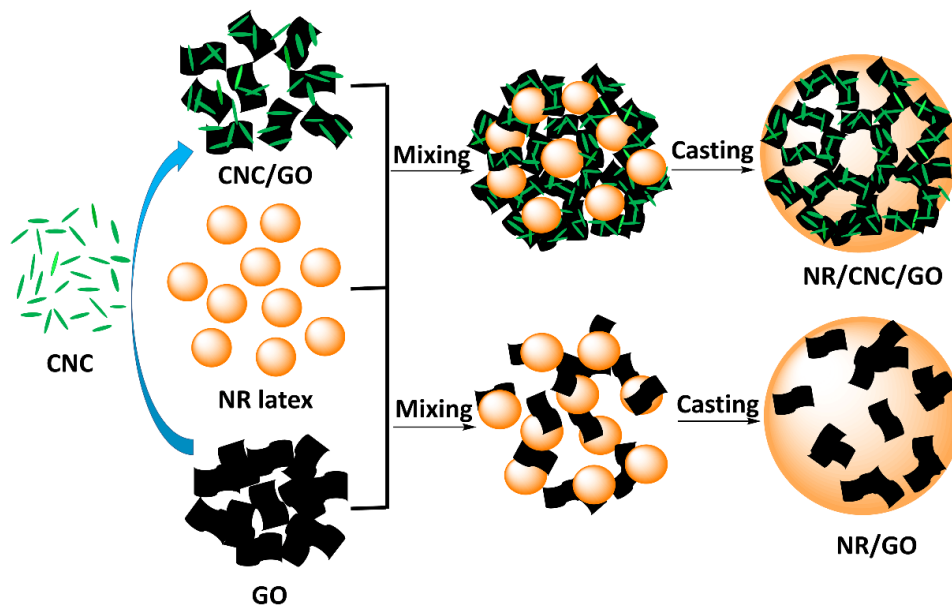


Figure 2. Illustration schématique de la préparation des nanocomposites NR/CNC/GO et NR/GO avec réseau conducteur 3D.

Le chapitre 3 s'est attaché au développement de composites fortement conducteurs avec un faible seuil de percolation, une bonne facilité de mise en œuvre et des propriétés mécaniques adéquates. Nous avons développé une stratégie efficace et facile à mettre en œuvre pour préparer des nanocomposites NR/CNC/GO présentant un réseau conducteur multi-échelle hiérarchique 3D basé sur une approche d'assemblage de latex

assistée par CNC, comme le montre la figure 2. Le CNC peut améliorer de manière significative la dispersion du GO dans un milieu aqueux par la formation de nanohybrides CNC/GO. Les nanohybrides CNC/GO préparés peuvent être associés au latex NR par une simple méthode de coulée/évaporation. Les microsphères de latex agissent comme des domaines impénétrables pendant la formation du film en raison de leur viscosité élevée et conditionnent la formation d'un réseau CNC/GO continu connecté en 3D. Les résultats de l'IRTF ont confirmé que de fortes interactions interfaciales se sont produites dans les hybrides CNC/GO. Cela peut être attribué à l'interaction par liaison hydrogène entre les groupes hydroxyle de surface du CNC et les groupes contenant de l'oxygène portés par le GO. Le seuil de percolation de la conductivité électrique des nanocomposites NR/CNC/GO était 3 fois inférieur à celui des nanocomposites NR/GO. De plus, la conductivité électrique du nanocomposite NR/CNC/GO-4 (échantillon avec 4 % en poids de GO) était supérieure de 9 ordres de grandeur par rapport à celle du nanocomposite NR/GO-4 (échantillon sans CNC avec 4 % en poids de GO). Le CNC a joué un rôle clé en aidant à la formation d'une structure conductrice assemblée en 3D et en améliorant la robustesse de la structure en tant que gabarit rigide, comme le montre l'amélioration de la résistance à la traction et du module d'Young. Cette combinaison unique de conductivité électrique élevée et de bonnes propriétés mécaniques fait des nanocomposites NR/CNC/GO développés de bons candidats pour des applications dans l'électronique flexible, les capteurs portables et le stockage d'énergie.

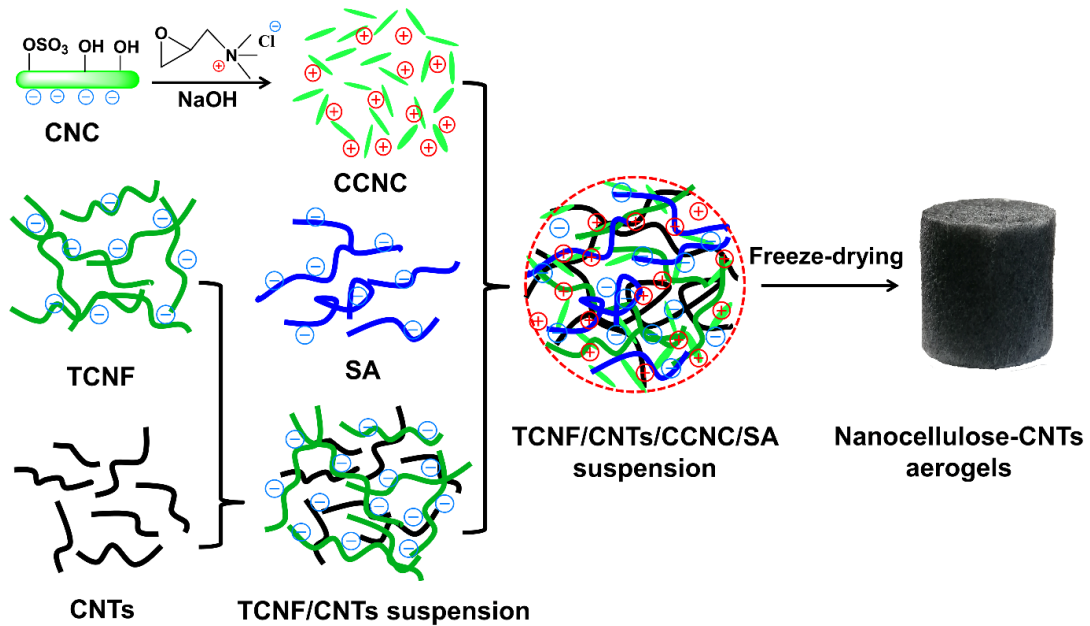


Figure 3. Illustration schématique des aérogels composites nanocellulose-CNTs.

Les composants spécialisés d'origine biologique apparaissent comme une tendance prometteuse pour limiter l'utilisation des dérivés du pétrole. Ainsi, les aérogels à base de nanocellulose, robustes, ultralégers et conducteurs, associés à des nanotubes de carbone, apparaissent comme un biomatériau de blindage contre les interférences électromagnétiques (IEM) prometteur pour réduire la dispersion des micro-ondes émises ou reçues d'un dispositif. Dans le chapitre 4, nous avons proposé un système d'aérogel fiable pour dévier les radiations en intégrant des nanofibrilles de cellulose tempo-oxydées (TCNF), des nanocristaux de cellulose cationiques (CCNC) et de l'alginate de sodium (SA), avec des nanotubes de carbone (CNT) à différentes concentrations, comme le montre la figure 3. Plus précisément, les suspensions de NTC et de CCNC présentent des charges électriques élevées, ce qui leur confère une bonne stabilité due à la répulsion électrostatique, les rendant moins enclins à l'agrégation et à l'augmentation de la taille des particules. Cette découverte valide l'utilisation de compositions de nanocellulose fortement chargée pour la mise en forme d'aérogels, car une stabilité colloïdale élevée est importante pour maintenir une surface spécifique et une porosité élevées de l'aérogel final. En outre, les CNC cationiques complémentaires des TCNF anioniques forment une matrice de nanocellulose avec des charges opposées,

dans laquelle les forces électrostatiques s'équilibrent pour obtenir une attraction nette globale entre les particules. Selon les données du potentiel Zeta et de l'analyse IRTF de la nanocellulose, la structure de l'aérogel a été induite par l'attraction électrostatique et les liaisons H entre la matrice cellulosique et la nanocharge. Enfin, des aérogels légers (densité < 73,05 mg/cm³), à haute porosité (porosité > 96,38 %), conducteurs (jusqu'à 71,43 S/cm), mécaniquement résistants et protecteurs contre les EMI (efficacité du blindage EMI > 20 dB) ont été obtenus, prouvant leur potentiel à être utilisés comme éléments de blindage verts et légers contre les rayonnements électromagnétiques.

References

- (1) Thomas, B.; Raj, M. C.; Athira, K. B.; Rubivah, M. H.; Joy, J.; Moores, A.; Drisko, G. L.; Sanchez, C. Nanocellulose, a Versatile Green Platform: From Biosources to Materials and Their Applications. *Chem. Rev.* **2018**, *118* (24), 11575–11625.
- (2) Metzger, J. O.; Hüttermann, A. Sustainable Global Energy Supply Based on Lignocellulosic Biomass from Afforestation of Degraded Areas. *Naturwissenschaften* **2009**, *96* (2), 279–288.
- (3) Mood, S. H.; Golfeshan, A. H.; Tabatabaei, M.; Jouzani, G. S.; Najafi, G. H.; Gholami, M.; Ardjmand, M. Lignocellulosic Biomass to Bioethanol, a Comprehensive Review with a Focus on Pretreatment. *Renewable and Sustainable Energy Reviews* **2013**, *27*, 77–93.
- (4) Limayem, A.; Ricke, S. C. Lignocellulosic Biomass for Bioethanol Production: Current Perspectives, Potential Issues and Future Prospects. *Progress in energy and combustion science* **2012**, *38* (4), 449–467.
- (5) Abitbol, T.; Rivkin, A.; Cao, Y.; Nevo, Y.; Abraham, E.; Ben-Shalom, T.; Lapidot, S.; Shoseyov, O. Nanocellulose, a Tiny Fiber with Huge Applications. *Current opinion in biotechnology* **2016**, *39*, 76–88.
- (6) Habibi, Y. Key Advances in the Chemical Modification of Nanocelluloses. *Chemical Society Reviews* **2014**, *43* (5), 1519–1542.
- (7) Klemm, D.; Kramer, F.; Moritz, S.; Lindström, T.; Ankerfors, M.; Gray, D.; Dorris, A. Nanocelluloses: A New Family of Nature-based Materials. *Angewandte Chemie International Edition* **2011**, *50* (24), 5438–5466.
- (8) Usov, I.; Nyström, G.; Adamcik, J.; Handschin, S.; Schütz, C.; Fall, A.; Bergström, L.; Mezzenga, R. Understanding Nanocellulose Chirality and Structure–Properties Relationship at the Single Fibril Level. *Nature*

- communications* **2015**, *6* (1), 1–11.
- (9) Reid, M. S.; Villalobos, M.; Cranston, E. D. Benchmarking Cellulose Nanocrystals: From the Laboratory to Industrial Production. *Langmuir* **2017**, *33* (7), 1583–1598.
- (10) Biyani, M. V.; Foster, E. J.; Weder, C. Light-Healable Supramolecular Nanocomposites Based on Modified Cellulose Nanocrystals. *ACS Macro Letters* **2013**, *2* (3), 236–240.
- (11) Carlmark, A.; Malmström, E. Atom Transfer Radical Polymerization from Cellulose Fibers at Ambient Temperature. *Journal of the American Chemical Society* **2002**, *124* (6), 900–901.
- (12) Roy, D.; Semsarilar, M.; Guthrie, J. T.; Perrier, S. Cellulose Modification by Polymer Grafting: A Review. *Chemical Society Reviews* **2009**, *38* (7), 2046–2064.
- (13) Zander, N. E.; Dong, H.; Steele, J.; Grant, J. T. Metal Cation Cross-Linked Nanocellulose Hydrogels as Tissue Engineering Substrates. *ACS applied materials & interfaces* **2014**, *6* (21), 18502–18510.
- (14) Wang, Z.; Carlsson, D. O.; Tammela, P.; Hua, K.; Zhang, P.; Nyholm, L.; Strømme, M. Surface Modified Nanocellulose Fibers Yield Conducting Polymer-Based Flexible Supercapacitors with Enhanced Capacitances. *ACS nano* **2015**, *9* (7), 7563–7571.
- (15) Luo, W.; Schardt, J.; Bommier, C.; Wang, B.; Razink, J.; Simonsen, J.; Ji, X. Carbon Nanofibers Derived from Cellulose Nanofibers as a Long-Life Anode Material for Rechargeable Sodium-Ion Batteries. *Journal of Materials Chemistry A* **2013**, *1* (36), 10662–10666.
- (16) Weishaupt, R.; Siqueira, G.; Schubert, M.; Kämpf, M. M.; Zimmermann, T.; Maniura-Weber, K.; Faccio, G. A Protein-Nanocellulose Paper for Sensing Copper Ions at the Nano-to Micromolar Level. *Advanced Functional Materials* **2017**, *27* (4), 1604291.
- (17) Khalil, H. A.; Bhat, A. H.; Yusra, A. I. Green Composites from Sustainable Cellulose Nanofibrils: A Review. *Carbohydrate polymers* **2012**, *87* (2), 963–979.
- (18) Siró, I.; Plackett, D. Microfibrillated Cellulose and New Nanocomposite Materials: A Review. *Cellulose* **2010**, *17* (3), 459–494.

Résumé

Ce projet avait pour but d'étudier certaines applications fonctionnelles de la nanocellulose. Pour améliorer la compatibilité interfaciale entre la nanocellulose et une matrice hydrophobe, des groupes thiol actifs ont été introduits à l'extrémité réductrice des nanofibrilles de cellulose. Des nœuds de réticulation covalents ont été formés entre groupes thiol et doubles liaisons du caoutchouc naturel via des réactions thiol-ène initiées par voie photochimique. Pour obtenir des composites fortement conducteurs avec un faible seuil de percolation et des propriétés mécaniques adéquates, des nanocomposites nanocristaux de cellulose/oxyde de graphène/caoutchouc naturel présentant un réseau conducteur multi-échelle hiérarchique en 3D ont été développés. Un aérogel a été préparé en intégrant des nanofibrilles de cellulose oxydée, des nanocristaux de cellulose cationiques, de l'alginate de sodium et des nanotubes de carbone. Une bonne efficacité de blindage EMI, une faible densité, une forte conductivité et une bonne résistance mécanique ont été obtenues.

Mots-clés: Nanocellulose; Modification de l'extrémité, Réaction click; Nanocomposites; Nanostructure hiérarchisée en 3D; Aérogels; Blindage EMI.

Abstract

The aim of this project was to investigate some functional application of nanocellulose. To improve the interfacial compatibility between nanocellulose and a hydrophobic matrix, active thiol groups were introduced at the reducing end of cellulose nanofibrils. Covalent cross-links were formed between thiol groups and double bonds of natural rubber via photochemically initiated thiol-ene reactions. To obtain highly conductive composites with low percolation threshold and adequate mechanical properties, cellulose nanocrystal/graphene oxide/natural rubber nanocomposites hosting a 3D hierarchical multiscale conductive network were developed. An aerogel was prepared by integrating oxidized cellulose nanofibrils, cationic cellulose nanocrystals, sodium alginate and carbon nanotubes. Good EMI shielding, low density, high conductivity and good mechanical strength were achieved.

Keywords : Nanocellulose; End modification, Click reaction; nanocomposites; 3D hierarchical nanostructure ; Aerogels; EMI shielding.